On the Oceanic Impacts of Greenland's Tip Jets

A thesis submitted to the School of Environmental Sciences of the University of East Anglia in partial fulfilment of the requirements for the degree of Doctor of Philosophy

By David Sproson

January 2011

Abstract

The steep terrain and high orography of Greenland, and its location in the central North Atlantic, leaves it ideally located to interact with atmospheric flow, particularly synoptic-scale weather systems as they move across the Atlantic storm-track between North America and Europe. This interaction leads to the formation of a variety of intense mesoscale weather systems around Greenland. Barrier winds form as air is advected towards the island, but is unable to pass over it, easterly and westerly tip jets form as air is accelerated around the southern-most tip of Greenland and mesocyclones may develop in the lee of the mountain.

All of these mesoscale systems have been shown to be associated with intense air-sea interaction. In particular the westerly tip jet has been implicated in forcing open-ocean convection in the Irminger Sea, and there has been speculation that the easterly jet may play a similar role in the Labrador Sea to the south-west of Cape Farewell. Here the impacts of both easterly and westerly tip jets on the oceanic circulation are investigated, through a combination of observational studies and numerical modelling: using firstly a simple 1-D mixed-layer model and secondly a 3-D global general circulation model.

We find that the easterly tip jet cannot force convection in the Labrador Sea in an analogous way to the westerly tip jet in the Irminger Sea; the synoptic conditions ubiquitously associated with the easterly jets result in only modest heat fluxes which cannot significantly impact the depth of the mixed-layer. However, once parameterized into an ocean general circulation model, both tip jets had an important impact on the circulation of the North Atlantic. Notably, the westerly jet caused a significant cooling in both the surface and deep waters in the Labrador Sea, an increase in subpolar gyre transport of up to 2.5 Sv and a spin-up of the Irminger Gyre, suggesting the jet plays a role in preconditioning for, as well as triggering of, open-ocean convection in the subpolar seas.

Acknowledgements

First of all, I would like to thank my supervisors, Ian Renfrew and Karen Heywood for their patience and guidance; for their interest and interesting discussions; and for their ability to subtly put boot to backside on the occasions it proved necessary. Thanks also for your efforts proofreading this thesis, without which it would undoubtedly be riddled with, grammatical errors and spelling mitsakes.

Thanks to Grant Bigg at Sheffield for getting me going with the FRUGAL model, and to Grant, Alan Condron and Martin Wadley for helping to diagnose various problems I encountered with it. I'm sure that without your input I would have spent significantly more time banging my head against my desk. For this, I suspect, my desk is also grateful. While we're on the subject, many thanks to Julie Harold and Chris Collins for all issues cluster related.

To all those who have spent too much time in the Grad bar, the Alex or those blurry places we end up at afterwards: cheers! I'll mention no names, but you all know who you are. Most of the time. Thanks also to the 3.16 geologists and their inexplicable collections of rocks for putting up with a slightly grumpy oceanographer skulking in the corner of the office.

I've been lucky enough to get away on fieldwork a couple of times during this Ph.D. Hat tips to everyone involved in the Greenland Flow Distortion experiment, particularly the folk from FAAM, and to Bob Pickart and everyone aboard the RV Knorr during KN194-4. Good times.

Finally, thanks to my family, particularly my parents, Jan & John, for their bottomless reserves of love, support & encouragement. I wouldn't be here without you, figuratively and literally.

This work was funded by a studentship from the Natural Environment Research Council (NERC).

Dave Sproson, June 2010.

Acronyms

(A)MOC	(Atlantic) Meridional Overturning Circulation
DSOW	Denmark Strait Overflow Water
DWBC	Deep Western Boundary Current
ECMWF	European Centre for Medium Range Weather Forecasting
EOF	Empirical Orthogonal Function
FRUGAL	Fine Resolution Greenland and Labrador (ocean model)
GFDex	Greenland Flow Distortion experiment
GIN	Greenland-Iceland-Norwegian
GIS	Greenland-Iceland-Scotland
GTS	Global Telecommunications System
ILLA	Icelandic Low Latitude
ISOW	Iceland-Scotland Overflow Water
LSW	Labrador Sea Water
MOM	Modular Ocean Model
NAO	North Atlantic Oscillation
NAC	North Atlantic Current
NARR	North American Regional Reanalysis
NCAR	National Center for Atmospheric Research
NCEP	National Center for Environmental Prediction
NOC	National Oceanography Centre
NWP	Numerical Weather Prediction
(O)GCM	(Ocean) General Circulation Model
PALACE	Profiling Autonomous Lagrangian Circulation Explorer
PV	Potential vorticity
SEA	Southampton-East Anglia (ocean model)
SPG	Subpolar gyre
UKMO	United Kingdom Meteorological Office
WOCE	World Ocean Circulation Experiment

Symbols

A_m	Horizontal eddy viscosity
A_h	Horizontal eddy diffusivity
b	Buoyancy
C_D	Drag coefficient
c_p	Specific heat capacity
E	Evaporation
f	Coriolis frequency
g	Gravitational constant
h	Mixed-layer depth
$\mathbf{i}$	Unit vector in x-direction
$\mathbf{j}$	Unit vector in y-direction
$\mathbf{k}$	Unit vector in z-direction
k	Von Kármán constant
K_m	Vertical eddy viscosity
K_h	Vertical eddy diffusivity
N^2	Brünt-Väisälä frequency
L	Specific heat of vaporization
P	Precipitation
p	Pressure
Q	Heat flux
R_b	Bulk Richardson number
R_g	Gradient Richardson number
Re	Reynolds Number
Ro	Rossby Number
S	Salinity
T	Temperature

t_*, q_*	Scaling lengths for temperature and humidity
u_*	Friction velocity
u	Zonal velocity
v	Meridional Velocity
w	Vertical velocity
z_0, z_{0t}, z_{0q}	Roughness lengths for momentum, temperature, moisture
α	Thermal expansion coefficient
β	Haline expansion coefficient
κ	Diffusivity
λ	Longitude
ρ	Density
τ	Wind stress
ϕ	Latitude
$\mathbf{\Omega}$	Angular rotation of the Earth

Contents

List of tables

List of figures

Chapter 1

Introduction

1.1 Oceans and Their Role in the Climate System

1.1.1 Climate

The Oxford English Dictionary defines climate as

> "[the] general weather conditions prevailing in an area over a long period."

Such a definition, however, is far from adequate and conceals the internal variability of the Earth system on almost every timescale and the highly complex interactions between the atmosphere, hydrosphere, cryosphere, biosphere and geosphere which together control such variability.

The oceans cover around 71% of the surface of the Earth to an average depth of around 4000 m. Such a vast quantity of any fluid could be expected to contain massive amounts of internal energy, and this is especially true for the ocean, whose main constituent, water, has one of the highest heat capacities (and latent heat of fusion and vaporisation) of any chemical. The upper few metres of the oceans thus exceeds heat capacity of the entire atmosphere, and the storage of such a vast quantity of thermal energy acts like the 'fly-wheel' of the climate system.

1.1.2 Heat Transport

The spherical nature of the Earth's surface and the inclination of the Earth to the Sun results in a large discrepancy between the solar radiation received on the surface of the Earth between the equator and the high latitudes. This discrepancy leads to a constant

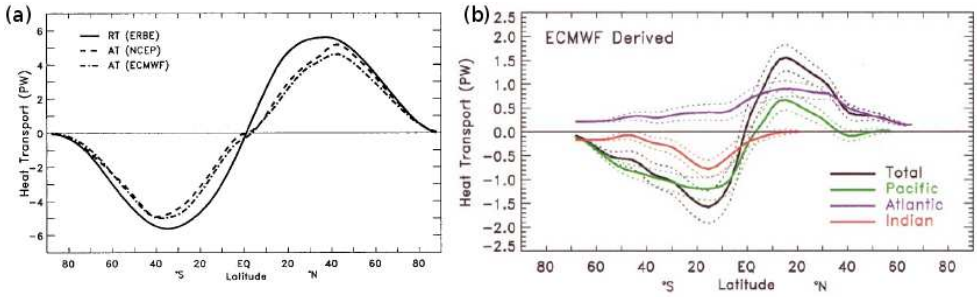

Figure 1.1: (a) Meridional heat transport required to maintain the observed temperature distribution calculated from top of atmosphere (TOA) radiation fluxes and estimates of the atmospheric contribution to this transport calculated from NCEP and ECMWF global reanalysis products. (b) Meridional heat transport provided by the oceans, total and per-basin. Both panels adapted from Trenberth and Caron (2001).

radiative heating in the low latitudes and a constant radiative cooling in the polar regions (Gill, 1982). In order to maintain the climate and heat distribution observed, there must be a significant transport of heat between the equator and the poles. In Figure 1.1(a) we can see the total meridional heat transport that is required to balance this radiative discrepancy, which peaks at around 35 °N/S. Also shown is the total atmospheric meridional heat transport, $\iint c_p \rho_a v T \, \mathrm{d}z \, \mathrm{d}\lambda$, calculated from NCEP (dashed line) and ECMWF (dot-dashed line) are also shown. Clearly the atmosphere cannot provide all of the heat transport required to account for the observed temperature distribution; the residual between these is the meridional heat transport provided by the oceans. In Figure 1.1(b) we can see the heat transport provided by the oceans as a whole and partitioned by the major basins. The oceanic heat transport peaks at around 15 ° N/S, where it may reach 2 PW, approximately the same heat transported poleward by the atmosphere at similar latitudes. Note that there is a distinct asymmetry in heat transport between the basins, with the Atlantic ocean transporting heat northwards at all latitudes, peaking at around 20 °N.

Estimates of oceanic meridional heat transport can also be made through direct measurements of ocean velocity and temperature. Much of the northward mass transport occurs in the region of the western boundary current. In the Atlantic, for example, this can be relatively easily measured as it passes the Florida Straits, where the boundary current is $<$100 km in zonal extent. Northward transport away from the western boundary is calculated as an Ekman transport, and the interior geostrophic transport is calculated from observed profiles of temperature and salinity, with a reference level set to ensure

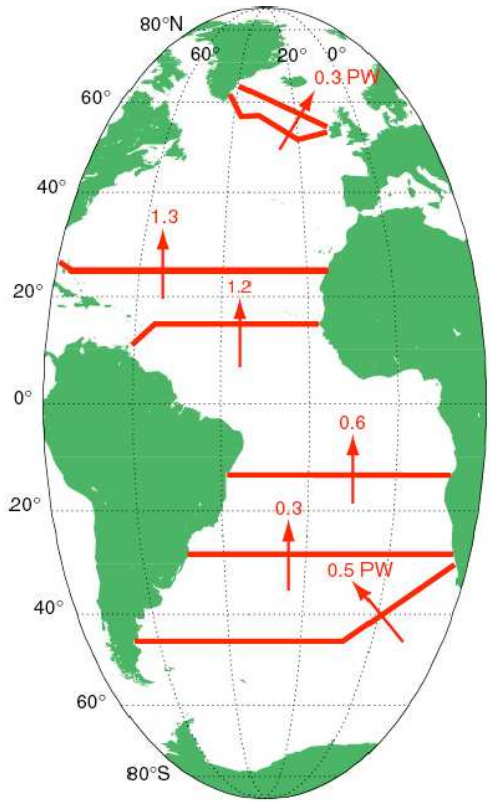

Figure 1.2: Northward ocean heat transport in PW ($= 1 \times 10^{15}$ W) through the Atlantic ocean, calculated from oceanic sections obtained during the WOCE, from Bryden and Imawaki (2001).

no net mass transport across the basin. Figure 1.2 shows the meridional heat transport in the Atlantic, derived from analysis of oceanographic sections recorded during the World Ocean Circulation Experiment (WOCE), from Bryden and Imawaki (2001). References for the individual studies are contained therein.

1.1.3 The Thermohaline Circulation

The existence of the thermohaline circulation, or meridional overturning circulation, is the primary reason for the northwards transport of heat at all latitudes in the Atlantic ocean. The circulation can be visualised as a conveyor-like system (Broecker, 1987), whereby warm water flows northward along the western boundary of the Atlantic basin towards the polar regions. On reaching these northerly latitudes, the large air-sea temperature differences cause this warm surface water to cool, and freshwater fluxes alter its salinity, thus increasing its density and eventually allowing it to sink, or convect, and then return south as the deep southern limb of the conveyor system. Although useful, such a picture is a

gross simplification and contains some factual inaccuracies. For example, the conversion of warm surface water to deep abyssal water in the North Atlantic is not a continuous process, but rather occurs sporadically in a very limited number of locations (Marshall and Schott, 1999). In addition, the majority of the return flow does not return to the Atlantic basin by passing through the Indonesian archipelago and south of Africa, but is advected through Drake Passage with the Antarctic Circumpolar Current (ACC), reentering the Atlantic in the south-west of the basin (Broecker, 1991). It is the thermohaline circulation which is thought to be responsible for the comparatively mild climate of northern Europe, with the Gulf Stream and North Atlantic Current carrying the warm surface waters towards the north-east Atlantic at a rate of up to 10^{15} W (Ganachaud and Wunsch, 2000), where it begins to give up its heat content to the atmosphere. Kallberg and Berrisford (2005) illustrate the spatial patterns of heat loss in the North Atlantic region, calculated from the ECMWF ERA-40 reanalysis. In the annual mean, most sensible heat is lost from the GIN Seas, the Labrador Sea and the region where the Gulf Stream separates from the coast of North America, with average heat losses to the atmosphere peaking around 80 W m^{-2}, 80 W m^{-2} and 60 W m^{-2}, respectively. Mean sensible heat loss in the Boreal winter (December-January-February) are around double these values, and heat losses of up to 100 W m^{-2} occur over much of the subpolar North Atlantic. Latent heat loss is strongest over the Gulf Stream separation region during all seasons, with mean losses ranging from around 120 W m^{-2} during June–July–August to around 290 W m^{-2} during September–October–November.

It has been suggested that the thermohaline circulation may exist in two distinct stable states, one in the current configuration, whereby warm water is transported north before sinking and returning south, and another where this circulation collapses, and is replaced by a slow, diapycnal upwelling in the north Atlantic, reminiscent of the present day Pacific Ocean (Stömmel, 1961; Rahmstorf, 1995; Broecker, 1997; Marotzke and Willebrand, 1991). Hysteresis behaviour indicative of bi-stable thermohaline regimes have been seen in a wide range of intermediate complexity climate models (Rahmstorf *et al.*, 2005), although general circulation models tend to show a more linear response to fresh water forcing (e.g. Rind *et al.* (2001)).

Attempts have been made to evaluate whether any changes are occurring in the transport of the thermohaline circulation. For example Bryden *et al.* (2005), using a series of measurements starting in 1957, suggested that the overturning may have weakened by as much as 30% over 10 years. However the measurements were sparse in time, and little was known about the variability of the circulation, so this decrease could easily be an artifact of aliasing. Since the RAPID monitoring array has been installed across 26.5 °N in the Atlantic, it has become much easier to record the high-frequency variability of the MOC. Transports across the array are estimated as 18.7 ± 5.6 Sv, with a range of over 30 Sv, and no significant trend (Cunningham *et al.*, 2007). More recently, efforts have been made to combine the ARGO float array with satellite altimetry to calculate the transport in the upper 1000 m of the Atlantic (Willis, 2010). This method allows the construction of a relatively long timeseries of the overturning. Between 2004 and 2006 the upper-limb of the meridional overturning circulation at 41 °N was estimated as 15.5 ± 2.4 Sv. Again a very strong high-frequency variability and significant interseasonal–interannual variability was observed, but no significant trend was observed in the last 7 years, and probably not within the last 20.

1.1.4 Circulation in the North Atlantic

In the previous section we described the meridional overturning circulation as a northward flow of warm water, which then sinks in the polar regions before returning south as a deep flow. This is, however, a significant simplification of the processes occurring in the North Atlantic. Figure 1.3 shows the topography/bathymetry and relevant locations in the North Atlantic region, and Figure 1.4 shows two schematics of circulation in the North Atlantic, the first due to Worthington (1970) and the second a modified version of this by McCartney and Talley (1984), both from McCartney and Talley (1984). These two pictures of the circulation are qualitatively similar: they both describe the northward flow of warm water in the North Atlantic Current, some of which is recirculated around the subpolar gyre, traversing the Irminger and Labrador basins. The remainder of this water continues northwards into the Greenland-Iceland-Norwegian (GIN) Seas, passing primarily over the Iceland-Scotland Ridge, although some fluid does pass northwards through the Denmark Strait. As it flows cyclonically around the GIN Seas, this water loses large quantities of

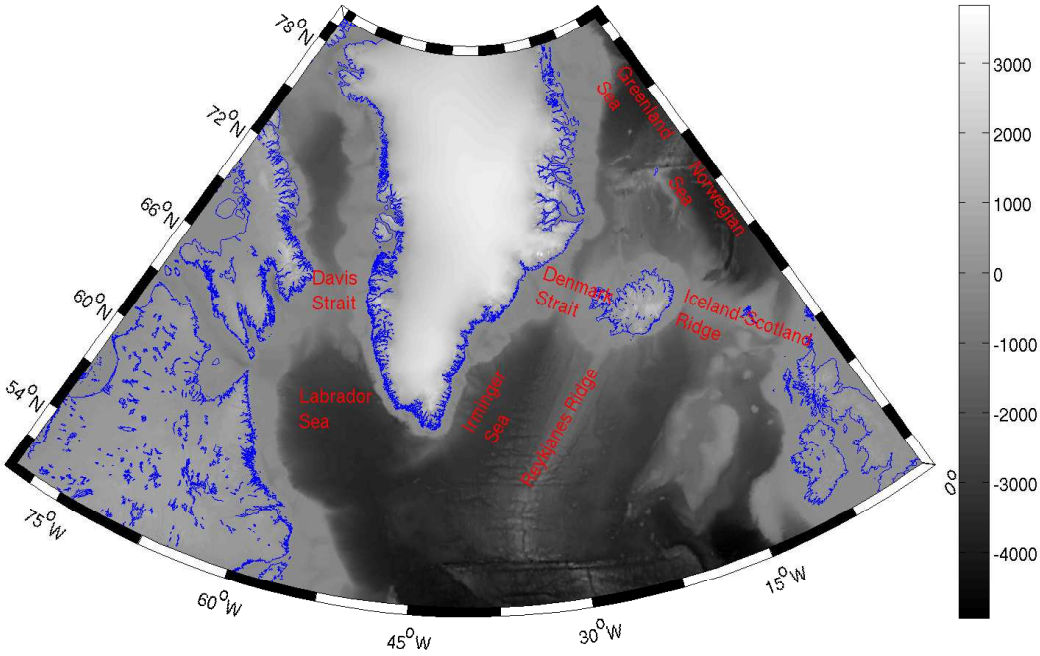

Figure 1.3: Topographic map of the North Atlantic sector, highlighting areas of relevance for this study. Shading shows elevation in metres.

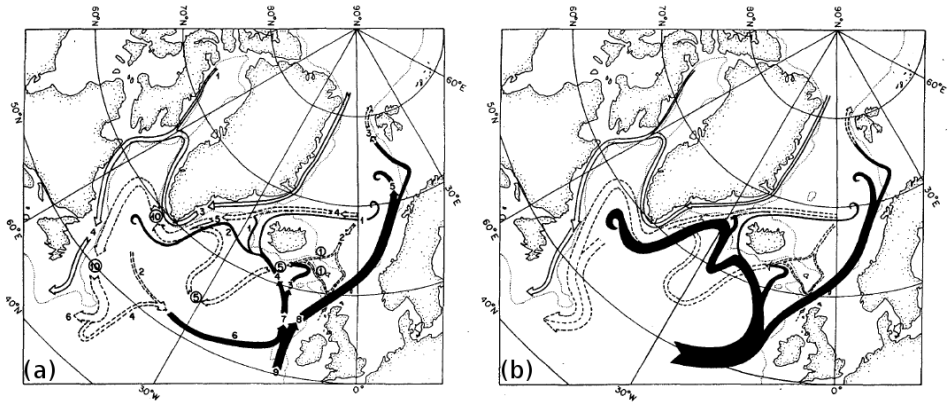

Figure 1.4: Schematics of the general circulation patterns of the North Atlantic from (a) Worthington (1970) and (b) McCartney and Talley (1984). Solid lines represent warm, saline currents, unfilled lines cold fresh currents and dashed lines the deep return flow. The curled terminations of the solid lines represent sites of deep convection.

heat to the atmosphere, resulting in the densification of the surface waters and erosion of the stratification of the water column. This may lead to near full depth convection and the production of bottom water (Marshall and Schott, 1999). This bottom water is dammed behind the Greenland-Iceland-Scotland (GIS) ridge, and eventually overflows the Denmark Strait and Iceland-Scotland ridges, forming Denmark Strait Overflow Water (DSOW) and Iceland-Scotland Overflow Water (ISOW) respectively, at a rate of approximately $\sim$5.6 Sv, divided approximately equally between the two overflows (Dickson and

Brown, 1994). This entrains significant quantities of ambient water (including Labrador Sea Water – we shall discuss this shortly) as it overflows, resulting in a transport of around 13 Sv (Dickson and Brown, 1994) in the Deep Western Boundary Current (DWBC) as it passes Cape Farewell, the southern-most point of Greenland.

The water in the North Atlantic Current (NAC) that does not pass over the GIS ridge progresses around the subpolar gyre. As it does so it becomes colder and fresher through interaction with the atmosphere, forming increasingly deep modal waters in the boundary current (Talley and McCartney, 1982). In the centre of the Labrador Sea, some of this water is 'trapped' within a recirculation. This is where the deepest mode water—Labrador Sea Water—is sporadically formed as the water column overturns to depths which can exceed 2000 m (Lazier *et al.*, 2002), in what is known as open-ocean convection (Marshall and Schott, 1999). Labrador Sea Water eventually forms an important constituent of North Atlantic Deep Water, which makes up much of the deep limb of the meridional overturning circulation. In the next section we will discuss the process of open-ocean convection globally and in particularly in the Labrador Sea.

1.2 Open-Ocean Convection

In the previous section we complicated the picture of a simple overturning circulation by considering in more detail the circulation in the North Atlantic. In this section, we look more closely at the process of water mass transformation, whereby the warm upper ocean water is densified, eventually coming to form the deep waters of the southward flowing limb of the overturning circulation. We follow the excellent review of Marshall and Schott (1999).

1.2.1 Conditioning the Ocean for Convection

The ocean is, in most places and at most times, a stably stratified fluid ($\partial\rho/\partial z > 0$), which is forced at its upper surface, the air/sea interface, by fluxes of buoyancy (a combination of heat and moisture/salt) and momentum. A useful measure of the static stability of the ocean is given by the Brunt-Väisäla frequency $N^2 = \partial b/\partial z \equiv -g'\partial\rho/\partial z$, where g' is the reduced gravity g/ρ and b is the buoyancy of the fluid. If $N^2 > 0$, then the fluid has a stable stratification, and the Brunt-Väisälä frequency represents the local frequency

with which a water parcel would oscillate if displaced in the vertical (i.e. it is the local frequency of internal gravity waves). If, on the other hand, $N^2 < 0$, then N becomes complex and the fluid is statically unstable, with dense water overlying less dense water, and convective overturning occurs. It is common to non-dimentionalise N by dividing through by a typical value of the Coriolis frequency, usually $f_0 = 10^{-4}$ s^{-1}. Typical values of N/f in the deep ocean can be as low as 5, rising to around 30–50 in the upper 1000 m of the water column and can reach a maximum of 100 near the ocean surface or in the pycnocline (Marshall and Schott, 1999). Given these relatively strong stratifications, it should come as no surprise that deep oceanic convection is limited to a small number of geographic locations, where a number of prerequisites are met.

The first of these prerequisites is that the water column is not too strongly stratified in the first instance, perhaps from a degree of convective mixing in the previous winter (this does leave a slight 'chicken and egg' situation, however one can imagine the stratification becoming progressively weaker over a number of harsh winters and not fully restratifying over the summer, eventually leading to true deep convection). The second prerequisite is the existence of a local recirculating cyclonic gyre. The impacts of such a feature are twofold. Firstly, it will act as a barrier, effectively trapping water within, allowing this water to be repeatedly modified by any strong buoyancy forcing that may be present in the area. Secondly, within such gyres, isopycnals tend to 'dome' towards the surface, which has the effect of weakening the stratification as deeper, less stratified fluid moves towards the surface. The surface water then does not have to become so strongly modified before it can overturn to significant depth. The final prerequisite is the most obvious – that there must be a significantly strong buoyancy flux at the ocean surface to cause the surface waters to increase sufficiently in density. Given the dependence of the density of seawater on both temperature and salinity, this increase of surface density can come from either intense cooling of the ocean surface through sensible and/or latent heat release to the atmosphere, or salinification through strong surface evaporation or brine rejection on the formation of sea-ice. There are thus a few very different sites where oceanic convection can occur.

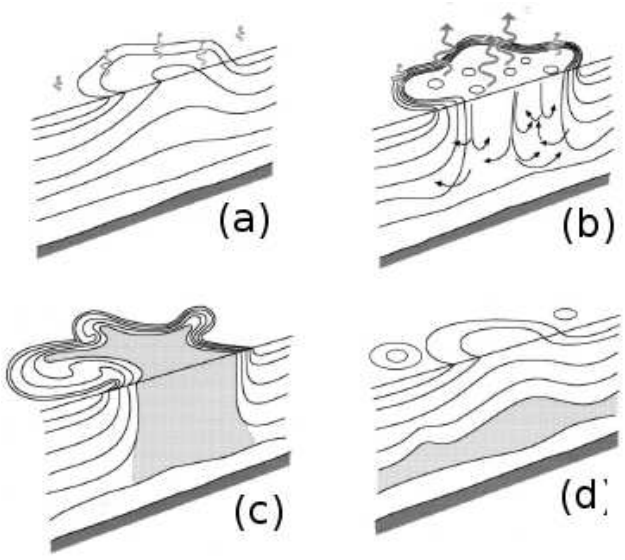

Figure 1.5: Schematic showing the stages of the convective process, adapted from Marshall and Schott (1999). (a) Preconditioning; (b) Deep convection; (c) Loss of balance and spreading; (d) Restratification. The curly arrows represent a buoyancy flux through the surface and the shading shows the volume of fluid which has been effectively mixed.

1.2.2 The Dynamics of Ocean Convection

What follows is a brief discussion of the dynamics associated with convection, following Marshall and Schott (1999). Figure 1.5 shows the basic stages associated with deep convective plumes. In 1.5(a) we can see the doming of isopycnals associated with the cyclonic circulation common to all convection sites (we will describe these shortly). Note that there is a moderate degree of buoyancy flux through the surface of the ocean, typical of the prevailing synoptic conditions during the onset of winter. These act to gradually erode the existing stratification, creating a relatively well mixed patch in the upper ocean, with lateral scales of order 100 km. In Figure 1.5(b), a series of meteorological events with strong buoyancy fluxes have allowed the onset of deep convection. Deep convection does not occur concurrently throughout the mixed patch, but occurs in convective plumes or 'chimneys' which typically have lateral scales of order 10 km, although they may be as small as 1 km. Since acoustic Döppler current profilers have become available, there have been numerous studies to measure the vertical velocities associated with these convective plumes (Schott and Leaman, 1991; Schott *et al.*, 1996; Gaillard *et al.*, 1997). Most of these studies have reported vertical velocities within the plumes of between 5 and 10 cm s^{-1}, which given the scale of the plumes would represent a significant mass transport

between the upper and deep oceans. However it still is not clear whether the plumes represent a true transport of mass into the deep ocean, or simply act as mixing agents which homogenise the water in the plumes down to depth. As the plumes descend, they become influenced by the rotation of the Earth, and become 'rigid' in a similar manner to Taylor columns, which acts to prevent the plumes from significant lateral spreading. The convectively mixed pillars then tend to become unstable (Figure 1.5c), and lead to the formation of mesoscale eddies, with a lateral extent scaling with the local Rossby deformation radius (Gascard, 1973). These eddies act to transport the modified deep water properties away from the formation region, along with a more general spreading into the interior along isoneutral surfaces (Figure 1.5d).

1.2.3 Locations of Oceanic Convection

1.2.3.1 The Labrador Sea

The subpolar gyre recirculates much of the North Atlantic Current around the Labrador Sea, and this cyclonic flow is enhanced by the West Greenland Current and Labrador Current which flow around the boundary of the basin, carrying relatively cold fresh water which has been transported from the Arctic in the narrow East Greenland Current. These currents, potentially with the influence of the strong climatological wind stress curl (Spall and Pickart, 2003) which occurs to the east (and to a lesser extent the west) of Greenland result in a closed recirculation in the central Labrador Sea, which has been documented as far back as Wüst (1935). This acts to precondition the Labrador Sea, both trapping water masses and doming isopycnals. The vertical structure of the central Labrador Sea at the beginning of a given winter generally involves relatively cold, fresh water in the upper 100–200 m of the water column, probably as a result of exchange with the boundary currents, with warmer, more saline Irminger Water extending down from here to around 700 m depth. Below this generally lies a large mass of nearly homogeneous, and therefore very weakly stratified water, remnants of homogenisation by deep convection in previous winters (Roach *et al.*, 1993; Aagaard, 1970; Marshall and Schott, 1999). Thus the central Labrador Sea is very well preconditioned for overturning to occur, given suitable buoyancy forcing. As the central Labrador Sea usually remains ice-free throughout the winter, and moisture fluxes at this latitude have a net freshening effect, this forcing can

only be provided by atmosphere-ocean heat fluxes. So-called 'cold-air outbreaks' are common across the wintertime Labrador Sea (LabSeaGroup, 1998). In a cold-air outbreak, very cold and dry continental air is advected across the Labrador Sea from Canada and the northern United States, and can cause combined latent and sensible heat fluxes of over 1000 W m^{-2} (Grossman and Betts, 1990; Renfrew and Moore, 1999; Pagowski and Moore, 2001). It is these heat fluxes, corresponding to buoyancy fluxes greater than 10^{-7} N m^{-2} s^{-1} (Marshall and Schott, 1999) which are strong enough to force convection in the Labrador Sea. It should be noted that it is not necessarily the number of these cold-air outbreaks which control the onset and extent of convection: a certain number of cold-air outbreaks spread equally throughout a winter may well cause significantly shallower convection than a smaller number of closely clustered events. We noted earlier that the formation of sea-ice and subsequent brine rejection does not play a significant role in the preconditioning for, or triggering of, convection in the Labrador Sea. However the presence and extent of sea-ice around the margins of the basin have been shown to have an important indirect effect. As the wind blows over the ocean surface, it inevitably exchanges heat and moisture with the ocean. In situations such as are present over the Labrador Sea in winter—where cold, dry air is blowing over a relatively warm ocean—the air will warm and moisten as it does so and thus become less effective at removing heat from the ocean further downstream. These exchanges do not happen anywhere near as effectively (if at all) over consolidated sea-ice, therefore a sea-ice edge which advances towards the Labrador convective site will result in colder, drier air removing more buoyancy from the ocean at the convective site and thus increasing the final depth of the mixed-layer. This was seen to be the case in the winter of 2008, when deep convection was observed in the Labrador Sea, despite a series of relatively mild winters meaning the ocean may not have been particularly well preconditioned (Våge *et al.*, 2009a). This extended ice edge was thought to be due to an unusually large amount of ice advection through the Davis Strait as a result of the ice-pack being less consolidated than normal. Almost paradoxically then, a series of mild winters resulted in deep convection returning to the Labrador Sea with less robust atmospheric forcing over the preceeding years than would usually be necessary.

Deep convection in the central Labrador Sea has been observed at Ocean Weather Ship Bravo (Lazier, 1973), and during oceanographic cruises on the CSS Hudson (Clarke

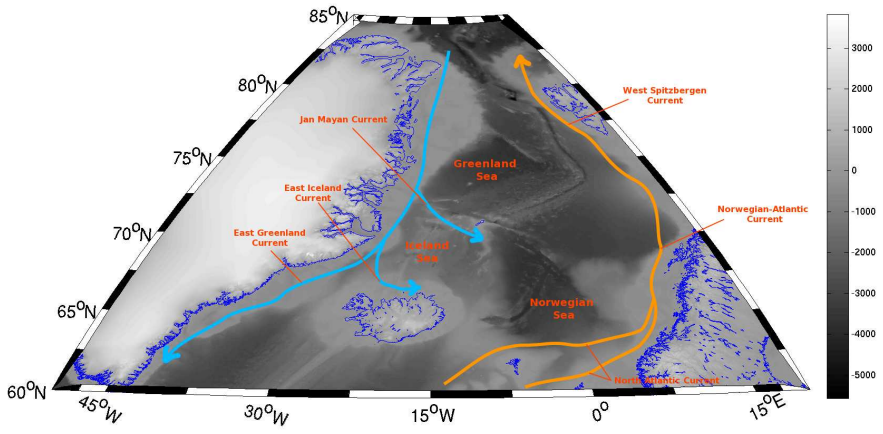

Figure 1.6: Topographic map of the Greenland-Iceland-Norwegian Seas, highlighting areas of relevance for this study. Shading shows elevation in metres, currents are schematic and indicate approximate location but not magnitude.

and Gascard, 1983) and the RV Knorr (Pickart *et al.*, 2002) to a depth of over 1400 m. It is both interesting and important to note that the rate, volume and properties of Labrador Sea water produced in the Central Labrador Sea are not constant, but vary quite considerably from year to year, depending on the nature of the winter (Lazier, 1995; Dickson *et al.*, 1996; Yashayaev, 2007). These changes contribute to the variability of the meridional overturning circulation.

1.2.3.2 The Greenland-Iceland-Norwegian Seas

The mechanism of oceanic convection in the GIN seas is to a large extent similar to that in the Labrador Sea, with one important exception: that, being further north, the formation of sea-ice becomes of direct importance in preconditioning the ocean. The general cyclonic flow around the GIN seas starts with the warm, salty North Atlantic current. As this crosses the Iceland-Scotland ridge, it becomes the Norwegian-Atlantic current, and continues to flow northwards, partly to the south-west of Spitzbergen as the West Spitzbergen

current before entering the Arctic Ocean. The return flow from the Arctic Ocean comprises the narrow, cold and fresh East-Greenland current, which bifurcates south of Jan Mayen forming the Jan Mayen Current, and to the north of Iceland, forming the East Iceland Current. The centre of this cyclonic flow, then, lies approximately half way between Jan Mayen and Spitzbergen (Figure 1.6). The vertical structure of the ocean here is fairly similar to that in the Labrador Sea. The very surface of the water column is cold and fresh, again most likely from lateral exchange with the East Greenland Current and its offshoots. Underlying this relatively thin surface layer is a layer of Atlantic Intermediate Water and then Greenland Sea Deep Water which, analogously to Labrador Sea Water, is weakly stratified due to convection in previous winters.

During the early boreal winter, sea-ice starts to form in the GIN seas, spreading eastwards from the coast of Greenland. The formation of this sea-ice salinifies the surface waters and causes the mixed-layer to begin to deepen, at the rate of approximately 1 m day^{-1} (Schott *et al.*, 1993). This, combined with reasonably modest heat fluxes (of the order of a few hundred W m^{-2}) can cause mixing down to around 300 m. This deepening of the thermocline may then increase the temperature of the surface water, causing a rapid retreat of the newly formed sea-ice (Roach *et al.*, 1993). This retreat generally leaves a tongue of ice, the 'Is-Odden', extending from Jan Mayen and curving cyclonically around the convection site. A thorough description of the formation of this feature is given by Wadhams *et al.* (1996). Deep convection thus generally occurs in the open-water embayment formed by the Odden, and so ice, while required to precondition the GIN seas for convection, does not play a dominant role in the triggering of deep convection (Visbeck *et al.*, 1995; Marshall and Schott, 1999). The extent of winter convection in the GIN seas appears to show a similar degree of variability as the Labrador Sea. Some winters are not strong enough to result in any (observed) deep convection, observational campaigns in the 1980s and 1990s showed convection not exceeding 1500 m (Rudels *et al.*, 1989; Schott *et al.*, 1993), although more recently (and interestingly when deep convection was not expected to take place) convective chimneys extending to as deep as 2400 m have been observed (Wadhams *et al.*, 2002).

Since around the year 2000, the Odden ice tongue has occurred only rarely (Rogers and Hung, 2008). However, during two cruises to the Greenland Sea in 2001, a convective

chimney was observed extending to greater than 2400 m depth (Wadhams *et al.*, 2002). The Odden had not been present in the area in either 2000 or 2001, suggesting that a mechanism other than brine rejection from the forming ice must have preconditioned for and triggered the deep convection. Wadhams et al. suggest that it was, in this case, simply strong surface cooling which was responsible for the triggering of deep convection in the Greenland Sea.

Marshall and Schott (1999) suggest that the sub-mesoscale eddies which form on the edge of the mixed patch following convection are important only in dissipating these mixed patches as they are formed through geostrophic adjustment at the edges of the well mixed area. This interpretation, however, has been questioned by Gascard *et al.* (2002), who observed numerous sub-mesoscale eddies, with a core diameter of around 5 km and lifetimes in excess of 9 months, extending to depths of around 2000 m, through the use of float and hydrographic tracer data. These eddies were shown to be formed from a combination of surface Arctic water and 'return Atlantic water' in approximately a 1:2 ratio, and had a SF6 concentration significantly lower than that of the surrounding water, into which it had been released as a tracer. The core of these small eddies are largely homogeneous, and thus they provide a mechanism for deep water formation, releasing their constituent water to depth as they decay. Gascard *et al.* (2002) that such eddiesand a significant contribution to the production of Greenland Sea Deep Water in the winter of 1996/1997.

Lilly and Rhines (2002) discussed observations from a mooring in the Labrador Sea, from which, through comparisons with a numerical model, they were able to infer the existence of very similar eddies to those observed in the Greenland Sea by Gascard *et al.* (2002) in the Labrador Sea during June–November 1994. In was noted explicitly that a number of these eddies could not be the result of in-situ convection, and were most likely formed in the boundary of the Irminger Current. It is thus likely that such features play a role in deep water formation in the Labrador Sea as well as in the Greenland Sea.

1.2.3.3 The Mediterranean

The Western Mediterranean

The cyclonic circulation around the Gulf of Lion in the northeastern Mediterranean

is dominated by the northward boundary currents of Corsica (the West Corsican current and the Tyrrhenian current) and westward flow along the coast of southern France, the North Mediterranean current and the Catalan current to the south-east of Spain (Astraldi and Gasparini, 1992; Marshall and Schott, 1999). The cyclonic circulation is closed by a seasonally varying northward transport of Levantine intermediate water (Millot, 1987). This results in a large doming of isopycnals in the centre of the Gulf of Lion, leaving it well preconditioned for deep convection. As in the Labrador and GIN seas, prior to the onset of convection, the vertical structure of the water column in the Gulf of Lion has three distinct layers (Marshall and Schott, 1999). At the surface, to around 150 m is a layer of modified Atlantic water which has flowed into the Mediterranean through the Strait of Gibraltar. Below this, extending up to approximately 500 m depth is the Levantine Intermediate Water and then a homogeneous mass of Western Mediterranean Deep Water.

Convection in the Gulf of Lion is primarily driven by the Mistral (Marshall and Schott, 1999), a low-level, orographically induced (primarily katabatic) northerly wind which flows off the coast of France, resulting in regular cold-air outbreaks over the Gulf (Caccia *et al.*, 2004). Due to the relative ease of access, the Gulf of Lions is probably the best studied convective site in the world oceans. Convection here shows strong interannual variability as it does in other locations. Some of the first measurements of convection here in 1969 (MEDOC-Group, 1970) showed strong convection, reaching depths in excess of 2000 m, however by 1971 convection was significantly shallower. In 1987, convection was again observed to as deep as 2200 m (Leaman and Schott, 1991) and to 1700 m in 1991. More recently, high resolution numerical modelling studies have suggested that it is not the total heat that is removed from the ocean that controls the extent of convection (for example total heat fluxes in the winters of 1998-1999 and 1999-2000 were similar, but convection in 1998-1999 penetrated to 2200 m while in 1999-2000 it reached a maximum of 1400 m) but the temporal distribution of strong heat flux events (Hong *et al.*, 2007).

Schroeder *et al.* (2008) discuss the results of five cruises between October 2004 and October 2006, in which they observed an extensive renewal of deep water in the Western Mediterranean, extending from the Gulf of Lions to the Catalan subbasin, and giving rise to a new deep water mass, with extremely high heat and salt content. The convective event

and subsequent deep water renewal is thought to have resulted from a combination of factors. The winter of 2004/2005 was the driest and most severe of the preceding 40 years, which was likely to have a bearing on forcing convection (Font *et al.*, 2007), however it is likely that an increase in the salt and heat content in the intermediate layer, through advection from the Eastern Mediterranean also played an important role (Schröder *et al.*, 2006). It is worth noting that although these convective events led to a strong increase in the temperature and salinity of the Western Mediterranean deep water, this water mass had been increasing in both temperature and salinity since the 1950s, and particularly since around 1985. Rixen (2005) note that this is probably forced by anomalies in the winter averaged heat flux anomalies in the region, which in turn are well correlated with heat fluxes averaged over the North Atlantic. It is thus suggested that changes in Western Mediterranean deep water, which are relatively easy and cheap to measure, may be used as a proxy for the more climatically sensitive changes of deep water in the North Atlantic.

The Eastern Mediterranean

Manca *et al.* (2002) describe the hydrography and meteorological forcing of the southern Adriatic Sea recorded during cruises between March 1997 and March 1999. A sub-basin scale cyclonic gyre exists in the Southern Adriatic, where the basin extends to well over 1000 m in depth. In addition, the area is predisposed to outbreaks of cold and dry continental air, thus providing both preconditioning and forcing for open ocean convection. In addition, the Southern Adriatic has the three-layer structure common to other sites of open ocean convection, caused by the inflow of high salinity Levantine Intermediate Water (LIW) through the Strait of Otranto. During this time period, convective mixing was only observed to depths of 400 m in 1998 and 700 m in 1999, however previous observational evidence exists suggesting convection to depths of around 800 m (Obchinnikov *et al.*, 1985).

Deep convection has also been observed in the Aegean Sea (Roether et al., 1996), given the correct conditions, and at times deep water from this source may have accounted for around 20% of the deep water below 1200 m in the Eastern Mediterranean, with this new source being known as the Eastern Mediterranean Transient. These large discharges from the Aegean Sea, the average from 1989 to 1995 though to be around 1.2 Sv (Lascaratos et al., 1999) are thought to have been brought about by long term changes in the

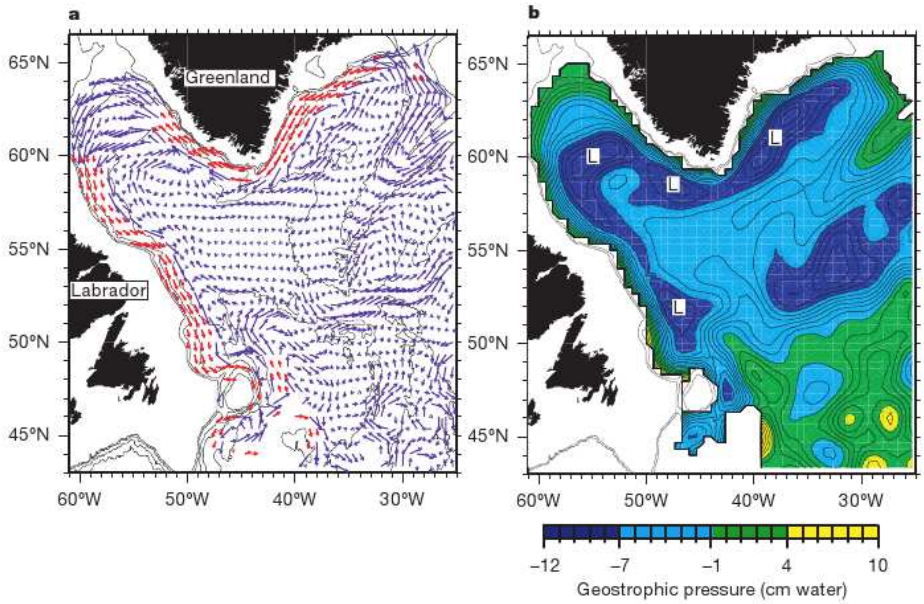

Figure 1.7: (a) Mid-depth ocean float displacements (red arrows scaled to 50%) and (b) geostrophic pressure at 700 m, from Lavender *et al.* (2000). Note the recirculations in the Irminger and south-eastern Labrador Seas.

salinity of intermediate water due to a decrease in river discharge, changes in the wind driven circulation, or changes in the local surface meteorology (Josey, 2003 and references therein).

1.2.4 Convection in the Irminger Sea?

During the World Ocean Circulation Experiment (WOCE), a number of oceanographic sections were occupied across the Labrador Basin, the Iceland Basin, the Rockall Trough and the Newfoundland Basin (amongst many others). Sy *et al.* (1997) used the data from these sections to study the spreading of LSW from its origin in the Labrador Sea, using temperature and salinity characteristics as well as CFC concentrations. CFCs act as a good passive tracer for LSW, as CFC concentration will be highest in water masses that have recently been in contact with the atmosphere (Wallace and Lazier, 1988). Using these observations, Sy *et al.* (1997) inferred a transit time for newly ventilated LSW in the Labrador Basin to travel into the Irminger Basin of only around 6 months. This transit time implied an average velocity for the ventilated water of around 4.5 cm s^{-1}, much faster than previous estimates of velocities of around 1.5 cm s^{-1} in the boundary currents, or 0.5 cm s^{-1} in the ocean interior (Read and Gould, 1992; Ellett, 1993; Cunningham and Haine, 1995). Significant differences were seen in the properties of the LSW water

masses between the Labrador and Irminger Basins, with the LSW in the Irminger basin being warmer and more saline. This is exactly what would be expected if LSW was formed in-situ in the Irminger Sea, as surface waters tend to freshen and cool as they travel around the subpolar gyre from the Irminger to the Labrador Basins. Despite this, Sy et al. attributed this change in LSW properties to mixing of the LSW with ambient mid-depth fluid as it spread from the Labrador to the Irminger Sea. Such a conclusion was not surprising, as at the time the extent of preconditioning in the Irminger Sea was not well known.

During the Labrador Sea Deep Convection Experiment (LabSeaGroup, 1998), again as part of the WOCE, a large number of PALACE (Profiling Autonomous Lagrangian Circulation Explorer) floats were released into the Atlantic subpolar gyre. Lavender *et al.* (2000) used these floats to study the structure and circulation of the subpolar Atlantic by collating over 7400 profiles and in excess of 200 years of drift velocities. The deepest mixed layers were observed to lie in the Labrador Sea, nearby a cyclonic recirculation where the ocean was very well preconditioned for overturning to take place. However, other isolated minima in the geostrophic pressure field were found. One of these was in the south-east Labrador Sea, suggestive of the possibility of a secondary convection site within the Labrador Sea, but arguably more important was the existence of a strong recirculation in the Irminger Sea. This suggested that the Irminger Sea could also be a site of LSW formation, if the atmospheric forcing here was sufficiently strong. The gyre had remained undiscovered despite numerous occupations of sections across the Irminger Sea as it is of a very barotropic nature, and thus cannot be seen in velocities calculated from conductivity-temperature-depth (CTD) sections, which rely on geostrophic shear from a reference level (Pickart *et al.*, 2003a).

Pickart *et al.* (2003a) used oceanographic sections obtained in 1991, much earlier in the year than those used in the study of LSW spreading, meaning that the buoyant cap which forms on the surface ocean every spring was less developed. These observations were used to argue that LSW was indeed being formed in the Irminger Basin as they were indicative of a convective water mass which had recently begun to restratify. In addition, climatological data (in particular potential vorticity) were examined, and showed an “extremum of LSW properties” in the Irminger Sea, with less indication of Labrador

Sea Water between the Irminger and Labrador Basins. Such a distribution is difficult to explain without a source of LSW located in the Irminger Basin. Pickart et al. also used an advective-diffusive model, based on the circulation patterns of Lavender *et al.* (2000), adjusted to become non-divergent, to examine the spreading rate of LSW, with various diffusivities and in both high and low LSW production regimes. It was found that, in order for a passive tracer (e.g. the CFC signal of LSW) to spread into the Irminger Basin in the 6 months reported by Sy et al. (1997), an internal spreading rate of around 13 cm s^{-1} was required – a speed so fast for an interior pathway that it verges on the unphysical.

Bacon *et al.* (2003) used a combination of profile data from floats and CTD sections to look for convective activity in the Irminger Sea. A mixed-layer between 300 m and 1000 m was observed, with the upper 300 m of the water column said to have been sheared away by a vigorous high salinity eddy. This mixed-layer was assumed to have formed in-situ in the Irminger Sea, as a simple heat flux calculation suggested that the heat loss seen over the winter in the Irminger Sea was consistent with observed extent of the mixed-layer. This required an average heat flux over the winter of 255 W m^{-2}, some 30 W m^{-2} greater than was observed in the previous winter. Bacon et al. attribute this difference to the existence of the Greenland tip jet (Doyle and Shapiro, 1999), which is capable of removing large quantities of heat from the ocean over relatively short periods of time. We shall discuss the tip jet in detail shortly. It was noted that only around 9 days of tip jet enhanced forcing over the winter could provide the missing 30 W m^{-2} required for the observed mixed-layer to form. However, no discussion of the frequency of these jets was given (9 days of consecutive forcing is likely to result in a deeper mixed-layer than 9 days spread equally throughout the winter). Additionally the assumed 800 W m^{-2} heat flux attributed to the tip jet may be somewhat too low (see for example Doyle and Shapiro (1999), Figure 18, which shows a sensible heat flux in excess of 800 W m^{-2}).

Pickart *et al.* (2003b) used an idealised setup of the MIT general circulation model to study the impact of a very idealised tip jet on the ocean. The model was set up with a horizontal resolution of 5 km, with 20 levels in the vertical and a very simple 'sinusoidal' representation of Greenland and simple shelf bathymetry to provide a highly idealised representation of the North Atlantic Ocean. A climatology of tip jet events was constructed from historical meteorological data from Cape Farewell, and this was used to assign a

frequency of occurrence to the tip jet. The tip jet itself was simply an area of strong heat flux and wind stress curl periodically applied to the ocean, which was otherwise unforced apart from relaxation to a prescribed buoyancy and velocity structure at the southern and eastern boundaries. The hydrographic structure was initialised to represent the temperature and salinity structure typical in the Irminger Sea in late summer. Over the winter, under the forcing of the tip jet, the model mixed-layer was seen to deepen to in excess of 1500 m, within a cyclonic gyre which span up in response to the strong wind stress curl imposed by the tip jet. Despite the simplicity of the model setup, this provided the first evidence of tip jets forcing convection in the Irminger Sea.

Falina *et al.* (2007) used a series of oceanographic sections between 1991 and 2002 to study the variability of LSW in the Irminger Sea. It was found that to a large extent, the variability of the hydrographic properties in the Irminger Basin were controlled by earlier convection in the Labrador Sea and the subsequent advection of these water masses into the Irminger Sea. However, it was noted that the LSW in the Irminger Basin had a distinct bi-modal structure. Thus, while there was water in the Irminger Sea which had been convectively formed in the Labrador Basin, this was modified by deep convection in the Irminger Sea. Furthermore, it was shown that in 1997, oxygen concentrations in LSW in the southern Irminger Sea were higher than in the eastern Labrador Sea, again suggesting a water mass which was convectively formed within the Irminger Sea.

Våge *et al.* (2008) reported the results from some moorings which were placed in the Irminger Sea to the east of Cape Farewell in the winters of 2002/2003 and 2003/2004. Unfortunately these winters were lacking in strong atmospheric forcing, and the moored profilers recorded mixed-layer depths not exceeding 400 m and 300 m for the two winters, respectively. It was found that a simple mixed-layer model, based on Price *et al.* (1989), was able to reproduce the onset and extent of the observed mixed-layer deepening with good accuracy. If this same model was applied to the much more robust winter of 1996/1997, then the mixed-layer was seen to deepen to around 1600 m when forced by 'best estimate' meteorological variables. If the signal of any tip jets was removed from these forcing timeseries by smoothing over them, then the mixed-layer deepened by around 400 m less than it did when the tip jet forcing was included.

The studies we have discussed here are not conclusive; indeed the only way to conclusively prove that deep convection does occur in the Irminger Sea is to observe it during active convection, as has been done in the Labrador Sea. On the balance of evidence, however, it does seem very likely that a LSW-like water mass is formed in the Irminger Sea. This raises important questions with regard to the extent and variability of LSW production in the Irminger Sea, the influence of this on the general circulation and its representation within oceanic models. These are some questions which we will attempt to address in this thesis.

1.3 The North Atlantic Oscillation

The North Atlantic Oscillation (NAO) is the primary mode of atmospheric variability in the North Atlantic sector. It is manifested as a dipole in the variability in mean sea-level pressure between Iceland and the Azures. A good review of the impacts of the NAO is given by Hurrell and Deser (2009). One of the major impacts of the NAO is in the North Atlantic stormtrack, which describes the path likely to be taken by synoptic-scale cyclones in the area during the boreal winter. When the NAO is in its positive phase, the stormtrack is displaced to the north-east, with proportionally more cyclones moving into the Irminger Sea region, and an increase in storminess in the GIN seas. Correspondingly, the cyclone activity further south tends to decrease when the NAO is in a positive phase. When the NAO is in its opposite, negative phase, cyclones tend to track further to the south, generally moving across the North Atlantic towards the United Kingdom. There are associated changes in near-surface temperature with milder winters over northern Europe during NAO+ conditions, for example see Hurrell (1995). These changes also influence the transport of moisture by atmospheric convergence, and thus are also reflected in the mean precipitation patterns (Hurrell, 1995). The NAO is also related to anomalies in sea-surface temperature (SST) in the North Atlantic on monthly and seasonal timescales, both through changes in air-sea heat fluxes and changes in the wind driven currents associated with the varying atmospheric circulation.

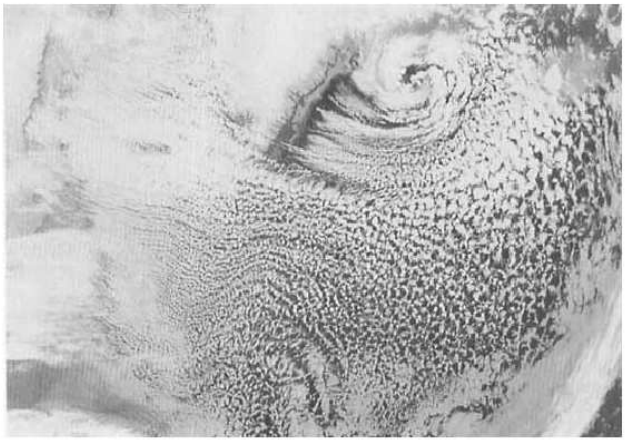

Figure 1.8: A infra-red satellite image of the North Atlantic, showing a mesoscale cyclone formed in the lee of Greenland, a dry slot formed by the descent of dry air from the Greenland plateau, and an acceleration of air around Cape Farewell, from Scorer (1988).

1.4 Mesoscale Features Forced by the Orography of Greenland

Greenland is, in effect, a massive mountain situated in the North Atlantic Ocean, approximately the size of the Tibetan Plateau, although approximately half the height, reaching elevations in excess of 3500 m, and so plays an important role in the weather of the North Atlantic (Scorer, 1988). This is partly facilitated by the location of the North Atlantic storm track, which is ideally situated to interact with Greenland (Hoskins and Valdes, 1990). Kristjánsson and McInnes (1999) showed, in a series of model integrations in which the elevation of Greenland was varied, that the landmass may act to temper the deepening of cyclones passing between Greenland and Iceland, by blocking or deflecting the advection of cold air at the rear of the cyclone, and thereby reducing the local baroclinicity. However Petersen *et al.* (2003) suggested that the strengthening of the geopotential gradient to the south-east of Greenland may lead to the deepening of synoptic scale cyclones which track across the Atlantic to the south of Greenland and towards Scotland. This may have been the case with the case study described by Cammas (1999).

Greenland has also been shown to play an important role in the formation of polar-mesoscale cyclones in the Labrador Sea, and lee cyclones in the Irminger Sea. Klein and Heinemann (2002) describe how vortex stretching in fjords on the east coast of Greenland during piteraqs (extremely strong low-level winds formed by an interaction of the synoptic-scale flow and katabatic winds) may lead to cyclogenesis in the lee of Greenland.

A case study of such an event was presented by Mills and Anderson (2003). Moore and Vachon (2002) describe how the orography of Greenland led to the splitting of a synoptic-scale cyclone, the remnant of which in the Labrador Sea interacted with an upper-level potential vorticity anomaly and led to the spin-up of a polar low. Polar lows (Montgomery and Farrell, 1992; Businger, 1985) are small-scale, intense cyclonic storms, which have been shown to increase deep water formation, and thus may lead to an increase in the meridional overturning circulation (Condron *et al.*, 2008). Figure 1.8 illustrates a number of features which may be formed by the interaction of Greenland and the atmospheric flow.

An area of climatologically high wind speeds with high directional consistency was identified along the east coast of Greenland by Moore (2003). This was indicative of a barrier flow parallel to the coast. Barrier flows (Ólafsson and Bougeault, 1996; King and Turner, 1997) form where flow with a low Froude number[1] impinges on a barrier. The flow is unable to pass over the barrier, which thus acts like a dam. This leads to a pressure gradient forming perpendicular to the barrier, and a resultant flow parallel to the coast which is in approximate geostrophic balance. Barrier winds along the coast of Greenland can reach speeds in excess of 30 m s^{-1}, extending around 400 km from the coast in the zonal direction, the local Rossby deformation radius (Moore and Renfrew, 2005). The wind stress curl applied to the ocean by such a flow has been implicated in the spin-up of gyres in the Irminger and Labrador Seas (Spall and Pickart, 2003), which as we have seen are important in preconditioning the ocean for convection.

The final mesoscale systems caused by the interaction of Greenland and synoptic scale flow are tip jets. These are intense, low-level jets which originate at Cape Farewell, the southern-most point of Greenland 1.9. The impact of these jets on the ocean is the primary theme of this thesis, and we shall now discuss them in some detail.

1.4.1 Tip Jets

1.4.1.1 Westerly tip jets

Doyle and Shapiro (1999) undertook one of the first studies of the (westerly) tip jet,

[1]The Froude number, given by $Fr = U/NH$, where U is a typical velocity, N is the buoyancy frequency and H is the obstacle height, gives a measure of the ability of a flow to pass over an obstacle. Small values (less than unity) of Fr indicate blocking of the flow. Moore and Renfrew (2005) estimate typical Froude numbers near the east coast of Greenland to be around 0.3.

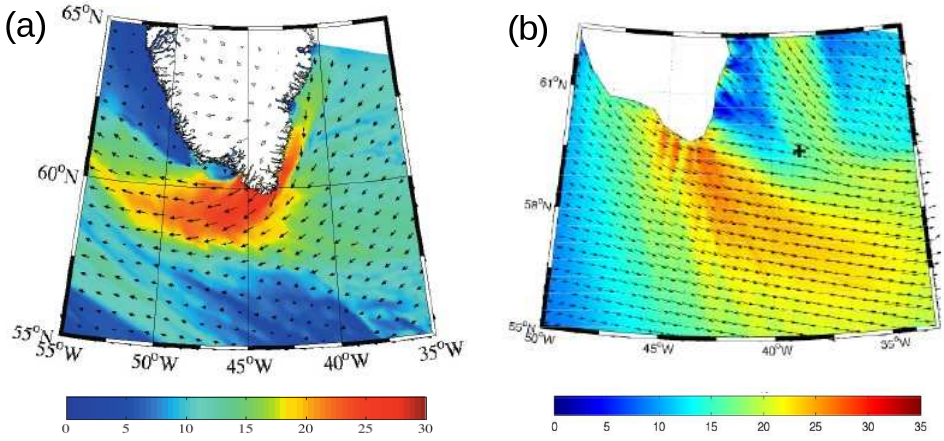

Figure 1.9: Mesoscale simulations of (a) a typical easterly tip jet, using MM5, and (b) a typical westerly tip jet, using WRF. Adapted from Martin and Moore (2007) and Hay *et al.* (2009) respectively.

analysing a number of mesoscale model simulations of Greenland for real case studies (29/01/1997 and 18/02/1997), idealised case studies, and for flow over a Gaussian mountain using the Coupled Ocean-Atmosphere Mesoscale Prediction System (COAMPS) model at 15 km resolution. Qualitatively similar behaviour was seen in both the Gaussian mountain and idealised Greenland simulations, with tip jets forming from the southern-most point of the mountain in both cases. With the real Greenland topography, however, the downstream flow was significantly altered due to the non-symmetrical mountain and complex topography (e.g. fjords) on the lee side. Similar jets were also observed in the case study simulations, although they were modified by interaction with the background synoptic-scale flow. Doyle and Shapiro (1999) attributed the existence of the tip jet to conservation of the Bernoulli function $c_pT + v^2/2 + gz$, requiring an acceleration of the flow as air descended from the plateau of Greenland, thus losing gravitational potential. In the case study simulations, 10 m wind speeds of up to 35 m s^{-1}, and "an upward surface heat flux $>$ 500 W m^{-2} extending $>$ 800 km downstream"[2] were found. This led to speculation that the tip jet, through both these very strong heat fluxes and very high wind stress curl associated with the strong winds and spatial scale of the jet, was likely to have a significant impact on the oceanic thermohaline circulation.

Dörnbrack *et al.* (2004) discussed some of the first measurements of a westerly tip jet, through the use of LIDAR during a research flight over the Irminger Sea. They observed

[2]Note that although Doyle and Shapiro (1999) refer simply to 'surface heat flux', it is clear from their Fig. 18 that they are only discussing sensible heat fluxes.

near-surface wind speeds in excess of 30 m s^{-1}, which extended vertically to the top of the observation window (approximately 4 km). Two distinct jets were observed, with a turbulent wake between them.

Moore and Renfrew (2005) used satellite-derived ocean vector winds (the Seawinds instrument aboard QuikSCAT) to derive a 5 year climatology of high wind speed events around Greenland. They noted a low directional consistency and large standard deviation in the wind field around Cape Farewell which, in combination with a high probability of observing a high wind speed event here, suggested that westerly tip jets are a common winter time feature. A composite analysis of westerly tip jets showed that they are related to the existence of a low-pressure centre between Greenland and Iceland, which provides the necessary synoptic conditions to accelerate air around Cape Farewell. Moore and Renfrew (2005) were unable to discuss the dynamics of westerly tip jets, as the QuikSCAT dataset used to create their climatology only provided surface winds and only over the open ocean. They suggested, however, that the conservation of Bernoulli function described by Doyle and Shapiro (1999) was probably not the only mechanism responsible for creating the westerly tip jet, but that acceleration of air as it is deflected around Cape Farewell by the cyclone between Greenland and Iceland was also likely to be important, e.g. see Petersen *et al.* (2003).

Bakalian *et al.* (2007) looked at the influence of the Iceland low latitude (ILLA) on the frequency of the westerly tip jet, and the implications of this for oceanic convection in the Irminger Sea. They noted that there was a correlation between the ILLA and the frequency of tip jets, partly, although not completely related to the link between the NAO and the frequency of tip jet events (the correlation between the ILLA and tip jet frequency was stronger than that between the NAO phase and tip jet frequency). It was also noted that there was a statistically significant correlation between the tip jet frequency and the two year lagged ILLA. This correlation is not well understood, however a speculative mechanism was suggested, whereby topographic Rossby waves generated by strong wind stress curl east of Greenland, described by Spall and Pickart (2003) traverse the North Atlantic in approximately 2 years, at which point they may interact with the Irminger Gyre. This may lead to a change in heat content or temperature gradients within the Irminger gyre, which may in turn influence cyclone development in the lee of Greenland,

and thus the formation of tip jets.

Våge *et al.* (2009b) used 40 years of reanalysis data (between 1957 and 2002 from the ECMWF ERA-40 reanalysis project, Uppala *et al.* (2005)), and empirical orthogonal function (EOF) identification, to find 586 westerly tip jet events which were then analysed. Våge *et al.* (2009b) noted that the frequency of the westerly tip jet was related to both the phase and strength of the NAO and to the ILLA. Additionally, an analysis of the trajectories of air parcels that made up these tip jets was carried out. It was found that the vast majority of air parcels in westerly tip jets originate to the west of Greenland, in a low Froude number regime, and are accelerated as they are deflected around Cape Farewell, in accordance with the suggestion of Moore and Renfrew (2005). There was however, an along-track pressure decrease over southern Greenland, suggesting that a minority of the air parcels were accelerated as they descended from Greenland, as suggested by Doyle and Shapiro (1999). Våge *et al.* (2009b) also noted that westerly tip jets were associated with a northward shift and downward extension of the upper tropospheric jet stream.

1.4.1.2 Easterly tip jets

Moore (2003) used the NCEP/NCAR global reanalysis dataset to develop a climatology of high wind speed events (> 17 m s^{-1}) around Greenland. Moore was able to identify the westerly tip jet described by Doyle and Shapiro (1999), but also identified a periodic strong easterly wind to the south-west of Cape Farewell, associated with a low pressure system to the south of Greenland. Moore dubbed this the 'reverse' tip jet; it is now more commonly referred to as the easterly tip jet. Renfrew *et al.* (2009) provide justification for this change of nomenclature. The frequency of this easterly tip jet was seen to be related to the strength and phase of the NAO, but on average the chance of observing one of these jets during a typical winter is around 10%. In hindsight, Moore (2003) suggested that the feature described by Moore and Vachon (2002) was probably associated with a typical easterly tip jet. It was also noted that, while the westerly tip jet was an almost totally zonal feature, the easterly tip jet had a stronger meridional component to the flow. Doyle and Shapiro (1999) discussed the extremely high heat fluxes that were seen to be associated with the westerly tip jet and Moore (2003) suggested that the same was probably true of the easterly tip jet, although he did note that the air masses that make up the easterly jet

were likely to be warmer and more moist than air in the westerly jets, due to a longer transit time over the ocean.

Moore and Renfrew (2005) included a discussion of the easterly tip jet in their QuikSCAT climatology of high wind speeds around Greenland. They described the easterly jet as an extension of a barrier flow immediately to the north-east of Cape Farewell. As the barrier disappears, the flow becomes supergeostrophic, and accelerates as it curves anticyclonically away from Cape Farewell. Assuming no synoptic (background) pressure gradient, Moore and Renfrew (2005) showed that the radius of this anticyclonic curvature is $R = -v/f$, and this agreed to first order with the easterly tip jet composites, despite the presence of a background pressure gradient.

Martin and Moore (2007) performed a simulation of an easterly tip jet using the MM5 mesoscale model. Simulated surface wind speeds in the jet were up to 30 m s^{-1}. Martin and Moore (2007) suggested that the heat fluxes associated with these high wind speeds could significantly contribute to convective overturning to the south-west of Greenland, around the recirculation described by Lavender *et al.* (2000). Sensible heat fluxes were seen to reach up to 100 W m^{-2} over a small area, and latent heat fluxes up to 150 W m^{-2} over much of the jet. These fluxes are significantly lower than those seen by Doyle and Shapiro (1999) associated with the westerly tip jet, however buoyancy fluxes were of the order of those which Marshall and Schott (1999) noted were required for open ocean convection.

Renfrew *et al.* (2009) described the structure of an easterly tip jet from flight-level data and dropsonde data recorded during the Greenland Flow Distortion Experiment (GFDex) during February & March 2007. Wind speeds of up to 50 m s^{-1} were observed at altitudes between 600 and 800 metres near the Greenland coast. The vertical extent of the core of the jet was seen to vary between 1500 m and 2500 m, depending on the strength of the jet, increasing with increasing jet speed. The atmospheric boundary layer was observed to be conditionally unstable, suggestive of relatively high ocean-atmosphere heat fluxes. Extremely strong momentum fluxes, corresponding to the high wind speeds were also observed.

Outten *et al.* (2009) performed numerical simulations of the easterly tip jet observed by Renfrew *et al.* (2009) and used these to perform a dynamical analysis of the easterly

jet. An analysis of the momentum budget in the core of the jet suggested that the jet exists in three distinct regimes, depending on the position along the jet locus. In regime 1, the jet is well described as a barrier flow, in geostrophic balance across the jet, but under an acceleration forced by the pressure-gradient force along the jet. As the height of Greenland decreases, the jet enters regime 2, where the Coriolis term becomes dominant, with the resulting anticyclonic curvature leading to a strong centrifugal force acting upon the jet. Above the level of the topography, the jet is in approximate gradient wind balance, but below this level turbulent flux convergence is important. The final regime exists where the anticyclonic curvature of the jet decreases, and the dynamics of the jet become better described by the geostrophic relationship, before the jet finally dissipates into the background synoptic-scale wind field.

It is clear that in the subpolar seas around Greenland a host of strong mesoscale weather systems are active and both observational and modelling studies have suggested that these features are often associated with strong atmospheric forcing of the ocean.

1.5 Representation of Air-Sea fluxes in the Analyses

Ocean-only general circulation models (OGCMs) are generally driven through the application of fluxes of heat, moisture and momentum, which are prescribed at the ocean surface, often from fields provided by atmospheric model products. It is thus important that these analyses are accurate, so that they can correctly force the oceans. However, it has been seen that the fluxes in some global atmospheric (re)analyses are not accurately represented, particularly the fluxes associated with small scale atmospheric phenomena. Josey (2001) compared fluxes from the European Centre for Medium Range Weather Forecasting (ECMWF) and National Center for Environmental Prediction (NCEP) global reanalyses as well as National Oceanography Centre (NOC) climatologies of heat fluxes with fluxes calculated from buoy-derived fluxes in the North Atlantic. It was found that the reanalyses (ECMWF/NCEP) underestimated the gain of heat through shortwave radiation and overestimated the latent release of heat to the atmosphere. This led to an underestimation of net heat gain by the ocean of up to 30 W m^{-2}. The NOC climatology, based on ship meteorological data was found to perform significantly better. Much of the error

in the reanalyses was attributed to the choice of bulk algorithm employed in the reanalysis models. Smith *et al.* (2001) compared the NCEP reanalysis with meteorological data from research ships, finding an underestimation in wind speed at all latitudes, increasing with increasing wind speed. Renfrew *et al.* (2002) presented a comparison of surface turbulent fluxes of ECMWF and NCEP reanalyses with data from a ship-based meteorological station in the Labrador Sea. It was found that the NCEP reanalysis overestimated sensible and latent heat fluxes by 50% and 27% respectively, while fluxes in the ECMWF reanalysis were generally within 10% of those calculated from observations. The poor performance of the NCEP reanalysis was attributed to roughness lengths in the bulk flux formulations which were unsuitable for high wind speeds, particularly in areas with large air-sea temperature differences, such as the Labrador Sea. Josey *et al.* (2002) compared wind stress forcing of the ocean in ECMWF and NCEP reanalyses and the NOC climatology, among others, finding an underestimation of wind stress in the tropical oceans in the NCEP reanalysis. Sun *et al.* (2003) compared surface meteorological and turbulent heat flux variables in a number of analysis products, including NCEP and ECMWF with buoy data in the Atlantic Ocean. It was again seen that heat loss, particularly in the NCEP reanalysis could be overestimated by up to 60%. Chelton and Freilich (2005) compared ECMWF and NCEP winds with satellite-derived winds from QuikSCAT and NSCAT. They found no consistent bias in the NCEP product, however ECMWF was seen to underestimate wind speeds by around 0.4 m s^{-1} on average, equivalent to up to a 10% under-representation of wind stress. Chelton *et al.* (2006) discussed using QuikSCAT winds for marine weather forecasting. This included a discussion of the power spectral density of wind speed in ECMWF and NCEP reanalyses, which were seen to significantly lack power at scales of less than around 1000 km, suggesting a poor representation of small scale atmospheric features in the reanalyses. Condron *et al.* (2006) showed that the ECMWF ERA-40 reanalysis does not capture the majority of polar mesocyclones with diameter less than 500 km in the north-east Atlantic. We shall discuss the representation of small-scale atmospheric features in the reanalyses further in Chapter 3.

1.6 Thesis Outline

In Chapter 2, we investigate the ability of the easterly tip jet to force oceanic convection in the south-east Labrador Sea, using oceanic float data, reanalysis data and an implementation of a one-dimensional mixed-layer model. In Chapter 3 we discuss the representation of small-scale atmospheric features in the ECMWF and NCEP reanalyses, and the performance of these reanalyses around Greenland. This is achieved through the validation of reanalysis fields and QuikSCAT winds with low-level flight data gathered during the Greenland Flow Distortion Experiment (GFDex). In Chapter 4 we discuss the formulation of ocean general circulation models, particularly the FRUGAL OGCM, which is used in Chapter 6, and the air-sea flux algorithms that are used in this model. We also discuss the spinning-up of the FRUGAL model and creation of a control run for the experiments in Chapter 6. In Chapter 5 we develop a parametrisation of the westerly and easterly tip jets. A number of metrics are employed to show that the parametrisation results in an improvement in the wind speed distributions around Greenland, and a one dimensional mixed-layer model is used to demonstrate the impact of the parametrisation on mixed-layer development over a single winter. In Chapter 6 we use the tip jet parametrisation within the FRUGAL OCGM to perform a number of perturbation/control experiments to gain an understanding of the impact of the tip jet on the ocean. Chapter 7 gives a summary of this thesis, and suggests directions for future work.

Chapter 2

The Role of Easterly Tip Jets in Forcing Oceanic Convection.

It has been speculated that low-level easterly tip jets, caused by the interaction of synoptic-scale atmospheric flow and Greenland, are an important mechanism for forcing open ocean convection in the south-east Labrador Sea. Here float data and meteorological reanalysis fields from the winter of 1996/1997, in combination with a simple mixed-layer ocean model, are used to show that, although relatively deep ocean convection did occur during this winter, the primary forcing mechanism was cold-air outbreaks from the Labrador coast rather than the smaller scale easterly tip jets. During this winter, the North Atlantic Oscillation (NAO) was in a weak positive phase. Similar treatments of the winters of 1994/1995 (strong, positive NAO) and 1995/1996 (strong, negative NAO) suggest that the result is robust regardless of the state of the NAO. This work has been published in *Geophysical Research Letters*, doi:10.1029/2007GL032971.

2.1 Introduction

The interaction of the steep, high topography of Greenland and synoptic and smaller scale cyclones causes a number of intense, small scale wind phenomena around the coast of Greenland. The first of these, so-called 'tip jets' (Doyle and Shapiro, 1999), are low-level westerly jets emanating from Cape Farewell characterised by a small meridional extent of around 200 km, a zonal extent of up to 1000 km and surface wind speeds generally exceeding 25 m s^{-1} (Moore and Renfrew, 2005). In addition, an easterly 'easterly tip

jet' was later suggested by NCEP reanalysis (Moore, 2003). A climatology of high wind speed events using QuikSCAT-derived surface winds (Moore and Renfrew, 2005) showed that both westerly tip jets and easterly tip jets were common wintertime features. Doyle and Shapiro (1999) noted that there were often extremely high ocean to atmosphere heat fluxes associated with these events, up to around 800 W m^{-2}, possibly with significant effects on the ocean below.

Ocean observations (Lavender *et al.*, 2000) revealed recirculations and relatively deep mixed-layers indicative of open ocean convection in the Irminger and south-east Labrador Seas. Such circulations are important in preconditioning the ocean for convection (Marshall and Schott, 1999), doming up isopycnals, so exposing more weakly stratified water to the atmospheric forcing, as well as isolating the water column, thus allowing repeated modification by the atmosphere. This, together with the enhanced heat fluxes associated with the Greenland westerly tip jet, rekindled interest in the Irminger Sea as a possible convection site, with potentially important implications for the meridional overturning circulation (Pickart *et al.*, 2003a,b; Bacon *et al.*, 2003; Centurioni and Gould, 2004).

In an idealised modelling study, Pickart *et al.* (2003a) used a climatological representation of the tip jet and a simple representation of Greenland to show that the tip jet was important both in the preconditioning of the model ocean through the provision of cyclonic wind stress curl and in the triggering of deep convection up to 1800 m, supporting theories that deep water formation does take place in the Irminger Sea Pickart *et al.* (2003b).

Bacon *et al.* (2003) observed two convective chimneys in the Irminger Sea extending to depths of 700 m and 1000 m, from three hydrographic sections in October–November 1996, August–September 1997 and July 1997 and a profiling float launched on 27 October, 1996. It was shown, by predicting the extent of convection that would result from the observed heat fluxes in the Irminger Sea that the 700 m convective column was formed in-situ in the winter of 1996/1997. Additionally, it was shown that the 1000 m column could not have been advected from convective sites as far afield as the Labrador Sea, and that the most likely region of formation for this column was in the vicinity of Cape Farewell. Bacon et al. noted that convection to the depth of 1000 m would have required an average surface heat flux some 30 W m^{-2} stronger than that observed near Cape Farewell,

however it was suggested that only a few days of very strong heat flux forcing, possibly associated with the westerly tip jet, could result in the formation of a 1000 m deep convective column.

Centurioni and Gould (2004) described wintertime conditions in the interior of the Irminger Sea, as observed by profiling floats between 1997 and 2003. They reported that potential temperature and salinity minima were most apparent in the south-west Irminger Sea and that this is where convection was most likely to occur. It was also noted that the south-west Irminger Sea is where the ocean will be most strongly forced by the Greenland westerly tip jet. To investigate the impact of the tip jet in mixed-layer deepening in this region, an idealised tip jet heat flux was applied to three one-dimensional mixed-layer models initialised with float profiles, describing linear rotating convection, non-linear rotating convection and static adjustment. The deepest winter mean mixed- layer depths produced were 550 db in the case of non-linear rotating convection, however it was concluded that, at least during the period of the study, there was not significant Labrador Sea Water renewal within the Irminger Sea.

Wintertime observations of mixed-layer depth in the Irminger Sea are relatively scarce, due largely to the inhospitable winter conditions in the area. However, direct measurements in the winters of 2002/2003 and 2003/2004 (Våge *et al.*, 2008) showed mixed-layers deepening to around 400 m before the onset of restratification during the spring. During these winters, the North Atlantic Oscillation (NAO) index was not strongly positive, reducing the number of robust tip jets (Moore, 2003). A one dimensional mixed-layer model (Price *et al.*, 1989) was able to reproduce the deepening of the mixed-layer. However if the signature of the tip jets was removed from the forcing fields, the mixed-layer only deepened to around 300 m (Våge *et al.*, 2008). Application of the same model to the high NAO winter of 1994/1995 showed a deepening of the mixed-layer exceeding 1600 m with the tip jet signature present, and only around 1200 m once the signature had been removed (Våge *et al.*, 2008). Thus it is clear that tip jets have a strong influence on ocean processes in the Irminger Sea.

An important question, first raised by Moore and Renfrew (2005), which currently remains unanswered is whether easterly tip jets have a similar such effect on the south-east Labrador Sea. A simulation of one of the strongest easterly tip jets identified by

Moore and Renfrew (2005), using a high resolution atmosphere only model, showed fairly strong heat fluxes, up to 250 W m^{-2} in the core of the jet, in the vicinity of the south-east Labrador recirculation (Martin and Moore, 2007). An examination of buoyancy flux through the surface of the ocean led Martin and Moore (2007) to speculate that easterly tip jets could indeed be important in the deepening of the mixed-layer. Våge *et al.* (2008) also speculate on the possibility that easterly tip jets have an impact on deep water formation, though they note that the air in the jets may be too modified to strongly affect the ocean.

In this chapter we present an analysis of heat fluxes in the ECMWF ERA-40 reanalysis over the secondary convective site in the Labrador Sea, to the south-west of Cape Farewell in Greenland. Ocean float data are used to establish the extent of oceanic convection and a one-dimensional mixed-layer model is then employed to highlight the meteorological conditions that control the onset and extent of open-ocean convection in the area. An atmospheric trajectory model is used to investigate the immediate history of air parcels that reach the secondary convective site, both when there are strong ocean-atmosphere heat fluxes in the area, and during easterly tip jets.

2.2 Ocean Observations

Float observations of the ocean are generally relatively sparse. As of 2007, the ARGO program has become fully operational, with 3000 profiling floats deployed throughout the global ocean. Even so, there is not enough data for the construction of a time series of mixed-layer depth in the small area in which we are interested. We thus consider the winter of 1996/1997, during which a large number of Profiling Autonomous Lagrangian Explorer (PALACE) floats (Davis, 1998) were released into the subpolar north Atlantic during the Labrador Sea Deep Convection experiment, at the height of the World Ocean Circulation Experiment (WOCE). These floats descend to a depth of approximately 1000 dB, where they drift freely for around a week before returning to the surface, measuring profiles of conductivity and temperature around every 10 dB. Once on the surface, they transmit this data to the Service ARGOS satellite system. The location of the float at the time of transmission is calculated by the Döppler frequency shift of the transmitted signal. This temporary period of high float concentration in the north Atlantic allows the construction of a timeseries of mixed-layer depth within the recirculation in the south-east

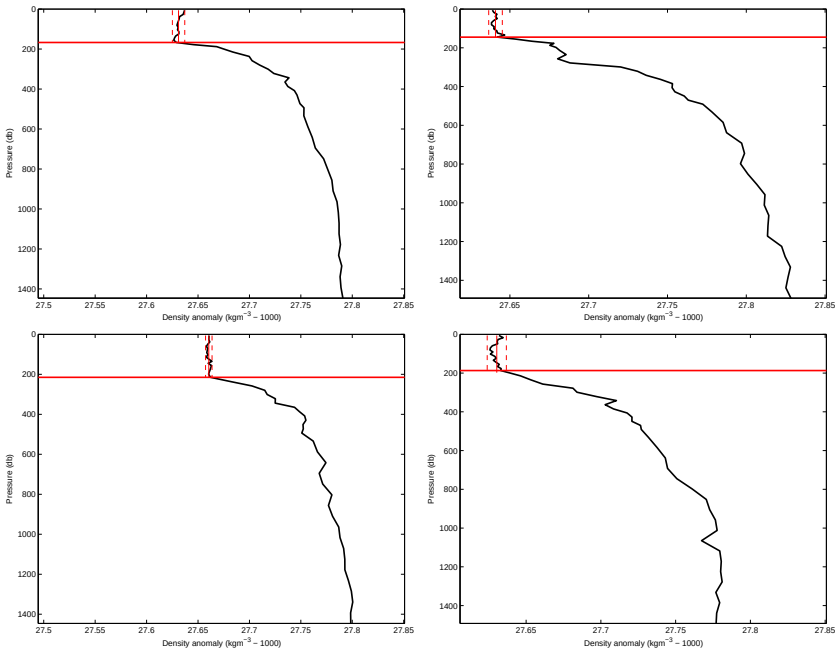

Figure 2.1: Density profiles showing the mixed-layer depth calculated using the method of Pickart *et al.* (2002). The vertical red lines show the mean and two standard deviation envelope over the subjectively estimated mixed-layer.

Labrador Sea, first identified by Lavender *et al.* (2000).

Temperature and salinity profiles recorded from the floats were used to calculate mixed-layer depth using the method of Pickart *et al.* (2002), whereby a subjective estimation of mixed-layer depth is made using a potential density profile, and the mean and standard deviation from the surface to this point are calculated. The depth of the mixed-layer is then taken to be the depth at which the potential density profile permanently moves further than two standard deviations from the mean. Some graphical examples of these calculations are shown in Figure 2.1. The vertical, solid red lines show the mean density over the subjectively estimated mixed layer, and the vertical dashed red lines show the two standard deviation envelope. The horizontal red line shows the calculated depth of the mixed-layer, that is, where the density profile permanently leaves the two standard deviation envelope.

The calculated depths of the mixed-layer are shown in Figure 2.2. These are found to be consistent with those found in a previous study Lavender *et al.* (2002), with the deepest mixed layers in this area lying between 600 and 800 m. The calculated depths of the mixed-layer in the region 57–60 °N, 45–50°W are shown in Figure 2.2. A total of 60

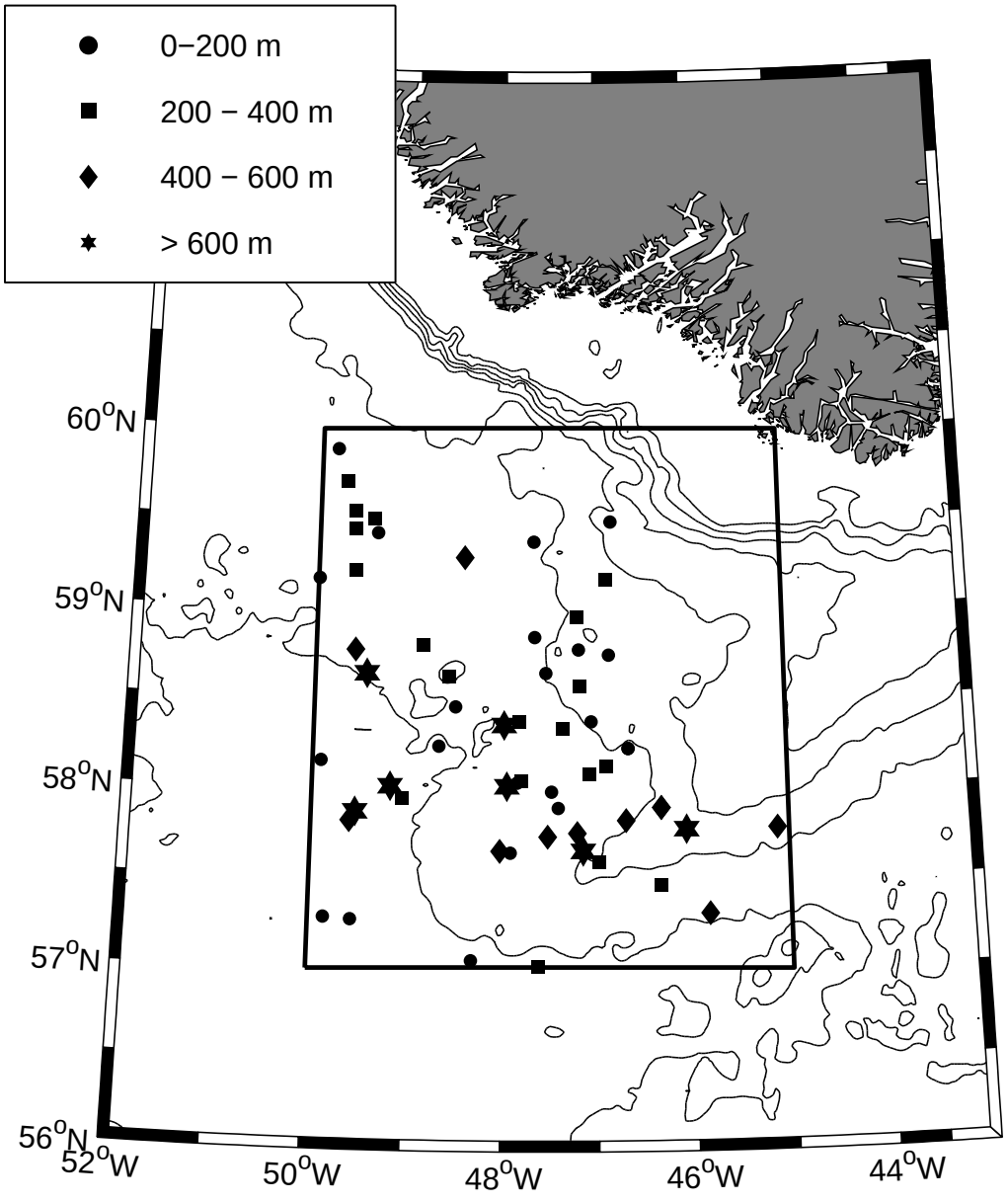

Figure 2.2: Mixed-layer depths in the south-east Labrador Sea measured by profiling floats. The box shows the area over which float data was collected. Bathymetry is contoured every 500 m.

Table 2.1: Dates, times and mixed-layer depths of the float profiles used in this study.

Date	Time	MLD (m)	Date	Time	MLD (m)
1996-11-14	2136	70	1997-01-17	2136	251
1996-11-16	0224	92	1997-01-18	0448	281
1996-11-16	0712	71	1997-01-23	2136	321
1996-11-18	0448	145	1997-01-25	0224	280
1996-11-19	0936	125	1997-01-27	0448	363
1996-11-24	2136	27	1997-01-28	0224	321
1996-11-26	0712	60	1997-02-02	0224	106
1996-11-26	1200	27	1997-02-02	2136	406
1996-11-28	0448	198	1997-02-04	0224	344
1996-12-04	2136	49	1997-02-04	0224	344
1996-12-06	0448	93	1997-02-07	0224	361
1996-12-06	1200	167	1997-02-12	0224	203
1996-12-08	0448	214	1997-02-12	2136	585
1996-12-08	1912	48	1997-02-14	0224	451
1996-12-14	2136	145	1997-02-14	0224	451
1996-12-16	0224	215	1997-02-17	0224	437
1996-12-16	0448	125	1997-02-19	1219	800
1996-12-18	0448	214	1997-02-22	1912	638
1996-12-24	2136	187	1997-02-24	0224	534
1996-12-26	0224	178	1997-02-24	1200	502
1996-12-26	0224	178	1997-02-27	0224	617
1996-12-28	0448	17	1997-03-04	1912	745
1996-12-29	0224	69	1997-03-06	0224	642
1996-12-29	1200	311	1997-03-09	0448	617
1997-01-03	2136	278	1997-03-19	0448	637
1997-01-05	0224	237	1997-03-26	1200	695
1997-01-05	0224	237	1997-03-31	1912	92
1997-01-07	0448	166			
1997-01-08	1200	111			
1997-01-13	2136	257			
1997-01-15	0224	258			
1997-01-15	0224	258			
1997-01-17	0448	187			

float profiles with mixed-layer depths ranging from 27 m in mid-November to 800 m in mid February were found, detailed in Table 2.1. The results here are consistent with those presented by Lavender *et al.* (2002), who used float data from the same WOCE period to describe open-ocean deep convection in the Labrador Sea. Lavender *et al.* (2002) noted that mixed-layers in excess of 400 m were present throughout the Labrador basin, however all of the deepest mixed layers (in excess of 1000 m) were observed to occur in a small area in the west of the basin, dubbed the ‘convective region’. This convective region was

seen to coincide with one of the strong recirculations discovered by Lavender *et al.* (2000), where the ocean is well preconditioned for deep convection. Lavender *et al.* (2002) also noted that there was an unexpected cluster of profiles with a mixed-layer deeper than 500 m to the south-wast of Cape Farewell (the area we are concerned with here), but no full discussion was given.

It is worth noting, that this study would be relatively difficult to repeat for current winters using the ARGO network, as this is still not as dense as was the float array in the North Atlantic during the WOCE, although it may be possible depending on the temporal distribution of float profiles through the winter. For example, in the study area during the winters of 2007/2008 and 2008/2009, there were 39 and 42 floats respectively, around 2/3 the number used in this study. If these are relatively evenly distributed throughout the winter, then this study may be repeatable for those winters. However in the winter of 2009/2010 only 20 float profiles were recorded in the study area, which would probably not provide a high enough resolution timeseries of mixed-layer depth to repeat this analysis.

2.3 A 1-D Mixed-Layer Ocean Model

The model we employ is an implementation of the Price, Weller and Pinkel (hereafter PWP) mixed-layer water-column model (Price *et al.*, 1989). This model evolves fields of salinity, S (PSU), temperature, T (°C) and meridional and zonal currents, (u, v) (m s^{-1}) and includes parameterisations of convection due to static instability and mixing due to shear instability. This allows the model to give a representation of the depth of the mixed layer as it evolves with time, forced by prescribed fluxes at the air-sea interface.

2.3.1 Formulation

The model equations are now described. Temperature evolves according to

$$\frac{\partial T}{\partial t} = \frac{-1}{\rho_0 c}\frac{\partial Q}{\partial z},$$

where $Q = q_{\mathrm{sw_{net}}} + q_{\mathrm{lw_{net}}} + q_{\mathrm{S}} + q_{\mathrm{L}}$ is the sum of net shortwave, longwave, sensible and latent heat fluxes respectively, ρ_0 is a reference density for sea water (≈ 1025 kg m^{-3})

and c is the specific heat capacity for sea water. The fluxes $q_{\mathrm{lw_{net}}}$, q_{S} and q_{L} are applied to the surface of the water column, while $q_{\mathrm{sw_{net}}}$ is absorbed throughout the water column, according to a double exponential depth dependence, given by

$$I(z) = I(0)\left[I_1 e^{z/\lambda_1} + I_2 e^{-z/\lambda_2}\right].$$

The values of I_1, I_2, λ_1 and λ_2 are highly dependent of the properties of the water under consideration. The values used in this study are those for reasonably clear, mid-ocean water, and are given by

$$\begin{aligned} I_1 &= 0.62 & \lambda_1 &= 0.6 \text{ m} \\ I_2 &= 1 - I_1 & \lambda_2 &= 20 \text{ m}. \end{aligned}$$

Salt/moisture fluxes are only enforced on the surface of the water column and are given by

$$\frac{\partial S}{\partial t} = -\frac{\partial \left[E - P\right]}{\partial z},$$

where E is the total evaporation and P the total precipitation.

Momentum is introduced into the entire mixed layer according to

$$\frac{\partial \mathbf{v}}{\partial t} = -f\mathbf{k} \times \mathbf{v} - \frac{1}{\rho_0}\frac{\partial \tau}{\partial t},$$

where $\mathbf{v} = (u, v)$ is the horizontal velocity vector, $\mathbf{k}$ is the unit vector normal to the ocean surface, $\tau = (\tau_x, \tau_y)$ is the horizontal wind stress vector and f is the Coriolis frequency. Momentum is removed at the bottom of the ocean with a drag coefficient of 0.001.

The density of the water column is approximated using a linear equation of state,

$$\rho = \rho_0 + \alpha\left(T - T_0\right) + \beta\left(S - S_0\right),$$

where α and β are the thermal and haline expansion coefficients respectively. The prescribed values for these are $\alpha = -0.23$ kg m^{-3} K^{-1} and $\beta = 0.76$ kg m^{-3} PSU^{-1}.

All of the differentials are calculated using a first-order finite difference scheme. When the momentum equation is time stepped, the Coriolis rotation $-f\mathbf{k} \times \mathbf{v}$ is applied

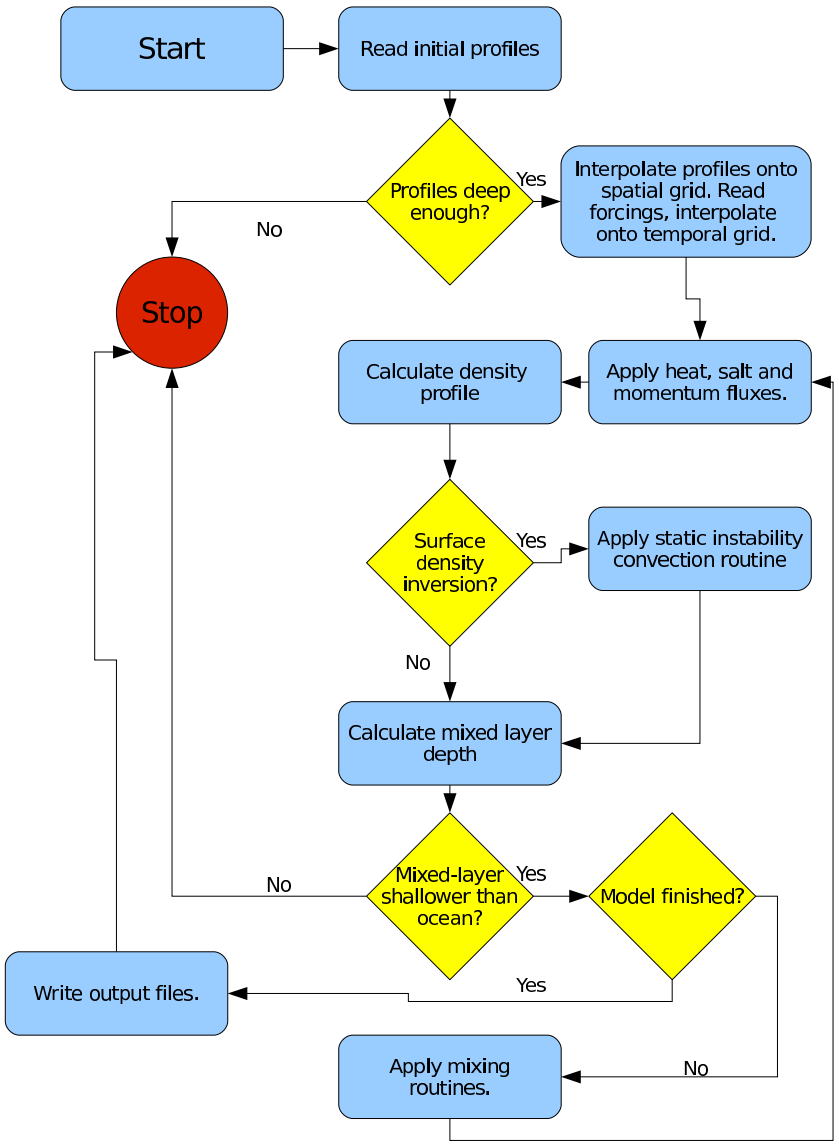

Figure 2.3: A simplified flow chart showing the major routines in the PWP model.

by rotating the water column through half an inertial rotation for the time step, before applying the momentum flux due to the wind stress τ, and finally rotating the fluid through the rest of the rotation for the time step. A simplified representation of the flow of the program is shown in Figure 2.3.

2.3.2 Vertical Motion

Vertical velocities are not considered in the model, however there are four processes by horizontal momentum, as well as T, S characteristics are transferred between layers.

2.3.2.1 Background diffusion

The model has a vertical diffusion scheme, given by

$$\frac{\partial \Phi}{\partial t} = \kappa \frac{\partial^2 \Phi}{\partial z^2},$$

where κ is a diffusion coefficient, and Φ is T, S or $\mathbf{v}$. The value of κ is free to be chosen, though numerous observational campaigns (e.g. see Wunsch and Ferrari (2004)) have measured pelagic dissipation to be of the order of 10^{-5} m^2 s^{-1}, and this is the value that we adopt in this study.

2.3.2.2 Static instability

A static instability mixing routine is called whenever $\partial\rho/\partial z < 0$ at the surface. If this is found to be the case, then characteristics are progressively homogenised from the surface down until $\partial\rho/\partial z \geq 0$ everywhere in the profile.

2.3.2.3 Bulk mixing

Bulk mixing takes place whenever the bulk Richardson number,

$$R_b = \frac{g\Delta\rho h}{\rho_0 \left(\Delta \mathbf{v}\right)^2} < 0.65.$$

Here g is the acceleration due to gravity, h the depth of the mixed layer, and Δ denotes the difference in some characteristic between the mixed layer and the top of the stratified part of the fluid column. If any layers are found to have $R_b < 0.65$ then T, S and $\mathbf{v}$ characteristics are homogenised from the surface to the first layer where $R_b \geq 0.65$.

2.3.2.4 Gradient mixing

The gradient Richardson number is given by

$$R_g = \frac{g\left(\partial\rho/\partial z\right)}{\rho_0 \left(\partial \mathbf{v}/\partial z\right)^2}.$$

If $R_g < 0.25$ anywhere in the profile, then it is assumed that the vertical shear of horizontal velocity is large enough to bring about vertical mixing. R_g is first calculated over

the stratified part of the profile. If the smallest value of R_g is found to be less than 0.25, then the two levels that produced this value, for instance j and $j+1$ are partially mixed according to

$$\Phi'_j = \Phi_j - \left(1 - \frac{R_g}{R'_g}\right)(\Phi_j - \Phi_{j+1}) \Big/ 2,$$

$$\Phi'_{j+1} = \Phi_{j+1} - \left(1 - \frac{R_g}{R'_g}\right)(\Phi_j - \Phi_{j+1}) \Big/ 2.$$

R_g is then recalculated from $j-1$ to $j+2$ and the search continues until $R_g \geq 0.25$ everywhere in the profile. This vertical shear mixing has the effect of smoothing out the jump in T, S and $\mathbf{v}$ characteristics at the base of the mixed-layer.

2.3.3 Model forcing and initialisation

The model is forced with 6-hourly timeseries of latent and sensible heat fluxes, net incoming solar and outgoing longwave radiation, convective and stratiform precipitation, evaporation and meridional and zonal wind stress. These are generated from the ECMWF ERA-40 reanalysis (Uppala *et al.*, 2005), by averaging over the area 57–60 °N, 45–50 °W, an area to the south-west of Cape Farewell encompassing the south-east Labrador Sea gyre identified by Lavender *et al.* (2000).

The model was initialised on the 14$^{\text{th}}$ November, 1996, as this was when sufficient data became available, using temperature and salinity profiles obtained from the PALACE floats, Figure 2.4. No ocean velocity profiles were available, so zonal and meridional velocities were initialised to be 0.1 m s^{-1} in the mixed layer, decreasing linearly to zero at depth.

To gain an understanding of the uncertainty introduced into the model by using an arbitrary float profile at the beginning of the winter period to be representative of the mixed layer throughout the domain, we initialise the model from every observed profile throughout the integration period (a period of 139 days from the 14$^{\text{th}}$ of November, 1996 until the end of March, 1997) which was suitable to initialise the model, i.e. those which were deep enough (at least 1200 m) and suitably stratified. The results of these integrations are shown in Figure 2.5. The grey lines in 2.5 (a) show the evolution of the modelled mixed-layer when initialised by all of the observed profiles from the PALACE floats (the mixed-layer depths of which are shown as red dots). As expected, given both

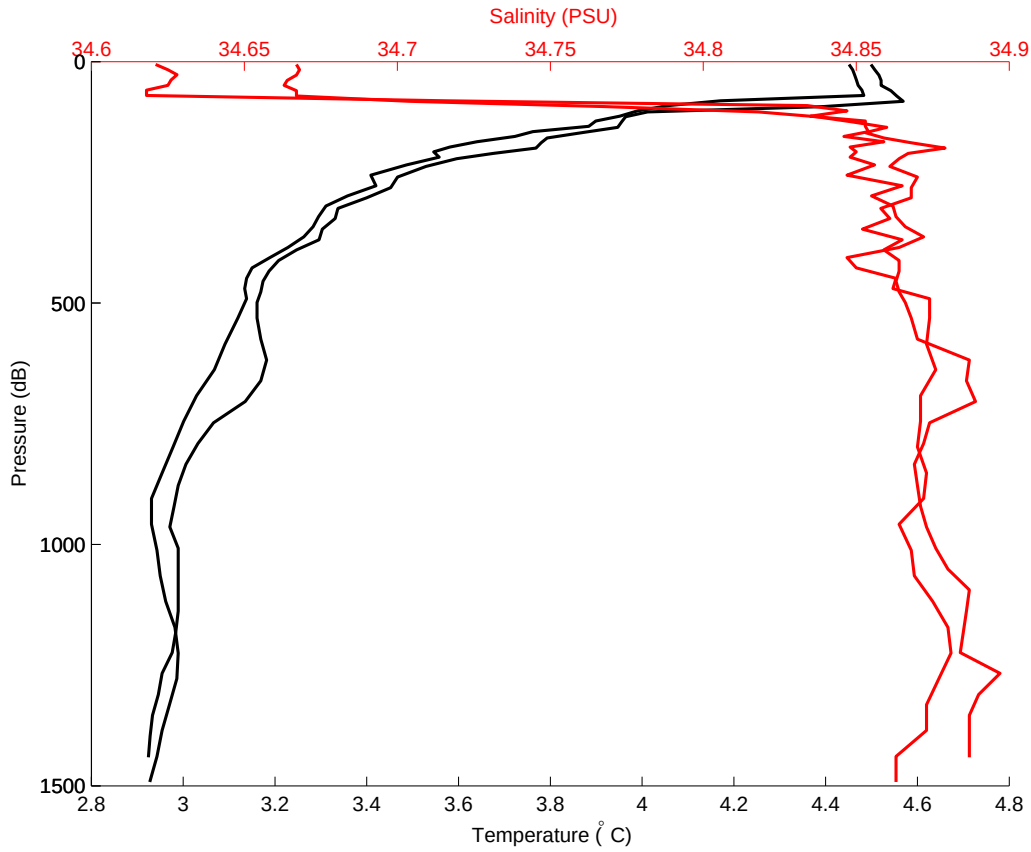

Figure 2.4: The two profile sets of temperature (°C, black) and salinity (PSU, red) which were used to initialise the PWP model.

the temporal and spatial spread of the initial profiles, the range of the final mixed-layer depth in the model is relatively large. Having said this, the evolution of the mixed layer in the majority of the model integrations shows a similar pattern. The model shows a fairly slow deepening of the mixed-layer though the first half of the integration, consistent with the observations. Through February and the beginning of March, the model generally shows an increased rate of mixed-layer deepening, again consistent with the observations, although by this time there is a fairly large spread in the modelled mixed-layer. Mixed-layer deepening generally slows in the model after the middle of March, corresponding well with a cessation of mixed-layer deepening in the observations. A suggestion of re-stratification is seen in the observations towards the end of March; this is not seen in any of the model integrations which were initialised before this time. Figure 2.5 (b) shows the mean of all of the initialised model integrations as well as the one and two standard deviation envelopes.

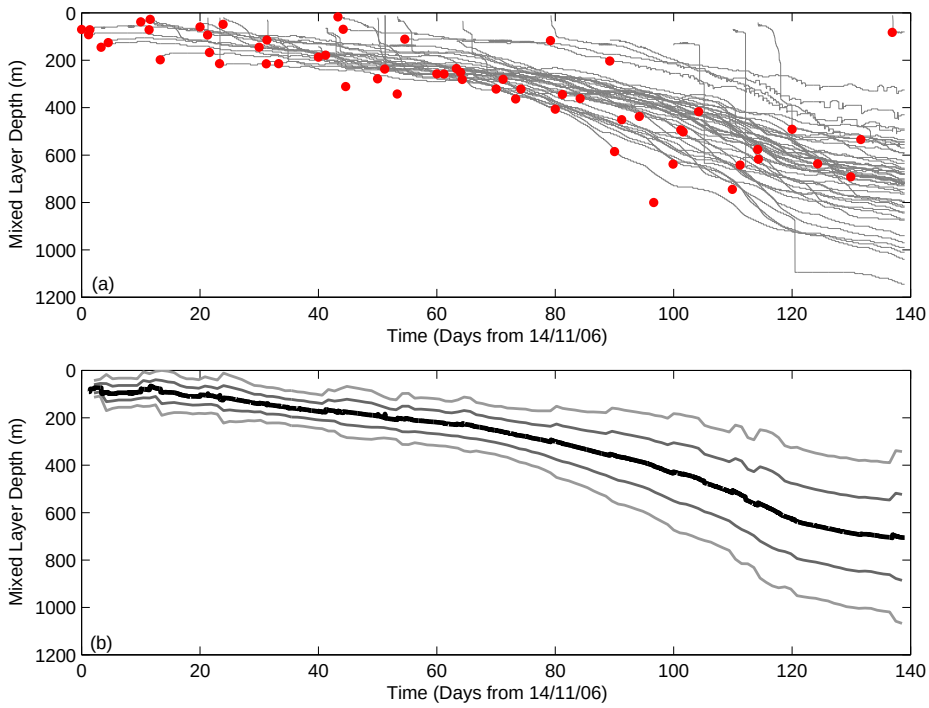

Figure 2.5: Quantifying uncertainty in the PWP model. The top panel shows the evolution of the model when initialised from each suitable observed profile; the bottom panel shows the mean of all of the initialised profiles, as well as the one and two standard deviation envelopes.

2.4 Atmospheric Forcing

Having ascertained from the float data that moderately deep convection occurred in the South-East Labrador Sea in the winter of 1996/1997, we now evaluate the importance of easterly tip jets in triggering these events.

2.4.1 The ERA-40 Dataset

The ERA-40 dataset is a reanalysis project, run by the ECMWF for a period of 45 years from September 1957. The aim of the project is to produce a long term atmospheric dataset using a consistent data assimilation system. As one of the only multi-decadal reanalysis datasets (a notable exception being the NCEP/NCAR ongoing atmospheric reanalysis), ERA-40 offers perhaps the best representation of the atmosphere over the past four decades, and as such the surface layers of the reanalysis are often used as the boundary conditions for forcing ocean-only general circulation models. The model runs at a resolution of T159, which is equivalent to around 125 km with 60 vertical levels. For

Table 2.2: North Atlantic Oscillation (NAO) index for the three winters considered in this study.

Winter (DJFM)	NAO Index
1994/1995	$+2.44$
1995/1996	-2.32
1996/1997	$+0.18$

further details on ERA-40, see Uppala et al. (2005), or Chapter 3.

2.4.2 Easterly Tip Jets in ERA-40

Easterly tip jets are objectively identified in the ERA-40 re-analysis as times when the peak wind speed in the box bounded by 57–60 °N, 45–50 °W is at least 15 m s^{-1}, Figure 2.6(b) and the average wind direction is between 45 and 135 degrees from north, Figure 2.6(c). During this winter, the majority of the easterly tip jets occurred in two clusters, the first occurring in early January and the second in late March. All of the high heat flux events (greater in magnitude than 400 W m^{-2}) lie in between these two clusters of easterly tip jet activity. Indeed it can be seen in Figure 2.6(d) that the easterly tip jets identified in the reanalysis are associated with lower than average heat fluxes in the area, with atmosphere to ocean fluxes (i.e. a warming of the ocean) at times.

We may filter the signature of the easterly tip jet out of the timeseries used to force the 1-dimensional ocean model by replacing points in the timeseries which are identified as tip jets with mean values over the rest of the winter. Forcing the model with these modified timeseries thus allows us to evaluate the impact of the easterly tip jet on mixed-layer deepening. When forced with this modified 'no tipjet' forcing, the mixed-layer evolution is essentially indistinguishable from that seen in Figure 2.6(a), and the final difference between the two runs is 5 m (a single grid point), with the deeper mixed-layer forming in the run in which the tip jet forcing is removed. This suggests, that at least in our idealised set-up, that the easterly tip jet has no net effect on mixed-layer deepening in the south-east Labrador Sea.

2.4.3 The NAO

Moore (2003) showed that there exists a negative correlation between the incidence of easterly tip jets and the NAO index, and a positive correlation between the NAO index

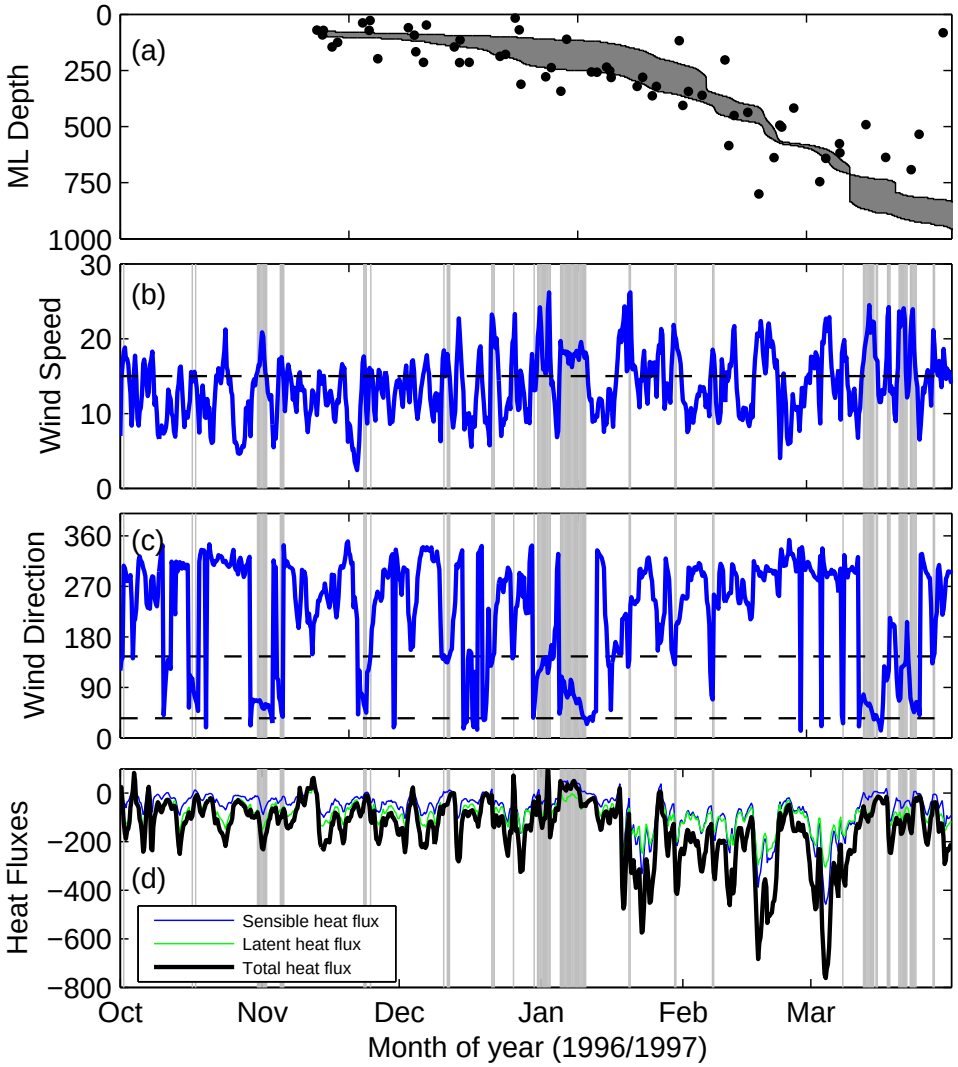

Figure 2.6: Timeseries for October–March 1996/1997 showing (a) Mixed-layer depth from float profiles and PWP model (shading shows spread from two initial profiles), for convenience, (b) 10 metre peak wind speed (m s^{-1}), showing the 15 m s^{-1} threshold for a easterly tip jet, (c) 10 metre wind direction, showing the 45° and 135° thresholds for a easterly tip jet, (d) Latent, sensible and total turbulent heat fluxes (W m^{-2}) over the south-east Labrador Sea in the ECMWF ERA-40 dataset. Vertical shaded areas show the objectively defined easterly tip jets. Note that large heat flux events do not generally co-incide with the easterly tip jets.

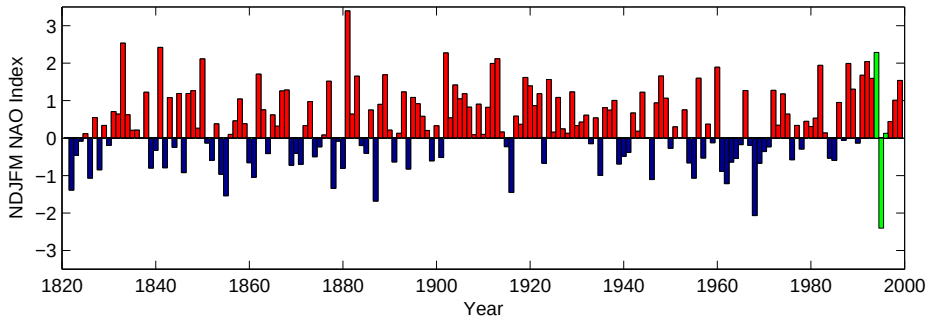

Figure 2.7: Winter (November–March) NAO indicies from 1820 to 2000. The three winters we have considered in this study are highlighted in green. NAO data obtained from `http://www.cru.uea.ac.uk/cru/data/nao.htm`, accessed 4th March, 2008.

and the incidence of forward tip jets. Given that during the winter of 1996/1997 the NAO was in a weakly positive phase (Table 2.2), we would expect there to be fewer than average easterly tip jets during this time. It is possible, therefore, that if we only consider this winter we may underestimate the role that easterly tip jets play in forcing oceanic convection. To address this issue, we have considered two further winters: 1994/1995, when the NAO was in a strongly positive phase, and 1995/1996 when the NAO was strongly negative. Significantly more easterly tip jets were observed in the winter of 1995/1996, and significantly fewer in the winter of 1994/1995. This is consistent with the observations of Moore (2003). During both of these winters easterly tip jets were associated with weaker than average air-sea heat fluxes, as was the case in the winter of 1996/1997. A timeseries of the NAO index from 1820 to 2000 is show in Figure 2.7. The three winters which we study in this chapter are highlighted in green. Note that the NAO index during two of the winters which we study are some of the strongest on record.

2.4.4 Average Atmospheric Conditions

Figures 2.6 and 2.8 show that the vast majority of events in the three winters that we have considered when ocean to atmosphere heat fluxes were large, between 400 and 800 W m^{-2}, were associated with flow from the north or north west. Composites of the 20 analysis times with the largest heat flux out of the ocean (in ERA-40, 1.125° gridded 6 hourly data) are shown in Fig. 2.9 for the winters of 1996/1997 (weakly positive NAO, top), 1994/1995 (strongly positive NAO, middle) and 1995/1996 (strongly negative NAO, bottom). The composite synoptic situation for all of these cases shows a low pressure

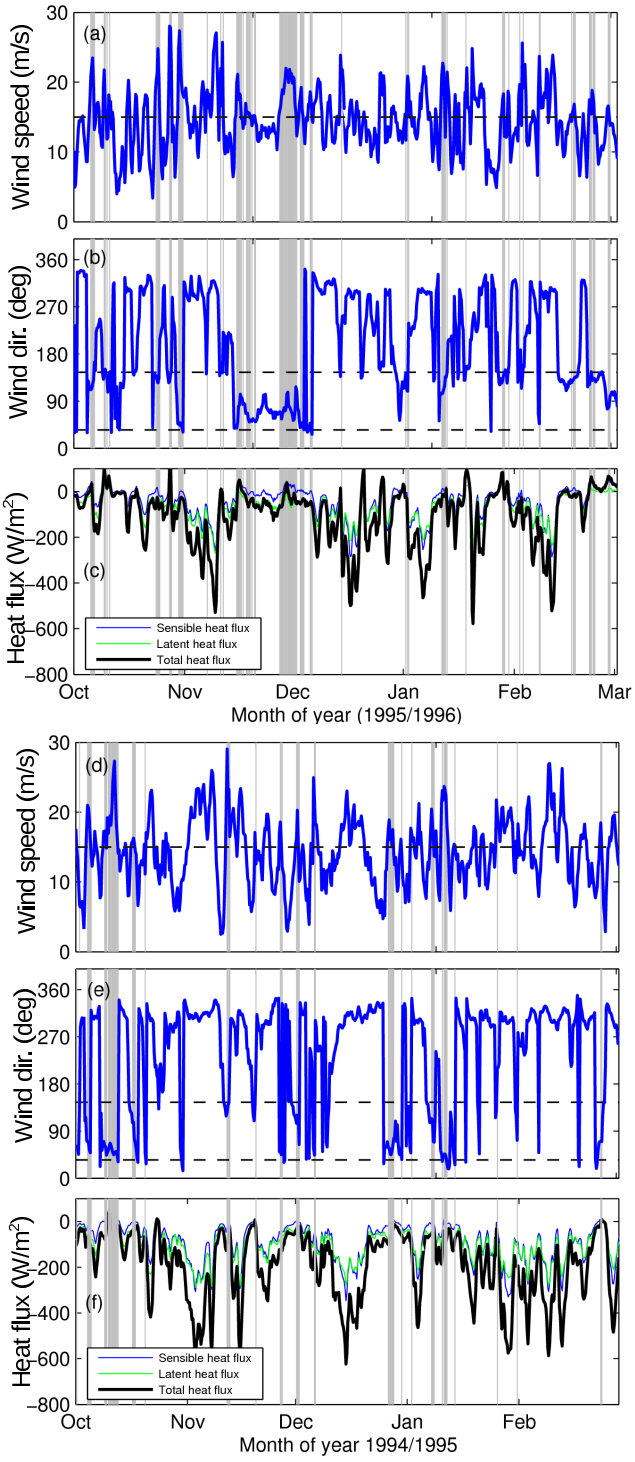

Figure 2.8: As Figure 2.6 (b)–(d), but for the winters of 1995/1996, (a)–(c), and 1994/1995, (d)–(f).

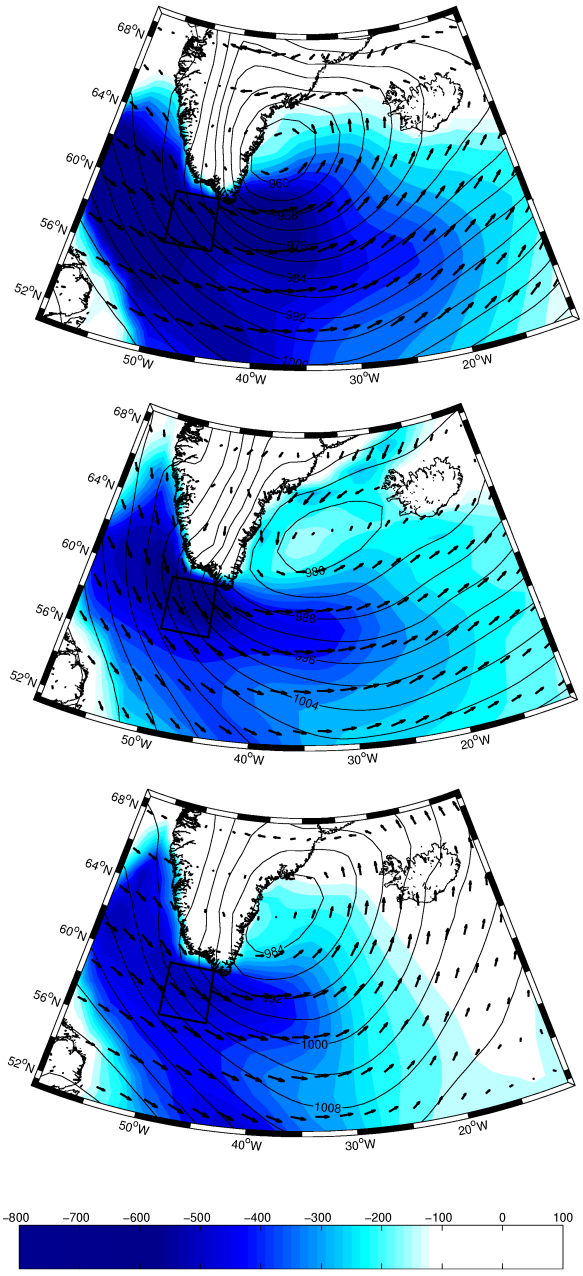

Figure 2.9: Composite of combined latent and sensible heat flux (W m^{-2}, shaded), 10 m wind vectors every 2.25° and mean sea level pressure (contours, every 4 hPa) for the 20 highest heat flux events in 1996/1997 (top), 1994/1995 (middle), 1995/1996 (bottom). The box to the south-west of Cape Farewell shows the area over which float data were collected and meteorological variables were averaged.

centre off the south-east coast of Greenland, with a generally north-westerly flow over the bulk of the Labrador Sea, including the secondary convection site in the south east of the basin. The strongest heat fluxes are generally seen in the central Labrador Sea, around 60° N, 55° W, near the primary convection site, however the fluxes in the secondary convection site exceed 600 W m^{-2} during the positive NAO winters, which could be strong enough to trigger deep convection if the ocean is suitably preconditioned. Note also that the heat fluxes and wind field show the signature of a westerly tip jet to the east of Cape Farewell, indicating that this synoptic situation is also providing enhanced atmospheric forcing of the Irminger Sea convection site. A previous study of this area (Lavender *et al.*, 2002) showed a January–April mean of heat fluxes, constructed using a bias-corrected version of the NCEP reanalysis. This displayed no maximum in the South-East Labrador Sea. This is not inconsistent with the results presented in Fig. 2.9 which shows a maximum in this area; when the ERA-40 heat fluxes used in this study are averaged over the same January–April period, broadly the same spatial features are seen (not shown). Equally, when the NCEP reanalysis is composited by high heat flux events in the South-East Labrador Sea, a picture similar to Fig. 2.9 emerges.

When constructing a climatology of easterly tip jets, Moore (2003) subjectively defined easterly tip jets in the NCEP/NCAR reanalysis as times when the peak wind speed was gale force or greater (i.e. at least 17 m s^{-1}). Here we use a slightly lower threshold of 15 m s^{-1}, to ensure that we identify all easterly tip jets in our objective, automatic analysis. The number of easterly tip jets identified in the analysis will clearly be sensitive to this choice of threshold, however the composite synoptic situation is not. The high heat flux events are entirely independent of easterly tip jets, thus the composite of the 20 highest heat flux events is unaffected by changing the easterly tip jet threshold wind speed. The composite of all of the easterly tip jets in the winter of 1995/1996 is shown in Figure 2.10. The panel on the left shows the composite when the threshold is set to 15 m s^{-1} and the panel on the right shows the composite when the threshold is set to 20 m s^{-1}. The synoptic situation is similar in both, with a low pressure centre to the south-west of Cape Farewell. As one would expect, the heat fluxes are stronger in the right-hand panel where the winds are on average stronger, however these fluxes are still not large when compared to the largest heat fluxes when the atmosphere in this area is in a westerly regime. This

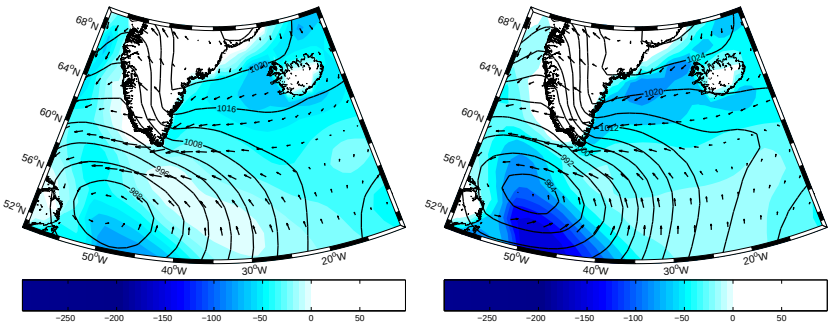

Figure 2.10: A comparison of composited heat fluxes (W m^{-2}, shaded), 10 m wind vectors every 2.25 degrees, and mean sea-level pressure (contours, every 4 hPa) during easterly tip jets in the 1996/1997 winter for (left) a tip jet threshold of 15 m s^{-1}, (right) a tip jet threshold of 20 m s^{-1}.

is especially true in the area immediately to the south-west of Cape Farewell, the area we are interested in this study, where there is very little difference between the two panels.

2.4.5 Air Mass History

In order to help understand why heat fluxes associated with easterly tip jets are comparatively weak despite the relatively strong winds, we now examine the short term history of air parcels which are located over the centre of the secondary convection site, and one degree north, east, south and west, at 950 hPa, during high heat flux and easterly tip jet events. We consider the history of the three highest heat flux events and the three strongest easterly tip jet events during the winter of 1996/1997.

The history of the air parcels is calculated using the British Atmospheric Data Centre atmospheric trajectory model, with air parcels advected by the ECMWF archive $2.5^\circ \times 2.5^\circ$ winds, which are a combination of ERA-15 and operational winds, archived every 6 hours. The winds are linearly interpolated in space and time onto the parcel position, which are then advected using a 4^{th} order Runge-Kutta time stepping scheme, following Dritschel and Ambaum (1997).

Figure 2.11 shows the trajectories of air parcels during the 24 hours immediately prior to the high heat flux or robust easterly tip jet event. As one may expect from the synoptic composites (Figure 2.9), air parcels which are located over the south-east Labrador Sea during high heat flux events (red, green, cyan) have been advected in from the west (Hudson Bay area) or from the north-west around Baffin Island. All of these air parcels have been advected at fairly low levels, generally below 900 hPa and arrive at the south-east

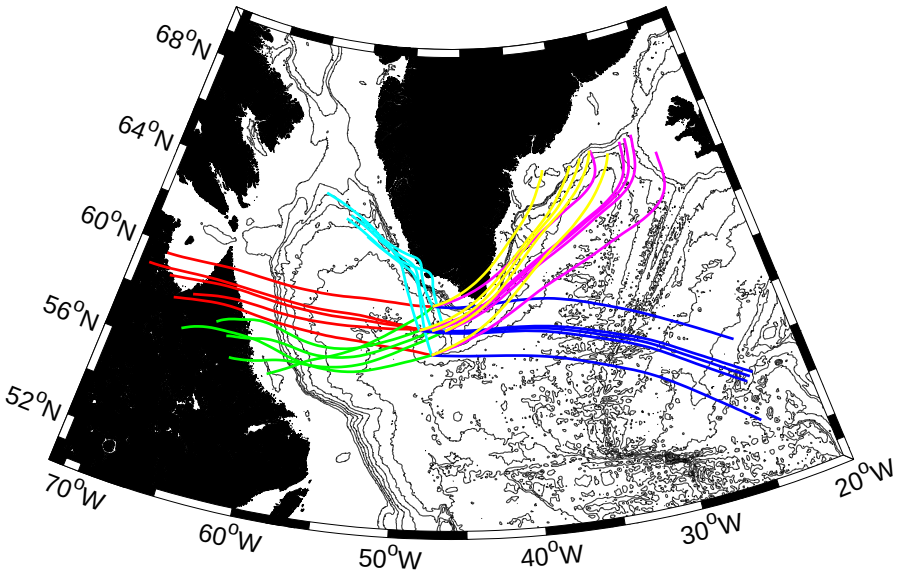

Figure 2.11: 24 hour trajectory history of air parcels centred at 58.5 °N, 47.5 °W at 950 hPa, with a 1° spread. The red, green and cyan trajectories are for the three highest heat flux events in the winter of 1996/1997 and the blue, yellow and magenta are for the three strongest easterly tip jets of the same winter. Bathymetry is contoured every 500 m.

convection site with potential temperatures between -10 °C and -3 °C (Figure 2.12).

Conversely, during easterly tip jets (blue, yellow, magenta), the air parcels are advected to the convection site from the west and north west. The parcels during two of the easterly tip jets are advected from the Denmark Strait area, with the third set being advected in from much further from the south. Running the trajectory model for a series of other easterly tip jets shows that this is an exception to the norm, and the majority of air parcels during easterly tip jets are advected from the Denmark Strait area. Again, the parcels generally remain at fairly low levels, generally below 850 hPa, and arrive at the convection site with potential temperatures between -3 °C and 0 °C for the parcels advected from the north-east and a potential temperature of over 5 °C for the parcels advected in from further south (Figure 2.13).

The temperature difference over the secondary convection site during these two regimes goes some way to explain why heat fluxes are so reduced during easterly tip jets (the average sea surface temperature in this area during the winter is around 4 °C), however it does not tell the whole story; one must also consider how much moisture there is in the air. Unfortunately the atmospheric trajectory model used does not output any information on atmospheric moisture, so we cannot see how this evolves with time along the model

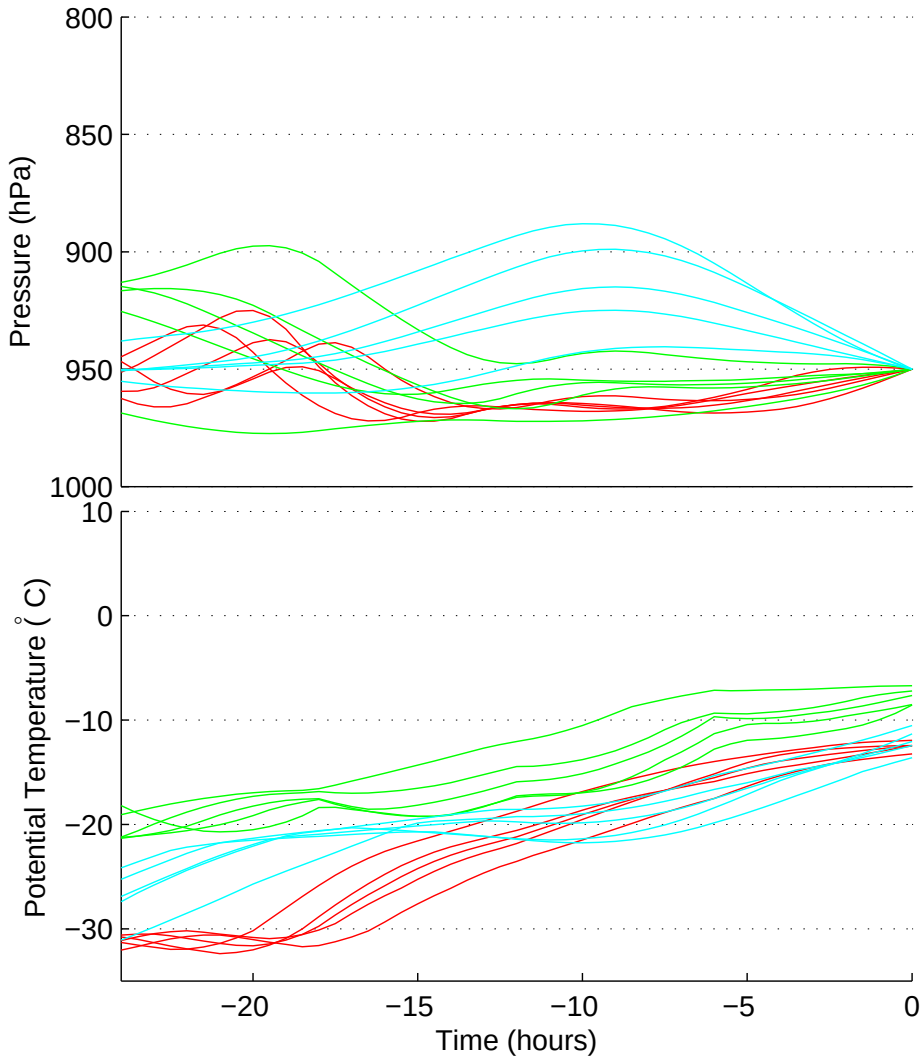

Figure 2.12: 24 hour history of air parcels centred at 58.5 °N, 47.5 ◦W at 950 hPa, with a 1° spread for the three highest heat flux events in the winter of 1996/1997 showing (top) pressure (hPa) (bottom) potential temperature (°C).

trajectories, however we can look at atmospheric moisture in the vicinity in the ERA-40 dataset. Figure 2.14 shows the average relative humidity in ERA-40 during high heat flux events (left) and easterly tip jets (right). During high heat flux events, the air over the secondary convection site has a relative humidity of around 70% and during easterly tip jets there is a meridional gradient of relative humidity from 70% in the north of the domain to around 83% in the south. The comparatively high relative humidity during easterly tip jets will further reduce heat fluxes at these times. Note that relative humidity has been used here as an indication of the relative strengths of the latent heat flux in easterly tip jet and high heat flux conditions. A full treatment, however, requires consideration of the

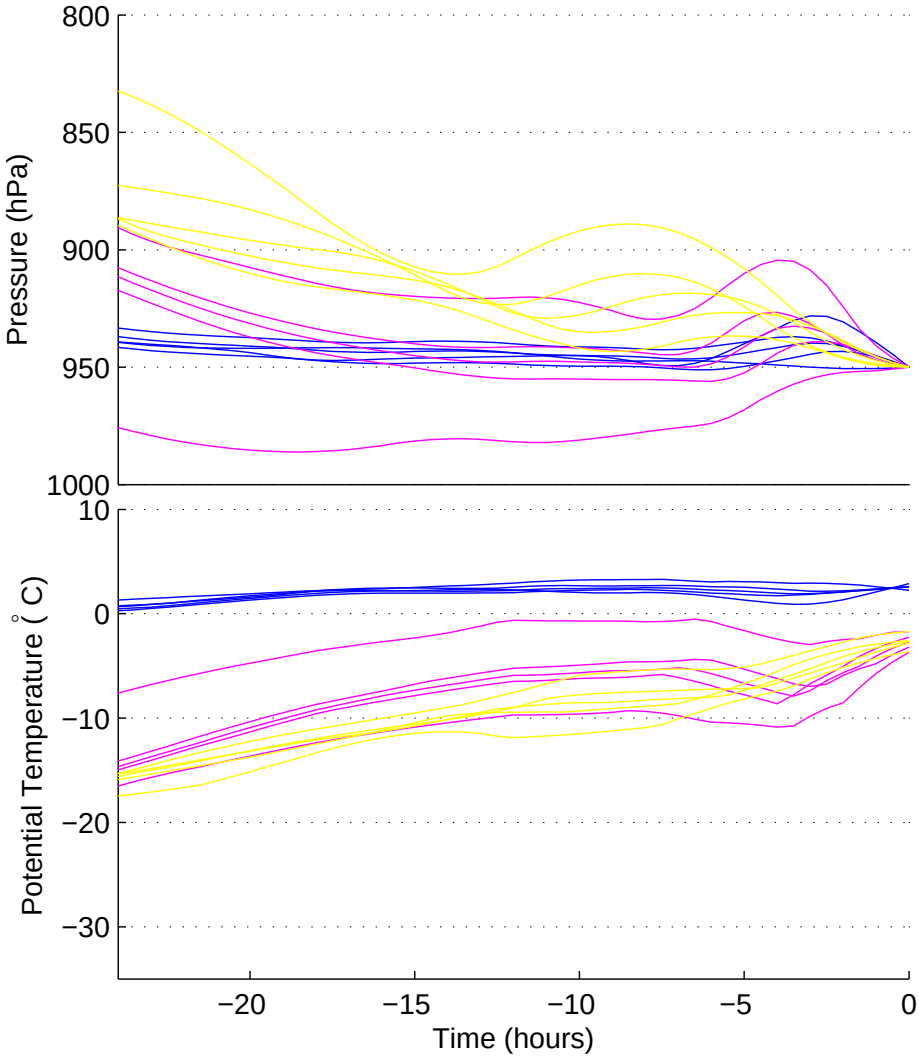

Figure 2.13: 24 hour history of air parcels centred at 58.5 °N, 47.5 ◦W at 950 hPa, with a 1° spread for the three strongest tip jet events in the winter of 1996/1997 showing (top) pressure (hPa) (bottom) potential temperature (°C).

air-sea humidity difference.

2.5 Discussion and Conclusions

Through the study of ocean temperature and salinity profiles during the winter of 1996/1997 we have confirmed that deep convection occurred at the secondary convection site in the south east Labrador Sea. Convection in the area was observed to penetrate to over 800 m depth, consistent with mixed-layer depths seen by Lavender et al. (2002), and represent

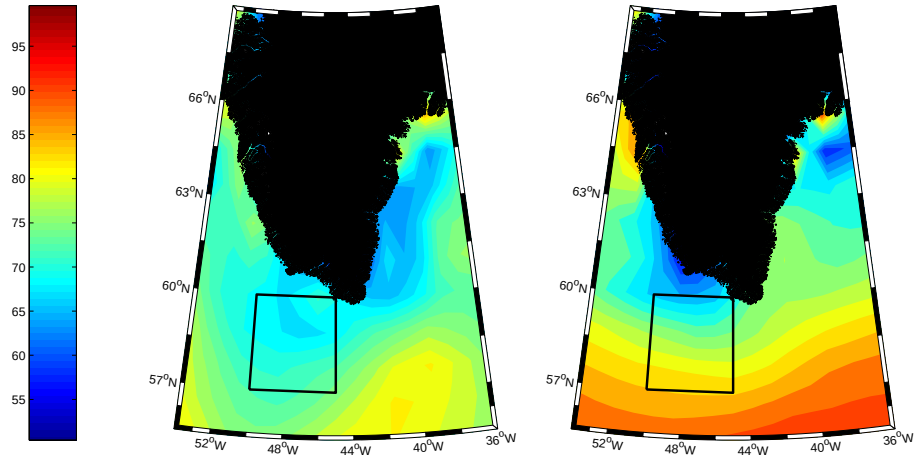

Figure 2.14: Composite of 2 m relative humidity (%) during the winter of 1996/1997 for (left) the three highest heat flux events, and (right) the three strongest easterly tip jet events.

the deepest mixed-layers observed in the eastern Labrador Sea. It should be noted, however, that in the western Labrador Sea, where the ocean is equally well preconditioned, but heat fluxes tend to be stronger due to the proximity of the site to the North American Continent, mixed-layers were observed to penetrate to depths of around 1350 m during the same winter as this study (Lavender et al, 2002). In stronger winters, mixed- layers in the western Labrador Sea convective region have been observed to as deep as 2300 m (Dickson et al., 1996).

It has been speculated (Moore, 2003; Moore and Renfrew, 2005; Martin and Moore, 2007) that easterly tip jets may be important in causing convection in this area, in a similar manner to the way that westerly tip jets have been shown to trigger convection in the Irminger gyre (Pickart *et al.*, 2003a,b; Våge *et al.*, 2008). Martin and Moore (2007) showed through a high resolution numerical study of a particularly robust jet that heat fluxes can be relatively high during easterly tip jets, with latent fluxes of up to 150 W m^{-2} and sensible heat fluxes of between 50 and 100 W m^{-2}. These enhanced fluxes are not well resolved in the ECMWF ERA-40 dataset, but there is a representation of the jet in the reanalysis, albeit a somewhat coarse representation with a core wind speed some 10-15 m s^{-1} too low. The instantaneous latent and sensible heat fluxes based on ECMWF winds, temperature and humidity for 0000 UTC on December 21, 2000 (the case simulated by Martin and Moore (2007)) are around -10 W m^{-2} and -40 W m^{-2} respectively. We suggest that these small negative fluxes are due to an excessive advection

of warm air from the south by the parent cyclone and a lack of advection of cold air from the north east of Cape Farewell, resulting in an overestimation of surface air temperature in the south-east Labrador Sea at this time. Despite this drawback, it is worth emphasising that the 250 W m^{-2} heat fluxes associated with this strong easterly tip jet in the mesoscale model (Martin and Moore, 2007) are significantly smaller than the largest heat fluxes seen in this area (Fig. 2d). Recall that the average of the 20 largest heat flux events is 600 W m^{-2}, with peak values around 750 W m^{-2}. Despite the weak representation of the fluxes associated with easterly tip jets in ERA-40, the deepening of the mixed-layer is well captured (in fact overestimated) in the 1-dimensional model when forced by this dataset. This suggests that despite the crude representation of easterly tip jets in ERA-40, the heat flux fields are well represented on the scale of the Labrador recirculation.

Although ERA-40 does not show enhanced heat fluxes during easterly tip jets, periods of strong heat fluxes over the secondary Labrador Sea convection site are observed in the dataset, with peak values of around 750 W m^{-2}. These strong fluxes coincide with the onset of the deepening of the mixed-layer, and are associated with cold-air outbreaks from the Labrador coast. During these periods the atmosphere over the Labrador Sea is in a westerly regime and elevated ocean-atmosphere fluxes of over 600 W m^{-2} have been observed (Renfrew and Moore, 1999; Renfrew *et al.*, 2002). Hence we conclude that open ocean convection in the south-east Labrador Sea is being forced primarily by westerly cold-air outbreaks off the Labrador Coast and not easterly tip jets. Thus, in terms of atmospheric forcing, the south-east Labrador Sea convection site is part of the central Labrador Sea and Irminger Sea convection regime, i.e. open ocean convection at these three sites may be triggered by broadly the same synoptic-scale meteorological situation. We note, however, that a definitive conclusion on the role that easterly tip jets play in this area requires a much longer climatology using a high resolution dataset which correctly represents the detail of the structure of, and fluxes associated with, easterly tip jets.

Chapter 3

The Greenland Flow Distortion Experiment

3.1 Introduction

Ocean only general circulation models (OGCMs) are an important tool in increasing our understanding of the three dimensional structure and flow of the oceans, allowing relatively quick integrations by avoiding the added complexity and computational cost of a model atmosphere. Such models, however, rely on surface boundary conditions (i.e. surface meteorological variables) to be prescribed for every model timestep, thus it is important for these forcing fields to accurately represent the state of the atmosphere at the air-sea interface. This is especially important in regions of open-ocean convection; the Labrador Sea, Irminger Sea and Greenland-Iceland-Norwegian Seas as well as the Mediterranean and Weddell Seas. It is here, where the ocean is weakly stratified, that the atmosphere is strongly coupled to abyssal waters and the properties of the deep ocean are set. In many of these regions, however, the observational network is sparse due to their remote location and often inhospitable conditions, thus it is difficult to reliably validate the atmospheric models which are used to force OGCMs.

In the late winter of 2007/2008, an aircraft based observational campaign, using the Facility for Airborne Atmospheric Measurement (FAAM), was run out of Keflavík, Iceland: The Greenland Flow Distortion Experiment (GFDex). The primary aim of this campaign was to gain the first in-situ measurements of the flow distortion effects of Greenland,

and how these affect weather systems, both local and remote, and air-sea interactions in the Irminger, Greenland, and Labrador Seas. The large quantity of high quality surface layer data recorded during low-level flight legs also presents an ideal opportunity to validate model surface fields in these areas, and gain an understanding of how well flow distortion effects such as barrier winds and tip jets are represented in meteorological analyses.

In this chapter we compare the aircraft measurements with meteorological surface variables from the ECMWF operational analysis, retrieved at both N400 and N80 resolution, the latter being used as a proxy for the ERA-40 reanalysis which is unavailable post mid-2002. We also include the lower resolution NCEP/NCAR ongoing reanalysis, archived at 2.5×2.5 degrees, which, although not used subsequently in this thesis, is one of the most commonly used datasets for forcing ocean models. In addition, QuikSCAT vector winds are considered to see how they perform in the area of study. QuikSCAT winds will later be used in the creation of a general characterisation of tip jets and the subsequent development of a technique for bogussing the Greenland tip jet into the ERA-40 reanalysis (Chapter 5). This works makes up part of a larger study, which has been published in the *Quarterly Journal of the Royal Meteorological Society*.

3.2 Datasets

3.2.1 Observational Data

3.2.1.1 GFDex

The Greenland Flow Distortion experiment was centred on an aircraft-based field campaign based in Keflavík, Iceland. The aircraft used was a modified BAe-146, a four engined former passenger jet, now capable of carrying 18 scientists and three crew, along with a variety of scientific equipment (Figure 3.1). The aircraft was capable of operating down to altitudes as low as 100 ft (approx. 30 m), allowing measurements representative of the air-sea interface to be made. The fields of interest to us are those which are important for air-sea interaction at the surface, namely sea surface temperature, 2 m air temperature, mean sea-level pressure, 2 m specific and relative humidity, 10 m wind speed and direction, as well as latent heat, sensible heat and momentum fluxes through the ocean

Figure 3.1: The Facility for Airborne Atmospheric Measurement (FAAM) aircraft. The BAe-146 is equipped with high quality instrumentation, capable of recording high frequency measurements of temperature, humidity and three dimensional winds, amongst other variables.

surface. Timeseries[1] of these fields along the flight track, along with a number of others, have been compiled into the GFDex 'turbulent flux database'. The instrumentation and measurement techniques used, along with the quality control procedure, are described in detail by Petersen and Renfrew (2009), however for completeness a brief discussion of the aircraft instrumentation and construction of the database in included here.

- **Three dimensional winds and flight-level pressure.** A five port pressure system on the nose of the aircraft, along with symmetrically placed static pressure ports on either side of the aircraft allowed angles of attack, sideslip and true airspeed to be measured. When these are combined with measurements of the aircraft velocity and altitude from the aircraft's Inertial Navigation Unit (INU), it is possible to derive three-dimensional winds at a frequency of 32 Hz. A pre-detachment calibration flight suggested horizontal wind measurement uncertainties $<$0.27 m s^{-1}. During the campaign, the measurement uncertainty was taken to be $< \pm 0.5$ m s^{-1}, with relative errors of < 0.1 m s^{-1}.

  Flight level static pressure is recorded with a measurement uncertainty of 0.5 hPa.

[1] We refer to the aircraft data as a timeseries, however strictly speaking this is not accurate. Due to the relative speed of the aircraft and scale and longevity of the features being sampled, the data are closer to a spatial series at one moment in time.

- **Flight level temperature.** Temperature is recorded through the use of two Rosemount temperature sensors, one of which is deiced with a heating element. The sensors have a measurement uncertainty of $< \pm 0.3$ K, with relative errors of < 0.01 K. We were able to use the non-deiced sensor for all flights other than B274, where it became frozen up and the deiced sensor had to be used. The heating element in the deiced sensor caused a small positive bias in the recorded temperature, which, by comparison with the non-deiced probe in non-icing conditions was determined to be 0.48 K. The temperature series for B274 was thus offset by -0.48 K to account for this bias. Temperature is recorded at 32 Hz.

- **Flight level specific humidity.** Specific humidity, or more accurately, total water content, is measured using a Lyman-Alpha hygrometer, which has a measurement uncertainty of ± 0.15 g kg^{-1}. As this instrument measures total water, it cannot be used to measure humidity when there is liquid water in the air. This constraint meant that four humidity points had to be removed from the flux database. The Lyman response tends to drift over time, and so must be carefully compared with the General Eastern hygrometer when in clear air (the General Eastern uses the chilled mirror technique, thus in essence measures dewpoint temperature and, although it records at 4 Hz, its response time can be up to 30 s). The Lyman records at a frequency of 64 Hz.

- **Sea Surface Temperature.** Sea surface temperature is estimated with the use of a Heimann downward facing radiometer. This measures brightness temperature in the wavelength range of 8–14 μm at a frequency of 4 Hz. Skin temperature is then calculated as

$$R_\lambda^\uparrow = \epsilon_\lambda B_\lambda \left(T_s\right) + \left(1 - \epsilon_\lambda\right) R_\lambda^\downarrow, \tag{3.1}$$

  where $R_\lambda^\uparrow$ is the upwelling radiance at wavelength λ, ϵ_λ is the surface emissivity, and B_λ is the Planck emission function for skin temperature T_s. The surface emissivity, ϵ_λ, is often taken as $\epsilon_\lambda \approx 0.987$, and thus the second term on the right hand side of Equation 3.1 is much smaller than the first and can be neglected. The Heimann probe has a measurement uncertainty of 0.7 K, this is discussed fully in Petersen and Renfrew (2009).

The Heimann probe needs to be calibrated over open water before the start of each low-level leg, and whenever the aircraft has been flying over something other than water (for example, sea-ice). This was the case during flight B276, however the second calibration, on leaving the sea-ice cover, was performed too early, while the aircraft was still over the marginal ice zone. This resulted in the recorded sea surface temperature after this point being biased high. Luckily, this flight included a repeat of the first leg, and thus the bias in the SST could be accounted for by a comparison between the legs before and after flying over the sea-ice. The post sea-ice legs were corrected downwards by 0.8 K.

During flights B268, B271 and B274, the Heimann probe was either not recording, or was not calibrated before use. In these instances there are no measurements of sea surface temperature available from the aircraft, and so for bulk flux calculations sea surface temperatures are derived from the high resolution UK Met Office OSTIA (Operational Sea surface Temperature and Ice Analysis) dataset. A comparison of this dataset and data from the Heimann probe when it was well calibrated showed that OSTIA was biased high by 1.5 K in this region, and so these were corrected downwards before they were used in the bulk flux calculations. This correction is corroborated by the direct covariance sensible heat flux observations (Petersen and Renfrew, 2009).

- **Altitude.** Altitude was measured using a radar altimeter, and at low levels had an uncertainty of < 1 m.

For the turbulent flux calculations, run lengths needed to be chosen so as to include several samples of the longest wavelength of the turbulence of interest (in this case this scaled with the height of the boundary layer, which, from dropsonde data, was approximately 1–2 km), while remaining short enough to ensure that sampling is over as homogeneous a surface as possible (Petersen and Renfrew, 2009). For the flux database, the run length was chosen to be 2 minutes, or approximately 12 km at the aircraft's science speed of 200 knots. Each point in the flux database represents the mean of a variable over a single run.

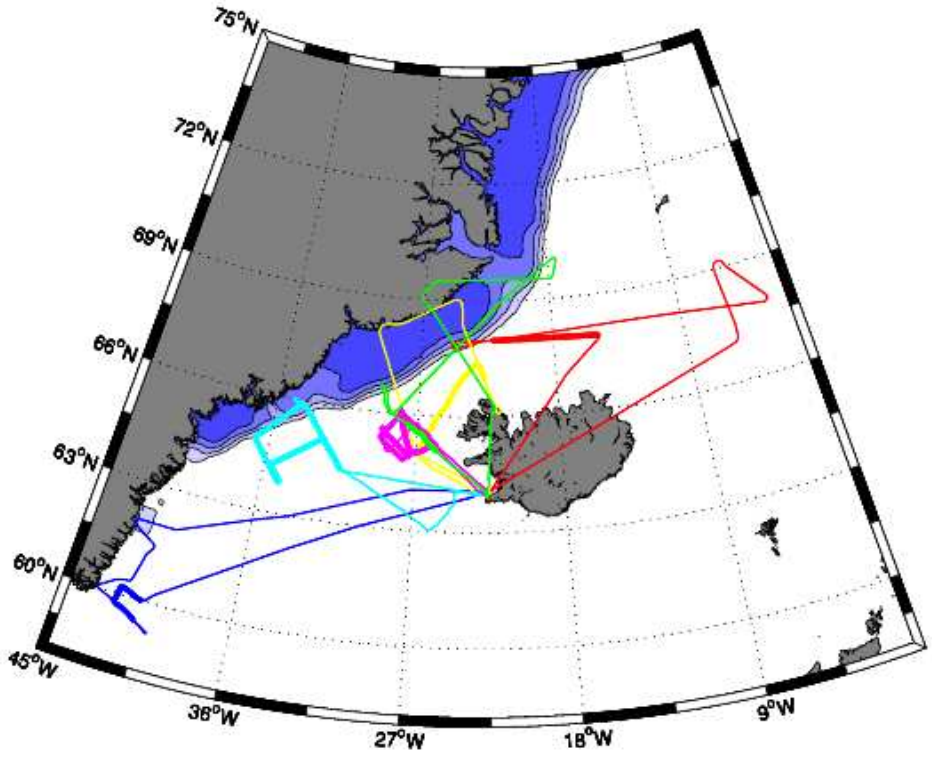

Figure 3.2: Flight legs that make up the GFDex flux database, from Petersen and Renfrew (2009). Low level flight legs are highlighted in bold for B269(blue), B271(red), B274(yellow), B276(cyan), B277(green), B278(magenta). Sea-ice concentration from the 5th March OSTIA data is shaded in blue with a contour interval of 20%.

All of the variables were adjusted onto standard meteorological levels (10 m for winds, 2 m for temperature and humidity, mean sea-level for static pressure) using stability-dependent surface-layer theory, for example see Smith (1988), Renfrew *et al.* (2002). In this case using the COARE 3.0 bulk flux algorithm (Fairall *et al.*, 2003) to calculate the scaling parameters and surface roughness lengths for wind, temperature and humidity. Wind speed was also calculated at 10 m assuming neutral stability for comparison with the winds from the QuikSCAT scatterometer, which calculates wind speed assuming neutral atmospheric stability. Flight level pressure was adjusted to mean sea-level assuming hydrostatic balance using the mean altitude and density over each run. Wind direction was assumed to be equal at flight level and at 10 m. For consistency in comparisons of relative humidity (RH), this was calculated from the saturated specific humidity at the 2 m Temperature in both the flux database and from the model data.

Bulk fluxes of latent heat, sensible heat and momentum were calculated from the surface meteorological variables using both the COARE 3.0 and the Smith (1988) algorithms. Note that although turbulent fluxes calculated using the eddy correlation method were available for most of the low level legs, these were not used in the model comparisons due to their relatively large variability caused by the "flux-sampling" or "random" errors.

There are 165 data points in the database, of which 19 are over or near sea-ice in either one or more of the models or in the aircraft data and are thus not used. Of the remaining 146 data points, 138 may be used for comparisons of wind speed and direction, 127 for comparisons of temperature, specific and relative humidity and 91 for sea surface temperature.

3.2.1.2 QuikSCAT

The seawinds scatterometer instrument aboard the QuikBird Satellite (known as QuikSCAT) was launched in mid-1999 to fill a data hole which was left following the premature failure of the Advanced Earth Observing Satellite (ADEOS-I), which carried NASA's NSCAT scatterometer.

Scatterometers are essentially active radiometers which measure the backscatter from wind induced centimetre-scale capillary waves on the surface of the ocean. The power of the backscatter is sensitive to both the size and the orientation of the capillary waves, allowing vector winds to be interpreted from a series of measurements at different azimuthal angles. This is done by using a 'geophysical model function', which relates surface wind stress to the size and direction of the surface capillary waves. The wind at 10 metres is then calculated assuming neutral atmospheric stratification. The data we use in this comparison are retrieved using the "Ku-2001" geophysical model function (see, for example, Wentz *et al.* (2001)). It is claimed that this is capable of wind speed retrievals of up to 70 m s^{-1}, however there is little to no validation of QuikSCAT retrievals at such high wind speeds.

Seawinds is a ku-band radiometer, operating at around 14 GHz, and has a swath width of around 1800 km (Spencer *et al.*, 1997), allowing it to provide near global coverage twice daily. The mission requirements for QuikSCAT was to be able to measure winds

with an uncertainty of less than 2 m s^{-1} for speed and 20° for direction. This seems to have been achieved for most commonly occurring conditions. Ebuchi *et al.* (2002) compared QuikSCAT winds to buoy data over the world oceans and found root mean squared errors of 1.01 m s^{-1} and 23°, although errors in direction were significantly reduced for wind speeds above 3 m s^{-1}. Correlation coefficients were $r = 0.925$ for speed and $0.959 \leq r \leq 0.977$ for direction. A similar study by Chelton *et al.* (2006) found component errors of 0.75 m s^{-1} in the along wind direction and 1.5 m s^{-1} in the cross wind direction. The discrepancy in these values explains why there can be large errors in the QuikSCAT wind direction at low wind speeds which diminish rapidly as the winds increase in magnitude. It is worth noting that neither of these studies included many data points which had winds stronger than 20 m s^{-1}, and those that did had significantly enlarged residuals, for example see Ebuchi *et al.* (2002), Figure 3. Moore *et al.* (2008) carried out a comparison between QuikSCAT winds and a single buoy moored off the south coast of Greenland, near Cape Farewell, the windiest area in the world ocean (Sampe and Xie, 2007). The buoy was only in operation from late July to early December 2004, and thus did not capture the windiest period of the year, from December to February (Moore, 2003), however there were still numerous data points with winds greater than 15 m s^{-1}. Root mean squared errors were found to be 2.6 m s^{-1} in the NASA QuikSCAT product and 2.3 m s^{-1} in the Remote Sensing Systems (RSS) product, which is the dataset used in this comparison; with the NASA product having a correlation coefficient to observed winds of $r = 0.87$ and the RSS product $r = 0.89$.

3.2.2 Analyses

3.2.2.1 NCEP Reanalysis

The NCEP/NCAR dataset is an atmospheric reanalysis, which uses an unchanged data assimilation system and numerical model from the start of 1957. The 3D-var data assimilation routine and the model itself are identical to the NCEP operational system which was in place on the 11th January, 1995, however the horizontal spectral truncation is at T62, giving a horizontal resolution of around 210 km. The model has 28 vertical levels, five of which are in the atmospheric boundary layer. This is clearly a very coarse resolution for a comparison with relatively high frequency aircraft observations, however

this dataset is still one of the most frequently used for setting the boundary conditions of ocean models, and it is thus important to attempt to evaluate how well it represents fluxes associated with the high impact weather systems in the subpolar North Atlantic, where the atmosphere and ocean are strongly coupled.

Oceanic boundary conditions post-1981 are derived from the NOAA operational sea surface temperature analysis, described by Reynolds and Smith (1994). This is a weekly SST average generated from buoy and ship observations, as well as satellite derived SSTs, using an optimal interpolation technique. Prior to this, the UK Met. Office GISST field is used. Each grid box is assigned either a 100% or 0% coverage of sea-ice, calculated from SSM/I satellite data.

It is worth noting that, as with many other reanalyses, although the data assimilation scheme is invariant over time, the availability and quality of the observations that are available for assimilation is not. NCEP assimilates land surface, ship, rawinsonde, pibal, aircraft and satellite data, much of which (particularly aircraft and satellite observations) were unavailable at the start of the reanalysis. It is therefore natural that the quality of the analysis will be higher currently than in, say, the 1950s.

The NCEP reanalysis is archived on a $2.5^\circ \times 2.5^\circ$ degree latitude/longitude grid and is available every 6 hours.

A number of previous studies, for example Renfrew *et al.* (2002) and Smith *et al.* (2001), have carried out comparisons between the NCEP reanalysis and observations. Both of these studies found that the surface-layer turbulent fluxes were grossly overestimated, with Renfrew *et al.* (2002) finding sensible and latent heat fluxes 51% and 27% too large, respectively. These errors were attributed to poorly represented sea surface temperatures and surface level humidity, as well as a roughness length used in the bulk flux calculations which is unsuitable for moderate to high wind speeds. It is worth noting that this study was during winter in the Labrador Sea, where there were very large air-sea temperature differences, where the model performed especially badly, however from an oceanographic point of view, such areas are some of the most important to have accurate air-sea fluxes. It was also noted in both studies that the wind speeds in the reanalysis were too low, especially at high wind speeds.

3.2.2.2 ECMWF Operational

The ECMWF data used are from the operational archive in use during the GFDex campaign, which was run at a spectral resolution of T799, equivalent to around 25 km, with 91 levels in the vertical and is available globally every 6 hours. Data were extracted at two resolutions, an N400 reduced Gaussian grid, the highest resolution available to us, and an N80 reduced Gaussian grid. The latter is the same grid on which the ECMWF ERA-40 reanalysis is provided, and thus can be used as a 'proxy' for the ERA-40 reanalysis, which is unavailable post-2002 but uses very similar surface-layer parameterisations etc. to the operational model. The use of data retrieved on two different grids from the same model also allows an indication of where model short comings are due to model resolution rather than limitations in the model dynamics or parameterisations.

The surface-layer fields provided are calculated from the lowest model level using stability dependent interpolation and surface flux fields are accumulated over a 3 hour forecast cycle initialised at 12 Z during the day of interest.

Oceanic boundary conditions are provided by NCEP on a 0.5° grid, and are thus very similar to those used in the NCEP/NCAR reanalysis (see above). Sea-ice is given as a fraction coverage at each grid cell, with fractions below 0.2 being set to 0. It is worth noting that since GFDex, ECMWF have changed to using the OSTIA dataset to prescribe boundary conditions, and this is likely to have an impact on the results presented here.

3.2.2.3 North American Regional Reanalysis

Although the North American Regional Reanalysis (NARR) is not considered in this chapter, it is used elsewhere in this thesis, and a brief description is thus included for completeness.

The NARR is a high resolution reanalysis, with a horizontal resolution of 32 km and 45 layers in the vertical. It is based on the 'Eta' model and 3D variational data assimilation scheme used operationally by NCEP during April 2003, at which time it was frozen for the reanalysis. The NARR domain covers most of North and Central America, as well as much of the North Pacific and Atlantic, a total of $106^\circ \times 80^\circ$ on a rotated latitude/longitude grid. The area relevant to us (i.e. the Labrador and Irminger Seas) are located in the far 'north-east' of this domain.

Atmospheric boundary conditions are provided from the NCEP global analysis and oceanic boundary conditions are derived from a 1° Reynolds SST. As with the NCEP global reanalysis, sea ice is either set to 100% or 0%.

3.2.2.4 An upper limit?

Part of the GFDex campaign was a 'targeted observations' programme, where dropsondes were released in areas which various operational NWP models predicted the extra observations would have the biggest positive impact on the forecasts. To facilitate this, data from the dropsondes were sent onto the Global Telecommunication System (GTS) in near real time, to allow the observations to be assimilated into the next forecast cycles. This was the case not only in the targeted observation missions, but also in the missions where dropsondes were used solely to investigate the vertical structure of the atmosphere, as was the case immediately before or after all of the low level legs. As these dropsondes were also sent onto the GTS, it is almost certain that the analyses will have been influenced by these additional data which were only available during GFDex. It is thus likely that the following comparisons will represent the best that the models are currently capable of in this area – an upper limit of their skill.

3.3 Low Level Flights

3.3.1 B268

The start of the GFDex campaign, on the 19th February, 2007, was greeted by a synoptic scale, barotropic low pressure system tracking eastward across the North Atlantic and deepening to around 964 hPa. Our limited area forecast products, supplied by the UK Met. Office, Icelandic Met. Office and the ECMWF all showed that this was due to result in an easterly flow into the east coast of Greenland, causing a barrier flow to develop off the east coast of Greenland over the Denmark Strait and Irminger Sea. This barrier flow was forecast to accelerate into an easterly tip jet at Cape Farewell, with 10 m winds expected to reach around 30 m s^{-1}. The morning QuikSCAT pass showed winds at Cape Farewell exceeding 40 m s^{-1} (Renfrew *et al.*, 2008). Although the surface winds were predicted to be very strong, the heat fluxes associated with the easterly tip jet were only

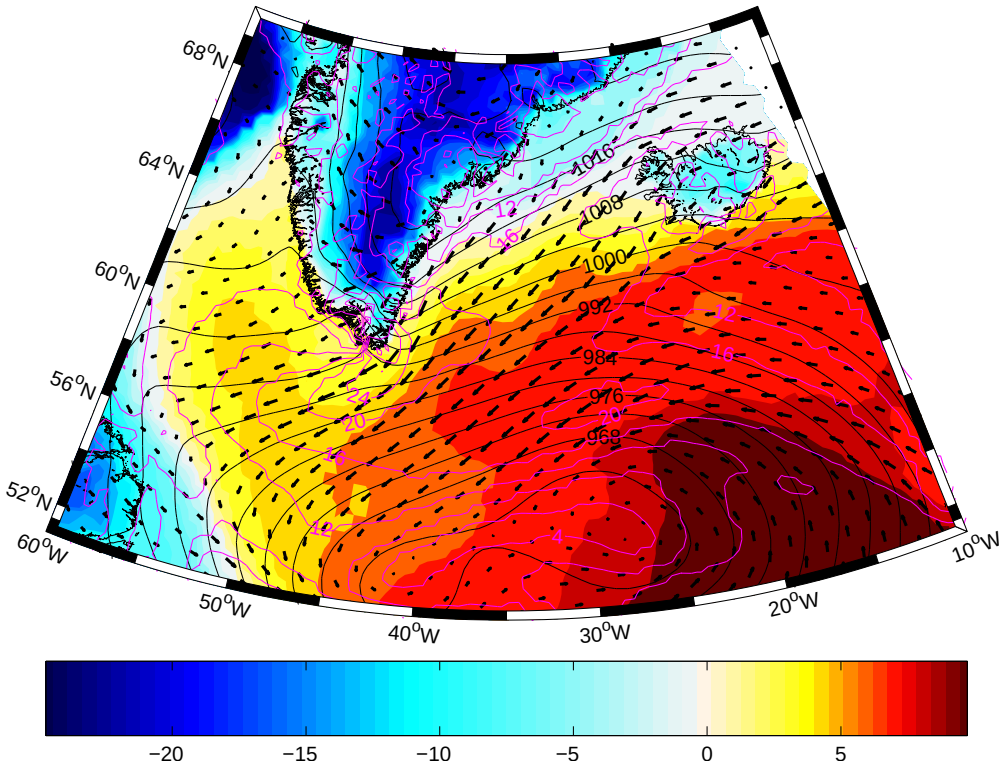

Figure 3.3: Synoptic situation from the NARR in the North Atlantic at 12 Z during B268. Temperature is coloured, with MSLP, black and 10 m wind speed, magenta, contoured. Wind vectors are shown every 3rd grid point.

expected to reach around 140 W m^{-2} for sensible and 200 W m^{-2} for latent heat fluxes. These are significantly less than the $\sim$ 800 W m^{-2} which have been speculated to occur during some forward tip jet events (Doyle & Shapiro, 1999). This is due to the relatively warm and moist air advected into the area by the synoptic cyclone. The synoptic situation from the NARR for 12 Z during B268 is shown in Figure 3.3. It is clear to see the relatively warm air being advected from the south east, and the acceleration of the winds at Cape Farewell, up to around 32 m s^{-1} in this analysis.

Flight B268 was planned to measure the structure and fluxes associated with the easterly tip jet. The aircraft took off at 1048 Z and proceeded at high levels to around 62 °N, 40 °W, where a dropsonde leg was carried out across the jet, to the coast of Greenland. Further dropsonde legs were then carried out heading south along the central axis of the jet, parallel to the Greenland coast, and then back across the jet just to the east of Cape Farewell. The aircraft then carried out a profile descent at around 59 °N, 39.5 °W, before two low-level legs, at $\sim$30 m, were carried out across the jet. The flight track of the

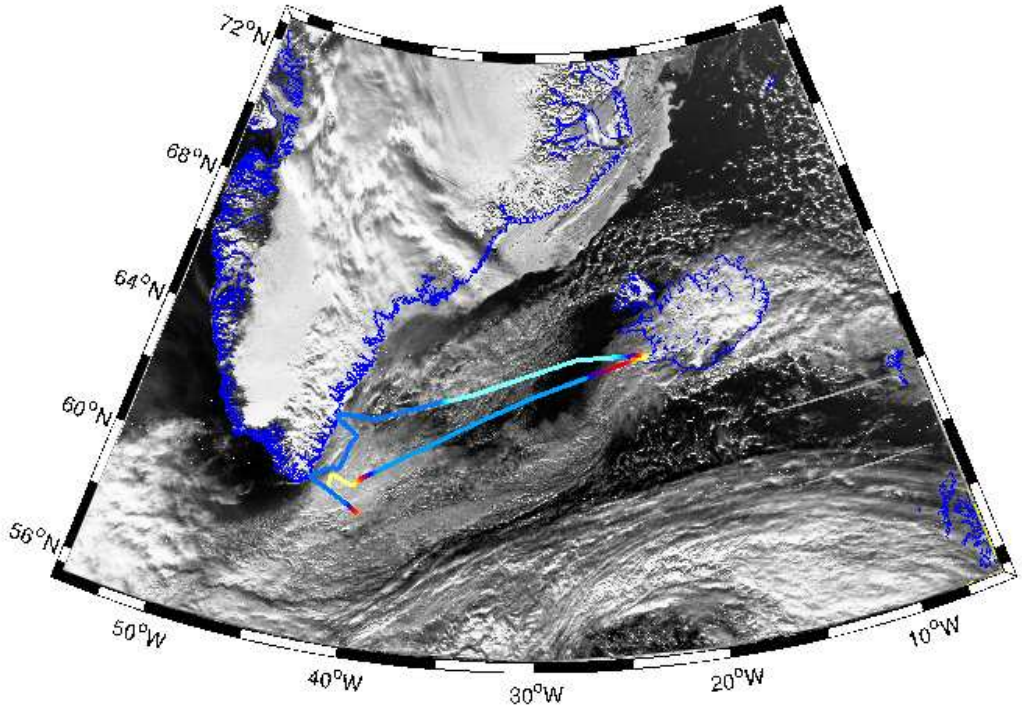

Figure 3.4: Visible satellite image from AVHRR, at 1435 Z on the 21st February, 2007. The B268 flight track is coloured by altitude, from low levels (yellow, around 30 m) to high levels (cyan, around 7.5 km).

aircraft during B268 is shown in Figure 3.4, overlaying the 1435 Z Advanced Very High Resolution Radiometer (AVHRR) visible satellite image. Unfortunately, due to sensor wetting on the descent, no temperature data were available during the low-level legs of B268.

3.3.2 B271

From the 23rd of February, the remnants of a polar mesocylone which had been tracking westward across the Norwegian sea started to redevelop into a true polar low, according to the definition of Rasmussen and Turner (2003), who define a polar low as "a small, but fairly intense maritime cyclone that forms poleward of the main baroclinic zone (the polar front or other major baroclinic zone). The horizontal scale of the polar low is approximately between 200 and 1000 kilometres and surface winds near or above gale force." By the 25th of February, the low was starting to fill, however it was still very much apparent in the satellite imagery (see Figure 3.5) and in the limited area forecasts, which were predicting sustained wind speeds of over 20 m s^{-1} on the western side of the storm centre.

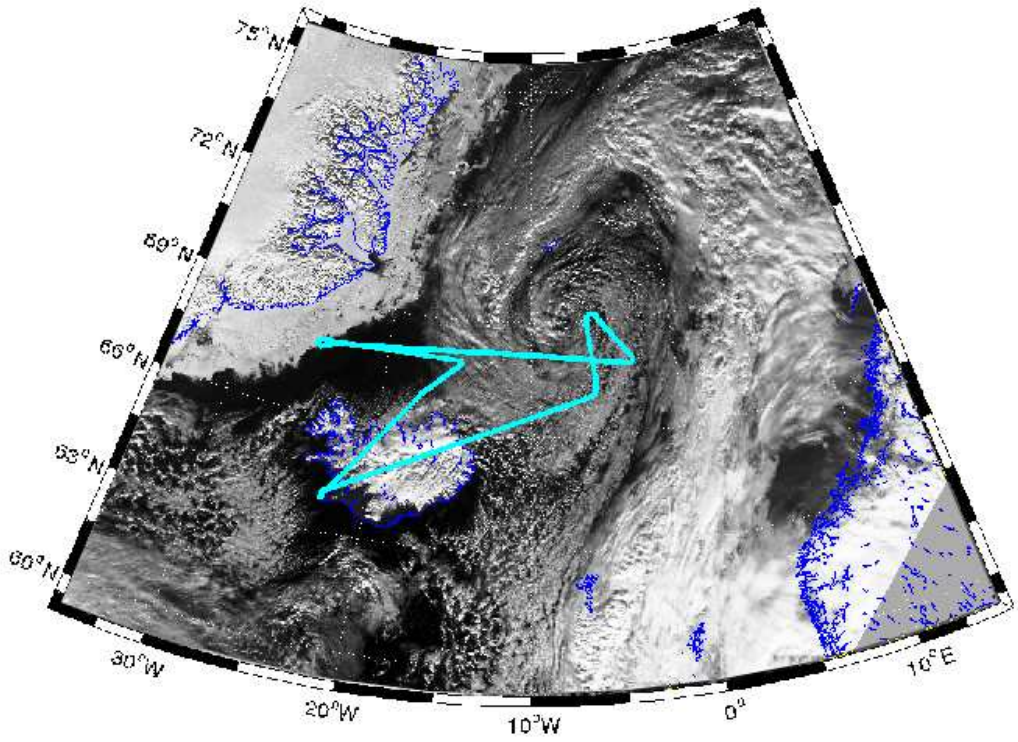

Figure 3.5: Visible satellite image from AVHRR, at 1236 Z on the 23rd February, 2007. The B271 flight track is shown in cyan.

The area of interest, north of Iceland is outside the NARR domain. Figure 3.6 shows the Icelandic Met. Office HIRLAM forcast from 12 Z, valid at 15 Z. The polar low is clearly visible to the north-east of Iceland.

The aim of GFDex mission B271 was to sample the structure of the polar low, and this included a low level leg, during which turbulent flux data were collected. The aircraft departed Keflavìk at 1035 Z and completed a dropsonde leg across each axis of the storm, before completing a profile descent over the edge of the Greenland sea-ice and a 300 km low level leg along 68 °N, just reaching the western flank of the polar low. Winds along the low level leg were northerly and relatively low at the start of the run, around 6 m s^{-1}, increasing to a local maximum exceeding 15 m s^{-1} before slackening to around 11 m s^{-1} and then linearly increasing to around 20 m s^{-1} as the aircraft approached the centre of the low. Renfrew *et al.* (2008) speculate that this local maximum is the result of a barrier flow caused by the high topography of 'Liverpool Land', a headland immediately to the north of Scoresbysund.

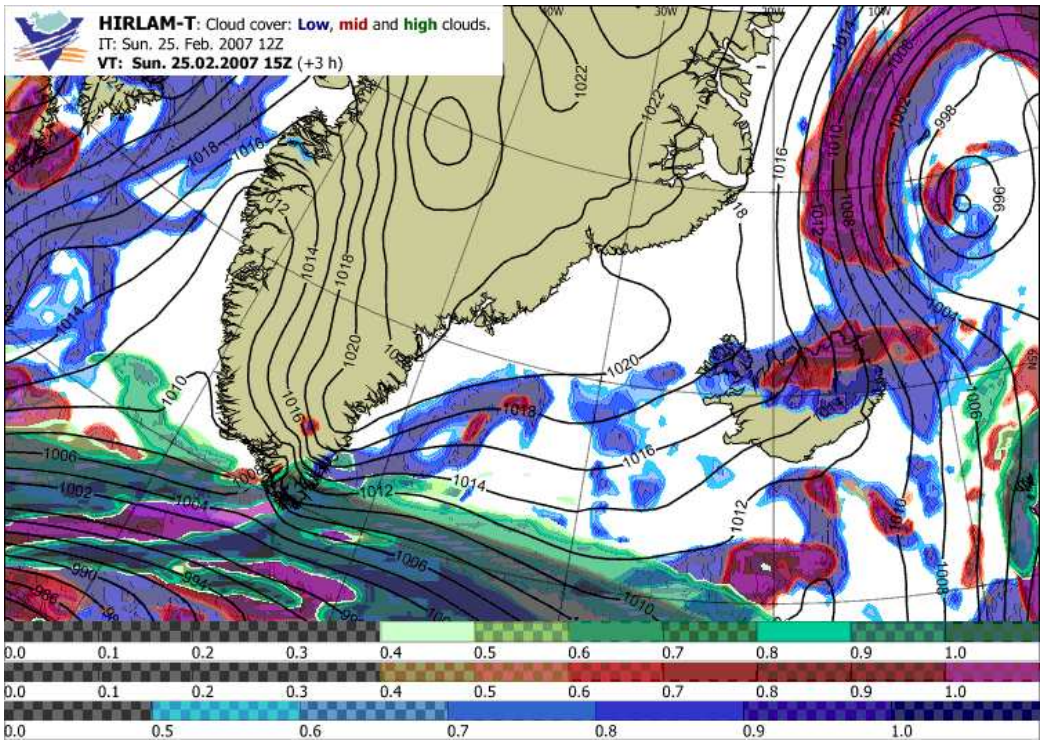

Figure 3.6: Synoptic conditions during B271 from the HIRLAM regional modal, provided by the Icelandic Met Office. Mean sea-level pressure is contoured and low, medium and high cloud cover is shaded. Note the polar low in the north-east of the domain.

3.3.3 B274

During the late hours of the 1st and early hours of the 2nd of March, a relatively weak cyclone of 980 hPa, which had been located to the south-west of Iceland started to deepen and move to the north-west towards Denmark Strait (Figure 3.7). The air advected towards the coast of Greenland caused the strengthening of a barrier flow in the Denmark Strait, which had previously been caused by a stronger synoptic scale cyclone to the north of Iceland and a mesoscale cyclone to the west of Iceland. Winds in the Denmark Strait were forecast to increase from around 15 m s^{-1} on the 1st to over 20 m s^{-1} during the 2nd.

Two flights were planned to sample this barrier flow as the synoptic situation evolved. The first, B273, was flown on the 1st of March but included only dropsonde measurements and no low-level legs. Flight B274 was flown on the 2nd of March, and included a dropsonde pattern identical to that executed during B273, before a profile descent over the north-west of Iceland and then a 300 km low-level leg, heading south-west along the core

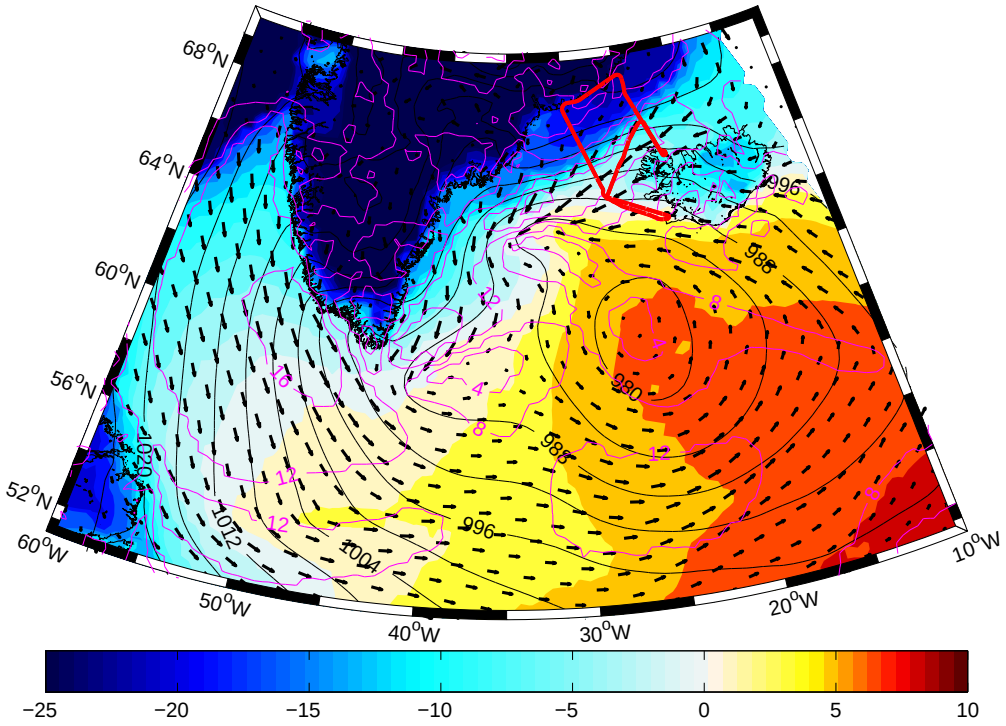

Figure 3.7: Synoptic situation from the NARR in the North Atlantic at 12 Z during B274. Temperature is coloured, with MSLP, black and 10 m wind speed, magenta, contoured. Wind vectors are shown every 3rd grid point.

of the jet. During the descent, the aircraft encountered severe icing and the turbulence probe was iced over and put out of action. This means that high frequency 3-D winds, whice are derived from the turbulence probe, are unavailable and heat fluxes must be calculated using the INU derived winds and bulk flux algorithms. Heat fluxes encountered during the low-level leg were typically around 300 W m^{-2} for the sensible flux and 200 W m^{-2} for the latent flux, the sum of which is greater than the clear sky solar radiation in the Denmark Strait at this time of year. Although the winds encountered, at around 20 m s^{-1} were significantly lower than those during the easterly tip jet flight (B268), the winds were from the north-east, leading to much colder air temperatures of around -8 °C.

Barrier flows such as the one encountered during B274 are very common wintertime features, and can persist for many days (Moore and Renfrew, 2005). Such sustained high heat fluxes must have an impact on the ocean. Renfrew *et al.* (2008) calculate that the buoyancy flux (the rate at which the ocean surface is losing or gaining density) for this barrier flow was around -2×10^{-7} m^2 s^{-3}. This is similar to the values that Marshall and Schott (1999) quote relating to open ocean convection of up to 2000 m in the Labrador

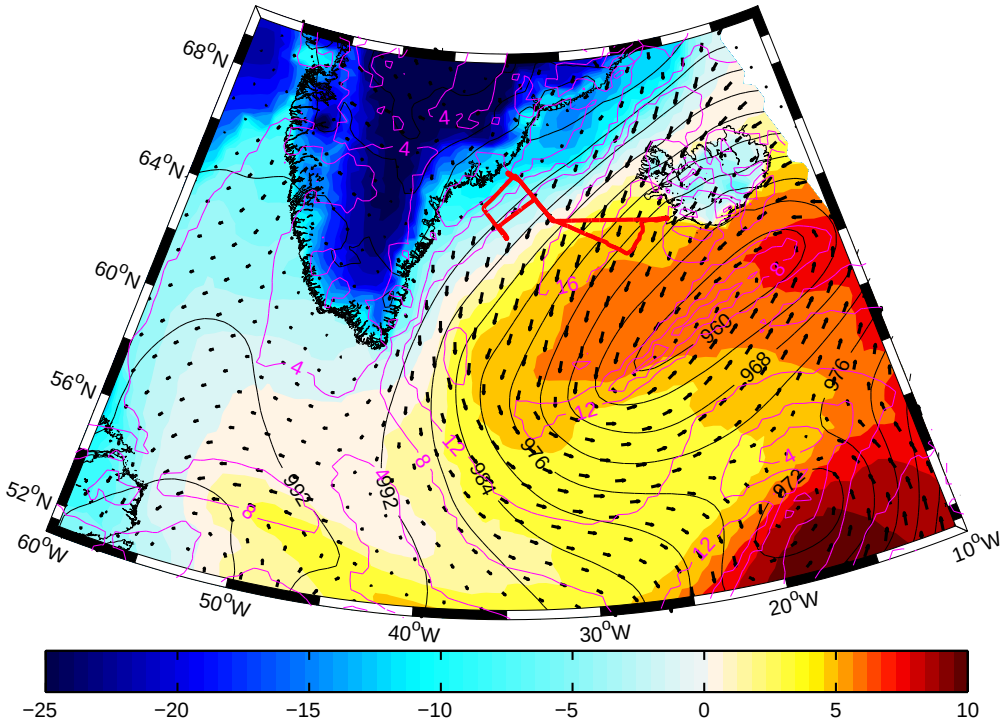

Figure 3.8: Synoptic situation from the NARR in the North Atlantic at 12 Z during B276. Temperature is coloured, with MSLP, black and 10 m wind speed, magenta, contoured. Wind vectors are shown every 3rd grid point.

Sea. It is worth bearing in mind, however, that the Labrador Sea is well preconditioned and thus much more prone to this sort of overturning than is the water in the Denmark Strait (Marshall and Schott, 1999; Lavender *et al.*, 2000).

3.3.4 B276

On the 6th March, a barrier flow with winds forecast to be around 15–20 m s^{-1} was still persisting in the Denmark Strait area (Figure 3.8). Flight B276 was planned to measure the structure of the jet at both low and high levels, over the open ocean, marginal ice zone and more consolidated sea-ice. Following take-off, the transit to the operational area was undertaken at relatively low-levels (< 300 m) to prevent the icing of the turbulence probe which had been a problem on some of the earlier flights. A total of six low-level legs were flown, across the jet and over sea-ice, before an ascent over the sea-ice and a leg across the jet at 2000 ft and then a single dropsonde leg across the jet.

Heat fluxes during the open water legs were reasonably modest, with sensible and latent fluxes of up to 150 and 200 W m^{-2}. These dropped markedly over the marginal

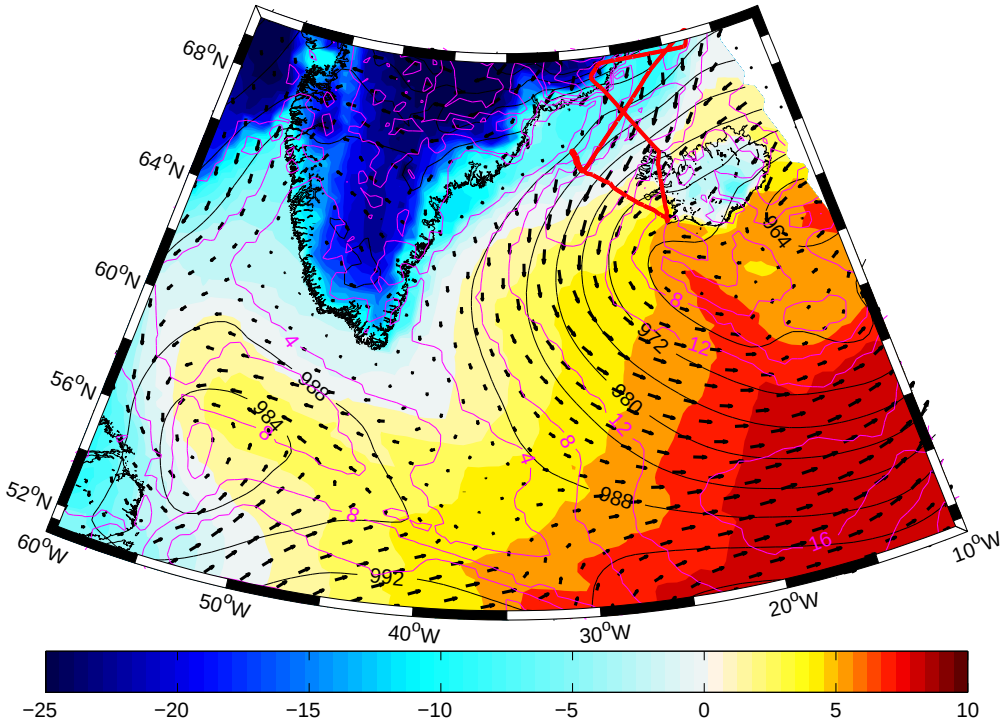

Figure 3.9: Synoptic situation from the NARR in the North Atlantic at 12 Z during B277. Temperature is coloured, with MSLP, black and 10 m wind speed, magenta, contoured. Wind vectors are shown every 3rd grid point.

ice-zone, and to near zero over the consolidated ice.

Wind speeds, as forecast, were around 15–20 m s^{-1} over open water, dropping to around 5 m s^{-1} over the ice.

3.3.5 B277

Flight B277, on the 6th of March, was again surveying the barrier flow in the Denmark Strait. Low level legs were planned along and across the jet at 100 ft, however due to poor visibility caused by low cloud, the aircraft could not always operate safely at this altitude, and so the low-level legs actually varied between 100 and 500 ft. Due to this and the relatively short legs, data from B277 makes up only 6 points in the GFDex flux database.

The parent synoptic cyclone, which had been responsible for the sustained period of barrier flow over the previous few days was starting to move off to the east of Iceland, Figure 3.9. This was causing a large amount of air to encroach on the east Greenland coast, and winds in the northern Denmark Strait were forcast to again increase to between 20 and 25 m s^{-1}. Winds during the low-level legs, once corrected to 10 m, rarely exceeded

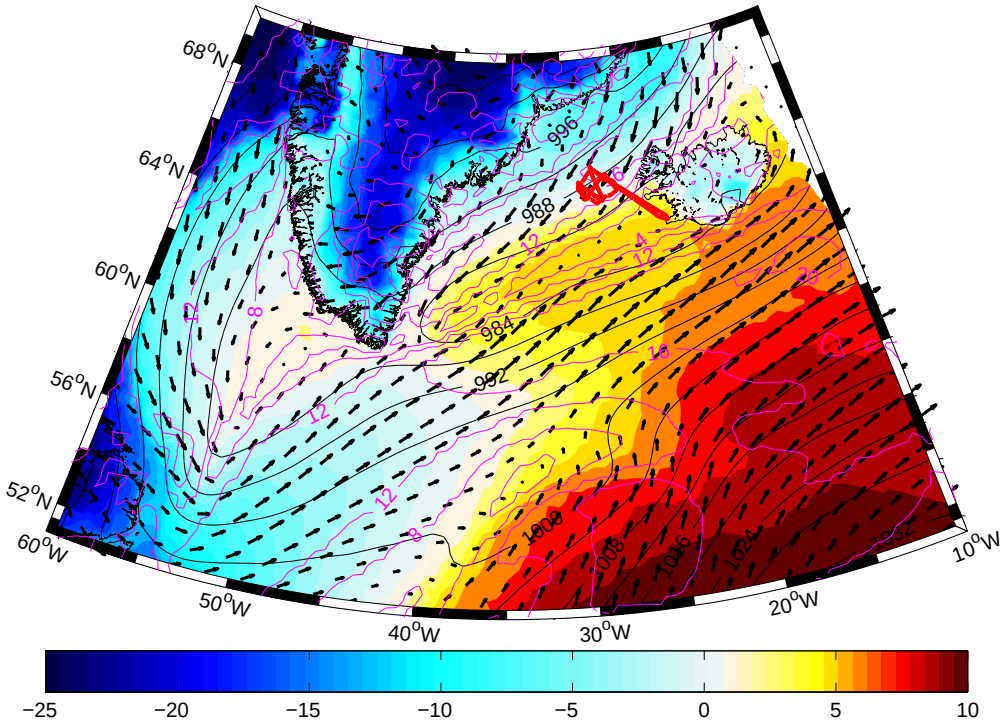

Figure 3.10: Synoptic situation from the NARR in the North Atlantic at 12 Z during B278. Temperature is coloured, with MSLP, black and 10 m wind speed, magenta, contoured. Wind vectors are shown every 3rd grid point.

20 m s^{-1}, but were generally greater than 15 m s^{-1}.

Heat fluxes were fairly typical for this barrier flow event, with combined latent and sensible not exceeding 300 W m^{-2}. There was however a strong spatial gradient in the heat fluxes, increasing as the aircraft approached cooler, drier air blowing off the edge of the sea-ice.

3.3.6 B278

On the 9th March, an elongated pressure trough was extending from Iceland south-west across the Irminger Sea to just east of Cape Farewell (Figure 3.10). Winds over the Denmark Strait were from the north-west, and forecast to be around 15–20 m s^{-1} in magnitude. Although this was not a classical barrier flow, it is likely that the winds in the area were still somewhat enhanced by the presence of Greenland. B278 was envisaged to be a 'Lagrangian surface fluxes' flight over Denmark Strait. Initially, four low-level legs of 100 km each were flown, forming a square with its sides aligned along and across the average wind direction. Once the aircraft had regained the starting position of the first leg,

further legs were then flown co-located with the first leg at heights of 100, 1500 and 2500 ft. Following this, the aircraft proceeded to the opposite side of the square and again flew legs at 100, 1500 and 2500 ft. In theory, due to the orientation of the box and the speed of the wind, this should have been resampling the the air parcel sampled upstream.

Sensible and latent heat fluxes were generally seen to be around 100 and 150 W m^{-2} respectively. The comparatively low values were caused by relatively warm (~ 0 °C) and moist (relative humidity $> 90\%$) air.

3.4 Dataset Comparisons

3.4.1 Methodology

3.4.1.1 Data Extraction

For each model (ECMWF-N400, ECMWF-N80 and NCEP/NCAR), data were extracted from the mid-day output, which was the most contemporaneous with the aircraft observations, which were generally made between 1100 Z and 1500 Z. For each included data point from the GFDex database a comparison data point was generated using a Delauney-based triangular linear interpolation to interpolate to the exact position of the database point. Such triangular interpolation has the benefit that it is easy to apply to irregular grids, such as the QuikSCAT swath.

3.4.1.2 Error Statistics

- Mean. The mean of a discrete set of data $\{x_i\}$, $\bar{x}$, is given by

$$\bar{x} = \frac{1}{n} \sum_{i=1}^{n} x_i.$$

- Standard deviation. The standard deviation of $\{x_i\}$, σ_x, is the root mean squared deviation from $\bar{x}$ (i.e. the square root of the variance) and is given by

$$\sigma_x = \sqrt{\frac{1}{n} \sum_{i=1}^{n} (x_i - \bar{x})^2}.$$

- Bias Error. For two linearly related sets, $\{x_i\}$ and $\{y_i\}$, with $\{x_i\}$ assumed the

independent variable, the bias error measures the mean difference between $\{y_i\}$ and $\{x_i\}$, and is given by

$$\text{Bias error} = \frac{1}{n}\sum_{i=1}^{n}(y_i - x_i)\,.$$

- RMS Error. The root mean squared (RMS) error is the average absolute deviation of the dependent variable $\{y_i\}$ from the independent variable $\{x_i\}$, and is given by

$$\text{RMS error} = \sqrt{\frac{1}{n}\sum_{i=1}^{n}(y_i - x_i)^2}.$$

- Correlation Coefficient. The Pearson correlation coefficient, r_{xy}, describes the strength and direction of a linear least squares relationship between two variables $\{x_i\}$ and $\{y_i\}$, and is defined by

$$r_{xy} = \frac{\sum_{i=1}^{n} x_i y_i - n\bar{x}\bar{y}}{(n-1)\,\sigma_x \sigma_y} \in [-1, 1]\,.$$

3.4.2 Comparisons

The top panel of Figure 3.11 shows that, in general, the mean sea level pressure field is well reproduced by both of the models in most circumstances, as one would expect given the relatively large scale and slow evolution of mean sea level pressure. One notable exception is the NCEP reanalysis during B268, which is on average around 6 hPa too low. This is most likely simply due to the coarse resolution of this reanalysis which means that the slight 'kink' in the mean sea-level pressure (MSLP) field in the vicinity of the easterly tip jet is not resolved. The NCEP reanalysis also performs worst in B274, B276 and B278, although in these cases it errs slightly on the high side of the observations. All of these flights were in barrier flow type regimes, which are mesoscale orographically influenced flows, where ageostrophic forcing is very pronounced (Petersen and Renfrew, 2009), and thus these shortcomings are also likely due to model resolution. Correlation coefficients for MSLP are high for all of the models: 0.99 for both ECMWF truncations and 0.92 for NCEP, showing that although NCEP often errs either high or low, it captures the spatial gradients fairly well.

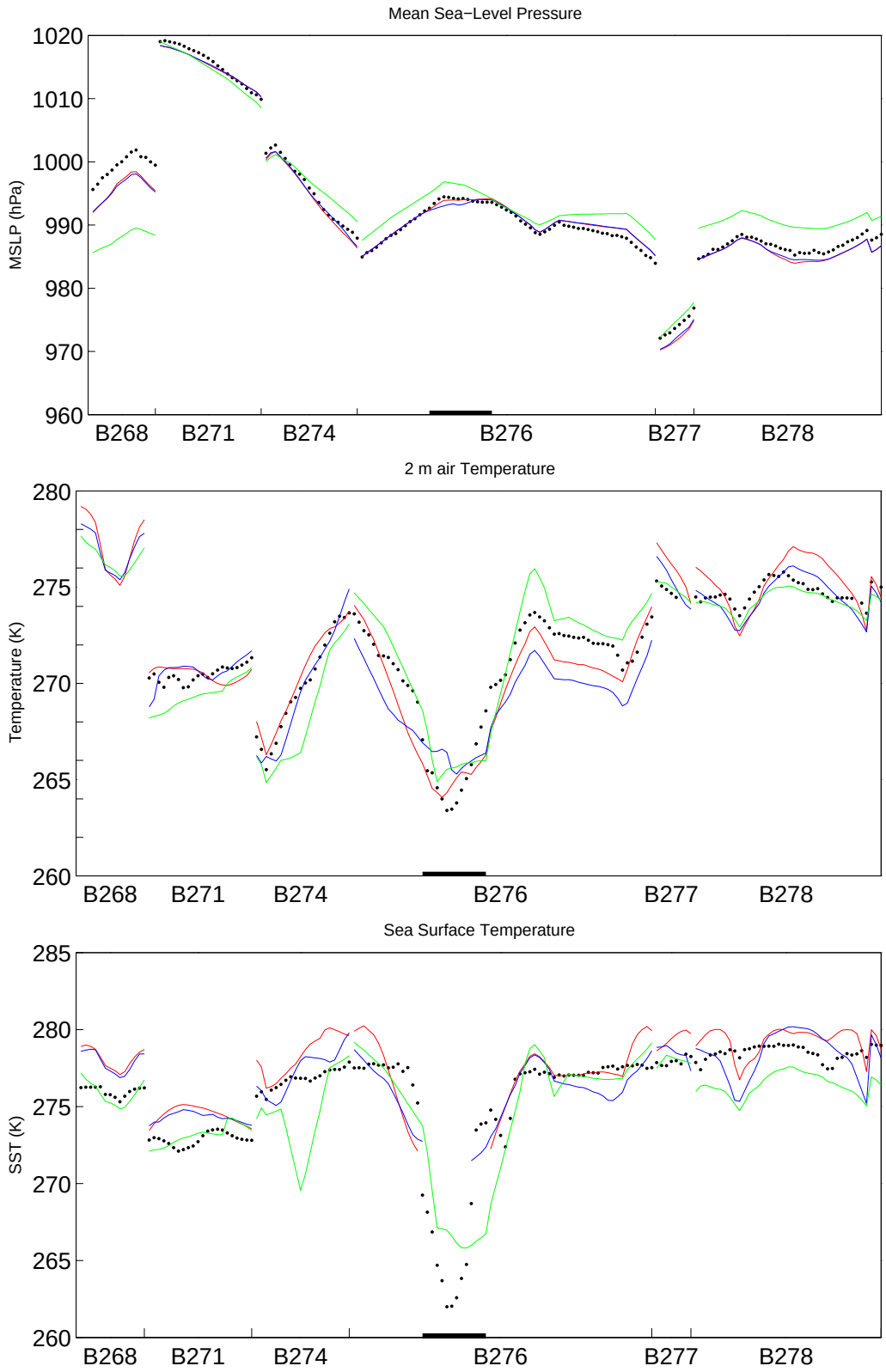

Figure 3.11: 'Spatial' timeseries plots showing the aircraft observations (black dots), NCEP/NCAR Reanalysis (green), ECMWF Analysis at N400 (red) and ECMWF analysis at N80 (blue). The top panel shows mean sea level pressure, the middle shows 2 metre temperature and the bottom shows sea surface temperature.

The lower two panels in Figure 3.11 show respectively the two metre air temperature and the sea surface temperature, where available. One feature that appears immediately obvious is, that although all of the models generally reproduce the gradients in the 2m temperature field very well, there is at times a surprisingly large spread in the model temperatures. For example, during a period of B276, there is a > 5 K difference between air temperatures in the warmest model (NCEP) and the coldest (ECMWF-N80). Much of this discrepancy can be traced back to the analysed sea surface temperature that the models use as boundary conditions. It can be seen in the bottom panel in Figure 3.11 that the details of the gradients in the model sea surface temperatures often bear little resemblance to the sea surface temperatures implied by the aircraft observations. The Irminger Sea and Denmark Strait, where these observations are taken, are areas of strong gradients in the SST, where the cold, southward flowing East Greenland Current meets the relatively warm and saline Irminger Current, an extension of the North Atlantic Current. Such strong, meandering fronts are likely under- or mis-represented in the relatively coarse SST analyses, and the strong coupling between the sea surface and the atmospheric surface layer causes these errors to be reflected in the two metre temperature.

The proximity of the sea-ice edge is also likely a source of error for two reasons. Firstly, the NCEP sea-ice field, as mentioned previously, has either a 0% or 100% coverage of sea-ice for each grid cell. Pagowski and Moore (2001) carried out mesoscale simulations with such a sea-ice field, as well as with fractional sea-ice cover and found that the former resulted in an atmospheric boundary layer (ABL) which was both too cold and too strongly stratified. Secondly, the coarse resolution of the NCEP model (and to a lesser degree, ECMWF-N80) means that the location of the ice edge could be badly represented.

It is interesting to note that, during the second half of B276, there is a significant discrepancy between the two ECMWF data sets, which can only be due to the truncation onto a lower resolution grid, possibly in effect making the ice edge closer to the observation.

Figure 3.12 shows that all of the model temperatures have a slope that is slightly greater than 1, with the N80 and N400 ECMWF products having slopes of 1.07 and 1.09 respectively, and NCEP a slope of 1.14. It is also worth noting that the ECMWF-N80 product has a significant bias of -0.7 K which is not present in the higher resolution

ECMWF dataset. It is difficult to draw many conclusions from the SST scatterplots (Figure 3.12) due to the small range of observed sea surface temperatures and large degree of scatter in the models. It is clear, however, that the model SSTs do not perform well in this area, possibly due to a lack of in-situ observations to assimilate into the analyses. Note that while these figures indicate that biases may be present in the various atmospheric (re)analyses, there may be an undersampling problem here. This is because two neighbouring flux runs may not be totally independent of each other, and are generally at a higher resolution that the models. This problem is apparent as 'loci' of points in the scatter diagrams, for example the bottom left panel of Figure 3.12.

The top panel of Figure 3.13 shows the model and aircraft recorded specific humidity. All of the models capture the spatial gradients reasonably well, as expected, however, the highest resolution ECMWF-N400 dataset is able to capture the sharpest gradients, while the coarse resolution of the NCEP reanalysis causes these to be smoothed out somewhat. There is a striking similarity between the spatial timeseries of specific humidity and those of 2 metre temperature — at these temperatures specific humidity and its associated errors are dominated by temperature. It is thus much more instructive to consider the relative humidity, shown in the centre panel of Figure 3.13. It can be seen here that both of the ECMWF datasets still perform reasonably well, particularly the higher resolution version, everywhere except over the sea-ice, where these are somewhat too dry (the error peaking at around 15% in the N400 dataset). Despite this, the statistics for these two compare well, with correlation coefficients of 0.72 and 0.83 for the low and high resolution versions respectively. Bias errors are less than 2% for both versions, albeit with different signs, and RMS errors are respectively 6.2% and 4.9%. The relative humidity in the NCEP reanalysis, on the other hand, performs very poorly and bears little resemblence to the observations. The correlation coefficient here is only 0.09, with a regression slope of 0.06 and large bias and RMS errors of 5.1% and 10.5% respectively. That the NCEP reanalysis performs poorly with respect to relative humidity in these conditions is not entirely unexpected – it has been seen before. Renfrew *et al.* (2002) compared *in situ* data from an oceanographic cruise in the Labrador Sea with both the NCEP and ECMWF (re)analyses and found the relative humidity in the NCEP model to be generally around 15% – 20% too high. They noted that convective rainfall in the model was around 15% too low versus

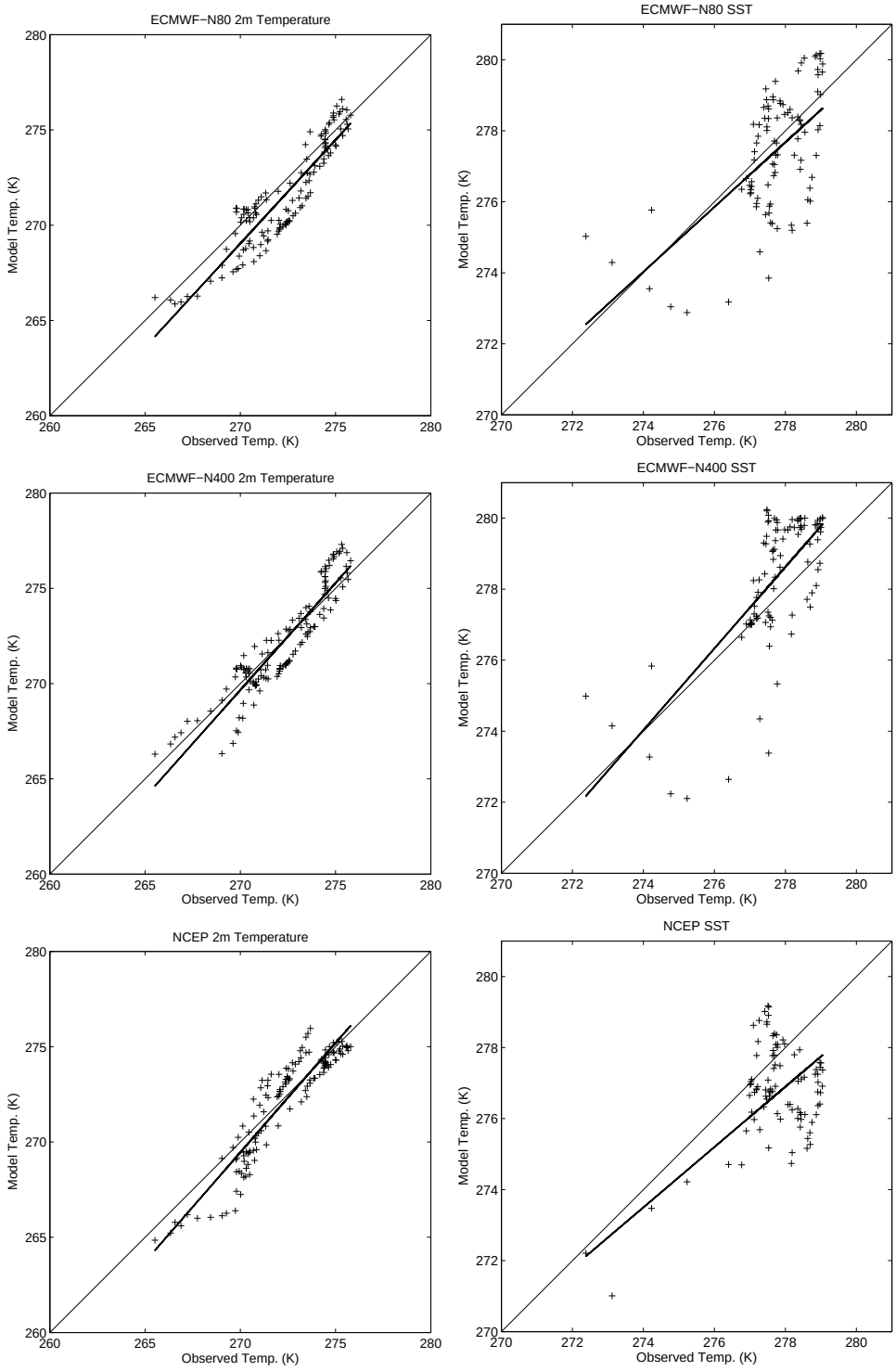

Figure 3.12: Scatter plots showing model/observation relationships for 2 metre temperature (left) and sea surface temperature (right). A linear least squared regression is fitted through the data.

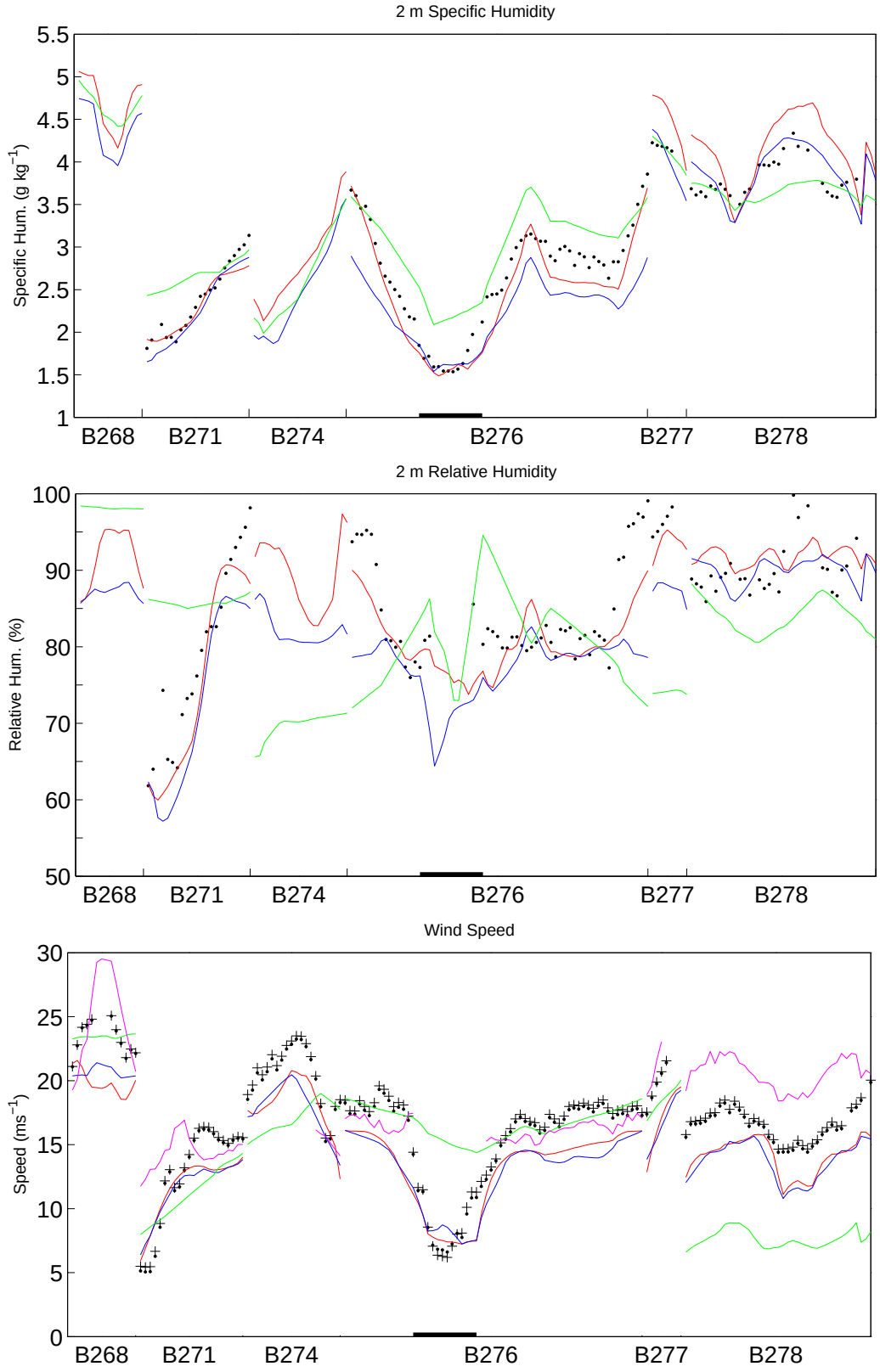

Figure 3.13: 'Spatial' timeseries plots showing the aircraft observations (black dots), NCEP/NCAR Reanalysis (green), ECMWF Analysis at N400 (red) and ECMWF analysis at N80 (blue). The bottom panel includes QuikSCAT-RSS in magenta. The top panel shows 2 metre specific humidity, the middle shows 2 metre relative humidity and the bottom shows 10 metre wind speed.

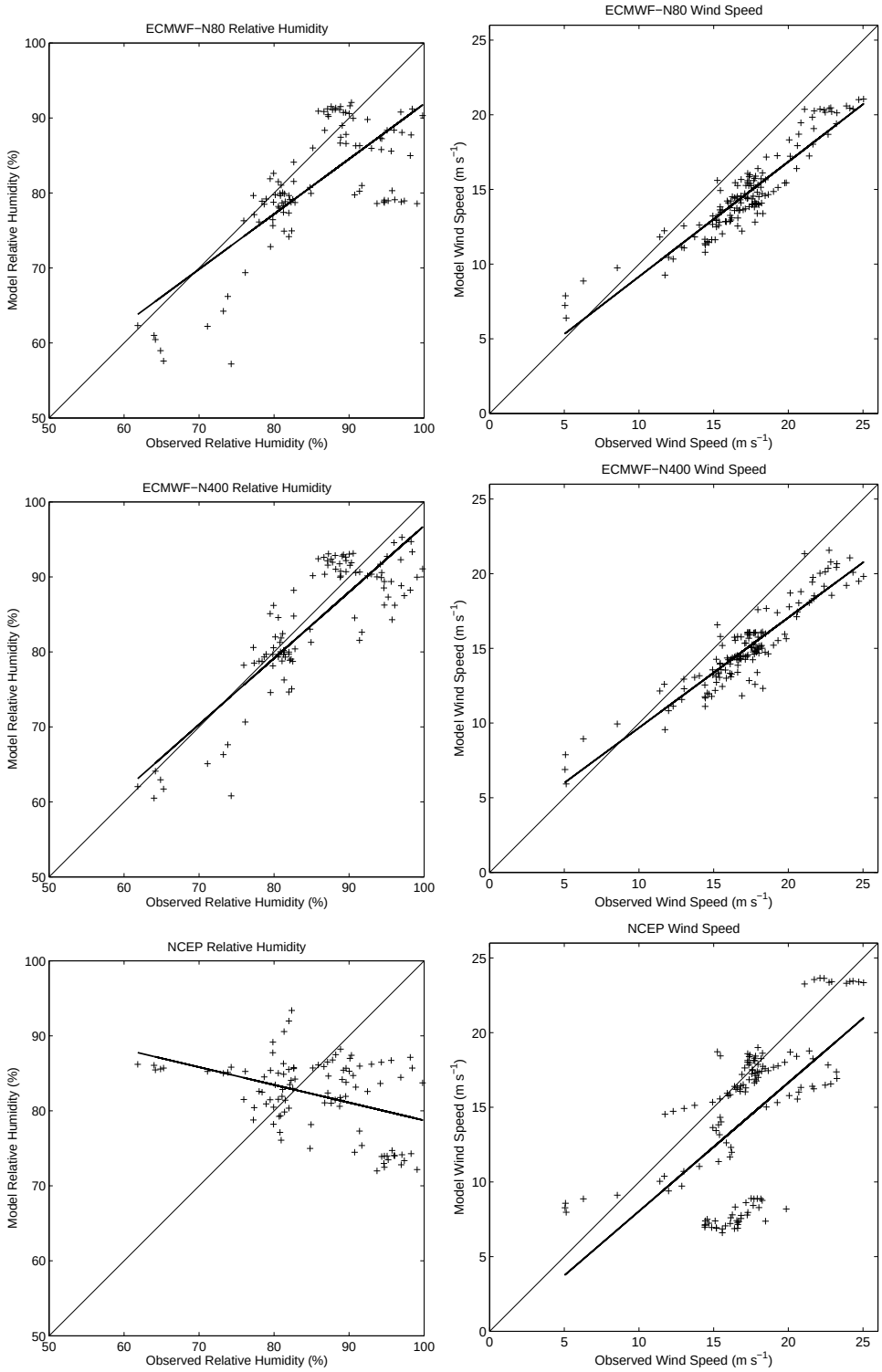

Figure 3.14: Scatter plots showing model/observation relationships for 2 metre relative humidity (left) and 10 metre wind speed (right). A linear least squared regression is fitted through the data.

the observations. If this is due to a lack of shallow convection and subsequent cloud formation in the model[2] then this could go some way to explain the overestimation of relative humidity in the ABL. The weather during the cruise could generally be classified as 'cold air outbreaks', similar to the conditions during much of the GFDex campaign, thus it is likely that a similar explanation for the overestimation of relative humidity can be used here.

The bottom panel of Figure 3.13 shows the 10 metre wind speed spatial timeseries. As well as the model data considered previously, this panel includes data from the Remote Sensing Systems (RSS) QuikSCAT retrieval and the 10 metre neutral wind speed for comparison with this (crosses). Both of the ECMWF timeseries capture the spatial gradients of windspeed well, as we have seen with the other fields, however they are significantly underestimating the magnitude of the wind almost everywhere. The correlation coefficients are 0.93 for ECMWF-N80 and 0.92 for ECMWF-N400, however their bias errors are -2.5 m s^{-1} and -2.2 m s^{-1} respectively. Both also perform worst at high wind speeds, indicated by the low value of their regression slopes: 0.77 for ECMWF-N80 and 0.73 for ECMWF-N400.

The NCEP reanalysis not only consistently underestimates the speed of the wind—by up to 10 m s^{-1} during B278—but also the spatial gradients. This, however, is inevitable in a model with such a coarse spatial resolution and does not necessarily reflect any shortcomings in the model dynamics. It is noteworthy that the NCEP reanalysis appears to perform best during the easterly tip jet flight (B268), with wind speed closest to the observations, around 23 m s^{-1}, albeit without the strong spatial gradients. It is likely, however, that this is due to the model making the best use of the data available to it from the dropsondes released during the flight, rather than it accurately resolving a easterly tip jet; the surface wind field shows an unphysical 'blob' of strong winds rather than any structure resembling a easterly tip jet. The NCEP model shows a correlation coefficient of 0.62, with a bias error of -3.1 m s^{-1} and a RMS error of 5.0 m s^{-1}.

The QuikSCAT wind retrieval, with its high spatial resolution, should be able to capture all but the strongest gradients seen in the observations and indeed it does capture these very well. QuikSCAT, however, as seen previously (Moore *et al.*, 2008; Ebuchi

[2]More specifically, Renfrew *et al.* (2002) speculate that this could be due to an underactive or poor representation of the Bergeron-Findeisen process, whereby ice clouds form at the expense of liquid water clouds.

Table 3.1: Means and standard deviations of surface meteorological fields from aircraft data and data extracted from the NCEP reanalysis and ECMWF analysis at N400 and N80.

	MSLP (hPa)	T_{2m} (K)	SST (K)	q_{2m} (g kg^{-1})	RH_{2m} (%)	U_{10m} (m s^{-1})	WD (°)	
Mean	993.1	272.3	277.8	3.10	84	17.3	29	Aircraft
	992.5	271.6	277.6	2.92	83	14.8	33	ECMWF-N80
	992.4	272.4	278.5	3.19	86	15.1	32	ECMWF-N400
	993.8	272.2	276.8	3.22	82	14.2	34	NCEP/NCAR
Std. dev	10.9	2.2	1.1	0.64	8	3.64	30	Aircraft
	10.8	2.6	1.6	0.79	8	2.8	26	ECMWF-N80
	10.9	2.6	1.6	0.85	8	2.7	26	ECMWF-N400
	9.7	2.8	1.3	0.51	5	5.0	39	NCEP/NCAR

et al., 2002), does not perform very well at high wind speed, overestimating by up to 4 m s^{-1} during some of the stronger wind events (e.g. B278 and some of B268). The QuikSCAT retrievals have a correlation coefficient of 0.88, bias error of 0.8 m s^{-1} and a RMS error of 3.3 m s^{-1}. The exaggeration of the wind speed at high speeds is clearly seen through the high value of the regression slope at 1.39.

We have mentioned previously that low resolution models, such as the NCEP reanalysis, cannot reproduce the strong gradients in wind speed seen in the observations. It may be natural, therefore, that one would expect a higher resolution model to better represent these gradients than a lower resolution model. This, however, does not always seem to be the case, for nearly everywhere both truncations of the ECMWF data show almost identical gradients, and where these are strong in the observations, they are equally underrepresented in the analyses. Chelton *et al.* (2006) showed through a spectral analysis against QuikSCAT data that all features smaller than around 1000 km were under represented in the ECMWF analysis, despite the fact that the resolution of around 40 km should have been sufficient to resolve much smaller features. It seems that there is something in the models which acts to smooth out mesoscale features which the model should be capable of representing. Once the resolution is increased further, however, this smoothing becomes much less apparent. For example the UK Met. Office NAE regional model, with a spatial resolution of of 12 km, simulated all of the gradients measured during the GFDex campaign very well (Renfrew *et al.*, 2009). A breakdown of the performance of surface meteorological variables in the two ECMWF analyses and the NCEP reanalysis is given in Tables 3.1 and 3.2.

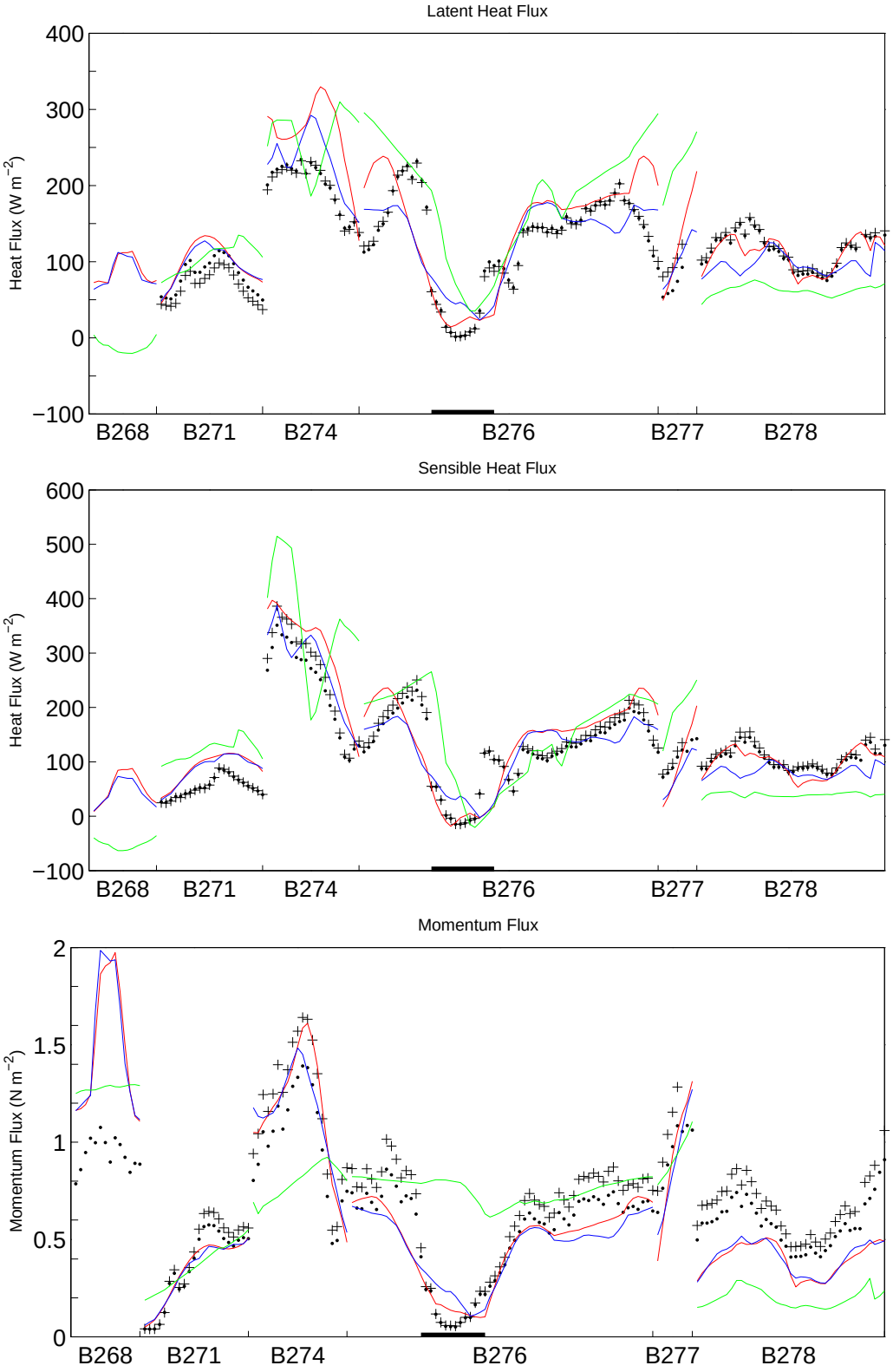

Figure 3.15: 'Spatial' timeseries plots showing the aircraft observations from the Smith (1988) algorithm (black dots) and the COARE 3.0 algorithm (black crosses), NCEP/NCAR Reanalysis (green), ECMWF Analysis at N400 (red) and ECMWF Analysis at N80 (blue). The top panel shows latent heat flux, the middle shows sensible heat flux and the bottom shows momentum flux.

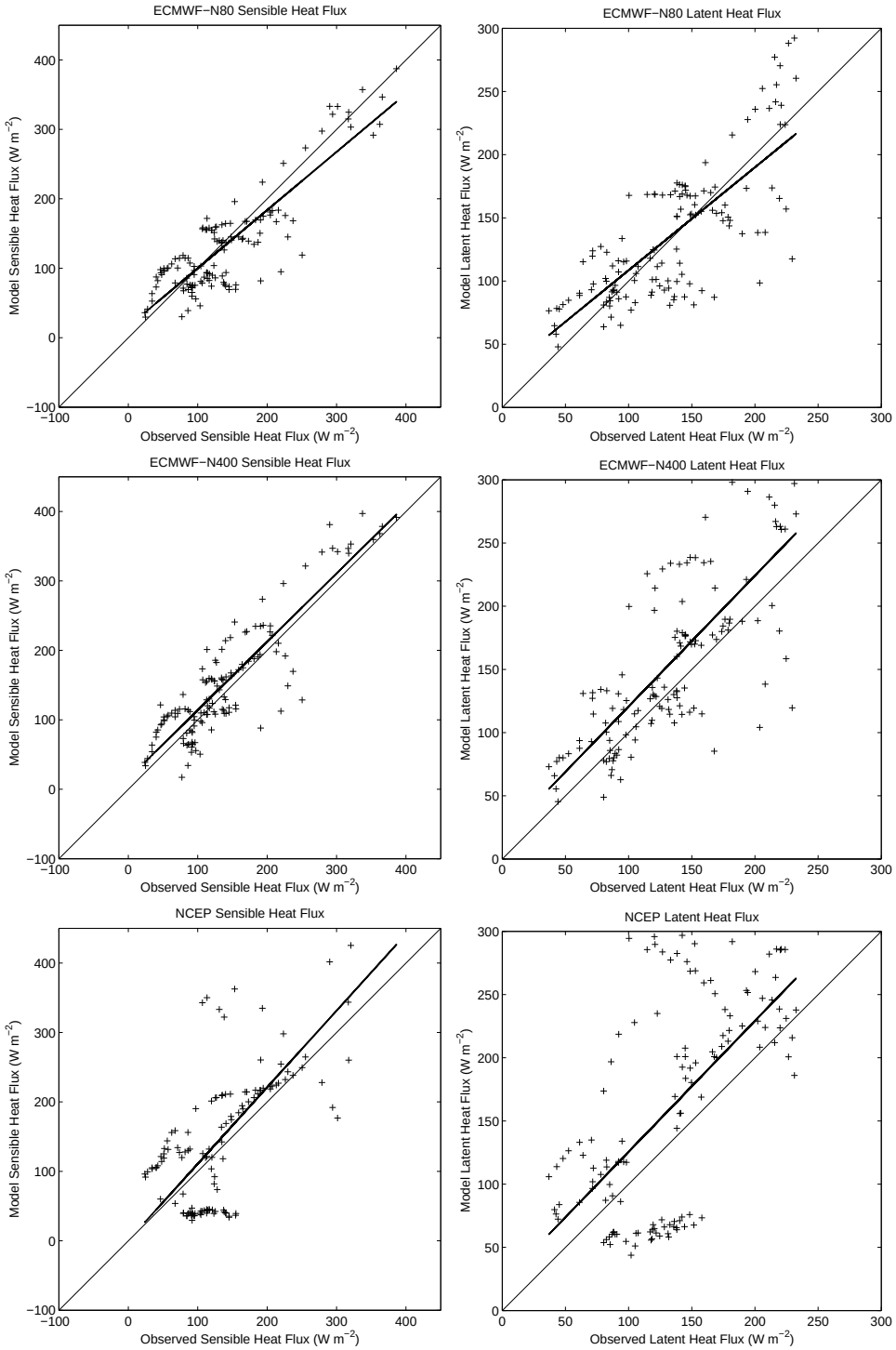

Figure 3.16: Scatter plots showing model/observation relationships for sensible heat flux (left) and latent heat flux (right). A linear least squared regression is fitted through the data.

Table 3.2: Statistical comparisons of aircraft data versus data extracted from the NCEP reanalysis, ECMWF analysis at N400 and N80 for surface meteorological fields.

	MSLP	T_{2m}	SST	q_{2m}	RH_{2m}	U_{10m}	WD	Aircraft vs.
Corr. Coeff.	0.99	0.91	0.51	0.94	0.72	0.93	0.94	ECMWF-N80
	0.99	0.92	0.62	0.96	0.83	0.92	0.94	ECMWF-N400
	0.92	0.92	0.42	0.87	−0.41	0.62	0.73	NCEP/NCAR
						0.88	0.81	QSCAT-RSS
Slope.	0.97	1.07	0.74	1.15	0.71	0.77	0.83	ECMWF-N80
	0.99	1.09	0.90	1.27	0.85	0.73	0.81	ECMWF-N400
	0.81	1.14	0.53	0.70	−2.46	0.93	0.95	NCEP/NCAR
						1.39	0.80	QSCAT-RSS
Bias err.	−0.7	−0.7	−0.2	−0.18	−1.7	−2.5	4	ECMWF-N80
	−0.7	0.0	0.7	0.09	1.2	−2.2	3	ECMWF-N400
	0.7	−0.2	−1.0	−0.19	−2.9	−3.1	5	NCEP/NCAR
						0.8	−7	QSCAT-RSS
RMS err.	1.5	1.3	1.4	0.34	6.2	2.8	11	ECMWF-N80
	1.5	1.0	1.4	0.31	4.9	2.6	11	ECMWF-N400
	4.4	1.2	1.6	0.34	10.0	5.0	27	NCEP/NCAR
						3.3	21	QSCAT-RSS

Table 3.3: Statistical comparisons of aircraft data versus data extracted from the NCEP reanalysis and ECMWF analysis at N400 and N80 for surface flux fields.

	τ	SH	LH	Aircraft vs.
Corr. Coeff.	0.89	0.88	0.78	ECMWF-N80
	0.90	0.90	0.79	ECMWF-N400
	0.56	0.75	0.60	NCEP/NCAR
Slope.	0.86	0.85	0.83	ECMWF-N80
	0.93	1.00	1.06	ECMWF-N400
	0.50	1.10	1.06	NCEP/NCAR
Bias err.	-0.18	-4	4	ECMWF-N80
	-0.16	16	24	ECMWF-N400
	-0.20	15	27	NCEP/NCAR
RMS err.	0.22	37	34	ECMWF-N80
	0.21	40	48	ECMWF-N400
	0.34	79	73	NCEP/NCAR

The three panels in Figure 3.15 show the latent (top) & latent (middle) heat fluxes and the momentum flux (bottom). The 'observed' values are from the Smith (1988) bulk flux algorithm (dots) and the COARE 3.0 bulk flux algorithm (crosses; Fairall *et al.* (2003)). Although turbulent fluxes calculated through the cross-correlation method are available during many of the low-level legs, we use bulk fluxes for the comparison as these are more directly comparable to the fluxes calculated in the models which use similar stability-dependent bulk flux algorithms. Although all of these algorithm are similar in theory, they differ in their details. This is primarily due to the fact that the transfer coefficients

which are used in the bulk formulae are poorly constrained, and are based on empirical relationships which together allow a relatively large range of fluxes to be inferred from the same set of surface meteorological conditions.

Both of the ECMWF truncations do well in all cases, with the errors generally being traced back to an underestimation of the 10 metre wind field. Paradoxically, the lower resolution ECMWF-N80 dataset often seems to perform better than the higher resolution ECMWF-N400, however this is a case of 'getting it right for the wrong reasons', as the improvement is caused by two errors—a generally low wind speed and high ocean-atmosphere temperature difference—cancelling each other out to a large degree. The ECMWF-N400 performs almost equally well at both high and low fluxes, with regression slopes of 0.93 for momentum, 1.00 for sensible heat, and 1.06 for latent heat. The lower resolution ECMWF-N80 tends to be biased low at high fluxes, with regression slopes of 0.86 for momentum, 0.85 for sensible heat, and 0.83 for latent heat.

The NCEP reanalysis generally overestimates both latent and sensible heat fluxes, at least where it has a good representation of the surface wind (the low wind speeds act to lower the heat fluxes). The correlation coefficients are significantly lower than either of the ECMWF datasets; 0.56 for momentum, 0.75 for sensible heat and 0.60 for latent heat. The RMS errors are also large; 0.34 N m^{-2} for momentum, 79 W m^{-2} for sensible heat and 73 W m^{-2} for latent heat, all of which are greater than 50% of the mean values for the respective observations (0.62 N m^{-2} for momentum, 122 W m^{-2} for sensible heat and 125 W m^{-2} for latent heat from the Smith (1988) algorithm). The poor performance of the NCEP reanalysis in the polar regions in high wind conditions is not solely due to insufficient model resolution. This was noted by Renfrew *et al.* (2002), who showed that the roughness length formulations used in the NCEP model are inappropriate for use in high wind speeds as the transfer coefficients become significantly too large, a problem exacerbated by a large air-sea temperature differences, a condition which was almost ubiquitous during GFDex.

3.5 Summary and Conclusions

The Greenland Flow Distortion experiment provided a large database of high quality observations of the atmospheric surface layer and sea surface, allowing the validation of

atmospheric analyses which may be used for forcing ocean models. Results are generally consistent with previous studies; surface meteorological variables were well represented, apart from consistent low biases in the wind speed and a distinct lack of skill in the NCEP representation of relative humidity, as seen by Renfrew *et al.* (2002). Often where consistent bias errors were present in the models they were attributable to errors in the prescribed boundary conditions. Spatial gradients were often under represented, a problem which is not only due to horizontal spatial resolution, but also due to processes in the models which act to smooth out steep spatial gradients. This was seen in, for example, the very similar performances of both of the ECMWF truncations and is in agreement with the spectral analysis of Chelton *et al.* (2006), which showed a drop in power below scales of about 1000 km.

The ECMWF models gave a reasonable representation of the surface fluxes, and, given the great difficulties in choosing appropriate values of transfer coefficients, are probably within the bounds of observational uncertainty. Conversely, in agreement with previous studies (Smith *et al.*, 2001; Renfrew *et al.*, 2002; Josey *et al.*, 2002), the NCEP surface heat fluxes are consistently biased high by up to around 50%. These large and systematic biases mean that the NCEP reanalysis, although often used, is inappropriate for forcing ocean models without recalculating the surface fluxes, for example see Large and Yeager (NCAR).

Despite the reasonable performance of the ECMWF analyses, it is clear that smaller atmospheric phenomena are not well represented, particularly in the N80 truncation. These kinds of reanalyses are often used to force ocean models, and these under represented mesoscale features may have a significant impact on the ocean (see, for example, Condron *et al.*, 2009). In Chapter 5 we will use the ECMWF ERA-40 reanalysis and operational analysis as the basis for developing a parametrisation of Greenland's tip jets, which will allow an improved representation of these mesoscale features to be included into the ERA-40 reanalysis.

Chapter 4

Modelling the General Ocean Circulation

4.1 Introduction

The equations that describe the flow of geophysical fluid are inherently complicated, being both non-linear and coupled, and so cannot be solved analytically. In order to make progress, one can choose either to simplify the equations to a point where the equations become soluble, or to approximate more complicated insoluble equations through numerical means. Although much value can be obtained from the former approach (for example consider the Eady model of baroclinic instability in the atmosphere (Eady, 1949), or the simple equations which describe Sverdrup balance in the ocean), in order to study the three dimensional evolution of a fluid, numerical approximations are required.

The first uses of numerical approximations to the primative equations were, perhaps unsuprisingly, in weather prediction. In 1904 Vilhelm Bjerknes set forth a manifesto designed to place the budding science of meteorology on a rigorous footing, calling for prediction of the future atmospheric state to be calculated from well known physical laws, rather than relying on guesswork based on the observed evolution of previous similar atmospheric states. The first serious attempt to do this was by Lewis Fry Richardson while operating a Quaker ambulance in France in 1916. Richardson attempted to solve the full primative equations by hand, and it is not suprising that he was not successful – his numerical scheme was unstable, resulting in a pressure change of 145 hPa in six

hours! At this time there was no such thing as a computer, and Richardson imagined that operational forecasts could be produced quickly by a large number of people, each performing the calculations for a single grid cell and directed by someone in the centre of the room. However the birth of numerical weather prediction came with the US military's ENIAC computer, and the solution of the barotropic vorticity equation by Charney *et al.* (1950).

Most of the ocean models used currently owe their existance to the work of Bryan (1969). He developed a coarse resolution ocean general circulation model with realistic boundaries and bathymetry, designed to study the large scale barotropic circulation of the ocean, which was all that could be hoped for, given the limited computer power of the time. It is testament to Bryan's numerical scheme that it has remained largely unchanged as computer power and model resolution has increased exponentially.

4.2 The Equations of Motion

4.2.1 Conservation Laws

4.2.1.1 A General Conservation Law

In this section we derive the equations of motion required to describe the general circulation of the ocean, following Haidvogel and Beckmann (1999).

Imagine a fluid property L, surrounded by an arbitrary control volume V. It is clear that we must have

$$\frac{\partial}{\partial t}\int_V L \, \mathrm{d}V = -\int_{\partial V} L\mathbf{u}\cdot\mathbf{n} \, \mathrm{d}s - \int_V \mathbf{Q} \, \mathrm{d}V,$$

where $\mathbf{u}$ is the velocity of the fluid, ∂V is the boundary of V, $\mathbf{n}$ is the unit normal to ∂V, and $\mathbf{Q}$ is a source or sink term. This merely states that a change of the amount of L in V can only be brought about by flow in or out of V or by sources or sinks of L in V. By the divergence theorem, we then have

$$\frac{\partial}{\partial t}\int_V L \, \mathrm{d}V = -\int_V \nabla\cdot(L\mathbf{u}) \, \mathrm{d}V - \int_V \mathbf{Q} \, \mathrm{d}V,$$

or, taking the derivative inside the integral and rearranging,

$$\int_V \left[\frac{\partial L}{\partial t} + \nabla \cdot (L\mathbf{u}) + \mathbf{Q} \right] \, \mathrm{d}V = 0. \tag{4.1}$$

Since Equation 4.1 must hold for any control volume V, it must be that the integrand is identically zero, i.e.

$$\frac{\partial L}{\partial t} + \nabla \cdot (L\mathbf{u}) + \mathbf{Q} = 0. \tag{4.2}$$

So for a property L, we have a general law conseving that property.

4.2.1.2 Conservation of Mass

The mass of fluid in V is given by $\int_V \rho \, \mathrm{d}V$, where ρ is the local density of the fluid. Thus, from (4.2), assuming we have no sources or sinks of mass, we have

$$\frac{\partial \rho}{\partial t} + \nabla \cdot (\rho \mathbf{u}) = 0. \tag{4.3}$$

4.2.1.3 Conservation of Momentum

Substituting the fluid's momentum field into (4.2), we obtain

$$\frac{\partial}{\partial t} (\rho \mathbf{u}) + \nabla \cdot (\rho \mathbf{u}\mathbf{u}) + \mathbf{Q} = 0, \tag{4.4}$$

where $\mathbf{u}\mathbf{u}$ is the dyadatic vector product. Now,

$$\begin{aligned} \nabla \cdot (\rho \mathbf{u}\mathbf{u}) &= \rho u_j \frac{\partial u_i}{\partial x_i} + \rho u_i \frac{\partial u_j}{\partial x_i} + u_i u_j \frac{\partial \rho}{\partial x_i} \\ &= \rho \mathbf{u} \left(\nabla \cdot \mathbf{u} \right) + \rho \mathbf{u} \cdot \nabla \mathbf{u} + \left(\mathbf{u} \cdot \nabla \rho \right) \mathbf{u}. \end{aligned}$$

So, on expanding the time derivative in (4.4), we have

$$\mathbf{u} \frac{\partial \rho}{\partial t} + \rho \frac{\partial \mathbf{u}}{\partial t} + \rho \mathbf{u} \left(\nabla \cdot \mathbf{u} \right) + \rho \mathbf{u} \cdot \nabla \mathbf{u} + \left(\mathbf{u} \cdot \nabla \rho \right) \mathbf{u} = \sum \text{Forces},$$

or

$$\mathbf{u} \left(\frac{\partial \rho}{\partial t} + \mathbf{u} \cdot \nabla \rho + \rho \nabla \cdot \mathbf{u} \right) + \rho \left(\frac{\partial \mathbf{u}}{\partial t} + \mathbf{u} \cdot \nabla \mathbf{u} \right) = \sum \text{Forces}. \tag{4.5}$$

By conservation of mass, (4.3), the first term on the left-hand side of (4.5) is identically zero, so we have

$$\rho\left(\frac{\partial \mathbf{u}}{\partial t} + \mathbf{u}\cdot\nabla\mathbf{u}\right) = \sum \text{Forces},$$

or using the Lagrangian derivative,

$$\rho\frac{D\mathbf{u}}{Dt} = \sum \text{Forces}. \tag{4.6}$$

The forces acting on the fluid can be split into 'body' forces, $\mathbf{b}$, which act throughout the fluid, and stress forces, so that we have

$$\rho\frac{D\mathbf{u}}{Dt} = \nabla\cdot\sigma_{ij} + \mathbf{b}. \tag{4.7}$$

Here, σ_{ij} is the (second order) stress tensor

$$\sigma_{ij} = \begin{pmatrix} \tau_{xx} & \tau_{xy} & \tau_{xz} \\ \tau_{yx} & \tau_{yy} & \tau_{yz} \\ \tau_{zx} & \tau_{zy} & \tau_{zz} \end{pmatrix},$$

with normal stresses τ_{ii} and shear stresses $\tau_{ij}, i \neq j$. We can thus write

$$\sigma_{ij} = -\begin{pmatrix} p & 0 & 0 \\ 0 & p & 0 \\ 0 & 0 & p \end{pmatrix} + \begin{pmatrix} \tau_{xx}+p & \tau_{xy} & \tau_{xz} \\ \tau_{yx} & \tau_{yy}+p & \tau_{yz} \\ \tau_{zx} & \tau_{zy} & \tau_{zz}+p \end{pmatrix} = pI + \mathbf{T},$$

where $p = \frac{1}{3}\left(\tau_{xx}+\tau_{yy}+\tau_{xx}\right)$ is the mean normal stress.

The primary body force of interest is that of gravity, and is given by

$$\mathbf{F}_g = -\int_V \rho g \nabla z \, \mathrm{d}V.$$

We thus arrive at the momentum conservation equation,

$$\rho\frac{D\mathbf{u}}{Dt} = -\nabla p + \nabla\cdot\mathbf{T} - \rho g\nabla z. \tag{4.8}$$

4.2.1.4 Conservation of Energy

The conservation of energy equation can be obtained from considering the total energy of the system,

$$E = \int_V \left(\frac{1}{2}\rho \mathbf{u} \cdot \mathbf{u} + \rho g z + \rho e \right) \, \mathrm{d}V,$$

where e is the internal energy per unit mass. The derivation is lengthy, and is omitted here, see Gill (1982) for details, however the equation in its final form is

$$\rho c_p \frac{DT}{Dt} - \beta T \frac{Dp}{Dt} = -\nabla \cdot \mathbf{q} - \sigma, \tag{4.9}$$

where c_p is the specific heat at constant pressure, T is the temperature, β is the thermal expansion coefficient, $\mathbf{q}$ is a heat flux and $\sigma = -\tau_{ij} \frac{\partial u_j}{\partial x_i}$

4.2.1.5 Conservation of Salt

In the absence of precipitation or evaporation, equation for the conservation of salt, S, is

$$\frac{DS}{Dt} = \kappa_S \nabla \cdot (\nabla S), \tag{4.10}$$

where κ_S is the molecular diffusion coefficient for salt.

4.2.2 A Rotating Planet

The momentum equation as outlined above assumes an inertial frame of reference, however at the time and length scales relevent to ocean circulation, the rotation of the earth cannot be ignored. Imagine an axis xyz, translating and rotating in relation to an inertial axis XYZ, with an origin at $\mathbf{r_0}$, and a point $\mathbf{p}$ whose location is $\mathbf{r}$ with respect to xyz and $\mathbf{r_I}$ with respect to XYZ. We must then have

$$\frac{D\mathbf{r_I}}{Dt} = \frac{D\mathbf{r_0}}{Dt} + \frac{D\mathbf{r}}{Dt} \tag{4.11}$$

$$= \mathbf{v_0} + \left(x\frac{D\hat{\mathbf{i}}}{Dt} + y\frac{D\hat{\mathbf{j}}}{Dt} + z\frac{D\hat{\mathbf{k}}}{Dt} \right) + \left(\hat{\mathbf{i}}\frac{Dx}{Dt} + \hat{\mathbf{j}}\frac{Dy}{Dt} + \hat{\mathbf{k}}\frac{Dz}{Dt} \right) \tag{4.12}$$

$$= \mathbf{v_0} + \boldsymbol{\Omega} \times \mathbf{r} + \mathbf{v}, \tag{4.13}$$

where $\mathbf{\Omega}$ is the angular velocity of the xyz system. Taking the time derivative of (4.13), we have

$$\frac{D\mathbf{v_I}}{Dt} = \frac{D\mathbf{v_0}}{Dt} + \frac{D}{Dt}\mathbf{\Omega} \times \mathbf{r} + \mathbf{\Omega} \times \frac{D\mathbf{r}}{Dt} + \frac{D\mathbf{v}}{Dt} \tag{4.14}$$

$$= \frac{D\mathbf{v_0}}{Dt} + \frac{D}{Dt}\mathbf{\Omega} \times \mathbf{r} + \mathbf{\Omega} \times (\mathbf{\Omega} \times \mathbf{r} + \mathbf{v}) + \mathbf{\Omega} \times \mathbf{v} + \frac{D\mathbf{v}}{Dt} \tag{4.15}$$

$$= \frac{D\mathbf{v_0}}{Dt} + \frac{D}{Dt}\mathbf{\Omega} \times \mathbf{r} + \mathbf{\Omega} \times \mathbf{\Omega} \times \mathbf{r} + 2\mathbf{\Omega} \times \mathbf{v}. \tag{4.16}$$

The first two terms on the right hand side of (4.16) represent, in a geophysical sense, the acceleration of the Earth as it moves through space, and the variance of the rotation rate of the Earth. These are unimportant to ocean dynamics and may be neglected, leaving us with

$$\rho\frac{D\mathbf{v_I}}{Dr} = \rho\left(\frac{D\mathbf{v}}{Dt} + \mathbf{\Omega} \times \mathbf{\Omega} \times \mathbf{r} + 2\mathbf{\Omega} \times \mathbf{v}\right) \tag{4.17}$$

$$= -\nabla p - \rho g\hat{\mathbf{k}} + \nabla \cdot \mathbf{T}. \tag{4.18}$$

The centripetal acceleration, $\mathbf{\Omega} \times \mathbf{\Omega} \times \mathbf{r}$, is a conservative force directed towards the centre of the Earth, with potential $\Omega^2 R^2/2$. We can thus combine its potential with the gravitational potential, Φ_g, and write

$$\Phi = \Phi_g - \frac{\Omega^2 R^2}{2},$$

so that

$$\frac{D\mathbf{v}}{Dt} = -\frac{1}{\rho}\nabla p - 2\mathbf{\Omega} \times \mathbf{v} - \nabla\Phi + \frac{1}{\rho}\nabla \cdot \mathbf{T}. \tag{4.19}$$

4.2.3 A Spherical Planet

The equations presented in the previous section are in the standard Cartesian co-ordinate system. When considering oceanic motions on the basin to global scale, the curvature of the Earth becomes important, and it is more convenient to represent the equations in a spherical coordinate system. The resulting equations, the non-hydrostatic primitive

equations, are, in component form (Gill, 1982),

$$\rho\left[\frac{Du}{Dt}-\frac{uv\tan\phi}{r}+\frac{uw}{r}\right]+2\Omega\rho\left(w\cos\phi-v\sin\phi\right)=-\frac{1}{r\cos\phi}\frac{\partial p}{\partial\lambda}+\left(\nabla\cdot\mathbf{T}\right)\cdot\hat{\lambda} \tag{4.20}$$

$$\rho\left[\frac{Dv}{Dt}-\frac{u^2\tan\phi}{r}+\frac{vw}{r}\right]+2\Omega\rho u\sin\phi=-\frac{1}{r}\frac{\partial p}{\partial\phi}+\left(\nabla\cdot\mathbf{T}\right)\cdot\hat{\phi} \tag{4.21}$$

$$\rho\left[\frac{Dw}{Dt}-\frac{u^2+v^2}{r}\right]-2\Omega\rho\cos\phi=-\frac{\partial p}{\partial r}-\rho g+\left(\nabla\cdot\mathbf{T}\right)\cdot\hat{r} \tag{4.22}$$

$$\frac{D\rho}{Dt}+\frac{\rho}{r\cos\phi}\left(\frac{\partial u}{\partial\lambda}+\frac{\partial\left(v\cos\phi\right)}{\partial\phi}\right)+\frac{\rho}{r^2}\frac{\partial\left(r^2w\right)}{\partial r}=0 \tag{4.23}$$

$$\frac{DT}{Dt}-\frac{\beta T}{\rho c_p}\frac{Dp}{Dt}=\frac{\nabla\cdot\left(\kappa\nabla T\right)}{\rho c_p}-\frac{\sigma}{\rho c_p} \tag{4.24}$$

$$\rho=\rho(p,T), \tag{4.25}$$

where the material derivative is given by

$$\frac{D}{Dt}=\frac{\partial}{\partial t}+\frac{u}{r\cos\phi}\frac{\partial}{\partial\lambda}+\frac{v}{r}\frac{\partial}{\partial\phi}+w\frac{\partial}{\partial r}.$$

4.2.4 Standard Approximations

In order to simplify the equations of motion, a number of approximations which are suitable for large scale oceanic flow are generally made.

4.2.4.1 The Boussinesq Approximation

Compared to the mean value of density in the ocean, the variations in density in time and space are relatively small. We can thus represent density as the sum of a space and time-invarient mean value and a spatially and temporally varying peturbation:

$$\rho\left(x,y,z,t\right)=\rho_0+\hat{\rho}\left(x,y,z,t\right),\qquad\rho_0\gg\hat{\rho}.$$

It is then appropriate to replace $\rho(\mathbf{x},t)$ with ρ_0 everywhere exept where it is multiplied by gravity, i.e. in a buoyancy term.

4.2.4.2 Incompressibility

Following on immediately from the Boussinesq approximation is the assumption that the ocean is non-divergent. Again splitting density into mean and peturbation parts, the statement of conservation of mass becomes

$$\rho_0 \left(\nabla \cdot \mathbf{u}\right) + \hat{\rho} \left(\nabla \cdot \mathbf{u}\right) + \frac{\partial \hat{\rho}}{\partial t} = 0.$$

The second term is clearly much smaller than the first, and can be neglected. Furthermore, assuming that the characteristic scaling lengths for the peturbation density are comparible to those for the velocity, the final term is also much smaller than the first, leaving us with

$$\nabla \cdot \mathbf{u} = 0. \tag{4.26}$$

4.2.4.3 The Hydrostatic Approximation

Using scaling lengths typical of the upper kilometre of the ocean, two terms in the vertical momentum equation can be shown to dominate by many orders of magnitude: the gravitational force and the vertical pressure gradient. The primary balance is thus between these two forces and we can write

$$g \approx -\frac{1}{\rho}\frac{\partial p}{\partial z}.$$

It is worth noting that making the hydrostatic approximation introduces spurious terms into the energy budget. To recover a physically meaningful energy budget, two further assumptions are needed: we must assume that $w = 0$ in the horizontal momentum equations, and must make the thin-shell approximation $r = r_E$, where r_E is the mean radius of the Earth.

4.3 The FRUGAL OGCM

4.3.1 Description

The Fine Resolution Greenland and Labrador (FRUGAL) Ocean General Circulation Model (OGCM) is a three-dimensional, hydrostatic, finite-difference ocean model, based

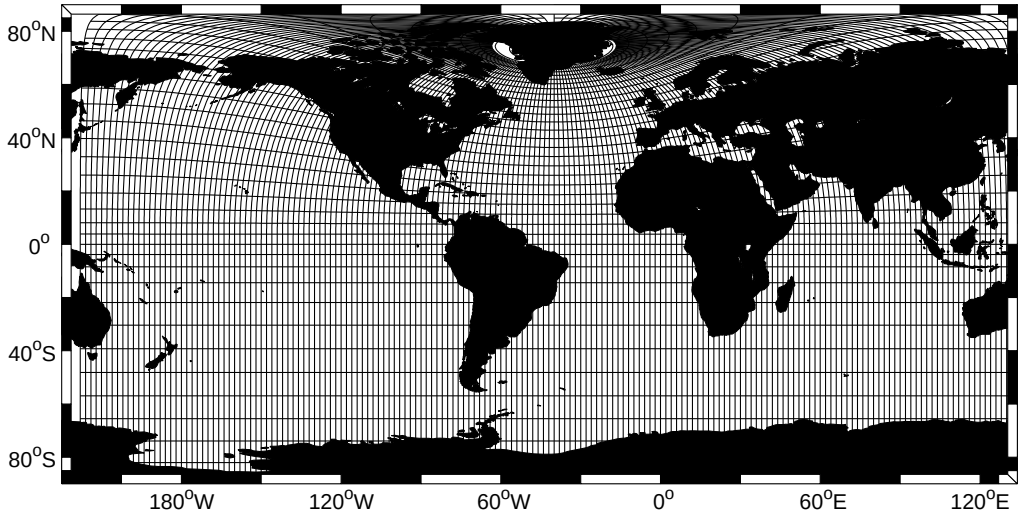

Figure 4.1: The FRUGAL grid is a curvilinear coordinate system. The resolution in the Southern Ocean is 2.5°, however placing the pole in Greenland increases the resolution in the Greenland and Labrador Seas to $< \frac{1}{3}^\circ$.

Table 4.1: Vertical distribution of model levels in the FRUGAL model. Note the increased resolution in the upper ocean.

Model Level	Depth (m)	Model Level	Depth (m)
1	0	11	2100
2	30	12	2600
3	90	13	3100
4	180	14	3600
5	300	15	4100
6	450	16	4600
7	650	17	5100
8	900	18	5600
9	1200	19	6100
10	1600		

on the Southampton-East Anglia (SEA) model, which was in turn was based on the Modular Ocean Model (MOM), developed from the 1960s by Bryan (1969), Semtner (1974) and Cox (1984). It has a curvilinear co-ordinate system, with 211×182 grid points, and the pole placed in Greenland at 72.5 °N, 40 °W. This allows a relatively coarse resolution of $2^\circ \times 1.5^\circ$ in the Southern Ocean which increases to around $\frac{1}{3}^\circ$ as the pole is neared (Figure 4.1). The model uses a z-based vertical co-ordinate, with a maximum of 19 levels, depending on the depth of the ocean. These are spaced unevenly in the vertical, ranging from 30 metres at the surface to 500 metres at depth (Table 4.1), allowing an improved

representation of physcial processes in the upper ocean.

The horizontal eddy viscosity is dependent on the local grid resolution, as is set to ensure that it exceeds the viscous western boundary and grid point Reynolds stability criteria by at least a factor of 2 (Wadley and Bigg, 2002). The model replaces the rigid lid approximation in MOM with a free surface formulation, and thus a new diagnostic variable is introduced representing the elevation of the surface. The free surface allows the representation of the barotropic mode, and thus a time splitting method is used whereby the barotropic timestep is typically 50–100 times smaller than the baroclinic timestep. This is to avoid fast moving barotropic gravity waves from violating CFL-type stability criteria. To increase the efficiency of the integration, the baroclinic time step is also dependent on grid resolution, varying from 2700 seconds in the Southern Ocean to 337.5 seconds along the coast of Greenland, where the resolution is highest (Wadley and Bigg, 2002).

Fluid density is calculated using a third order polynomial which closely approximates the nonlinear equation of state for sea water, but at a lower computational cost (Bryan and Cox, 1972).

Bathymetry is calculated from the ETOPO 5' dataset (1986) and sill depths are taken from Thompson (1995). An illustration of bathymetry on the FRUGAL model grid is provided in Figure 4.2.

4.3.2 Model Equations

The FRUGAL model equations, as given by Beare (1998) are:

· Horizontal Momentum Equations

$$\frac{\partial u}{\partial t} + \Gamma(u) - fv = -\frac{1}{\rho_0 a \cos\phi}\frac{\partial p}{\partial \lambda} + \frac{\partial}{\partial z}\left(K_m \frac{\partial u}{\partial z}\right) + A_m \nabla^2 u, \qquad (4.27)$$

$$\frac{\partial v}{\partial t} + \Gamma(v) + fu = -\frac{1}{\rho_0 a \cos\phi}\frac{\partial p}{\partial \phi} + \frac{\partial}{\partial z}\left(K_m \frac{\partial v}{\partial z}\right) + A_m \nabla^2 v, \qquad (4.28)$$

where $f = 2\Omega \sin\phi$ is the Coriolis parameter, and A_m and K_m are the horizontal and vertical coefficients of eddy viscosity. The advective operator, $\Gamma(\mu)$, is given by

$$\Gamma(\mu) = \frac{1}{a\cos\phi}\frac{\partial}{\partial \lambda}(u\mu) + \frac{1}{a}\frac{\partial}{\partial \phi}(v\mu) + \frac{\partial}{\partial z}(w\mu), \qquad (4.29)$$

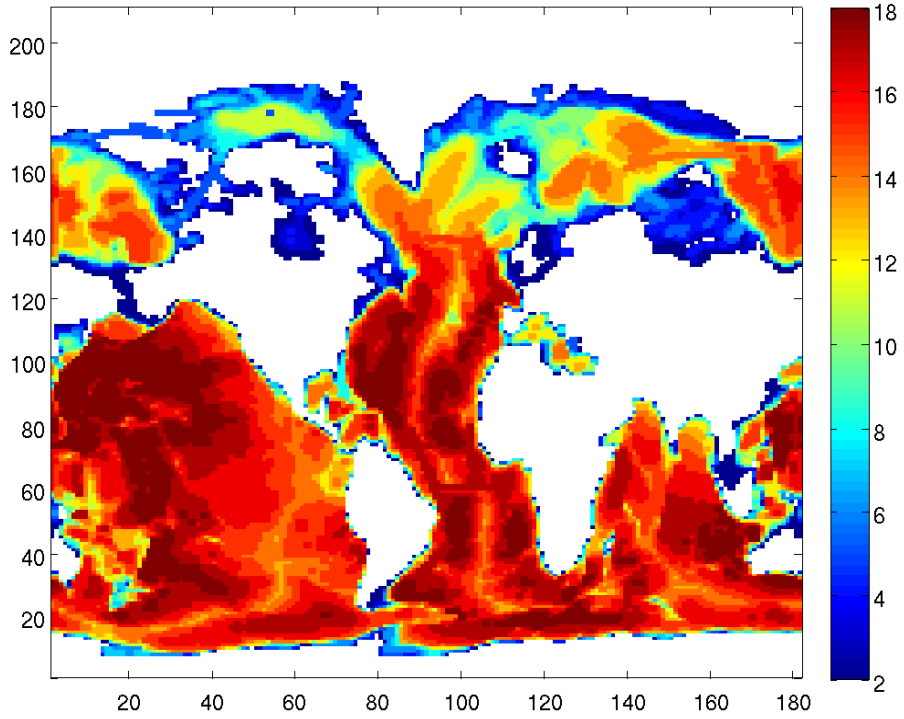

Figure 4.2: Bathymetry in model levels in the FRUGAL model domain. The depth of these levels is given in Table 4.1.

and the horizontal Laplacian operator is

$$\nabla^2(\mu) = \frac{1}{a^2 \cos^2\phi}\frac{\partial^2\mu}{\partial\lambda^2} + \frac{1}{a^2}\frac{\partial^2\mu}{\partial\phi^2}. \tag{4.30}$$

· Hydrostatic Balance:

$$\frac{\partial p}{\partial z} = -\rho g. \tag{4.31}$$

· Tracer (temperature, salinity, or any passive tracer, denoted $\mathcal{T}$) Conservation:

$$\frac{\partial \mathcal{T}}{\partial t} + \Gamma(\mathcal{T}) = \frac{\partial}{\partial z}\left(K_h \frac{\partial \mathcal{T}}{\partial z}\right) + A_h \nabla^2 \mathcal{T}, \tag{4.32}$$

where A_h and K_h are the horizontal and vertical eddy diffusivity.

· Continuity Equation

$$\Gamma(1) = 0. \tag{4.33}$$

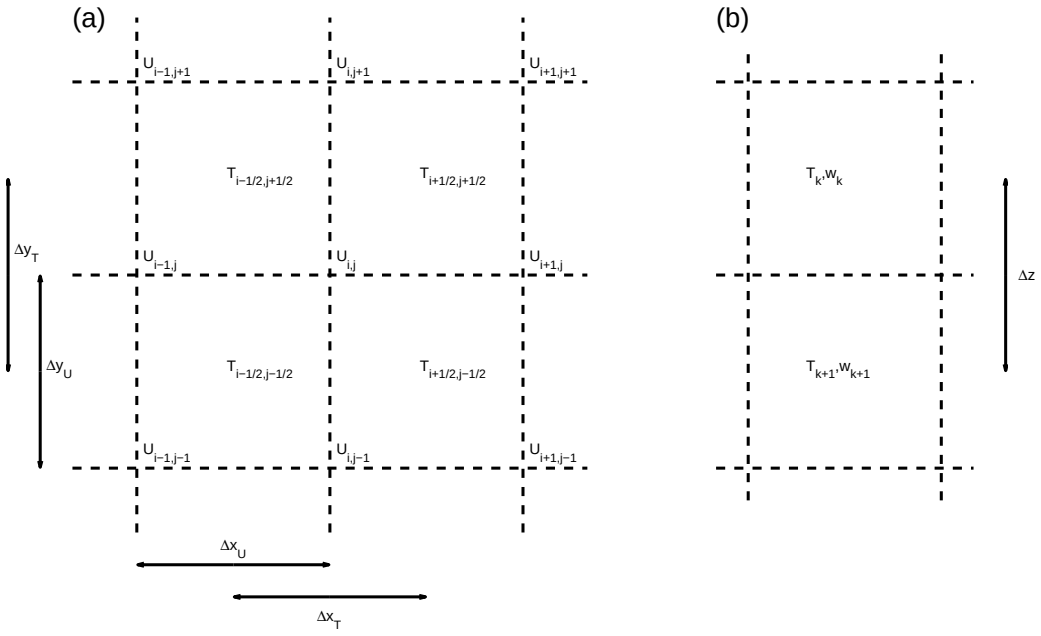

Figure 4.3: Model discretization on the Arakawa B grid. On the horizontal grid, velocity values are located on the corners of grid cells, with tracer values in the centre of the grid cells. On the vertical grid, both velocity and momentum values are located in the centre of the grid.

4.3.3 Model Discretisation

The equations described in the previous section are coupled and nonlinear, and cannot be solved analytically. Instead, they are discretised and solved numerically using a finite difference technique, following Bryan (1969) with modifications for the free surface (Killworth *et al.*, 1991).

The equations are discretised onto an Arakawa type B grid, whereby horizontal momentum values u and v are placed on the corners of the grid cells and tracer quantities $\mathcal{T}$ are placed in the centre of the grid cells. In the vertical discretisation, both momentum and tracers are placed in the middle of the grid cells, Figure 4.3. Given the values of a variable, at adjacent points, the finite difference and average values at the mid-point between them is

$$\partial_\lambda \left(\mu_i\right) = \frac{\mu_{i+\frac{1}{2}} - \mu_{i-\frac{1}{2}}}{\Delta\lambda}, \tag{4.34}$$

$$\bar{\mu}_i^\lambda = \frac{\mu_{i+\frac{1}{2}} - \mu_{i-\frac{1}{2}}}{2}, \tag{4.35}$$

with similar operators for the meridional and vertical directions, ϕ and z, respectively.

The model is timestepped forward in time using a centred leapfrog timestepping

scheme, given by

$$\partial_t(\mu) = \frac{\mu^{n+1} - \mu^{n-1}}{2\Delta t}. \tag{4.36}$$

The use of a leapfrogging method leads to a splitting of the solution into a physical and computational mode (Mesinger and Arakawa, 1976). The latter is removed from the solution by introducing a Euler-forward mixing timestep every 16 regular timesteps. Full details of the discetisation and numerical solution of the model equations is given in Beare (1998).

4.3.4 Model Parameterisations

4.3.4.1 Mixing

Mixing in the ocean mainly occurs along surfaces of equal potential density, so-called isoneutral (or often isopycnal) mixing, however mixing can also occur to a lesser degree in the vertical and horizontal, which generally induces a component of mixing across isoneutral surfaces (dianeutral or diapycnal). These mixing processes are generally forced by small scale phenomena, for example stirring by mesoscale eddies (generally < 50 km) in the case of isopycnal mixing or internal wave breaking in the case of diapycnal mixing. These processes are too small to be resolved in the FRUGAL model, and thus they must be parameterized. This is achieved by introducing diffusivities for tracers and momentum into the model equations.

- **Isopycnal Mixing** is implemented using the scheme of Griffies *et al.* (1998) which represents isopycnal mixing as a down-gradient diffusion in the isoneutral direction. Isopycnal diffusivities are taken from England (1993) and vary from 5×10^7 cm^2 s^{-1} at the surface to 1×10^7 cm^2 s^{-1} at depth. In regions where isopycnals are steeply sloping, this scheme can become unstable, so the tangent taper method of Danabasoglu and Mc Williams (1995) is employed to reduce the isopycnal mixing coefficients when the slope of the isopycnals exceeds a threshold value, thus retaining numerical stability.

- **Vertical Mixing** follows the scheme of Pacanowski and Philander (1981) whereby eddy viscosity and diffusivity are Richardson number dependent. Although this scheme was developed to produce a realistic representation of the thermocline in

the tropical oceans, they have been shown to work successfully in the sub-tropical and (sub-)polar seas. Tracer diffusivities vary from 0.3 $cm^2\ s^{-1}$ to 1.3 $cm^2\ s^{-1}$ and momentum diffusivities vary from 50 $cm^2\ s^{-1}$ in the mixed layer, diminishing rapidly below the thermocline.

- **Horizontal Mixing.** Tracer diffusivities vary from 0.75×10^7 $cm^2\ s^{-1}$ at the surface to 0.375×10^7 $cm^2\ s^{-1}$ at depth, following England (1993). Momentum diffusivity is set to 1×10^8 $cm^2\ s^{-1}$ in the Southern Ocean (smaller than those given by England for stability reasons), and varies with grid resolution Wadley and Bigg (2002).

4.3.4.2 Convection

Oceanic convection generally occurs on very small spatial scales (often < 1 km) in so-called 'convective plumes' (Marshall and Schott, 1999). These are obviously sub-gridscale and thus need to be parameterized. FRUGAL uses the convective scheme of Rahmstorf (1993), which involves a simple bulk adjustment to remove static instability from the water column. If any grid cell in the water column is found to have a greater density than the cell below it, then the two grid cells are homogenized. These cells are then compared to the next cell in the column, and so-on until all static instability has been removed. This is very similar to the static instability routine described in the PWP model in Chapter 2.

4.4 Atmospheric Boundary Conditions

The surface of the ocean is where the ocean and atmosphere interact, and thus where heat, moisture and momentum are exchanged between these two mediums. FRUGAL is an ocean-only GCM, having no atmospheric component, so in order to simulate this exchange, fluxes of heat, moisture and momentum must be prescribed at every gridpoint at every timestep. It is possible to obtain all of these fluxes directly from atmospheric reanalysis, such as ECMWF ERA-40, however these fluxes are completely decoupled from the state of the ocean and so the ocean can rapidly 'drift' away from a realistic state. Instead, one may calculate fluxes, incorporating the current state of the ocean model into these calculations. This provides a stabilizing influence on the ocean, preventing it from

drifting too far from a realistic state. In-situ flux calculations also allow flux fields to be perturbed by simply perturbing the wind speed. This will be important for the experiments which are to be carried out with the FRUGAL model.

4.4.1 Heat Flux

The heat fluxed between the atmosphere and ocean can be described as the sum of four separate components: shortwave radiation from the sun, the balance between longwave radiation emitted from the surface and that absorbed and re-emitted by the atmosphere, the sensible heat flux and the latent heat flux. FRUGAL has been designed to accept the net surface thermal radiation as provided from an atmospheric model, so we may write

$$Q_{\mathrm{TOT}} = Q_{\mathrm{SW_{net}}} + Q_{\mathrm{LW_{net}}} + Q_{\mathrm{S}} + Q_{\mathrm{L}}, \tag{4.37}$$

where Q_{TOT} is the total heat flux between the atmosphere and ocean, Q_{SW} is the incident shortwave radiation, $Q_{\mathrm{LW_{net}}}$ is the net longwave radiation at the surface, Q_{S} is the surface sensible heat flux, and Q_{L} is the surface latent heat flux. Q_{S} and Q_{L} are set by the strength of the turbulent transfer of heat and humidity in the atmospheric boundary layer, however these processes are far too small scale to be resolved, and so Q_{S} and Q_{L} must be calculated through the bulk formulae

$$Q_{\mathrm{S}} = C_{\mathrm{H}} c_{\mathrm{p}} \rho_{\mathrm{a}} U_{10} \Delta T, \tag{4.38}$$

$$Q_{\mathrm{L}} = C_{\mathrm{E}} L \rho_{\mathrm{a}} U_{10} \Delta Q, \tag{4.39}$$

where C_{H} and C_{E} are transfer coefficients for heat and moisture respectively, c_{p} is the specific heat capacity of sea water, L is the specific heat of vaporization of sea water, ρ_{a} is the density of air, U_{10} is the wind speed at 10 metres, and ΔT and ΔQ are the difference between the sea surface and 10 metres of temperature and specific humidity respectively. The transfer coefficients are not fixed but are dependent on both wind speed and the stability of the atmosphere (Zeng *et al.*, 1998; Fairall *et al.*, 2003). Fluxes are thus generally derived from the calculation of momentum, heat, and moisture roughness lengh scales (z_o, z_{ot} and z_{oq}), scaling temperature, t_*, and humidity, q_*, and a friction velocity,

u_*. These are given by Zeng *et al.* (1998) as

$$z_o = \alpha \frac{u_*^2}{g} + \beta \frac{\nu}{u_*}, \tag{4.40}$$

$$\ln\left(\frac{z_o}{z_{ot}}\right) = \beta \mathrm{Re}_*^{\frac{1}{4}} + \gamma, \tag{4.41}$$

$$z_{oq} = z_{ot} \tag{4.42}$$

where $\alpha = 0.013$, $\beta = 0.011$, ν is the dynamic viscosity of air and Re_* is the roughness Reynolds number. Note that in the FRUGAL model, to bring the algorithm into line with ECMWF flux calculations, $\alpha = 0.018$, ν is assumed to be fixed at 1.5×10^{-5} m s^{-1} and

$$z_{ot} = 0.4 \frac{\nu}{u_*}, \qquad z_{oq} = 0.62 \frac{\nu}{u_*}. \tag{4.43}$$

The roughness length scales and friction velocity are given as

$$u_* = \frac{U_{10} k}{\ln\left(\frac{z}{z_o}\right) - \psi_u}, \tag{4.44}$$

$$t_* = \frac{\Delta t k}{\ln\left(\frac{z}{z_o}\right) - \psi_t}, \tag{4.45}$$

$$q_* = \frac{\Delta q k}{\ln\left(\frac{z}{z_o}\right) - \psi_q}, \tag{4.46}$$

where $k = 0.4$ is the Von Kármán constant and ψ_i are corrective functions which are dependent on atmospheric stability. The sensible and latent heat fluxes may then be iteratively calculated through the relations

$$Q_\mathrm{S} = \rho_\mathrm{a} c_\mathrm{p} u_* t_* \tag{4.47}$$

$$Q_\mathrm{L} = \rho_\mathrm{a} L u_* q_* \tag{4.48}$$

4.4.2 Momentum Flux

The flux of momentum between the atmosphere and ocean can be calculated through the bulk relation

$$|\tau| = \rho_a C_D |U_{10}|^2, \tag{4.49}$$

however, as is the case with heat fluxes, the transfer coefficient, C_D, varies with both wind speed and atmospheric stability. Thus momentum flux must also be calculated recursively, and is given (Zeng *et al.*, 1998) by

$$|\tau| = \rho_a |u_*|^2. \tag{4.50}$$

4.4.3 Moisture Flux

Moisture flux in the model is simply the difference between precipitation and evaporation ($P - E$). Precipitation is derived directly from ERA-40 as the sum of the large-scale (stratiform) and convective precipitation fields. Evaporation is not taken from ERA-40, but is derived by dividing the latent heat flux, which is calculated within the model, by the specific heat of vaporization of sea water.

4.4.4 Sea Ice

The model is coupled to a simple thermodynamic sea-ice model (Parkinson and Washington, 1979). FRUGAL is capable of simulating sea-ice dynamics, however the dynamic model did not work correctly with the high temporal resolution atmospheric forcing, and so was not turned on. Bigg *et al.* (2005) note that there are only minor differences in the FRUGAL model between thermodynamic only and thermodynamics + dynamics simulations. The sea-ice model alters the fluxes between the ocean, following Parkinson *et al.* (1987): where the sea-ice concentration is greater than 0.25, latent heat flux is set to 0 W m^{-2} and sensible heat flux is reduced to 10% of its calculated value. The sea-ice field was initialized early on in the model spin-up to a constant thickness of 1 m everywhere to the north and south of the Arctic and Antarctic circles respectively. The ice then melted to equilibrium during the rest of the model spinup.

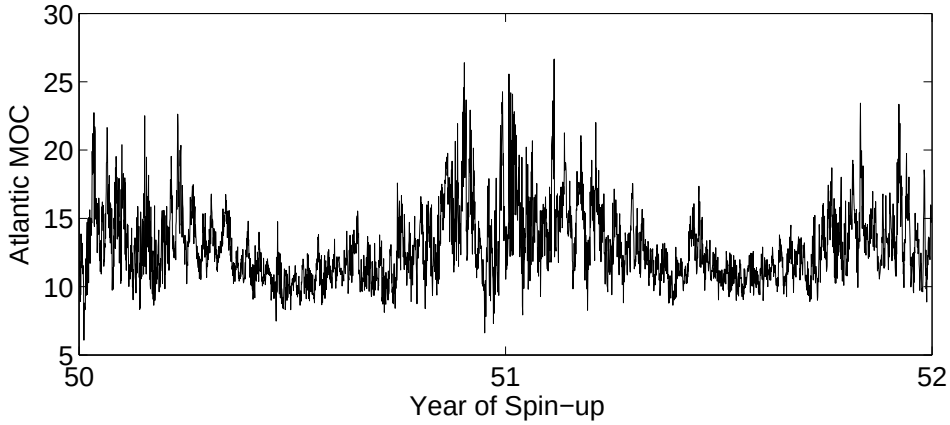

Figure 4.4: Atlantic meridional overturning circulation (AMOC) in the final two years of the spin-up, when the high-frequency ERA-40 fields were used to drive the model. The AMOC is shown every 6 hours.

(a)

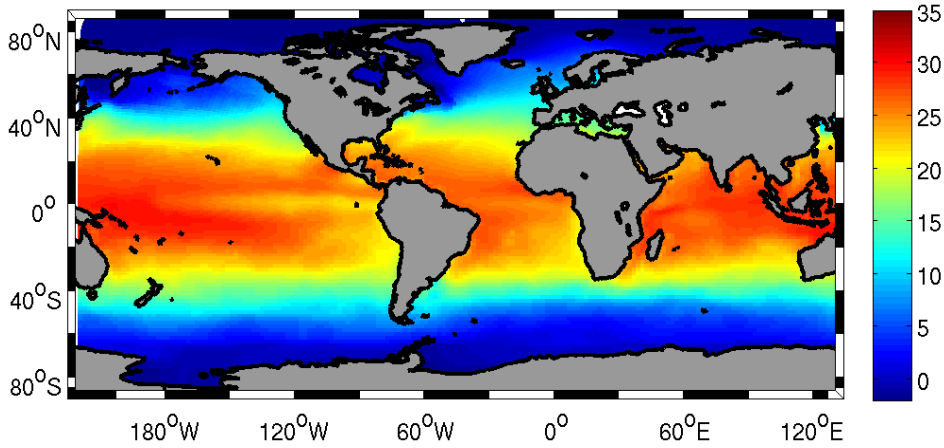

(b)

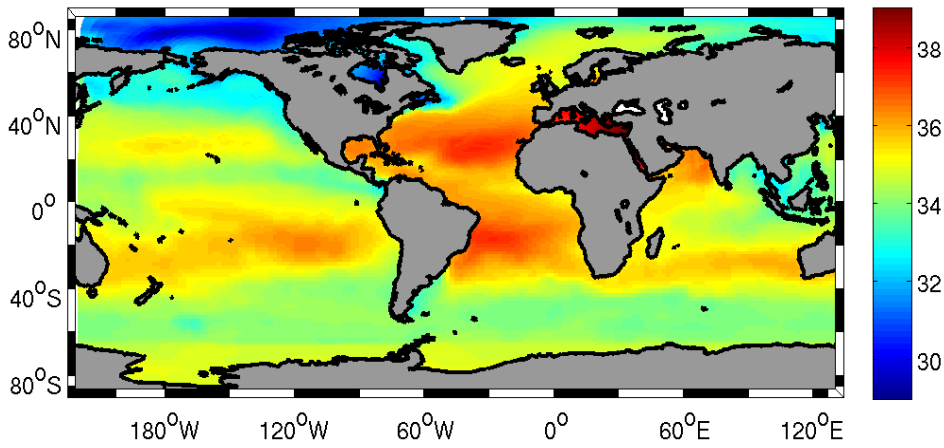

Figure 4.5: (a) Sea surface temperature (° C) and (b) sea surface salinity at the end of the spin up.

4.5 Initialising the model

4.5.1 Spin-up

The model is initialized to the temperature and salinity of Levitus and Boyer (1994). For the first year, temperature and salinity fields are robustly relaxed back to these climatologies with a timescale of 30 days on all model levels. Surface wind stress is derived from the climatology of Hellerman and Rosenstein (1983). For the next two years, the same robust relaxation occurred in the upper 1200 metres (9 levels) of the ocean, while below this the relaxation timescale was increased to 360 days. A further three years of the integration were then carried out with the relaxation to climatology confined to the surface of the ocean. During this time, the transports in the model are strongly constrained by the temperature and salinity climatologies, and so by the end of year 6 the meridional overturning has essentially stabilized. At the beginning of year 7 the wind forcing is changed to the ECMWF ERA-40 seasonal climatology, from which freshwater (precipitation−evaporation) and heat fluxes are also derived and applied to the surface of the model. To prevent model drift during the spin-up, the surface is continually restored to Levitus temperature and salinity on a timescale of 360 days. The ice model is initialised from the start of year 8, as described in Section 4.4.4. During the month following the initialisation of the sea ice model, the model timestep is decreased from 2700 s to 1350 s. From the start of year 9, the vertical mixing scheme of Pacanowski and Philander (1981) and the hyperbolic tangent taper method of Danabasoglu and Mc Williams (1995) are introduced. The model is then integrated for a further 50 years, allowing the circulation to approximately equilibrate to the ERA-40 forcing.

To complete the spin-up, the model was run for a further two years where forcing was provided by high-frequency winds, heat fluxes and moisture fluxes from the 6-hourly ERA-40 dataset, with the latent and sensible component of the heat fluxes calculated in-situ using the bulk formulae described earlier. Once the high-frequency forcing is applied, the Atlantic meridional overturning circulation becomes noisy, particularly in the winter as the north Atlantic region becomes increasingly stormy, ranging from 7–26 Sv, with a mean winter value of around 15 Sv (Figure 4.4). At the end of the spin-up period, the surface temperature and salinity fields still closely resemble the Levitus climatologies, due to the constant, slow relaxation back to these values (Figure 4.5). Once the spin up was

complete, all relaxation was turned off, and the temperature and salinity fields evolved only according to the fluxes applied to the ocean.

4.5.2 Control Run

At the end of the spinup, a control run for the numerical integration is created, integrating the model for 20 years with 6-hourly ECMWF ERA-40 forcing, between 1980 and 2000.

Chapter 5

Parameterizing Greenland's tip jets

5.1 Introduction

We have seen that small-scale, strong wind events such as westerly and easterly tip jets are not well captured in the relatively coarse resolution atmospheric reanalysis products which are used to set the boundary conditions of a wide array of ocean-only general circulation models. Wind speed is closely tied not only to the transfer of momentum between the atmosphere and ocean, but also to the transfer of latent and sensible heat. If the wind speed is underestimated, it is likely that these fluxes will also be underestimated, which, in areas of convective activity such as the Labrador and Irminger Seas, could have significant consequences for both the local hydrography and the global overturning circulation (Doyle and Shapiro, 1999; Pickart *et al.*, 2002; Våge *et al.*, 2008). In this chapter, we develop a parametrisation of easterly and westerly tip jets, which allows the fluxes of heat and momentum associated with these jets to be more accurately incorporated into the forcing fields of ocean-only general circulation models, or, with further work, coupled climate models at the coupling stage. This work has been accepted for publication in the *Journal of Geophysical Research (Oceans)*.

In the following two sections we describe the creation of a QuikSCAT-based data-set which is then used to develop a simplified spatial description of tip jets. In section 4 we describe how this can be introduced into an ocean or coupled model to improve the representation of tip jets. Section 5 discusses the improvements in the distributions of wind speeds around Greenland, Section 6 discusses a previous possible parametrisation and Section 7 describes the impact the increased extreme wind speeds have on the air/sea

fluxes over the Irminger and Labrador Seas. Finally, in Section 8 we use a 1-dimensional ocean mixed-layer model (Price *et al.*, 1989), used in previous studies of the impact of Greenland tip jets on the ocean (e.g. Våge *et al.* (2008) and Chapter 2), to provide an example of the impact that the parametrised tip jets have on the development of the winter mixed-layer in the Irminger Sea. Conclusions of the chapter are given in Section 9.

5.2 Data-sets

In order to create a data-set of tip jets for use in the development of the parametrisation, the archive of QuikSCAT passes from 1999 to 2007 was manually searched to identify passes in which a well-defined tip jet was present. QuikSCAT winds are available twice daily on a 0.25° grid (L3 gridded product), and are thus able to represent the strong wind speeds and spatial gradients associated with tip jets. If a tip jet was present in consecutive passes these were assumed to be the same jet, and only one of these passes was selected. The selected pass was that which occurred in the middle of the series. These remaining passes were then subjectively filtered to select only those which have a clear and distinctive tip jet, with little noise in the background wind field. The resulting data-set consists of 32 well-defined westerly and 42 well-defined easterly tip jets. The data-set spans all types of jet, from weak summer jets with peak winds less than 15 m s^{-1}, to robust winter jets with peak winds of over 35 m s^{-1}. Zonal extents range from approximately 100 km to over 1000 km.

Using this data-set, tip jets were isolated using a semi-objective method, whereby any point $\mathbf{p}$ on the QuikSCAT grid was considered to be part of the jet if $s_{\mathbf{p}} \geq \gamma s_{\max}$, where $s_{\max}$ is the maximum wind speed associated with the jet, $s_{\mathbf{p}}$ is the wind speed at $\mathbf{p}$, and $\gamma \in (0, 1)$ is a threshold value used to delineate the jet from the background wind field. Additionally, $\mathbf{p}$ must be connected to the point of maximum wind speed by other grid points with a wind speed greater than or equal to that at $\mathbf{p}$. This method is only semi-objective as, due to differing background wind fields, the value of γ had to be chosen for each case to successfully isolate the jet from the background field. The value of γ was chosen (subjectively) so that the edge of the jet was as close as possible to the point where the ECMWF analysis no longer substantially underestimated the wind speed in comparison with QuikSCAT. The value of γ over our data-set is fairly consistent,

Table 5.1: The maximum, minimum, mean and standard deviation of the r values of the linear fits to the decrease in wind speed along and across the jets, and the mean significance level of these fits.

	Max(r)	**Min(r)**	**Mean(r)**	**Std(r)**	**Mean(P)**
Westerly along-jet	0.96	0.56	0.86	0.10	99%
Easterly along-jet	0.95	0.16	0.79	0.17	97%
Westerly across-jet(N)	1.00	0.70	0.96	0.06	94%
Westerly across-jet(S)	1.00	0.75	0.96	0.05	96%
Easterly across-jet(N)	1.00	0.04	0.95	0.11	94%
Easterly across-jet(S)	1.00	0.15	0.95	0.12	94%

with a mean of 0.76 and standard deviation of 0.09. It is worth noting that although the subsequent parametrisation is dependent on this value of γ and on the cases in the data-set, the number of cases is large enough to ensure that case-to-case variability does not lead to biases in the parametrisation. This is discussed further later.

5.3 Spatial Description of a Tip Jet

5.3.1 Scaling the jets

Once the tip jets have been isolated from the background wind field, we study the spatial structure associated with the jets. In each case, the spatial evolution of wind speeds along the central axis of the jet and perpendicular to this axis at 25%, 50% and 75% of the distance along the central axis are extracted. Three examples of each of these are shown in Figure 5.1, with a linear least square fit overlaid. In these three cases the gradients both along and across the jet are approximately linear, with a strong correlation between wind speed and distance either along or across the jet. This pattern is seen generally in the 32 westerly and 42 easterly tip jet test cases. Over these test cases, the Pearson correlation coefficients between wind speed and distance along the jet axis both have means greater than 0.7, statistically significant above the 94% level (Table 5.1).

A total of 96 across-jet sections were taken from the 32 westerly tip jet test cases and 126 from the 42 easterly test cases. Again the decrease in wind speed can be well represented with simple linear gradients. There is, however, a small asymmetry between the gradients on the poleward and equator-ward sides of the jets (Figure 5.1d–f), and so these cases are treated separately. The Pearson correlation coefficients between wind speed

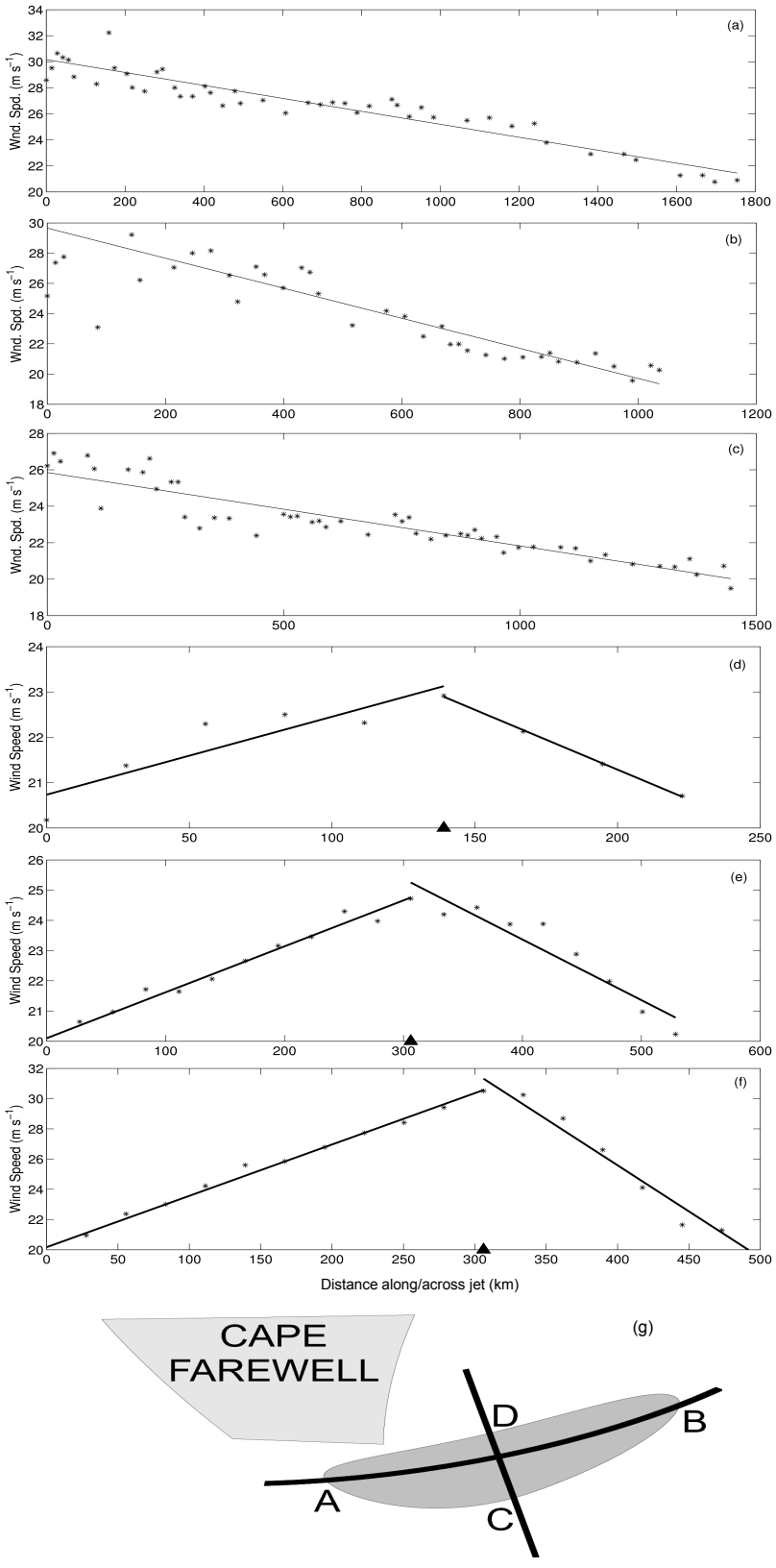

Figure 5.1: Examples of the decrease of wind speed from Cape Farewell along the centre of a tip-jet, line segment AB, (a–c) and across the jet at its mid-point, line segment CD, (d–f). In d–f the centre of the jet is highlighted with an arrowhead, to the left of this is the south flank of the jet and to the right is the north flank of the jet. The QuikSCAT winds are shown by the black stars, with a linear least squares fit overlaid. A cartoon showing where gradients were taken from is given in (g). (a)–(f) are on 18/02/2003, 03/02/2005, 16/01/2002, 10/01/2000, 09/04/2002 and 09/04/2002, respectively.

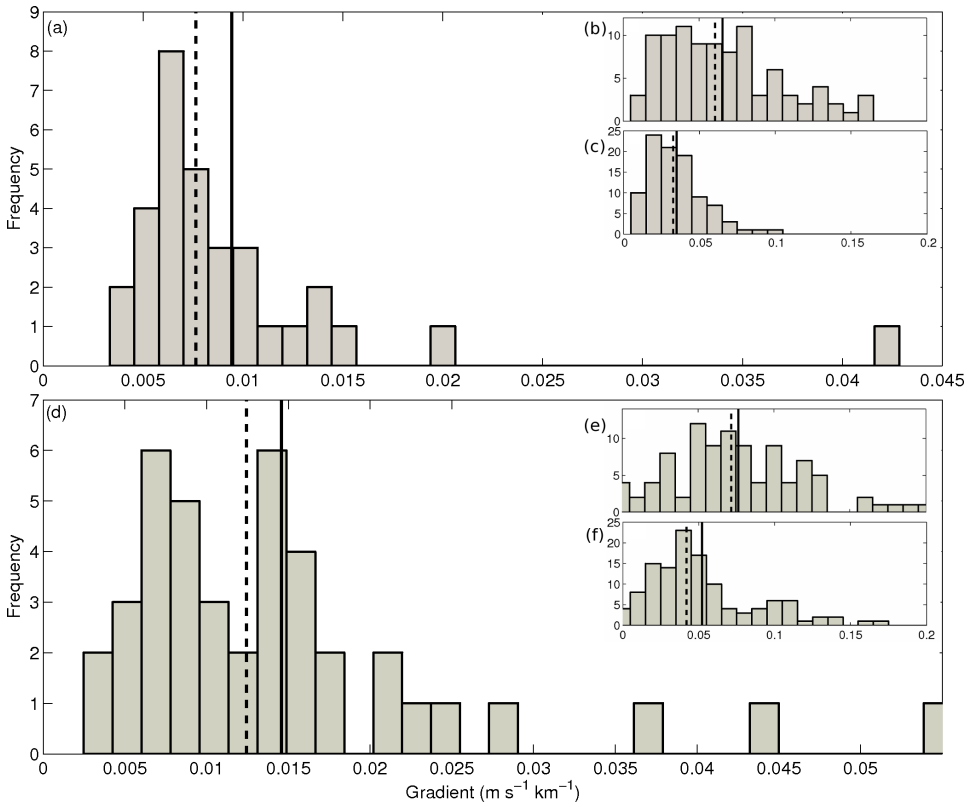

Figure 5.2: Distribution of wind speed gradients for the westerly (a–c) and easterly (d–f) tip jets from our QuikSCAT dataset, as illustrated in Figure 2. (a) Along the centre of the westerly jet; (b) Across the north flank of the westerly jet; (c) Across the south flank of the westerly jet; d) Along the centre of the easterly jet; (e) Across the north flank of the easterly jet; (f) Across the south flank of the easterly jet. Solid and dashed lines show the mean and median respectively.

and distance from the jet axes have mean values greater then 0.95, statistically significant above the 94% level (Table 5.1). Therefore, we can, to a reasonable approximation, describe the spatial structure of both the westerly and easterly tip jets by a linear decrease in wind speed along and across the core axis of the jet from an assumed maximum wind speed. Determining the maximum wind speed will be discussed shortly.

While the gradients along and across the jet are in general approximately linear, there are differences in these linear gradients from jet to jet. The range of these gradients along the jet and to the north/south of the jet for both the westerly and easterly jets is shown in Figure 5.2. These gradients may be thought of as free or 'tunable' variables for the parametrisation, dependent on the metric used to describe the error in the parametrisation. The approach we take here is to choose gradients which produce the best composite jet over all of our test cases while still maintaining an accurate characterisation of individual jets. The best composites are found by searching over $0.002 \leq g_l \leq 0.031$, $0.001 \leq$

$g_n, g_s \leq 0.21$, where g_l is the along-jet gradient and g_n and g_s are the north and south across-jet gradients, respectively (all m s^{-1} km^{-1}), and finding those where the 10, 15 and 20 m s^{-1} isotachs most closely mirror those of the QuikSCAT composite. The gradients chosen are 0.014 m s^{-1} km $^{-1}$ along the jet and 0.08 m s^{-1} km $^{-1}$ and 0.05 m s^{-1} km $^{-1}$ to the north and south of the jet respectively in the case of the westerly tip jet, and 0.016 m s^{-1} km $^{-1}$ along the jet and 0.08 m s^{-1} km $^{-1}$ and 0.05 m s^{-1} km $^{-1}$ to the north and south of the jet respectively in the case of the easterly tip jet. These are generally slightly higher than the mean and median observed gradients (See Figure 5.2), but are very close to these values and well within the range of gradients determined.

5.3.2 Placing the jets

One of the challenges of parameterizing the Greenland tip jet is the variation in character; no two tip jets are ever exactly the same in size, orientation or maximum wind speed. We thus need a robust technique for placing and scaling each jet based on the large-scale synoptic situation, which is in general skillfully reproduced in the atmospheric (re)analyses.

Both the westerly and easterly jets, to a good approximation, originate at the tip of Cape Farewell (Moore and Renfrew, 2005). The tip of Cape Farewell can thus be considered to be the start of the jets regardless of the synoptic situation. The jet then evolves downstream in approximate accordance with the surface wind field although, due to the surface drag re-orienting the surface wind vectors towards the parent low pressure centre, this is not exact – rather the wind vectors are oriented to the left of the axis of the jet (Figure 1).

Våge *et al.* (2009a) noted that, in a climatological sense, the westerly jet is a surface extension of the upper-level jet-stream, which thus acts partly to steer the jet. The upper level jet is high enough to be almost completely unaffected by drag imposed at the surface and is thus very well approximated by the geostrophic relationship $\mathbf{v_g} = \frac{\hat{\mathbf{k}}}{f} \times \nabla_p \Phi$, where $\mathbf{v}_g$ is the horizontal geostrophic velocity, f is the Coriolis parameter, Φ is the geopotential and $\hat{\mathbf{k}}$ is a unit vector in the vertical. Consequently, it may be expected that the path of the westerly jet axis may be better related to the mean sea-level geostrophic wind than the 10-metre wind, and this is indeed seen to be the case. Figure 5.3(a) shows a path generated using the 10-metre geostrophic wind which closely matches the path of a westerly tip

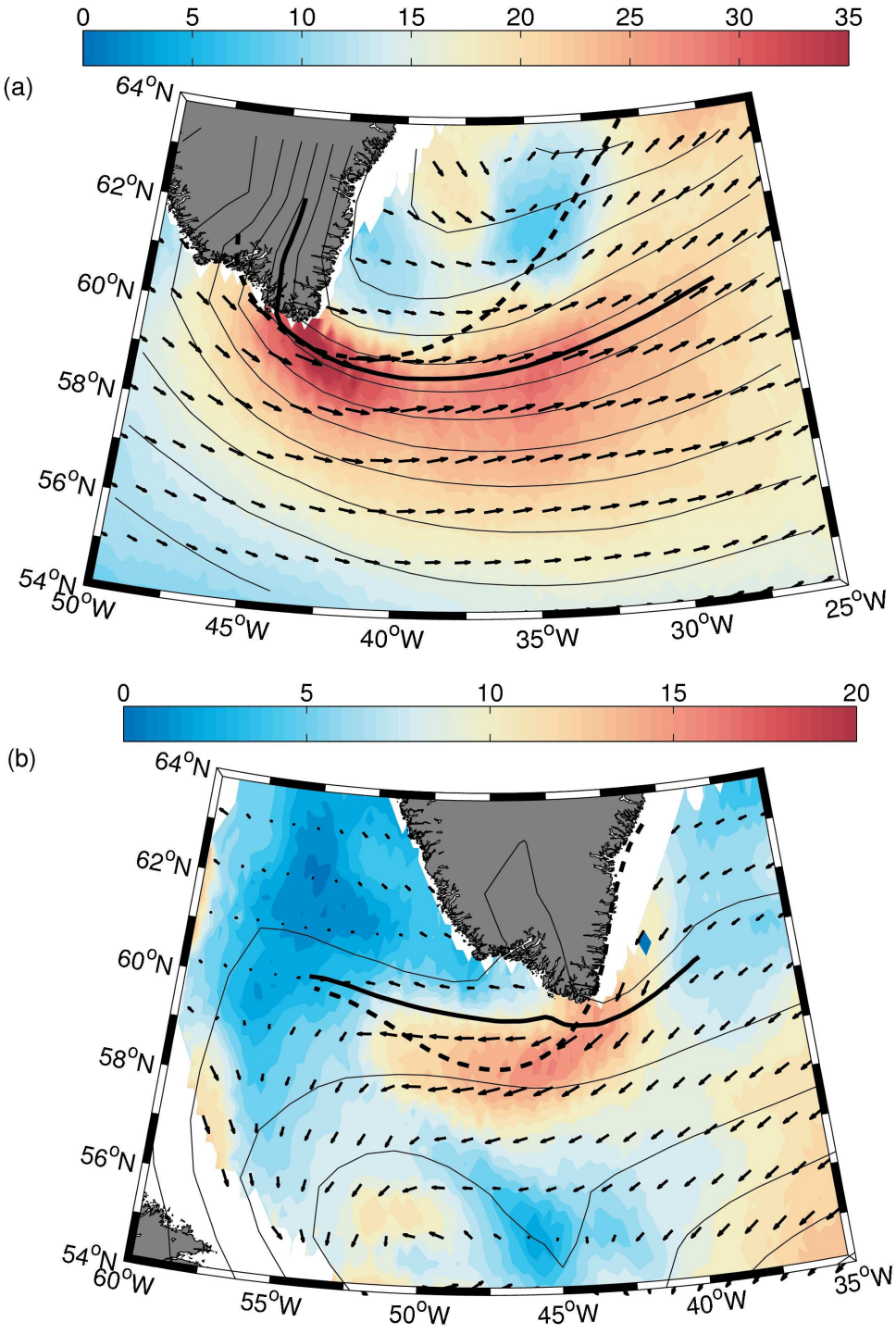

Figure 5.3: QuikSCAT wind speeds (shaded, m s^{-1}) and vectors (every 1 degree) showing typical (a) westerly (01/10/2000) and (b) easterly (18/04/2000) tip jets. Mean sea-level pressure from ECMWF is contoured every 4 hPa. The overlaid lines show the paths where the core of parametrised tip jets would be placed using the geostrophic (solid) or 10 metre (dashed) winds as a guide.

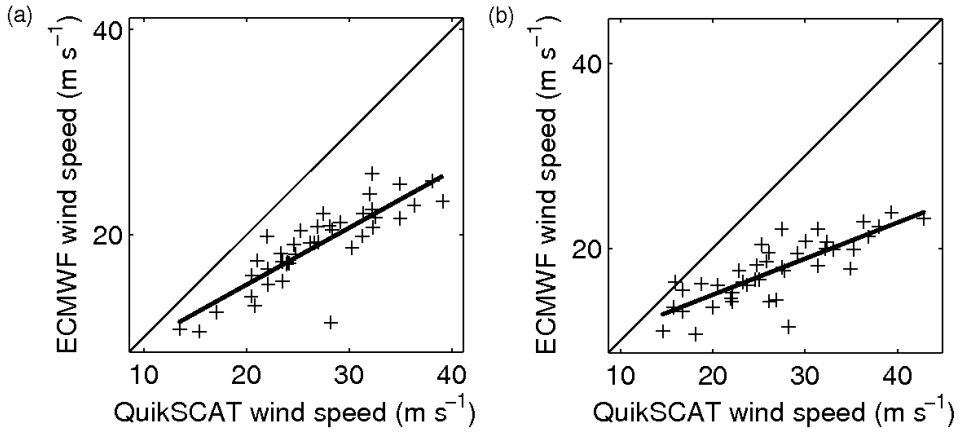

Figure 5.4: Scatter plots showing the relationship between the maximum wind speed in QuikSCAT and in ECMWF in the area (a) 56–60 °N, 36–44 °W, and (b) 56–62 °N, 40–54 °W, where westerly and easterly tip-jets respectively occur most commonly. A linear least squares fit is overlaid in each case.

jet observed by QuikSCAT. We therefore use the mean sea-level geostrophic wind in the parametrisation to determine the path for the westerly tip jet.

In general, easterly tip jets evolve from barrier flows along the south-east coast of Greenland (Moore, 2003; Moore and Renfrew, 2005; Outten *et al.*, 2009). Such flows have a strong ageostrophic component (i.e. the vector difference between the true wind and the geostrophic wind) and thus a path cannot be created using the geostrophic winds. Instead we must resort to using the 10 metre wind field to create a path for the jet. The easterly tip jet can thus be oriented slightly too far to the south, however this is to a much lesser degree than the westerly tip jet would be displaced to the north were the 10 metre wind field to be used to generate its path. Figure 5.3(b) shows a path generated using the 10-metre wind which closely matches the path of a easterly tip jet observed by QuikSCAT.

5.3.3 Peak wind speed

Here we use the ECMWF operational data-set, at ECMWF ERA-40 resolution, henceforth ECMWF, as a 'proxy' for the ECMWF ERA-40 reanalysis (henceforth ERA-40), which has too little temporal overlap with QuikSCAT. The ERA-40 reanalysis is of relatively high resolution (T159 $\sim 1.125°$) for a global reanalysis, and performs well in comparison to the NCEP/NCAR reanalysis in the sub-polar regions (Renfrew *et al.*, 2002, 2009). The

ERA-40 reanalysis does contain a representation of the Greenland tip jet, albeit one that is spatially too smooth and significantly too weak in magnitude (Våge *et al.*, 2009a). A comparison of the maximum wind speed in ECMWF with that in QuikSCAT for our 32 westerly test cases, over the area 56–60 °N, 36–44 °W, where tip jets are most likely to be observed (Moore and Renfrew, 2005), reveals that ECMWF underestimates the peak wind in a very linear fashion (Figure 5.4). Thus a least-squares linear fit provides a simple model to estimate the maximum wind speed in a westerly tip jet from the corresponding wind field in ECMWF:

$$S_{\text{tipjet}} = \frac{S_{\text{ECMWF}} - 6.241}{0.493}, \tag{5.1}$$

where S_{tipjet} is the maximum wind speed in the tip jet parametrisation, and S_{ECMWF} the maximum wind speed in ECMWF.

Note that there is some evidence, e.g. Ebuchi *et al.* (2002) that QuikSCAT winds may be biased high, particularly at high wind speeds, although this possible bias is not quantified. If the QuikSCAT product were biased high at all wind speeds, then this would present a potentially serious problem for our tip jet parameterisation. Note, however, that this doesn't seem to be the case. Ebuchi *et al.* (2002), while mentioning that they observed a few data points which seemed biased high at very high wind speeds, noted that there was no significant bias in the satellite retrieved winds at wind speeds of up to 20 m/s were observed. A similar result was reported by Bourassa *et al.* (2003), who reported no wind speed bias in their data set, which covered wind speeds from 0-20 m/s.

In the comparison of QuikSCAT data with GFDex data in Chapter 3, there also appeared to be a positive bias in the QuikSCAT winds, evidenced by the value of the regression slope being greater than 1. However, it should be noted that this is only a relatively small data set, and furthermore that the periods where QuikSCAT was over-estimating the wind speed were not necessarily the periods of highest wind speed. For example during the first period of B268, where wind speeds were between 20 and 25 m/s, QuikSCAT was underestimating slightly, as it was for most of B276, when wind speeds were between 15 and 20 m/s. However, during the first half of B271, QuikSCAT suggested winds of over 10 m/s, when those recorded were only 5 m/s.

It should come as no surprise that QuikSCAT wind retrievals become less accurate

at high wind speeds, while exhibiting little or no bias at lower winds speeds. In order to calculate the wind speed from a radar backscatter signal, a geophysical model function is used to relate the backscatter to the distribution of centimetre-scale capillary waves on the surface of the ocean, and then relate these to wind stress and finally wind speed. As wind speeds increase, the ocean surface become increasingly covered with whitecaps formed from wave breaking, and the atmospheric surface layer becomes filled with sea-spray. As the model function is generally formulated for relatively moderate conditions, it is not surprising that it becomes less accurate as the ocean surface becomes increasingly broken up (e.g. Quilfen *et al.*, 2007).

The data on which we have based the wind speed part of this parameterisation (Figure 5.4) does not show any obvious bias (i.e. deviation from a linear underestimation of wind speed in ECMWF) at higher wind speeds, and indeed removing, for example, the five highest wind speeds points, has only a minor effect on the slope of the regression line in both the westerly and easterly tip jet cases. To further reduce the chances of the parameterisation significantly overestimating the true wind speed associated with tip jet, we limit the maximum wind speed introduced by the parameterisation to 35 m/s (corresponding to ECMWF wind speeds of around 24 m/s for the westerly tip jet and 21 m/s for the easterly tip jet). Wind speeds of 35 m/s have been seen at the surface in high resolution mesoscale simulations of the Greenland tip jet (Doyle and Shapiro, 1999; Hay *et al.*, 2009; Outten *et al.*, 2009) and observed near the surface (Renfrew *et al.*, 2009). This gives us, for the westerly jet, the relationship

$$S_{\text{tipjet}} = \begin{cases} \frac{S_{\text{ECMWF}} - 6.241}{0.493} & \text{if } S_{\text{ECMWF}} < 23.496, \\ 35 & \text{otherwise.} \end{cases} \tag{5.2}$$

Proceeding similarly, the maximum speed in an easterly tip jet may be given by the relationship

$$S_{\text{tipjet}} = \begin{cases} \frac{S_{\text{ECMWF}} - 7.159}{0.391} & \text{if } S_{\text{ECMWF}} < 20.84, \\ 35 & \text{otherwise,} \end{cases} \tag{5.3}$$

over the area given by 56–62 °N, 40–54 °N. Note that it is still possible that the parameterisation over estimates the wind speed slightly, but we believe we have minimised

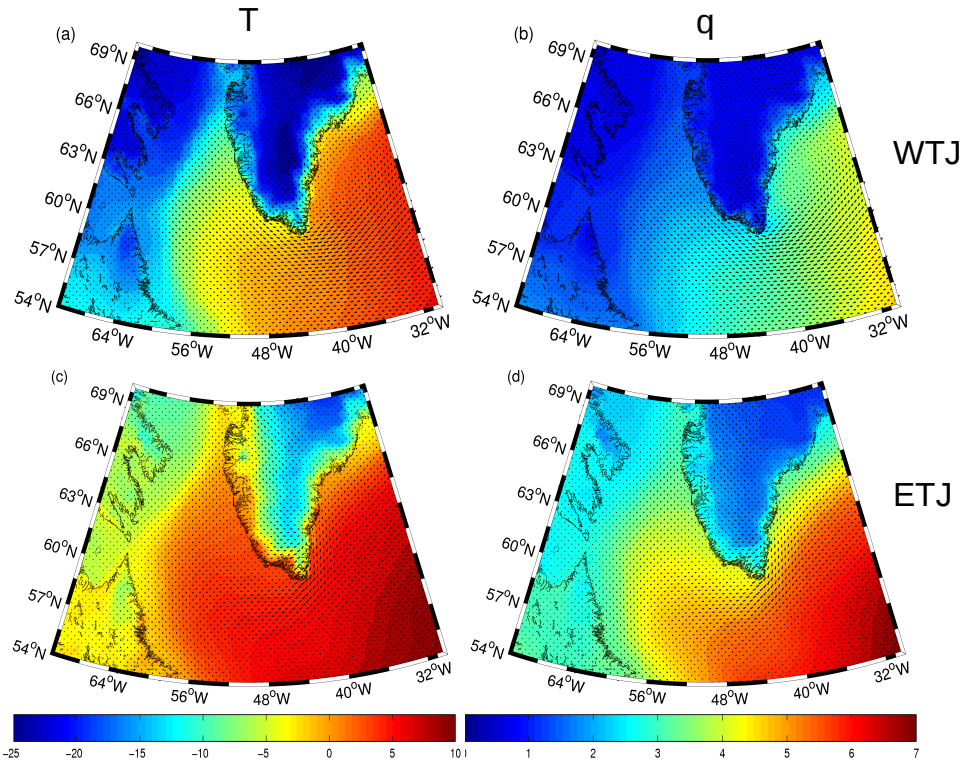

Figure 5.5: Composites of 2 metre Temperature (a,c, °C) and specific humidity (b,d, g kg^{-1}) for all of the 32 westerly (a–b) and 42 easterly (c–d) tip jet cases used in this study, from the North American Regional Analysis (NARR).

this error as much as possible given the limitations which are inherent in any QuikSCAT, which remains the best dataset for high frequency observations of the global surface wind field.

5.3.4 Temperature and Humidity

Although the wind speed is an important factor in setting the strength of air-sea heat and momentum exchange, both the vertical gradients of humidity and temperature also play important roles. Figure 5.5 shows composites of 2 metre temperature and specific humidity for the 32 westerly tip jets (a–b) and 42 easterly tip jets (c–d) on which the parametrisation is based. The composites are from the North American Regional Reanalysis (NARR) data-set (Mesinger *et al.*, 2006), which has a 32 km horizontal resolution. In the westerly case, the area around Cape Farewell is relatively cold and dry, with average temperatures of around 0 °C and specific humidities of around 2.5 g kg^{-1}. However these values are simply due to the prevailing synoptic conditions; there are no mesoscale features evident in Figure 5.5. Any such mesoscale features should be resolved in the relatively high resolution NARR data-set (Renfrew *et al.*, 2009), however they would be sub-grid scale and

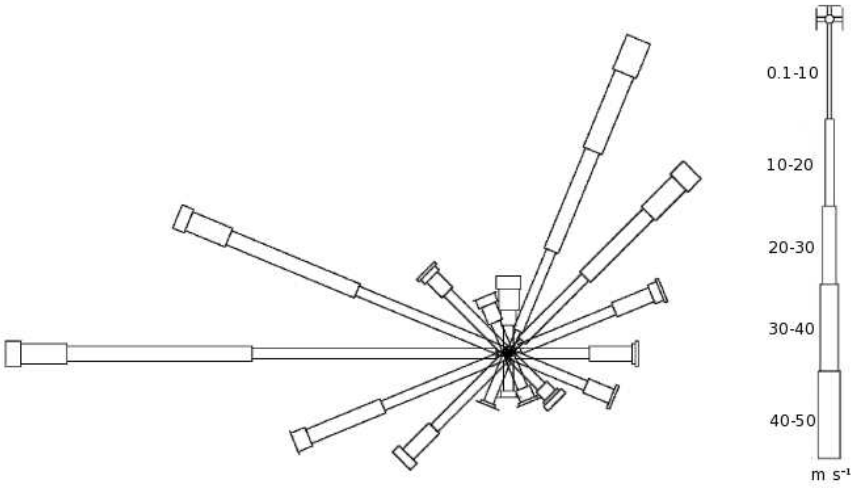

Figure 5.6: A wind-rose showing the direction and intensity of winds at Cape Farewell (DJF, 1999–2004), adapted from Moore and Renfrew (2005). Winds are binned into 22.5° and 10 m s^{-1} intervals.

therefore would not be consistently represented in the ECMWF (re)analysis. Similarly, for the easterly tip jet (Figure 5.5c–d), although humidities and temperatures are generally higher than in the westerly case, no mesoscale features are apparent.

5.4 The Bogussing Technique

The first consideration is *when* the parametrisation should be called to place a tip jet into the wind field. There are fairly well-defined synoptic conditions that are observed to give rise to tip jets (Moore and Renfrew, 2005). For example, both phenomena are tied to parent cyclones, between Greenland and Iceland in the case of the westerly tip jet and to the south of Greenland in the case of the easterly tip jet. However, while these large-scale situations may be necessary for the jets to exist, they are by no means sufficient and it would be very difficult to derive a robust method for calling the parametrisation based on large-scale features in the mean sea-level pressure field. During their construction of a QuikSCAT climatology of tip jets, Moore and Renfrew (2005) noted that the directions of strong winds around Cape Farewell were largely bimodal, with the vast majority coming from the west or north-east (Figure 5.6). These strong winds are closely associated with the (westerly and easterly, respectively) tip jets. We therefore assume that any strong wind from the west is associated with a westerly tip jet and any strong wind from the north-east

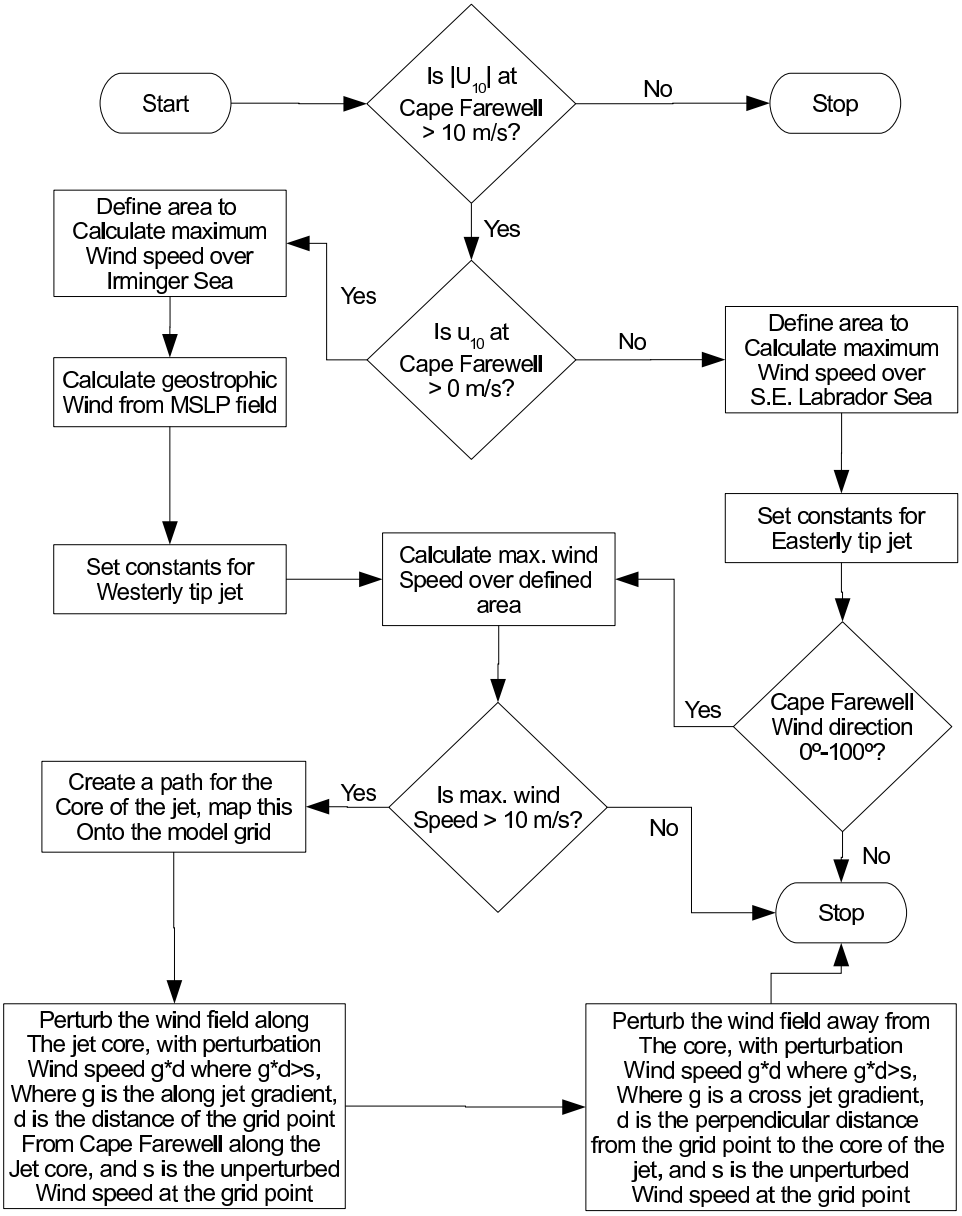

Figure 5.7: A flowchart describing the basic steps involved in inserting easterly and westerly tip jets into the wind field of an ocean model.

or east is associated with an easterly tip jet.

As illustrated via a flowchart in Figure 5.7, the algorithm proceeds as follows: firstly, the 10 m wind speed (u_{10}) immediately to the south of Cape Farewell is calculated. If this is found to be less than 10 m s^{-1} (the approximate wind speed at which Equations 5.2 and 5.3 start to cause an increase in the wind speed) then it is assumed that no tip jet is present and the parametrisation routine stops. If the wind speed is greater than 10 m s^{-1} then, depending on the sign of u_{10} at Cape Farewell, a maximum perturbation wind speed is calculated for the westerly or easterly tip jet (Equation 5.2 or 5.3). If this is found to be

less than 10 m s^{-1} then again the routine stops. In the case of the easterly tip jet, a final check is carried out, ensuring that the parametrisation is only called if the wind direction immediately to the south of Cape Farewell is between 0° and 100°. This prevents invoking the parametrisation in the case of any barrier type enhancement on the south-west coast of Greenland.

Figure 5.8 shows, in schematic form, how the tip jet parametrisation is implemented. Once it has been established that the parametrisation needs to be invoked, the u_g and v_g components of the geostrophic wind (in the case of the westerly tip jet) are calculated from the mean sea-level pressure field, which must be included as part of the atmospheric forcing data-set. A point particle is then initialised just off the coast of Cape Farewell, at the climatological wind speed maximum of Moore and Renfrew (2005). This maximum is around 15 m s^{-1} in the DJF mean, however it is its presence rather than its magnitude which is important here. This particle is then advected into Greenland by $-(u_g, v_g)$ for the westerly tip jet, or by $-(u_{10}, v_{10})$ for the easterly tip jet and away from Greenland by (u_g, v_g) for the westerly tip jet, or by (u_{10}, v_{10}) for the easterly tip jet, thus creating a path for the core of the tip jet. The exact length of this path will be dependent on the strength of (u_g, v_g) or (u_{10}, v_{10}), however it is advected for long enough to exceed the extent of the tip jet for that wind speed (recall that this is linearly dependent on the maximum wind speed in the jet). This path, which is generated on the rational plane, is then mapped onto the model grid using a simple nearest neighbour technique. Once the path is on the model grid, the wind speed at the point nearest the climatological maximum wind speed is perturbed according to Equation 5.2 or 5.3 as appropriate, and then the wind speed at each subsequent grid point along the path is perturbed by a slightly lesser amount, according to the model along-jet gradient described earlier. This process ceases once the perturbation to the next grid point in the sequence would result in a wind speed value less than that of the background wind field. Once this is complete, we have a representation of the core of the jet bogussed into the wind field, and all that remains is to 'flesh out' the jet. In order to achieve this, all of the grid points in a domain covering the Irminger and Labrador Seas are mapped onto the core of the jet, with the mapping simply defined by minimising the distance between each grid point and the core of the jet (Figure 5.9). This mapping ensures that the line connecting each point in the domain to that in the

Figure 5.8: A schematic showing how tip jets are bogussed into the wind speed field. (a) A point is advected from near Cape Farewell by the geostrophic winds calculated from the mean sea-level pressure field, thereby creating a path for the tip jet; (b) This path is then discretized onto the ocean model grid; (c) The wind field along the path is perturbed, starting from the maximum wind speed calculated via Equation 5.2 and decreasing linearly until this speed would be less than the background wind field; (d) Grid points 'suitably' near the path are mapped onto it in as perpendicular a fashion as is possible; (e) Points away from the central path are perturbed by a factor inversely proportional to their distance from it, as long as this results in a wind speed increase, otherwise they are left unperturbed (crosses); (f) The bogussed tip jet.

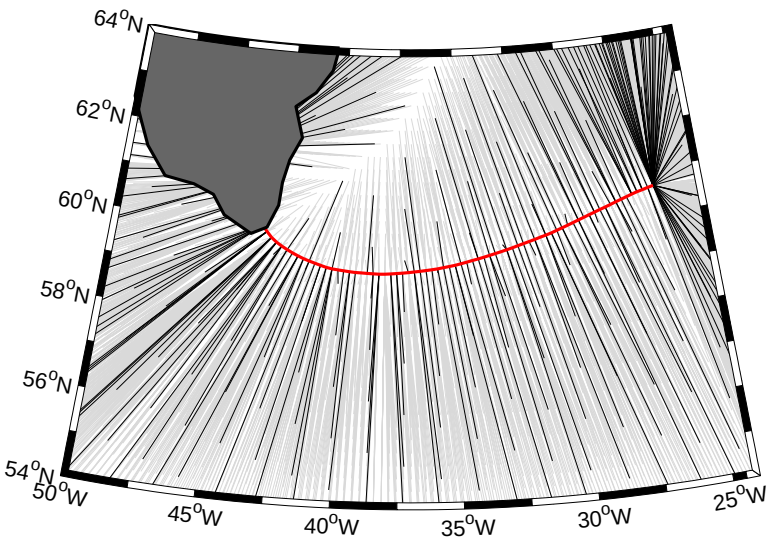

Figure 5.9: Mapping from each point in the domain onto the jet core in the most perpendicular fashion possible. For clarity, most of the mappings are shaded out.

image is as perpendicular as possible, given the discrete nature of the model grid. Each of these grid points is then adjusted to the strength of the wind at the point on the jet core onto which it is mapped, multiplied by the distance between these two points and the appropriate across-jet gradient, if and only if the resulting speed is stronger than the unperturbed wind speed at that grid point.

In Figure 5.10 a practical example of the parametrisation scheme 'in action' is given. In the unperturbed ECMWF wind speed field there is a representation of the jet, however the very strong winds in the core of the jet are not represented and the peak wind speeds are only around 20 m s^{-1} (Figure 5.10a). Figure 5.10b shows the wind speed field with just the core of the jet, which lies approximately along a line of constant mean sea-level pressure, perturbed. Figure 5.10c shows the complete parametrised jet; peak wind speeds in the core of the jet are now up to around 28 m s^{-1} and there is a relatively large area with wind speeds greater than 20 m s^{-1}. Note that the increased spatial gradients will also lead to an increase in wind stress curl on the flanks of the jet. Figure 5.10d shows the corresponding tip jet from the nearest QuikSCAT pass to this time. The location of the parametrised jet is not perfect when compared with QuikSCAT, however the spatial extent and the maximum in wind speed are very well reproduced. Note that while the core winds of the parametrised tip jet shown in Figure 5.10 are misplaced slightly to the south of the

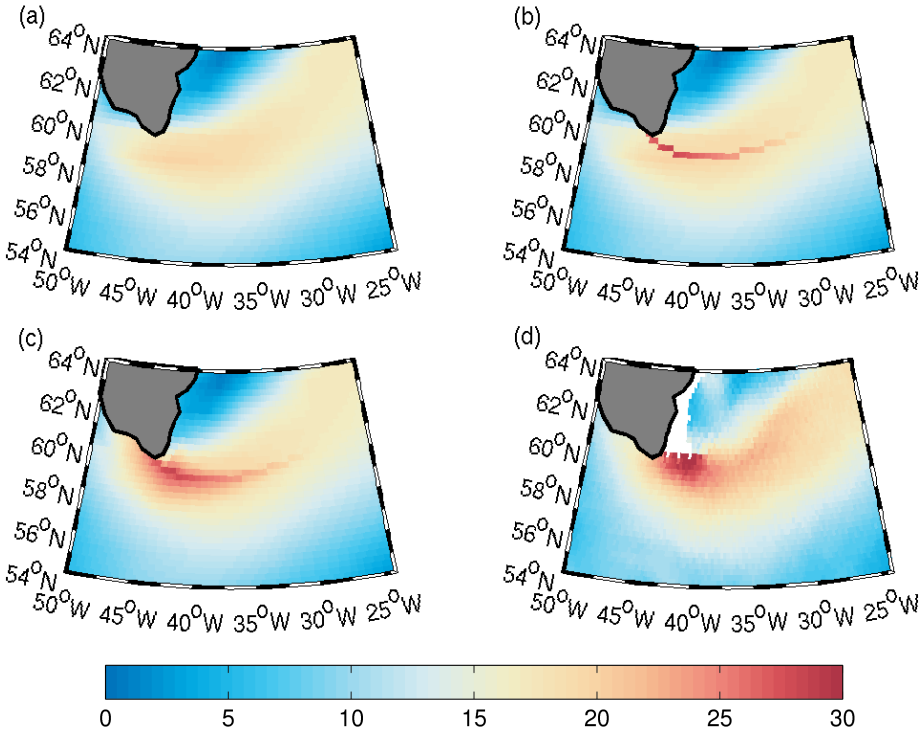

Figure 5.10: A practical example of the tip-jet bogussing algorithm on 09/04/2002. (a) The ECMWF wind speed field around Cape Farewell, interpolated onto a $\frac{1}{4}^{\circ}$ resolution grid. (b) The core of the jet laid out on the $\frac{1}{4}^{\circ}$ grid (c) The bogussed tip-jet; (d) The corresponding tip-jet from the nearest QuikSCAT pass.

jet seen in QuikSCAT, this error is not a systematic feature of the parametrisation scheme in the case of the westerly jet. Interpolating the ECMWF and ECMWF+TJ winds (Figure 5.10a and c) onto the QuikSCAT grid (Figure 5.10d) and then summing over all of the grid-points where QuikSCAT data are non-NaN provides a method of quantifying the improvement in the wind field around Cape Farewell. This summation over the QuikSCAT data yields a value of 50127 m s^{-1}, while over the ECMWF data it yields only 36534 m s^{-1}. The perturbed wind field, ECMWF+TJ, sums to 46879 m s^{-1}, significantly closer to the QuikSCAT value than to the ECMWF value.

Figure 5.11 shows composites of the entire data sets used to develop the westerly tip jet (32 cases) and the easterly tip jet (42 cases) parametrisations: for the ECMWF data, ECMWF with the parametrisation and QuikSCAT. The composites here are relevant as the impact of a single tip jet on the ocean is likely to be small, but the integrated effect of tip jets over an entire winter may be climatologically important, for example in forcing convection in the Irminger Sea. In the westerly tip jet case, the composite parametrisation is very well co-located with the composite QuikSCAT jet and compares very well in terms

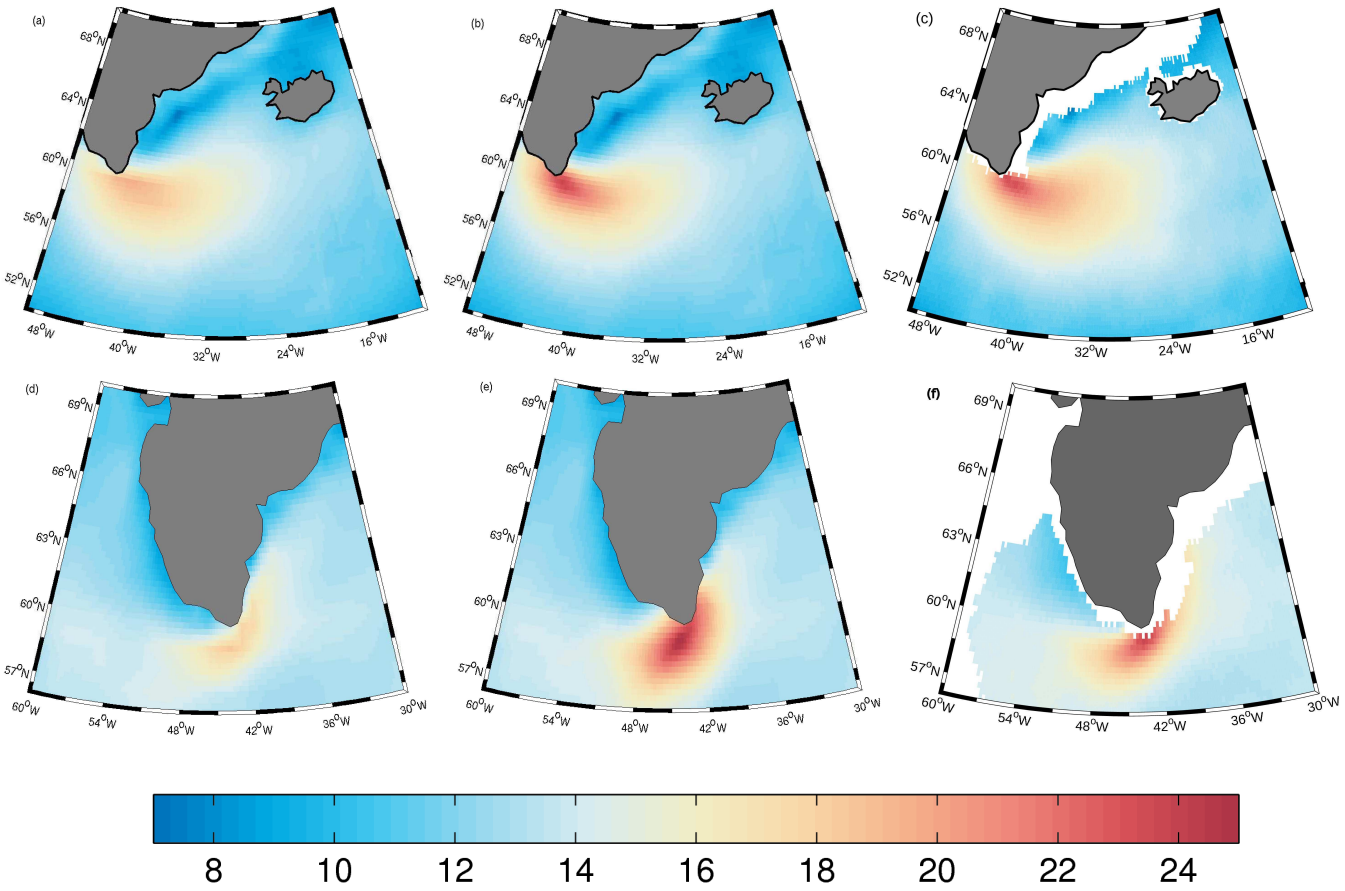

Figure 5.11: A composite of wind speed (coloured, m s^{-1}) during the Greenland westerly tip jet (a–c) and easterly tip jet (d–f) for all of the cases used in the current study for ECMWF (a,d), ECMWF with parametrisation (b,e) and QuikSCAT (c,f). White areas show where no QuikSCAT data were available due to the presence of sea-ice or consistent heavy rainfall.

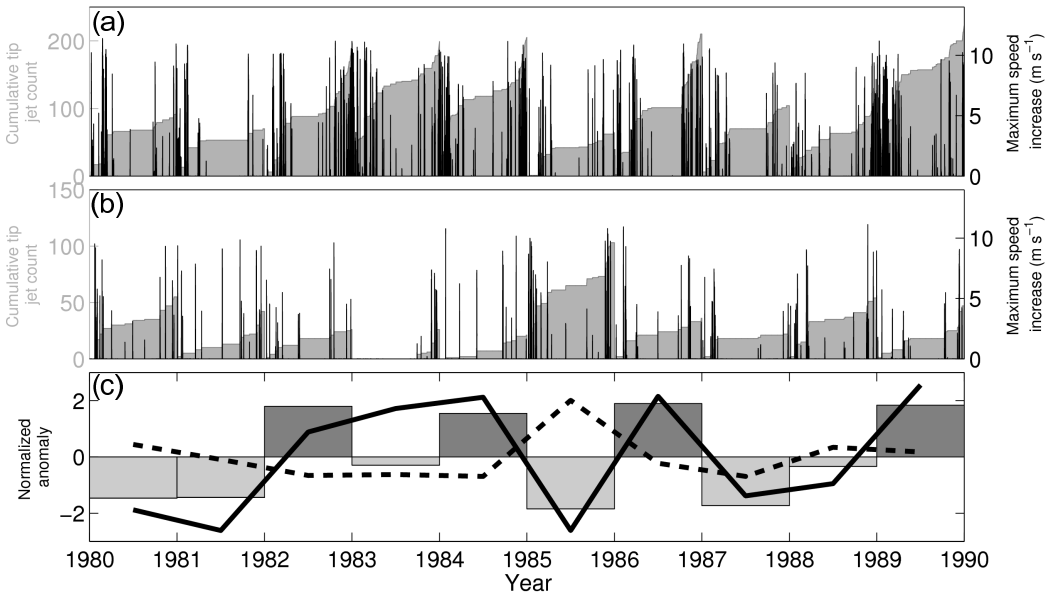

Figure 5.12: A representation of the tip jet parametrisation between 1980 and 1990. The light grey shading shows the cumulative tip jet count for each year, and the black lines show the maximum wind speed difference between the parametrisation and control for each tip jet. The top panel shows westerly tip jets and the middle panel easterly tip jets. The bottom panel shows the NAO index (bars), calculated from ERA-40, together with a normalised tip jet occurrence anomaly for westerly tip jets (solid line) and easterly tip jets (dotted line).

of wind speed magnitude. The easterly tip jet composite compares well in terms of wind speed magnitude, however it is not perfectly co-located with the easterly jet in QuikSCAT, but has a slightly stronger meridional component. It is possible that this slight error could be minimised with the use of some nudging, however the methodology of such a technique is likely to be dependent on the nature of the model grid. As this is intended as a generic concept paper, we do not include such a technique. Figure 5.11 illustrates that, on average, the westerly and easterly tip jet parametrisations work well and are very realistic compared to satellite-derived winds.

The number of occurrences of the westerly and easterly tip jet parametrisation in the ERA-40 from 1980 to 1990, are related to the North Atlantic Oscillation, calculated from the mean sea-level pressure difference between the Icelandic Low and the Azores High in the ERA-40 mean sea-level pressure (Figure 5.12). The relative occurrences of the tip jets are shown as normalised anomalies compared with the 1980–1990 mean. The occurrence of the westerly tip jet is very well reproduced, with nearly all of the tip jets occurring in the winter, and a strong correlation between the number of tip jets in a year and the sign of the

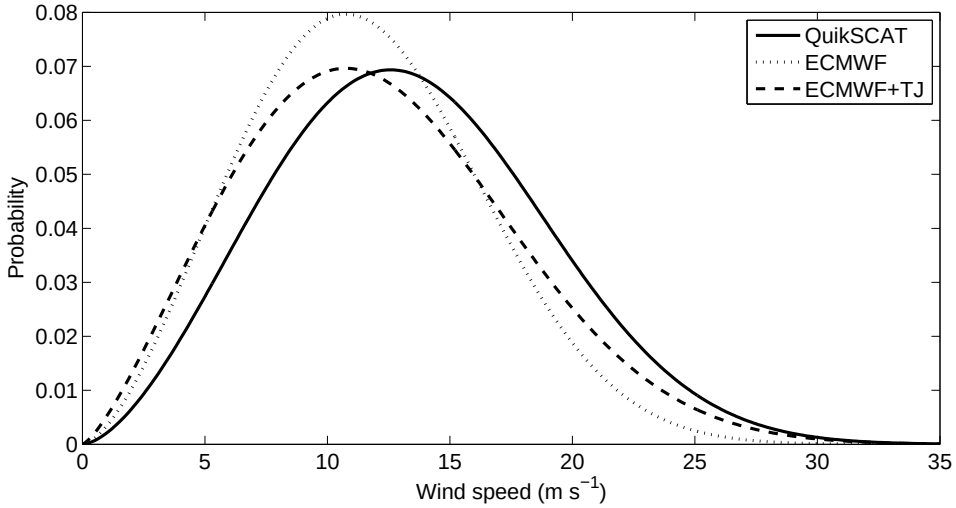

Figure 5.13: Weibull distributions of wind speed in the box given by 55–65 °N, 20–45 °W for QuikSCAT, ECMWF and ECMWF with tip jet parametrisation over the 32 test cases.

NAO, in agreement with previous studies of the Greenland tip jet (Moore, 2003; Moore and Renfrew, 2005; Bakalian *et al.*, 2007; Våge *et al.*, 2009a). The number of tip jets parametrised is slightly larger than the number calculated by Moore (2003) who observed tip jets occurring between 5% and 14% of the time, depending on the winter. The easterly tip jet is slightly under represented compared to the climatology of Moore (2003), who saw the easterly tip jet occurring between 6% and 12% of the time during the winter, depending on the phase and strength of the NAO. The difference is largely because we are considering a tip jet to occur whenever the parametrisation is called, whereas Moore (2003) only considered events with wind speeds greater than gale force (17 m s^{-1}). In cases where the wind is less than gale force, the parametrisation is called, but will result in only small perturbations to the ERA-40 wind field. Counting a tip jet to occur every time the wind field is perturbed over this period, approximately 3000 westerly and 2000 easterly tip jets are seen to occur, corresponding to 750 and 500 tip jet days respectively.

5.5 Wind Speed Distributions

A successful method of describing the distribution of the winds over the ocean is to use a two-parameter Weibull model (Pavia and O'Brien, 1986). The Weibull distribution for a random variable V, with parameters A and C, is given by

Table 5.2: Wind speed statistics in the box given by 55–65 °N, 20–45 °W for QuikSCAT, ECMWF and ECMWF with tip jet parametrisation over the 32 test cases. All values have units of m s^{-1} other than the Weibull shape parameter, C, which is dimensionless.

	ECMWF	**ECMWF+TJ**	**QuikSCAT**
Mean	11.55	12.14	13.42
Max.	25.95	35.00	42.31
Min.	0.22	0.22	1.00
S.dev.	4.8	5.5	5.47
A	13.00	13.71	15.12
C	2.58	2.32	2.62

$$f\left(V;A,C\right)=\left[\left(\frac{C}{A}\right)\left(\frac{V}{A}\right)^{C-1}\right]e^{\left(\frac{V}{A}\right)^{C}}, \tag{5.4}$$

where A (m s^{-1}) is a scaling parameter and C is a dimensionless shape parameter. Figure 5.13 shows Weibull distributions and illustrates that both the ECMWF wind speed distribution and the ECMWF+TJ parametrisation wind speed distribution are biased low when compared with the QuikSCAT distribution. This is to be expected given the systematic differences between ECMWF and QuikSCAT at high wind speeds seen in previous studies such as Ebuchi *et al.* (2002), or Chapter 3. The inclusion of a mesoscale feature such as a tip jet cannot be expected to remedy this systematic bias, however it should improve the wind speed distribution. This is indeed the case, with the shape of the distribution in the parametrised wind field more closely resembling that of QuikSCAT, giving an increased probability of observing wind speeds in excess of 17 m s^{-1}.

Improvements in the wind speed distribution can also be seen in simple statistics (Table 5.2). The changes caused by the parametrisation are all consistent with an improved representation of the tip jet: the maximum wind speed has increased by over 9 m s^{-1}, with the mean wind speed increased by only around 0.6 m s^{-1} because the increased wind speeds are limited to a small area. The minimum wind speed seen in ECMWF is unchanged. Arguably the most important statistic here is the standard deviation, giving a measure of the variability of the wind. If the parametrisation is behaving appropriately then the standard deviation should be similar in the ECMWF+TJ and QuikSCAT winds, as the tip jet accounts for much of the variability in wind speed in this area (Moore and Renfrew, 2005). Standard deviations of QuikSCAT and the ECMWF+TJ wind fields are

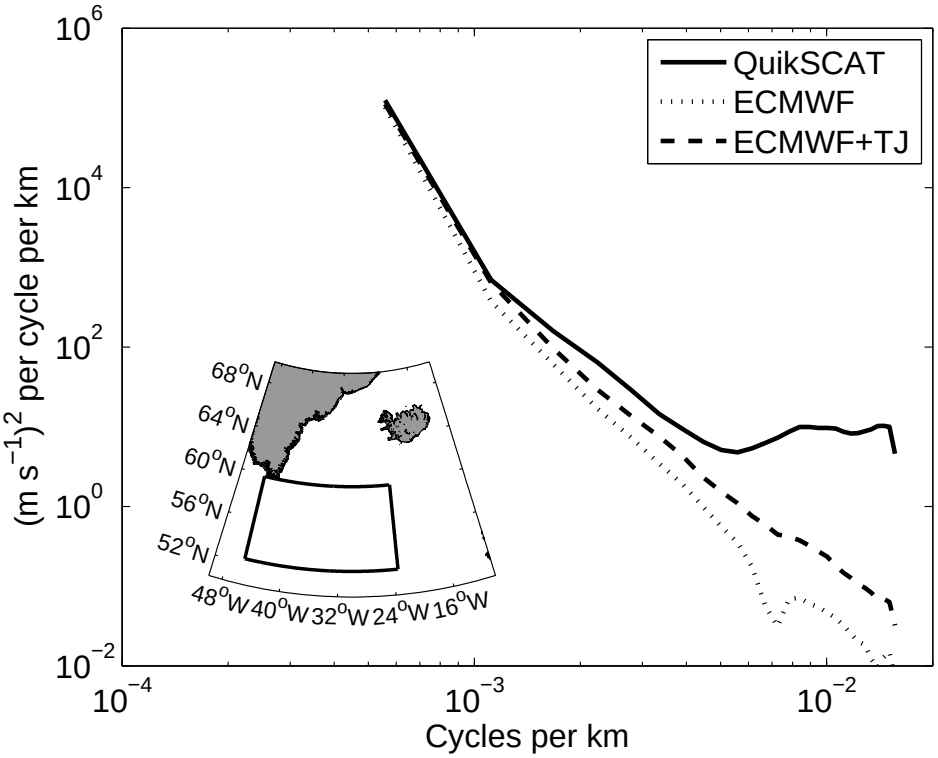

Figure 5.14: Power spectral density from the L3 gridded QuikSCAT data, ECMWF and ECMWF with the tip jet parametrisation in the area 52–60 °N, 23.5–45.5 °W, estimated via Welch's method, for the 32 tip jet test cases. ECMWF data were first bi-linearly interpolated onto the QuikSCAT grid and the QuikSCAT data were slightly smoothed using a 5 point smoother. The graphic inset shows the area over which the spectra were calculated.

5.5 m s^{-1} and 5.47 m s^{-1} respectively, while that of the unperturbed ECMWF wind field is 4.8 m s^{-1}, indicating that the inclusion of the tip jet does improve the spatial variability of the wind with respect to the best observations available.

Chelton *et al.* (2006) note that, in comparison with QuikSCAT, the surface wind fields in atmospheric (re)analyses lack power at high wave-numbers. For spatial scales that are comparable to the model resolution, this is to be expected, however significant differences were seen at scales much larger than this, which the higher resolution models should be capable of resolving. Is it possible that some of this 'missing' variability is due to an under-representation in the models of mesoscale features such as tip jets? Figure 5.14 shows power spectral density over the 32 westerly tip jet cases over the north-east Atlantic (note that the upturned tail of the QuikSCAT curve is erroneous, and is due to the gridding and/or smoothing of the QuikSCAT data). Power should continue decreasing approximately with k^{-2} – see Chelton *et al.* (2006)). It is clear that the ECMWF wind

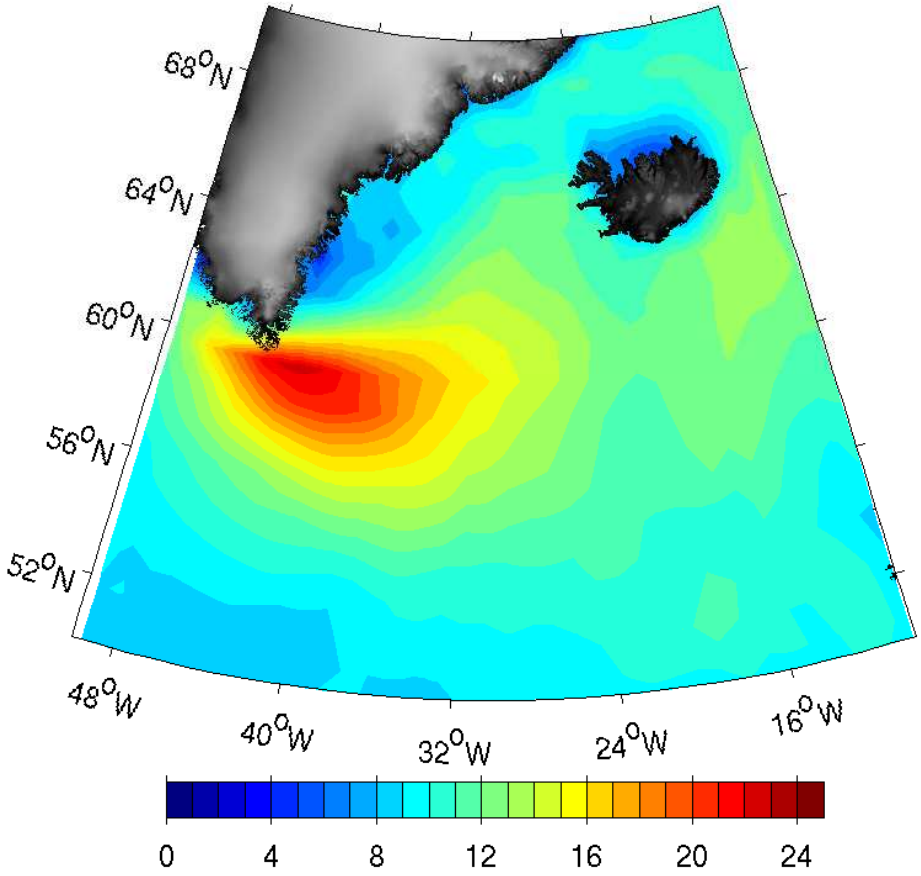

Figure 5.15: A composite of wind speed over the 32 westerly tip jets in our dataset, once a linear scaling has been used to increase the wind speeds in the domain. Note wind speeds away from the core of the jet are significantly too high.

field lacks power at all scales, but this is particularly clear at scales less than around 1000 km. Introducing the tip jet through the parametrisation adds power at scales between 100 km and 1000 km, bringing the power spectral density closer to that of QuikSCAT.

5.6 Previous Parametrisations

Våge *et al.* (2009a) noted, as we have seen here, that there is a good linear relationship between the maximum wind speed in ERA-40 and QuikSCAT over the Irminger Sea during tip jet conditions, as well as average winds over the Irminger Sea generally. Given such a relationship, it could be argued that a much simpler method of parameterizing the tip jet would be to apply this linear scaling to the wind field over the Irminger Sea whenever a tip jet is suspected to be present. This approach, however, has a number of problems. The

main problem is how to distinguish the tip jet from the background wind field and apply a scaling to only that area. ERA-40 has a reasonable representation of the outer fringes of the tip jet, it just does not resolve the 'core' of the jet where the highest wind speeds are to be found. If a linear scaling is applied to an arbitrary domain around the tip jet, then the wind field surrounding the tip jet will also be perturbed, resulting in a wind field which is too strong over most of the domain. For example, consider Figure 5.15, which shows a composite of ECMWF wind speeds over the 32 westerly tip jet cases to which a linear scaling (Equation 5.2) has been applied to the entire domain. The wind speed at the centre of the composite jet is comparable to that in the QuikSCAT and ECMWF+parametrisation composites (Figure 5.11), however away from the jet, wind speeds are significantly over-estimated. It would, of course, be possible to use a smaller domain over which to apply the scaling, however this would then not be guaranteed to capture the whole jet; it would be very difficult to choose a domain which would cover the whole jet and only the jet.

Another problem with this approach is, regardless of the domain the scaling is applied over, what happens at the edge of the domain. Simply stopping a scaling at a specific point could lead to a significant jump in the wind field over a single grid point, i.e. there would be spurious convergence and/or divergence introduced into the wind field, which could in turn lead to spurious up or downwelling in the ocean.

Finally, a simple linear scaling can only tighten spatial gradients which are already present in the analysis wind speed field, rather than introducing increased gradients. This could lead to an under-representation of the strong wind stress curl which occurs to the north and south of the tip jet and may be important for forcing local and remote recirculations (Pickart *et al.*, 2003a; Spall and Pickart, 2003).

5.7 Enhanced Surface Fluxes

5.7.1 Latent and Sensible Fluxes

The heat fluxes in ERA-40 in a typical westerly tip jet case (Figure 5.17a) are elevated around the tip of Cape Farewell, with values of around 650 W m^{-2}. However, once the parametrised tip jet has been inserted (Figure 5.17b), the total turbulent heat fluxes in the core of the jet are increased to over 1200 W m^{-2}. These are even greater than the

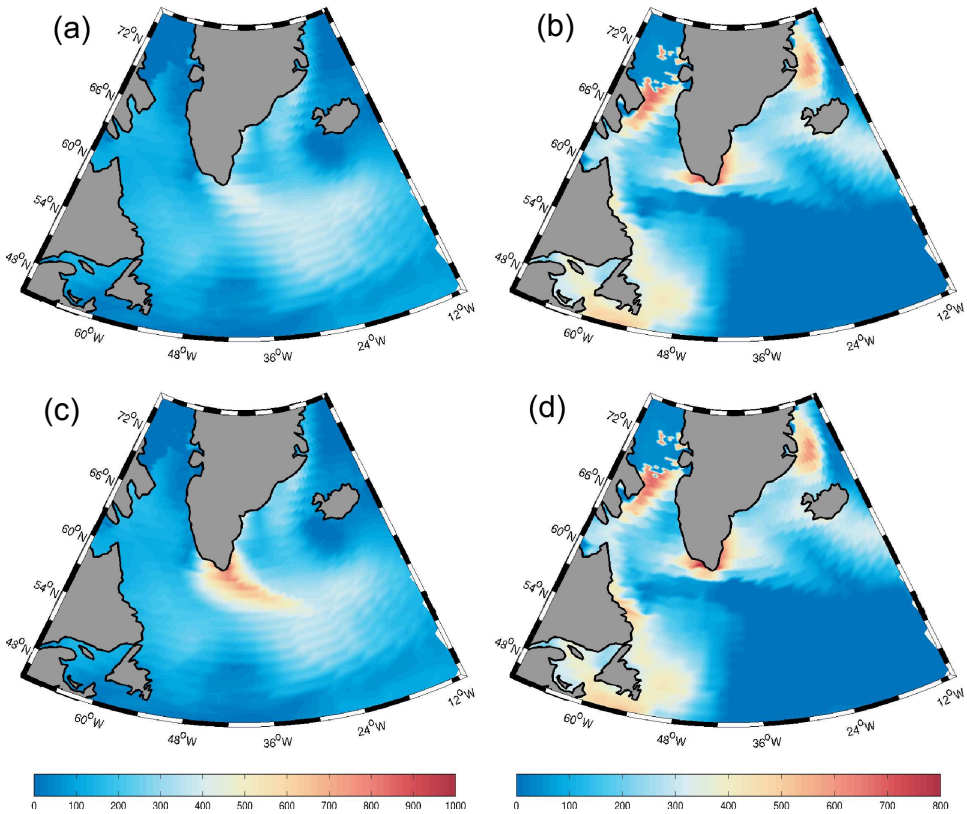

Figure 5.16: Total turbulent heat fluxes (W m^{-2}) in ERA-40 and ERA40+TJ for a typical westerly (a,c, 12Z, Oct. 25, 1981) and easterly (b,d, 12Z, Jan. 18, 1981) tip jet.

heat fluxes off the Labrador coast, which peak at around 1100 W m^{-2}. The causes of the strong fluxes in these two locations are somewhat different. Those in the Labrador Sea are caused by very cold, dry air being advected from the continent, while those in the tip jet are caused by stronger winds with a slightly smaller air/sea temperature difference. The sensible heat fluxes associated with the westerly tip jet seen here are consistent with those seen by Doyle and Shapiro (1999).

During testing both with and without the parametrisation over the winter (JFM) of 1980, the average combined sensible and latent heat flux over the southern Irminger Sea using the ERA-40 forcing was 123 W m^{-2}, with a maximum value of 846 W m^{-2}. Using the ERA40+TJ forcing, the average flux increased to 132 W m^{-2}, i.e. an increase of 9 W m^{-2} on average. While this may seem to be a modest increase, one must bear in mind that we are averaging over an area much larger than an average sized tip jet. Averaging for this period over just those grid points which were perturbed by the parametrisation

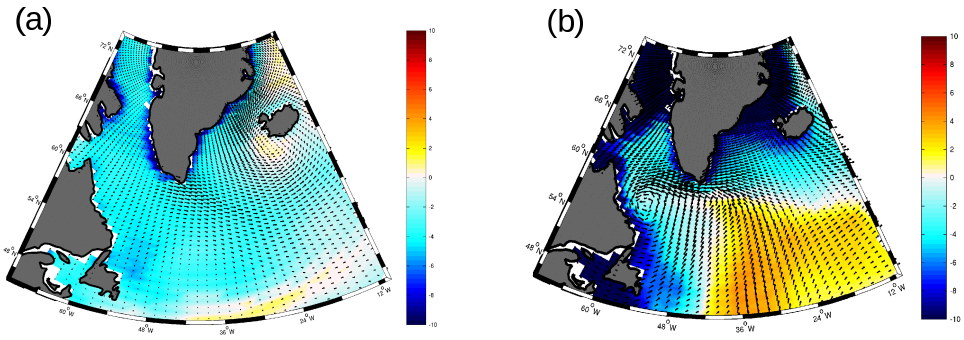

Figure 5.17: Difference between the 2 m air temperature and the sea-surface temperature, with the 10 m wind field overlaid, for the westerly and easterly tips shown in Figure 5.16. Note the northward advection of warm air and the generally smaller air-sea temperature difference around Cape Farewell during the easterly tip jet, despite this occurring in mid-winter, whereas the westerly case was in the autumn.

gives values of 254 W m^{-2} in ERA40+TJ, an increase of over 90 W m^{-2} over ERA-40. Furthermore the maximum flux increased to 1492 W m^{-2}, suggesting that significant changes in forcing occur in the Irminger Sea.

In contrast to the westerly tip jet, the easterly tip jet has a relatively minor impact on heat fluxes. In the example shown in Figure 5.17(c–d), heat fluxes are only increased in the region of the easterly tip jet by around 60 W m^{-2}. This is largely in agreement with Chapter 2, where we used synoptic-scale arguments and float data to show that the easterly tip jet is not of comparable importance to the westerly jet in forcing open ocean convection. This is due to the fact that air in the easterly tip jet has become heavily modified, and is of a warm, moist, maritime nature. It should be noted, however, that Martin and Moore (2007) did see modestly enhanced heat fluxes of around 200 W m^{-2} in the vicinity of a easterly tip jet. It seems, therefore, that conditions do arise in which the easterly jet can enhance air-sea heat exchange, although this is not generally the case.

In January–February–March 1980, the average sensible plus latent heat flux over the south-east Labrador Sea was 187 W m^{-2} with a maximum combined flux of 1116 W m^{-2}. Once the easterly tip jet had been bogussed into the wind field, the average combined flux showed a modest increase of 2 W m^{-2}, up to 189 W m^{-2}.

5.7.2 Momentum Fluxes

Figure 5.18 shows the momentum fluxes associated with the same parametrised westerly tip jet and easterly tip jet cases as in Figure 5.17. The momentum flux calculated from

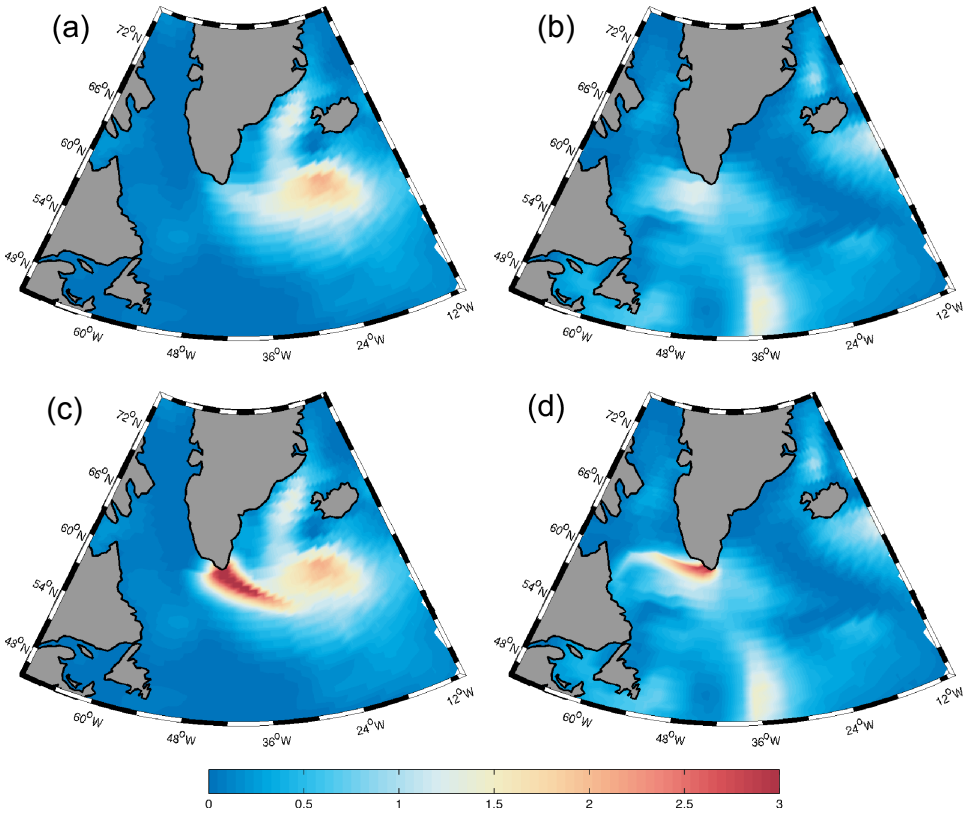

Figure 5.18: Momentum fluxes (N m^{-2}) in ERA-40 and ERA40+TJ for a typical westerly (a,c, 12Z, Oct. 25, 1981) and easterly (b,d, 12Z, Jan. 18, 1981) tip jet.

the unperturbed wind field does show an enhanced transfer of momentum between the atmosphere and ocean, in the vicinity of the westerly and easterly tip jets. However, due to the under-representation of the jets, the peak momentum flux is only of the order of 1.5 N m^{-2} for the westerly tip jet and 1 N m^{-2} for the easterly jet. Once the tip jet and easterly tip jet have been bogussed into the wind field, these peak values rise to 3.5 N m^{-2} for the westerly jet and 3 N m^{-2} for the easterly jet. Note that in the westerly case, there is a further area of relatively strong wind stress, which is associated with a synoptic-scale cyclone to the south of Iceland. It is also important to note the strong meridional gradients in the wind stress, which will provide locally large magnitudes of wind stress curl. Pickart *et al.* (2003b) and Spall and Pickart (2003) note the importance of localised strong wind stress curl in forcing the oceanic circulation, both in the immediate vicinity and elsewhere in the sub-polar gyre through the propagation of Rossby waves away from the source. For example, Spall and Pickart (2003) suggest that the Labrador Sea gyre is driven by localised wind stress curl east of Greenland, communicated by topographically steered Rossby waves.

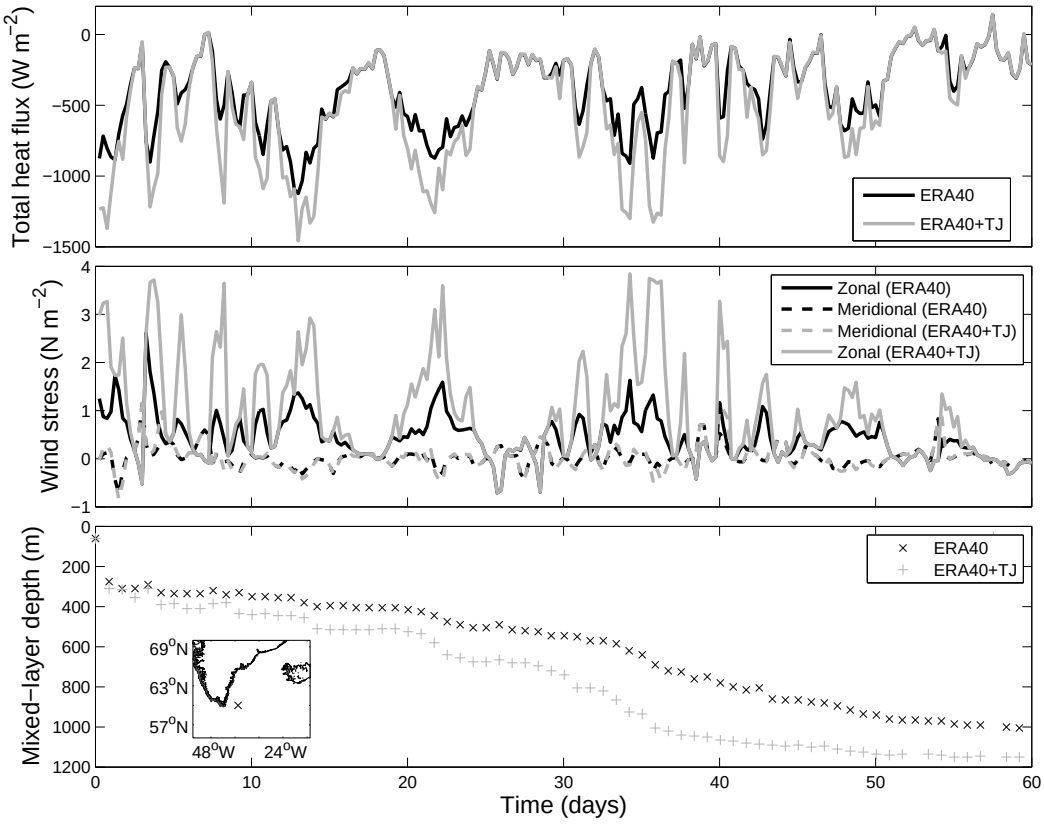

Figure 5.19: Mixed-layer development in the Irminger Sea in a 1-D model, using time-series of heat and momentum flux both with and without the tip jet parametrisation. The top panel shows the total heat flux applied to the model, the middle panel shows the surface meridional and zonal wind stress, and the bottom panel shows the development of the mixed-layer. The graphic inset shows the location from where the time-series were extracted.

5.8 Back to PWP

To provide a simple demonstration of the influence of the tip jet parametrisation on the ocean, we return to a one-dimensional mixed-layer ocean model (Price *et al.*, 1989), used previously in studies of the impact of Greenland tip jets on oceanic mixed-layer development by Våge *et al.* (2008) and in Chapter 2 of this thesis. To initialise the model, temperature and salinity profiles were obtained from an Argo float in the Irminger Sea (59.3 °N, 37.7 °W) on December 29th, 2008. Forcing time-series of total heat flux and wind stress were then extracted from the ERA-40 forcing fields for 60 days from 1st January, 1983, when the NAO was in a positive state (+1.8). Two runs were carried out, one using the standard ERA-40 forcing fields (control run), and one using the perturbed ERA40+TJ fields (perturbed run). In both runs, a vertical resolution of 5 m and temporal

resolution of 60 s were used, with a background diffusion coefficient of 10^{-5} m^2 s^{-1}.

Figure 5.19a shows the total heat flux that would be extracted from the ocean. As expected, the heat fluxes are similar when they are small; where they differ the fluxes from the tip jet run are stronger as the increased wind is introduced into the forcing fields. The largest differences between the perturbed and control runs are approximately 500 W m^{-2} around day 36 of the integration. Similar increases in the momentum flux are also seen (Figure 5.19b), although these are relatively larger, as $\tau \propto U^2$. The largest increases in momentum flux again occur around day 36, and are greater than 2 N m^{-2}. The zonality of the tip jet is maintained in the parametrisation, with nearly all of the momentum increase in the zonal direction. Depending on the orientation of the tip jet, increases can also be seen in the meridional component (for example there is an increase of around 0.5 N m^{-2} in the meridional wind stress component at day 40). Figure 5.19c shows the ocean mixed-layer development for each of the forcing time-series. The pattern of deepening is similar in both of the runs, but the run with the perturbed time-series deepens more during each high-flux event. The largest difference between the two runs occurs around day 36, with the perturbed run around 300 m deeper than the control. After this, the mixed-layer in the perturbed run encounters a layer of increased stratification. As there are no further robust tip jet events, the difference between the two runs decreases, resulting in a difference in mixed-layer depth of 170 m at the end of the 60 day integration. Although there are no validation data for this particular model run, previous studies (e.g. Våge *et al.* (2008)) have indicated that inclusion of the tip jet improves the evolution of the mixed-layer depth in the Irminger Sea as compared with observations, and by a comparable amount to the differences seen here.

5.9 Conclusions

In this chapter we have developed a method for bogussing both westerly and easterly Greenland tip jets into a wind field. The parametrisation development has made use of a dataset of 32 westerly and 42 easterly tip jets, but can be implemented without recourse to this dataset. The method allows for the variation of strength, shape, size and orientation that are observed in tip jets and thus accurately reproduces a tip jet, allowing it to be smoothly blended into the background field. The westerly tip jet can cause a significant,

if localised, increase in sensible and latent heat flux which we have demonstrated has a significant impact on ocean mixed-layer depth and thus potentially on convection in ocean models. The effect of the easterly jet is more modest. This is in agreement with previous work (Chapter 2), which suggests that the easterly tip jet is not of great importance in forcing open ocean convection. Both the westerly and easterly tip jets cause a large local increase in wind stress, and their relatively small meridional scale leads periodically to strong dipoles of wind stress curl, which have previously been linked to circulation patterns in the North Atlantic.

The parametrisation does not rely on any external data-sets, only mean sea-level pressure and surface wind fields, and can thus be easily implemented into either ocean only general circulation models or coupled climate models at the coupling stage, once consideration has been given to the transfer of heat between the ocean and atmosphere.

In the following chapter we will examine the impact of both westerly and easterly tip jets on local and global ocean circulation, by implementing the parametrisation into the FRUGAL global ocean general circulation model and examining ‘control’ and ‘perturbation’ experiments.

Chapter 6

The Impact of Tip Jets on the Ocean

In this chapter we present the results of a number of multi-year integrations of the FRUGAL OGCM in which various combinations of the Greenland tip jet parametrisation, developed in Chapter 5, have been incorporated into the model setup. The westerly tip jet causes a cold anomaly of around 0.2° to spread throughout the Labrador and parts of the Irminger Seas. A well defined cold anomaly is also seen in the deep western boundary current underneath the tip jet, which is then advected away from the source in the boundary current. In the first decade of the simulation the westerly tip jet results in a systematic increase of the MOC of up to around 0.3 Sv, however this behaviour changes to a seasonally cycling decrease in the MOC in the second decade of the experiment. A strong and systematic increase in the subpolar gyre of up to 2.5 Sv is seen throughout the integration.

The small increase in heat fluxes which is associated with easterly tip jets results in much smaller temperature anomalies than the westerly jet. However, the input of mechanical energy associated with the easterly jet has a significant impact on the MOC, showing a systematic increase of up to 1 Sv (over short periods) which remains through the duration of the experiment. The easterly tip jet is also seen to increase the circulation of the subpolar gyre, although less consistently than does the westerly jet.

When both tip jets are incorporated into the forcing fields the results are, broadly speaking, an additive combination of the two individual cases.

6.1 Experimental Design

6.1.1 Perturbation Experiments

The approach we take here is to perform a direct comparison between the control integration, which was described at the end of Chapter 4, and 'perturbation integrations'. These perturbation integrations are virtually identical to the control integration, differing only in that the tip jet parametrisation is incorporated into the model setup. It is thus clear that any differences between the control and perturbation integrations are directly attributable to the improved representation of Greenland's tip jets in the perturbation experiments.

Such a methodology has been used successfully in the past to evaluate the impact of improving the representation of small-scale atmospheric phenomena in the atmospheric boundary conditions of both ocean-only and atmosphere-ocean general circulation models. For example, Condron et al. (2008) developed a method of parameterizing polar mesocyclones into the forcing fields of an OGCM, based on a satellite climatology of polar mesocyclones in the Greenland-Iceland-Norwegian (GIN) Seas (Harold *et al.*, 1999). A perturbation/control simulation showed that the inclusion of these mesocyclones (which are usually sub-gridscale in global atmospheric reanalyses) led to a spin-up of the cyclonic circulation in the GIN Seas and an increase in the volume of Greenland Sea deep water (GSDW), which in turn led to an increase in volume flux of the Denmark Strait and Iceland-Faroe-Scotland overflows. Hu and Meehl (2009) evaluated the impact of Atlantic hurricanes on the meridional overturning circulation in an AOGCM by prescribing the path and strength of a number of hurricanes and incorporating these into the atmospheric surface level wind field. This led to a significant cooling of surface waters in the western North Atlantic and a small increase in meridional heat transport through an increase in the strength of the MOC.

One factor which must be considered when designing such experiments is how long the simulations can be run without the control and perturbation drifting apart, while still allowing the perturbations in the forcing fields time to impact on the larger scale ocean circulations. Condron *et al.* (2008) ran their perturbation experiments for only two years, limited by the length of the satellite-based mesocyclone climatology which was available. Although some significant differences were seen in the ocean circulation, it was conceded that the run was probably too short to see the full impacts of the parametrisation on the

ocean. For example, assuming an average deep western boundary current (DWBC) velocity of $\sim$ 10 cm s^{-1} (Fischer and Schott, 1997; Rhein, 1994; Pickart *et al.*, 1989) it would take approximately two years for an anomaly generated in the subpolar Atlantic to be propagated into the tropics by DWBC advection alone. Interior pathways, away from the DWBC, are significantly slower.

The ECMWF ERA-40 reanalysis, which we are using to set the atmospheric boundary conditions for these experiments, uses unchanging data assimilation throughout the length of the reanalysis (Uppala *et al.*, 2005). Despite this, the reanalysis does assimilate new sources of data as they become available, which may have an impact on the quality of the reanalysis. One of the largest shifts in the quantity of data which was available for assimilation into numerical weather prediction models came at the start of the satellite era. Temperature- and humidity-sensitive infrared radiances and surface pressure observations derived from satellites were first available for assimilation into ERA-40 from 1973, with temperature-sensitive microwave radiances and winds calculated by tracking of features by geostationary weather satellites first assimilated from 1980. Surface temperature, pressure and wind data from oceanic buoys were also first available in 1980.

Given that there is a stepwise increase in the availability of observational data from 1980, we choose to run the model integrations for 20 years, starting in 1980 (thus finishing at the end of 1999). This should allow the parametrisation sufficient time for its full effect to be seen, while not so long that a direct comparison between the perturbation and control runs becomes meaningless. It also means that there are as few as possible step changes in the data being assimilated into ERA-40. While this may seem unimportant as these changes apply equally to both the control and perturbation runs, it should be noted that the parametrisation developed in Chapter 5 was tuned using data from the mid-1990's onwards, thus is most appropriate for this quality of data. Its application during much earlier periods may be less justifiable.

6.1.2 The Modified Forcing Fields

Greenland's tip jets are events that lead to very strongly enhanced heat and momentum fluxes over short timescales, however it is still enlightening to consider the perturbations that the tip jets make to the flux fields in a time averaged sense. In Figures 6.1 and 6.2

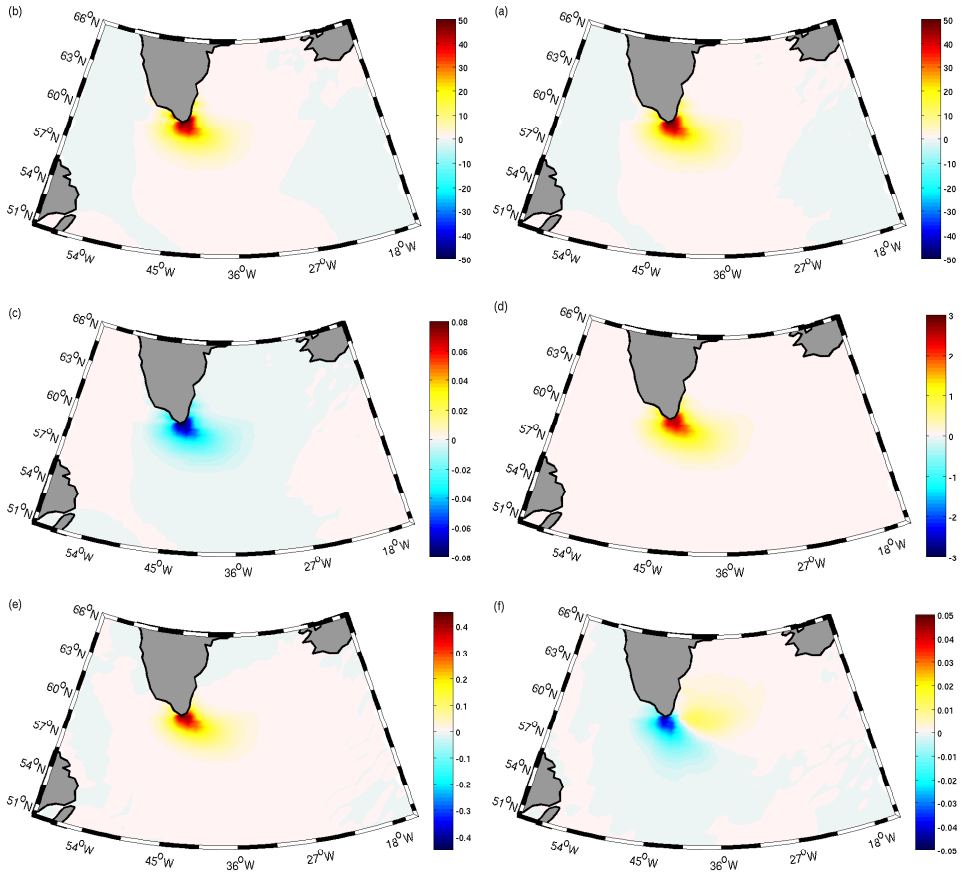

Figure 6.1: Average winter (NDJFM) anomalies of (a) sensible heat flux (W m^{-2}); (b) latent heat flux (W m^{-2}); (c) freshwater flux (mm day^{-1}); (d) wind speed (m s^{-1}); (e) zonal wind stress (N m^{-2}); (f) meridional wind stress (N m^{-2}) between 1980 and 1999 inclusive, caused by the inclusion of the westerly tip jet parametrisation. Values are positive into the ocean.

we can see the perturbations caused by the inclusion of the westerly and easterly tip jets respectively, averaged over all winters (NDJFM) between 1980 and 1999 inclusive. In these composites, the westerly tip jet causes local increases in both latent and sensible heat fluxes of up to around 50 W $m^{-}2$, i.e. an *average* winter increase in heat fluxes of up to 100 W m^{-2} in the southern Irminger Sea. The freshwater flux anomaly shows an average decrease (i.e. an evaporative increase) of 0.08 mm day^{-1}, resulting entirely from the increase in latent heat release from the ocean surface (precipitation fields are prescribed and are left unchanged by the tip jet parametrisation). The average wind speed increase exceeds 3 m s^{-1} at Cape Farewell. This increase in wind speed leads to an average increase of zonal wind stress of up to 0.45 N m^{-2}. The changes in the meridional component of wind stress are much more modest (as the westerly tip jets are generally zonal in orientation), and show a dipole structure varying from -0.05 N m^{-2} to 0.02 N m^{-2},

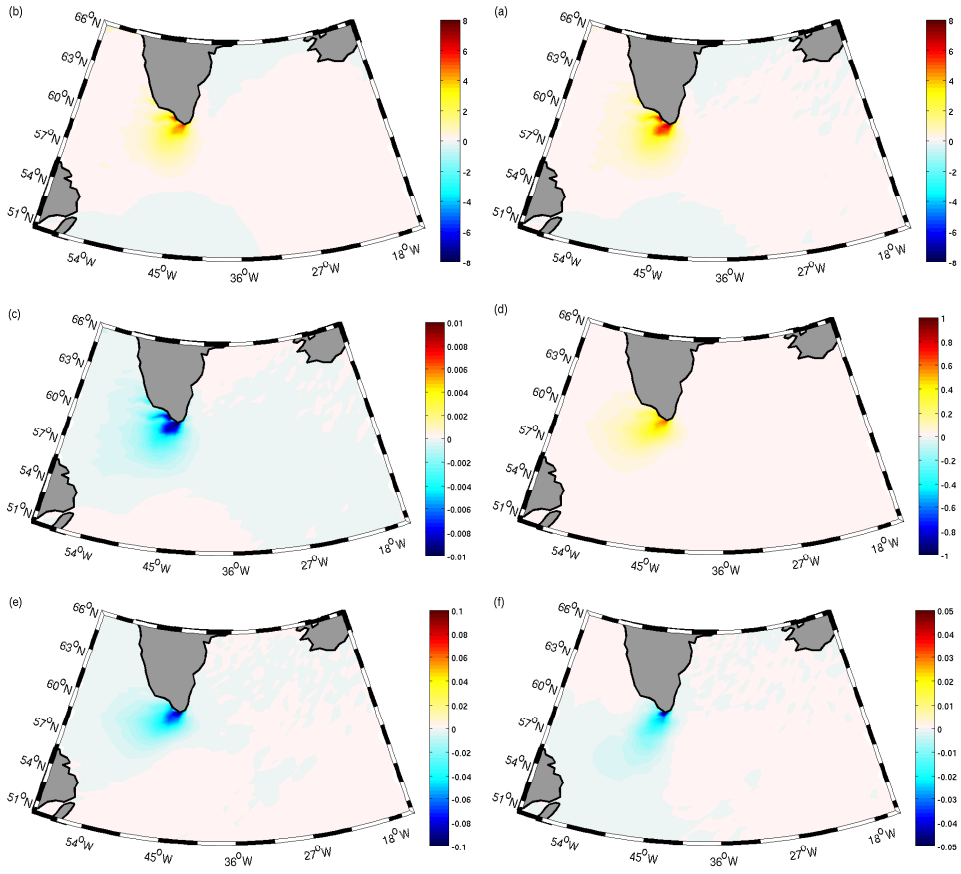

Figure 6.2: Average winter (NDJFM) anomalies of (a) sensible heat flux (W m^{-2}); (b) latent heat flux (W m^{-2}); (c) freshwater flux (mm day^{-1}); (d) wind speed (m s^{-1}); (e) zonal wind stress (N m^{-2}); (f) meridional wind stress (N m^{-2}) between 1980 and 1999 inclusive, caused by the inclusion of the easterly tip jet parametrisation. Fluxes are positive into the ocean. Note the generally different colour scales here, compared to Fig. 6.1.

caused by the cyclonic curvature of the tip jet around its parent low pressure system.

As expected, the flux anomalies resulting from the inclusion of the easterly tip jet parametrisation (Figure 6.2) are significantly lower than those from the westerly jet. These reduced fluxes are due to both the synoptic situation, which as we discussed in Chapter 2 are not conducive to high heat fluxes during easterly tip jets, and the fact that the easterly parametrisation is invoked less frequently than the westerly parametrisation. The average winter anomalies of sensible and latent heat flux under the easterly parametrisation achieve maximum values of 6 W m^{-2} and 8 W m^{-2} , just to the south-west of Cape Farewell. The slight increase in latent heat flux leads to a modest increase in evaporation, leading to a change in fresh water flux of -0.01 mm day^{-1}. Wind speed in the region increases on average by up to 0.6 m s^{-1} , leading to changes in the zonal and meridional wind stress of -0.1 N m^{-2} and -0.05 N m^{-2} respectively. Note that the easterly tip jet

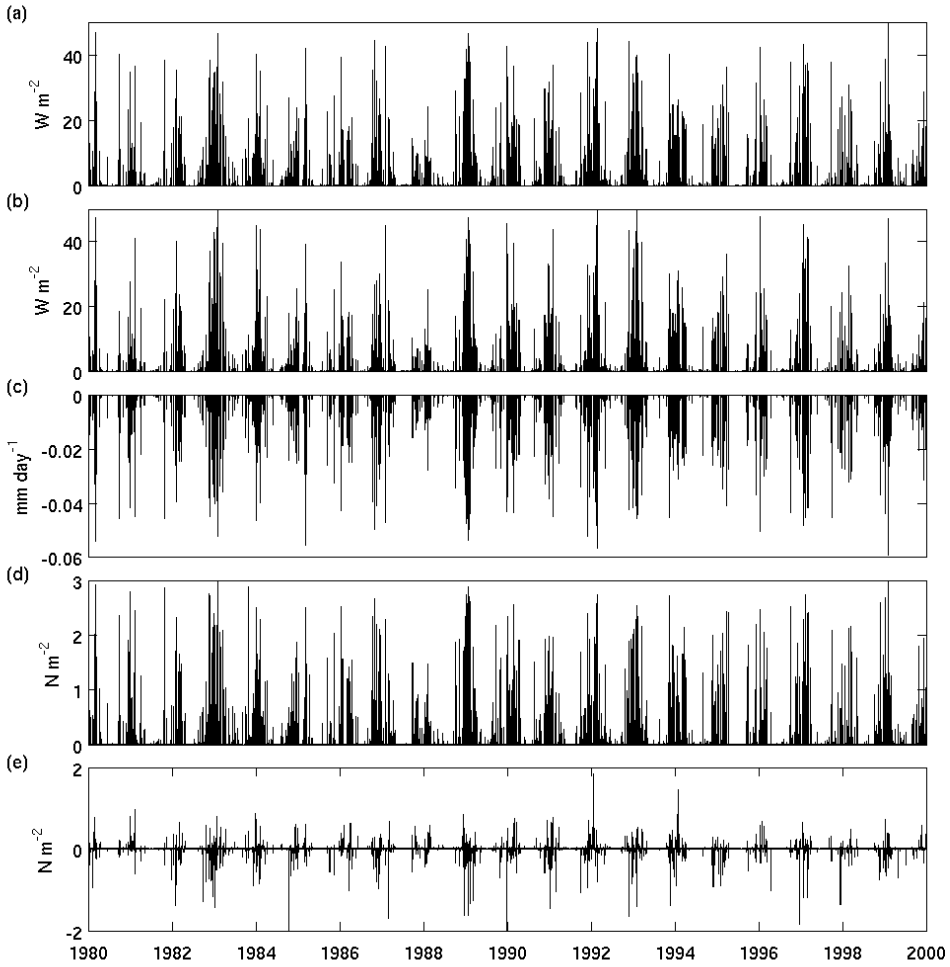

Figure 6.3: Timeseries of anomalies (perturbation−control) of (a) sensible heat flux (W m^{-2}); (b) latent heat flux (W m^{-2}); (c) freshwater flux (mm day^{-1}); (d) zonal wind stress (N m^{-2} ; (e) meridional wind stress (N m^{-2}), caused by the inclusion of the westerly tip jet, averaged over the area $[78, 139] \times [106, 170]$ on the FRUGAL grid. This is an area covering much of the subpolar north Atlantic, south of the Denmark Strait.

has a relatively stronger meridional component than the westerly jet, and the lack of a dipole in the meridional wind stress anomaly shows that the easterly jet tends to have less curvature than does the westerly jet.

Figures 6.3 and 6.4 show the timeseries of forcing anomalies averaged over the North Atlantic region. There is a strong seasonal variability in the occurrence of both westerly and easterly tip jets, with the majority of jets occurring in the winter months as an increased number of extra-tropical cyclones pass along the north Atlantic storm track. There is also a distinct intraseasonal/decadal variability, due to the relationship between the frequency of tip jets and the phase and strength of the North Atlantic Oscillation (Moore, 2003; Moore and Renfrew, 2005; Bakalian *et al.*, 2007). When integrated over this North Atlantic region, the westerly tip jet regularly produces area-averaged sensible and latent

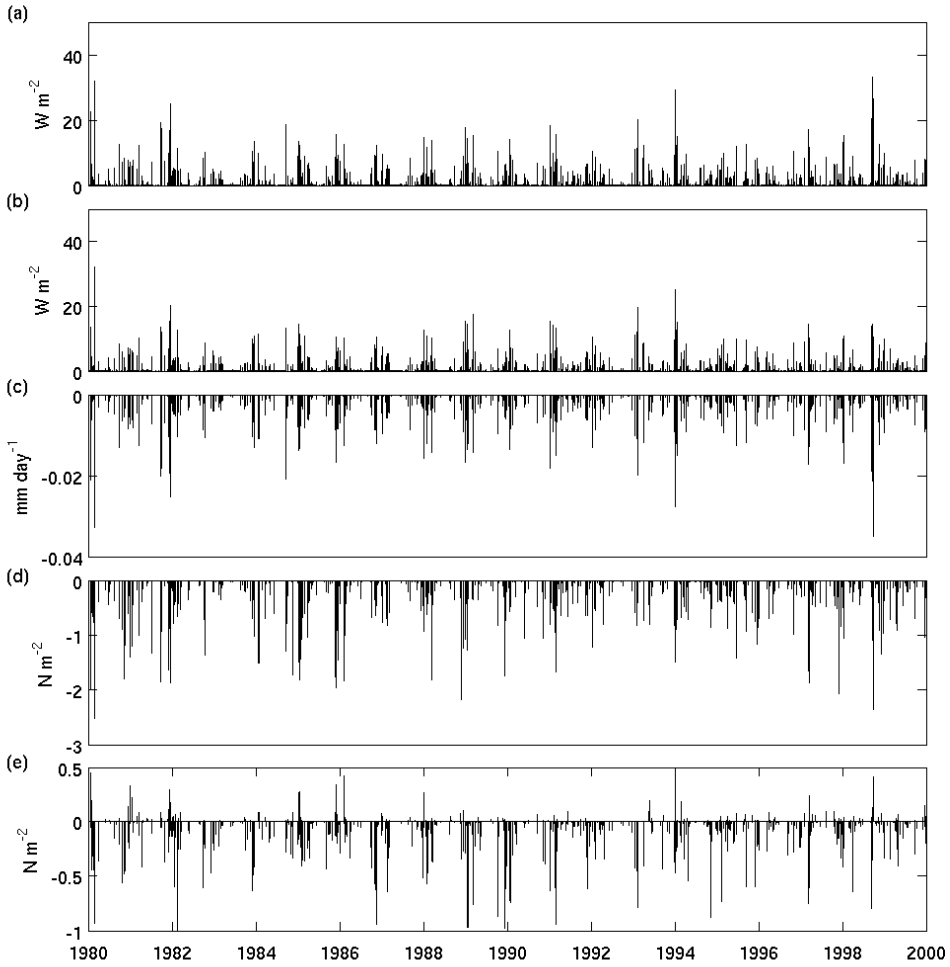

Figure 6.4: Timeseries of anomalies (perturbation−control) of (a) sensible heat flux (W m^{-2}); (b) latent heat flux (W m^{-2}); (c) freshwater flux (mm day^{-1}); (d) zonal wind stress (N m^{-2}); (e) meridional wind stress (N m^{-2}), caused by the inclusion of the easterly tip jet, averaged over the area $[78, 139] \times [106, 170]$ on the FRUGAL grid. This is an area covering much of the subpolar north Atlantic, south of the Denmark Strait.

heat fluxes of around 20 W m^{-2} , with extreme area-averages around 40 W m^{-2}. Again we see much weaker latent and sensible heat fluxes associated with the easterly jet. These are generally area-averages around 10 W m^{-2} in both cases, with extreme values rarely exceeding 20 W m^{-2}.

6.1.3 Calculation of Diagnostics

6.1.3.1 Mixed-Layer Depth

As we saw in Chapter 4, the FRUGAL OGCM has a hydrostatic formulation and grid size ~ 50 km and so is unable to explicitly model oceanic convection, which occurs at spatial scales of $O(1)$ km. However the model does allow a representation of vertical mixing

by homogenising vertically adjacent grid cells wherever the water column is statically unstable. Thus the depth of the surface mixed-layer gives a good indication of convective activity.

Defining the depth of the mixed-layer, however, is not straight-forward – a variety of definition are commonly used. The definition generally relies on temperature criteria, where the bottom of the mixed layer is where the temperature $T = \text{SST} - \Delta T$ for some previously defined ΔT, or similar criteria using density or potential density referenced to a near surface depth. Kara *et al.* (2000) and de Boyer Montégut *et al.* (2004) both provide good reviews of the mixed-layer depth criteria which have been used in previous studies. Temperature criteria use a ΔT varying from 1.0 °C (Lamb, 1984) to 0.1 °C (Martin, 1985). The most common value used for density-based criteria is $\Delta\sigma = 0.125\sigma_t$, where σ_t is the density-1000 kg m^{-3} at or near the ocean surface (Miller, 1976; Spall, 1991; Huang and Russell, 1994). This corresponds to the characteristics of subtropical mode water in the north Atlantic given by Levitus (1982). 'Optimal' definitions of mixed-layer depth have been given by Kara *et al.* (2000) as $\Delta T = 0.8$ °C and by de Boyer Montégut *et al.* (2004) as $\Delta T = 0.2$ °C or $\Delta\sigma_\theta$ = 0.03 kg m^{-3} for the global ocean.

Given the wide range of definitions of mixed-layer depth available in the literature, it is not immediately clear how best to calculate the depth of the mixed-layer in this instance. We find the isothermal formulation to be successful, and choose a ΔT of 0.2 °C, following Thompson (1976), although the mixed-layer depth differences in the range $0.1\ ^\circ\text{C} \leq \Delta T \leq 0.3\ ^\circ\text{C}$ are only small. The vertical resolution of the FRUGAL model is fairly coarse, with only 19 levels in the vertical, leading to a gap of up to 500 m between levels in the deep ocean. This leads to the calculation of mixed-layer depth being either very insensitive or very oversensitive to small changes in temperature. We thus choose to linearly interpolate the temperature profile between model levels, allowing us to calculate the exact depth at which the temperature threshold, ΔT is exceeded.

6.1.3.2 Potential Vorticity

In a frictionless, incompressible flow, we have (Pedlosky, 1987)

$$\frac{D}{Dt}\left(\frac{\zeta + f}{H}\right) = 0,$$

where $\zeta = \nabla_z \times \mathbf{u} = \frac{\partial v}{\partial x} - \frac{\partial u}{\partial y}$ is the relative vorticity, f is the planetary vorticity, $H = H(x, y, t)$ is the vertical distance between the ocean floor and the free surface and $\frac{D}{Dt} = \frac{\partial}{\partial t} + u\frac{\partial}{\partial x} + v\frac{\partial}{\partial y}$ is the horizonal material derivative. Thus the quantity

$$\Pi = \frac{\zeta + f}{H} \tag{6.1}$$

is conserved along fluid trajectories, and is known as the potential vorticity (PV). Equation 6.1 may be rewritten for a barotropic, stratified flow (Pedlosky, 1987) as

$$\Pi = \frac{\zeta + f}{\rho} \cdot \nabla\lambda, \tag{6.2}$$

where λ is any conserved property of the fluid flow. If we take λ to be the density of the fluid, ρ, then we have

$$\Pi \approx \frac{\zeta + f}{\rho}\frac{\partial \rho}{\partial z}, \tag{6.3}$$

where we have assumed that the horizontal density gradients are much smaller than those in the vertical, a valid assumption over the majority of the ocean. In addition $\zeta \ll f$, excpet in areas with exceptionally strong shear in the flow (for example near the edge of western boundary currents such as the Gulf Stream or Kuroshio). We may thus neglect the relative vorticity in the interior of the ocean, leaving us with

$$\Pi \approx \frac{f}{\rho}\frac{\partial \rho}{\partial z}. \tag{6.4}$$

PV is thus a quantity that is approximately conserved with the flow, and appears as a minimum in areas of weak stratification such as mode waters and thus acts as a tracer for convectively formed water masses (e.g. LSW). Talley and McCartney (1982) used PV signals to calculate the pathways of Labrador Sea Water from its point of origin in the Labrador Sea as far south as the equator. In our control/perturbation experiments, we can interpret negative anomalies of potential vorticity as increased production or penetration of mode water in the North Atlantic. It should be noted however, that we must calculate the vertical gradient of density through finite differencing, which, given the low vertical resolution of FRUGAL at mid-depths, may be a significant source of error.

6.2 The Local, Fast Response to a Tip Jet

Although it is likely to be the integrated effects of a number of winters worth of tip jets which has the largest effect on the oceanic circulation, single tip jets can still have some interesting transient local effects. In this section we investigate this by considering the immediate impacts of the first strong westerly and easterly tip jets in the model integrations on the ocean characteristics in the subpolar north Atlantic.

6.2.1 A Westerly Jet

Figure 6.5 shows the entire life cycle of the first strong tip jet event in the model integration, commencing at 1800Z on the 7th January, 1980 and continuing for 30 hours. At the start of the sequence, a small synoptic low pressure system has moved along the north Atlantic storm track and into the lee of Greenland. Strong winds of up to 21 m s^{-1} are seen to flank the low pressure system to the north and south, in the central Irminger Sea and south-east of Cape Farewell. The tip jet parametrisation has, as yet, left the wind field unmodified. After six hours (Figure 6.5b) the low pressure centre has deepened and moved northwards, and the parametrisation inserts a small tip jet into the wind field, with strong cyclonic curvature around the low pressure. The maximum wind speed in the jet is now 26 m s^{-1}, around 5 m s^{-1} stronger than the unperturbed wind field. Over the next 18 hours (Figure 6.5c–e), a very robust tip jet has been bogussed into the wind field, superimposed on an area of strong winds in ERA-40, with wind speeds peaking at 34 m s^{-1} at 1200Z on the 8th of January. This represents an increase in wind speed in excess of 11 m s^{-1} over the unperturbed wind field. By 0000Z on the 9th of January, the low pressure system has filled and moved away from the lee of Greenland. At this point the parametrisation is no longer modifying the wind field, although there is still an area of relatively high wind speeds to the south and west of Cape Farewell.

Such a strong enhancement to the surface wind speeds may be expected to have a large influence on the ocean velocity fields directly underneath the tip jet. Figure 6.6 shows the ocean velocity anomaly (perturbation−control) at the sea surface. In Figure 6.6(a), at the start of the sequence, the two velocity fields are almost identical as the case study we are considering is very close to the start of the integration. As the westerly tip jet manifests itself, a positive anomaly appears directly beneath the jet. The velocity anomaly is not

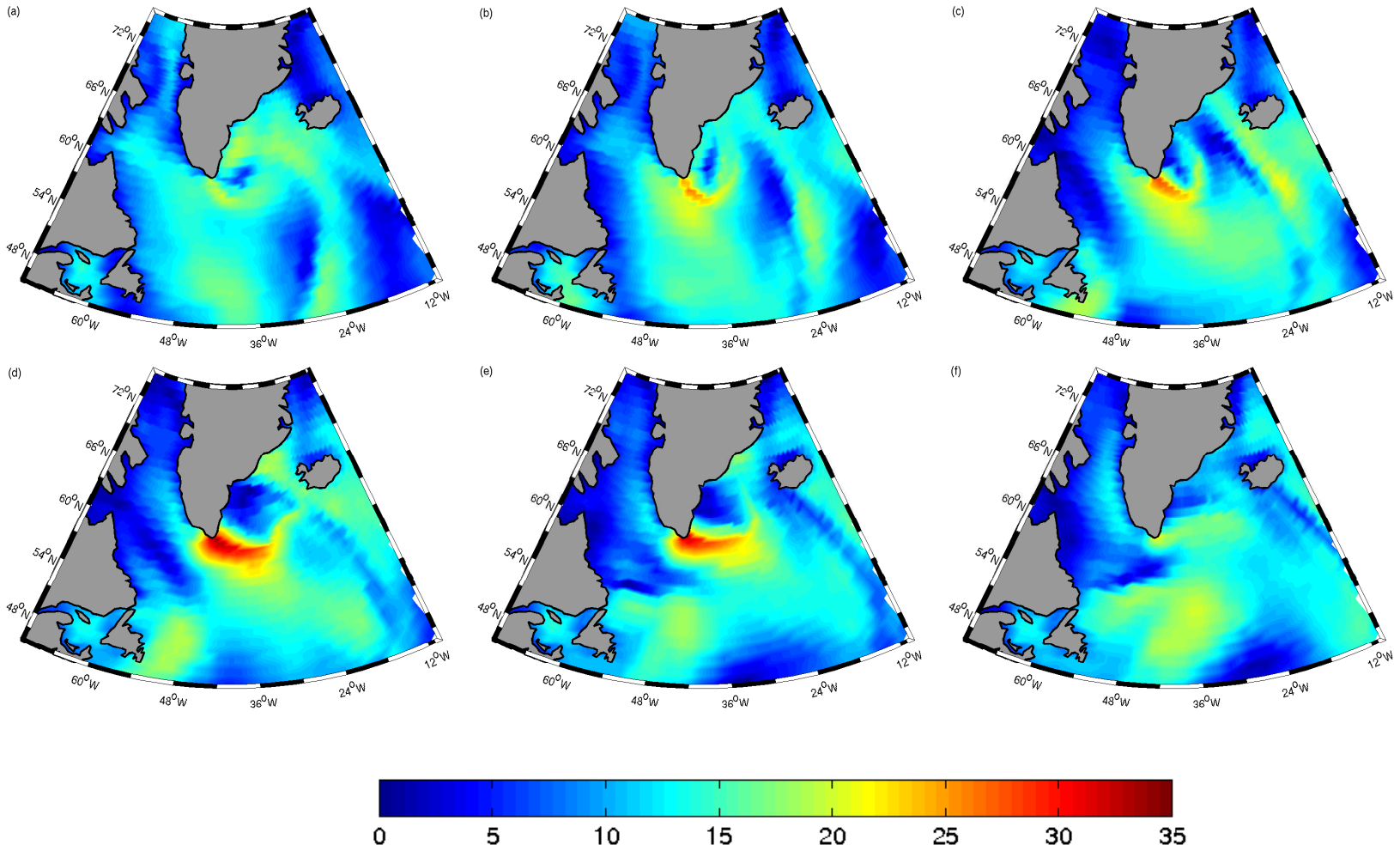

Figure 6.5: 10 metre wind speed at 6-hourly intervals (m s^{-1}) showing the life cycle of a parametrised westerly tip jet. The start of the sequence, panel (a) corresponds to 1800Z, 7th January, 1980.

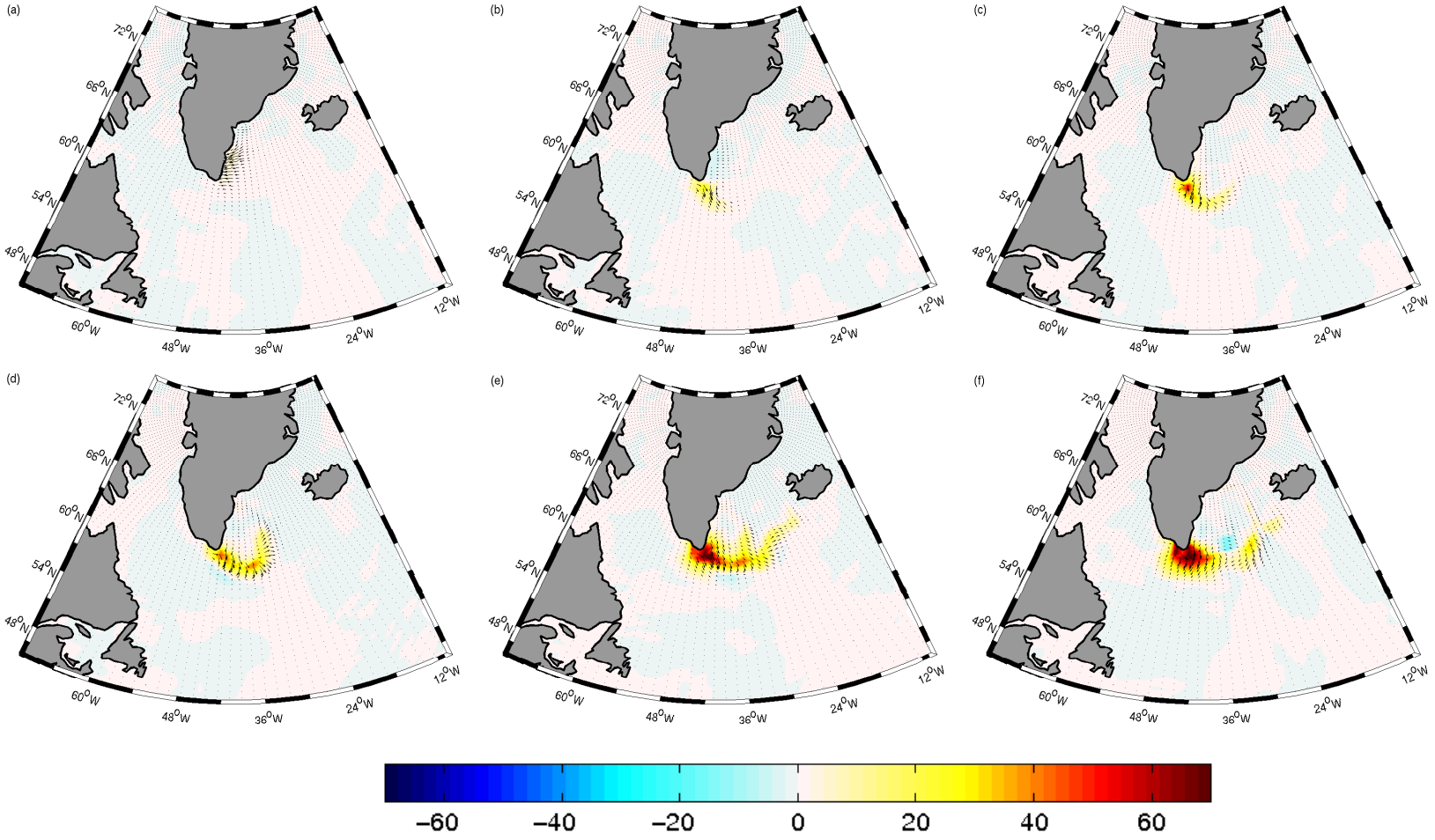

Figure 6.6: Surface horizontal velocity anomaly at 6-hourly intervals (cm s^{-1}) during a westerly tip jet event. The start of the sequence, panel (a) corresponds to 1800Z, 7th January, 1980.

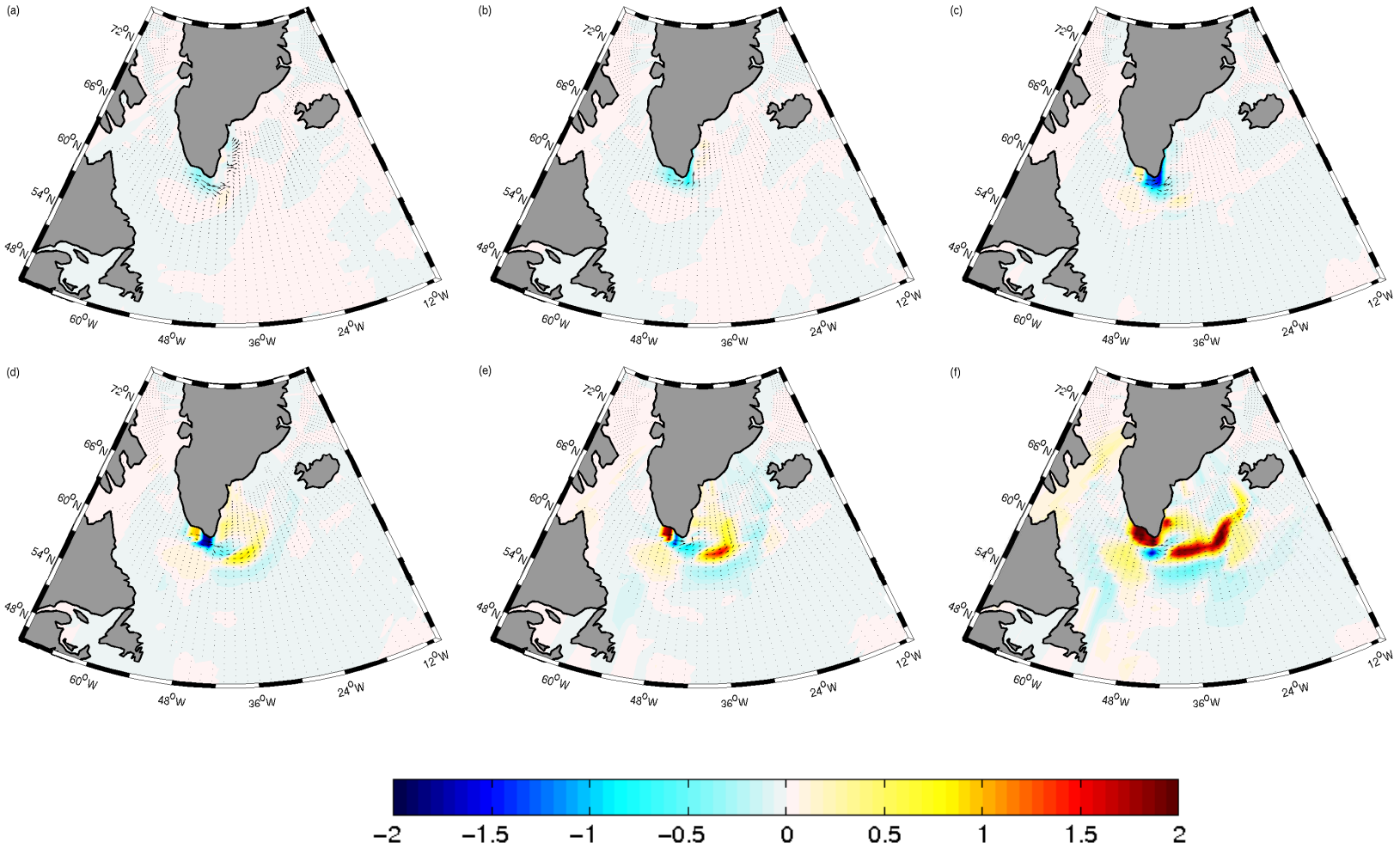

Figure 6.7: Horizontal velocity anomaly on model level 6 (450 m) at 6-hourly intervals (cm s^{-1}) during a westerly tip jet event. The start of the sequence, panel (a) corresponds to 1800Z, 7th January, 1980.

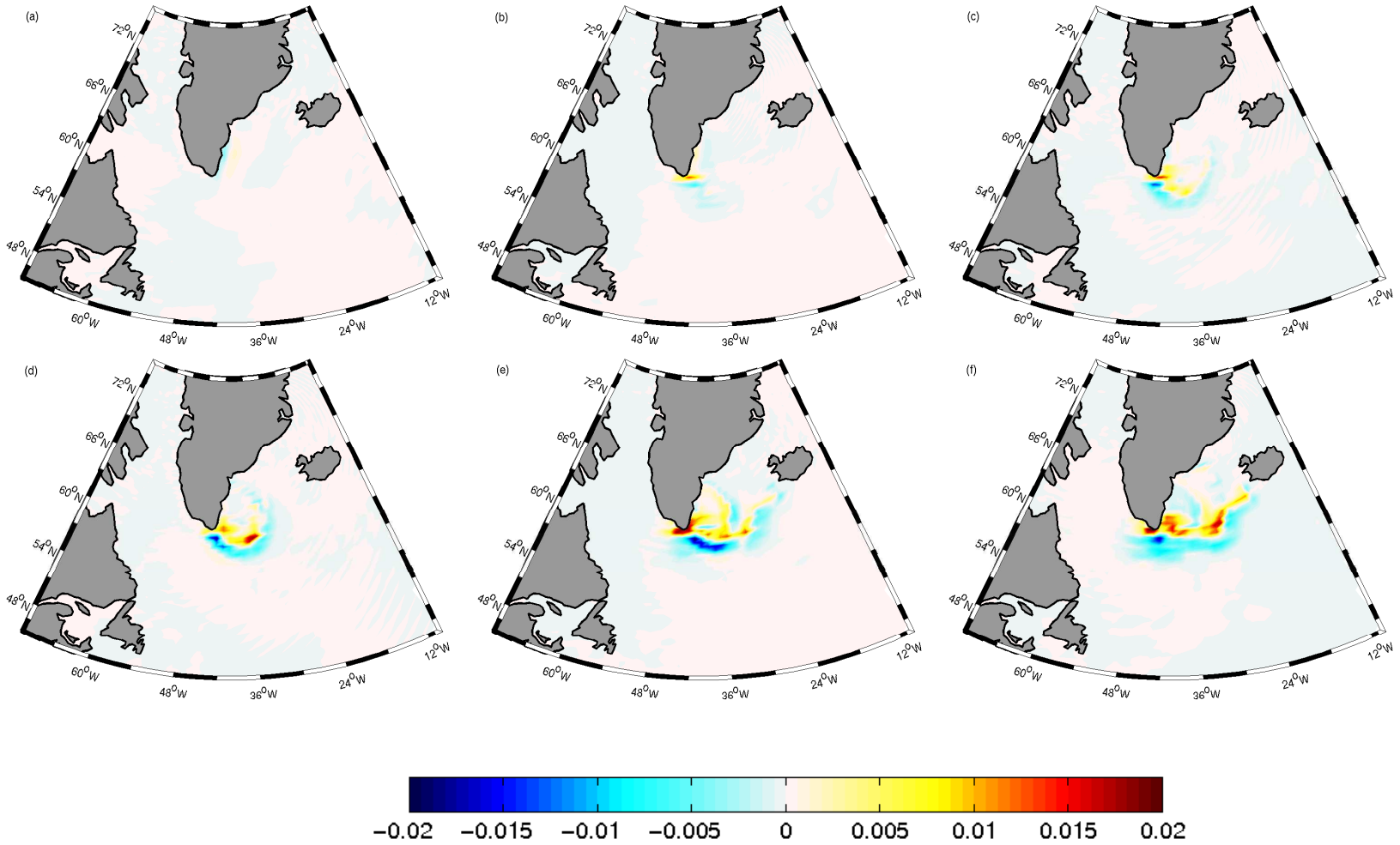

Figure 6.8: Surface vertical velocity anomaly at 6-hourly intervals (cm s^{-1}) during a westerly tip jet event. The start of the sequence, panel (a) corresponds to 1800Z, 7th January, 1980.

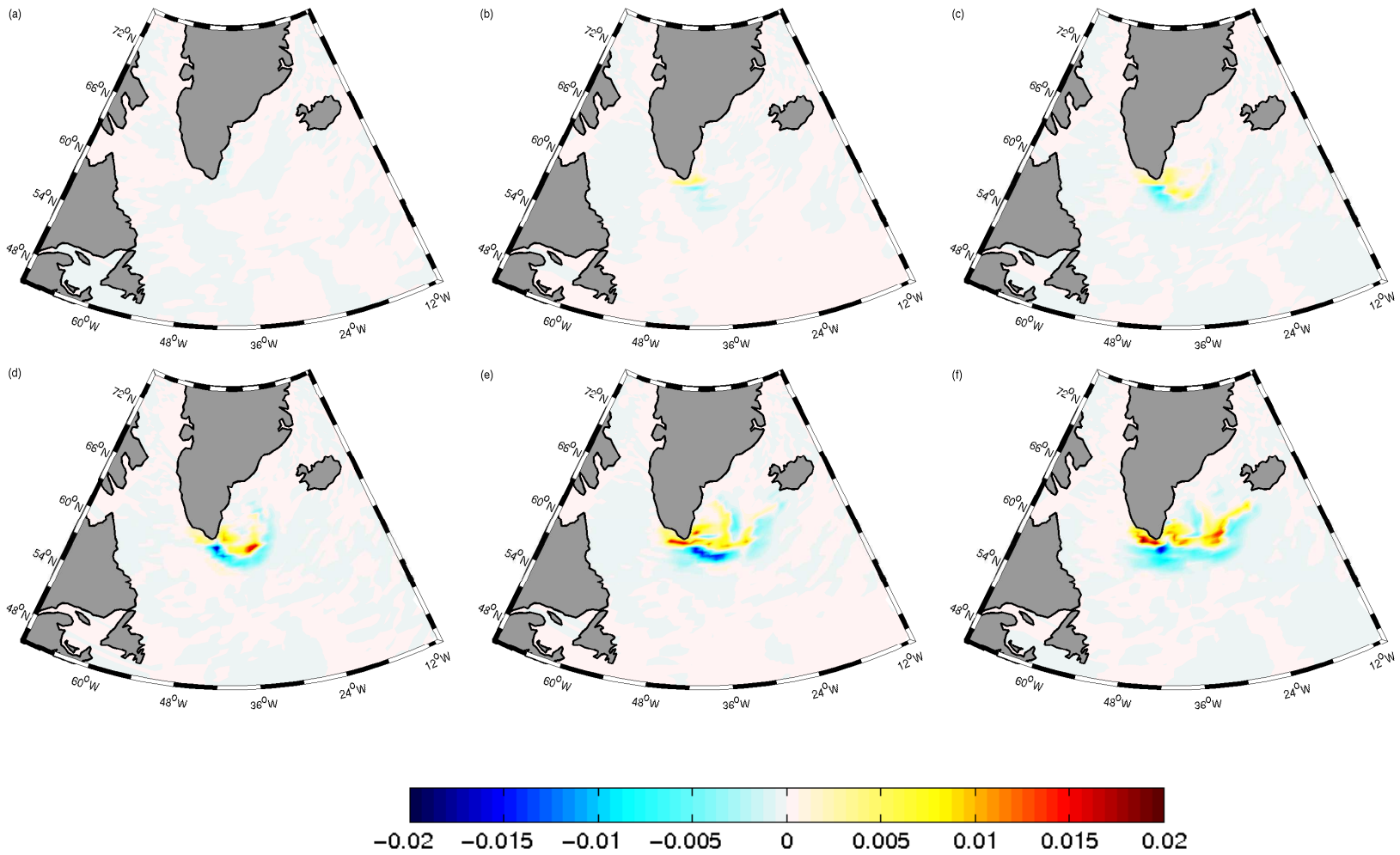

Figure 6.9: Vertical velocity anomaly at 6-hourly intervals (cm s^{-1}) during a westerly tip jet event on model level 6 (450 m). The start of the sequence, panel (a) corresponds to 1800Z, 7th January, 1980.

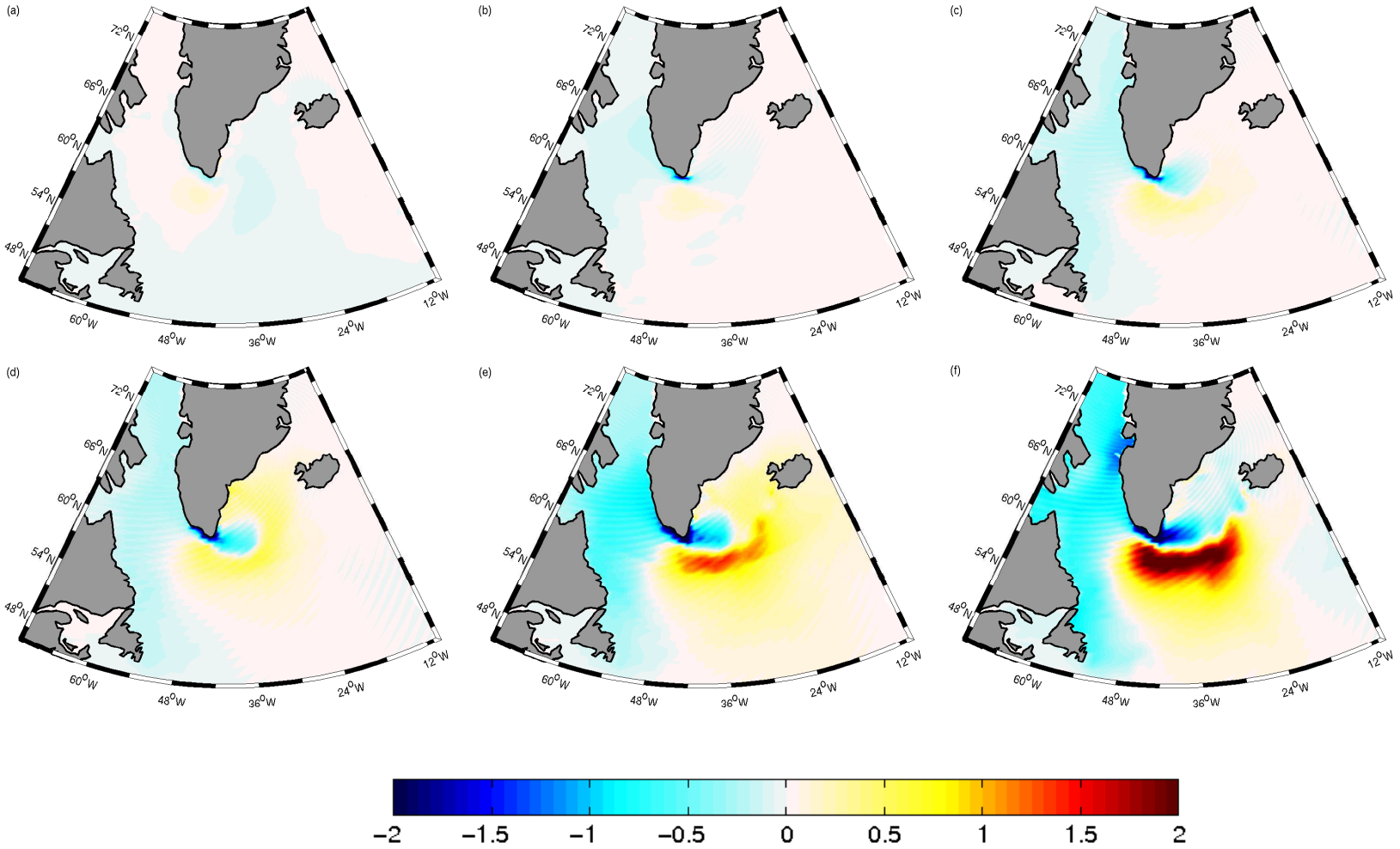

Figure 6.10: Free surface elevation anomaly at 6-hourly intervals (cm) during a westerly tip jet event. The start of the sequence, panel (a) corresponds to 1800Z, 7th January, 1980.

aligned with the direction of the wind stress associated with the tip jet, but is directed mainly towards the south as a result of Ekman transport and a loss of geostrophic balance in the flow. The anomaly increases in magnitude roughly in synchrony with the tip jet, peaking 6 hours after the strongest wind speeds are observed. The surface anomaly becomes the dominant feature in the surface flow field, reaching up to 70 cm s^{-1} at its peak, in comparison to the mean flow, which peaks at around 10 cm s^{-1} in the East Greenland Current (EGC). Although the velocity response of the surface ocean is large, it is confined to the area directly underneath the tip jet and does not propagate away from this source region. The response is also transient; it decays quickly, becoming indistinguishable from the background state after approximately 1 day.

As one may expect, the response to the enhanced surface forcing is very baroclinic, and decays rapidly with depth. At 450 m depth (Figure 6.7) the response reaches a maximum of only around 2 cm s^{-1}. At this depth the response is also less coherent, appearing as a wave-like anomaly which propagates much further away from the source region, probably through the generation of internal waves by the enhanced wind stress at the surface (Garrett and Munk, 1979).

In Figures 6.8 and 6.9 we can see the vertical velocity anomaly at the surface and at 450 m (model level 6) respectively. The general pattern is a strong upwelling on the north flank of the jet and a down-welling on the south flank, driven by the strong dipole of wind stress curl associated with the narrow area of strong winds typical of a tip jet. Note that although these maps are showing anomalies, these dominate over the background vertical velocities in the model and so can be directly interpreted as areas of upwelling or down-welling. In contrast to the horizontal velocity anomalies, the vertical anomalies are rather barotropic and show little variation within the upper 1000 m of the ocean. These upwelling and down-welling regions correspond to a continuum response to the increase in divergence and convergence respectively at the surface, forced by the anomalous wind stress curl; so-called Ekman pumping and suction. The typical vertical velocities seen in the unperturbed integration in this area are around 10^{-5} cm s^{-1}, in good agreement with observations (Johnson *et al.*, 2001). The perturbed values peak at around 2×10^{-3} cm s^{-1}, somewhat stronger than is typical of observed areas of enhanced oceanic upwelling associated with strong synoptic systems (Ren *et al.*, 2004).

The sea surface height anomaly (Figure 6.10) pattern shows a dipole-like structure just to the south of Cape Farewell, with a minimum immediately to the south and east of the Cape, and lowered sea-surface heights throughout the Labrador Sea. Further to the south of Cape Farewell we see a strong maximum in sea-surface height, increasing throughout the period of enhanced forcing to a maximum of 2 cm. This dipole leads to a short-lived increase in the north-south gradient of sea-surface height, reminiscent of the second empirical orthogonal function (EOF) of sea-surface height in a wind stress only model integration shown by Häkkinen (2001), suggestive that the tip jet may have a role in setting SSH variability around Cape Farewell. The anomalous structure shown in Figure 6.10 again dissipates within about a day of the end of the period of enhanced atmospheric forcing.

6.2.2 An Easterly Jet

In Figure 6.11 we can see the first strong easterly tip jet event of the integration, with the start of the sequence on the 24th of January, 1980. In Figure 6.11(a) there are no high wind speeds around Cape Farewell associated with an easterly jet, however there is an area of fairly strong winds, approximately 15 m s^{-1} to the south-west of Cape Farewell, associated with a synoptic-scale cyclone. In panel (b), we can see that the area of strong winds has moved north and has approached Cape Farewell, causing the parametrisation to insert an easterly tip jet into the wind field. This increases the maximum wind speed around Cape Farewell to around 20 m s^{-1}. Six hours later the cyclone has again moved further north, causing a strong barrier flow to form off the south-east coast of Greenland, which the parametrisation accelerates into a very robust easterly tip jet (panel c). Peak wind speed are now around 35 m s^{-1}. Over the next 18 hours, the cyclone continues to track slowly north, and the parametrisation weakens the tip jet (panel d) before switching off as the wind field around Cape Farewell slackens (panels e and f).

In general, the local fast response of the ocean to the easterly tip jet is very similar to that of the westerly tip jet. The upper ocean responds quickly and strongly to the enhanced wind stress, with a velocity anomaly of up to 70 cm s^{-1} at the surface during the tip jet (Figure 6.12 b–d), which quickly decays once the enhanced forcing is no longer present. It should be noted, however, that the easterly tip jet enhances the surface flow

in the direction in which it is already flowing, i.e. it acts to enhance the flow along the eastern Labrador Sea arm of the subpolar gyre. Again, however, this velocity response is confined to the upper ocean, with a maximum response of only around 1 cm s^{-1} at 450 m depth (not shown).

The vertical velocity response at the surface (Figure 6.13) and at mid-depth (450 m, Figure 6.14) is again rather similar to the westerly jet, showing strong upwelling and down-welling regions of up to 10^{-3} cm s^{-1} with little variation in the vertical. As we have already seen, vertical velocity anomalies of this magnitude dominate over the mean flow, so these are genuinely up- and down-welling regions. Interestingly, the vertical velocity response to the easterly tip jet initially shows a dipole structure, as did the response to the westerly jet. However, as the easterly jet weakens, the anomaly develops into a tripole/wave-like structure, with two zonally oriented down-welling regions flanking an upwelling region of similar strength. This is in contrast to the response of the westerly jet, which showed only a dipole structure which gradually loses coherence as the enhanced forcing passes. This difference in behaviour is most likely due to the fact that that the easterly tip jet is, in this instance, fairly consistent in both size and location, whereas the extent, curvature and position of the westerly jet changes considerably during the period the parametrisation is active, as the parent cyclone tracks north across the Irminger Sea.

In Figure 6.15 we can see the anomalous response of the free surface to the easterly tip jet, which shows a dipole around Cape Farewell. The response here is comparable to, although in the opposite sense to that of the westerly jet, as the anomalous circulation is anticyclonic. The localised negative anomaly of around 3 cm in the Labrador Sea suggests that the easterly tip jet may play a significant role in the spin-up or maintainance of the recirculating feature in the south-east Labrador Sea first seen by Lavender *et al.* (2000). Although it cannot be seen from Figure 6.15, this negative anomaly is much more persistent than the positive anomaly associated with the westerly tip jet, as it is enhancing the climatological low in sea-surface height present in the Labrador Sea. This persistence results in a feature such as that seen in Figure 6.15(f) being almost ubiquitous in the winter sea-surface height anomaly field in the model integrations.

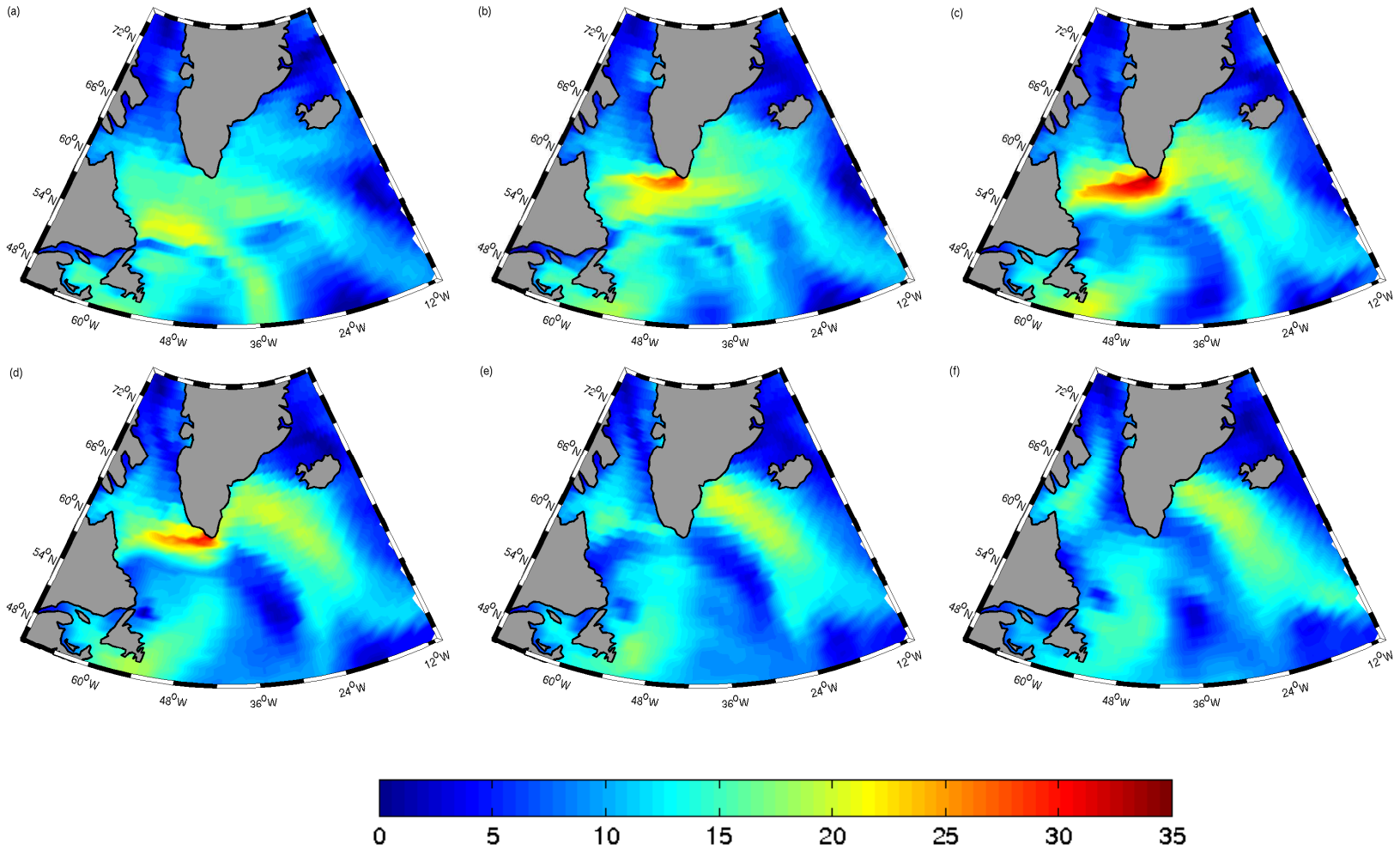

Figure 6.11: 10 metre wind speed at 6-hourly intervals (m s^{-1}) showing the life cycle of a parametrised easterly tip jet. The start of the sequence, panel (a) corresponds to 0000Z, 24th January, 1980.

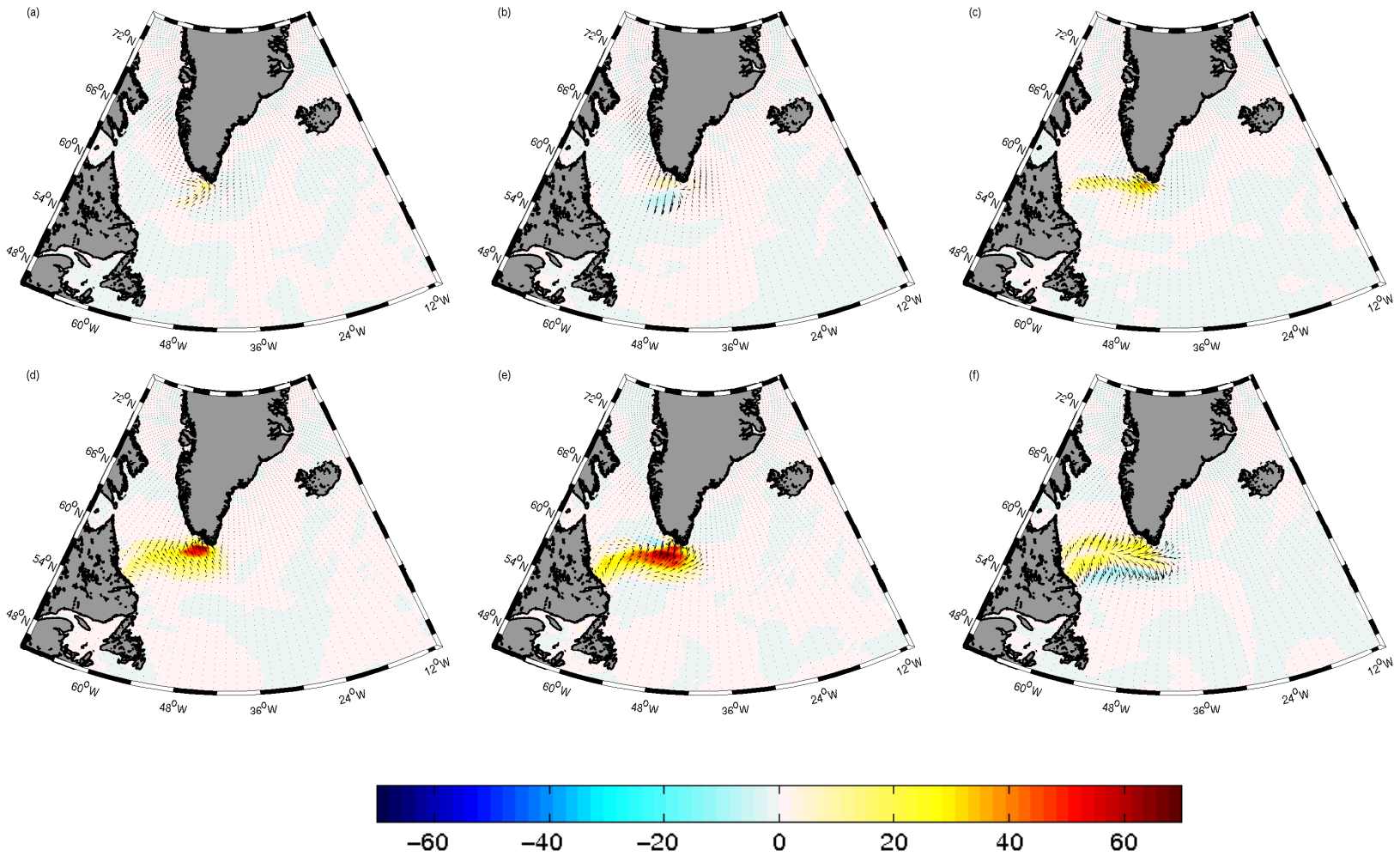

Figure 6.12: Surface horizontal velocity anomaly at 6-hourly intervals (cm s^{-1}) during an easterly tip jet event. The start of the sequence, panel (a) corresponds to 0000Z, 24th January, 1980.

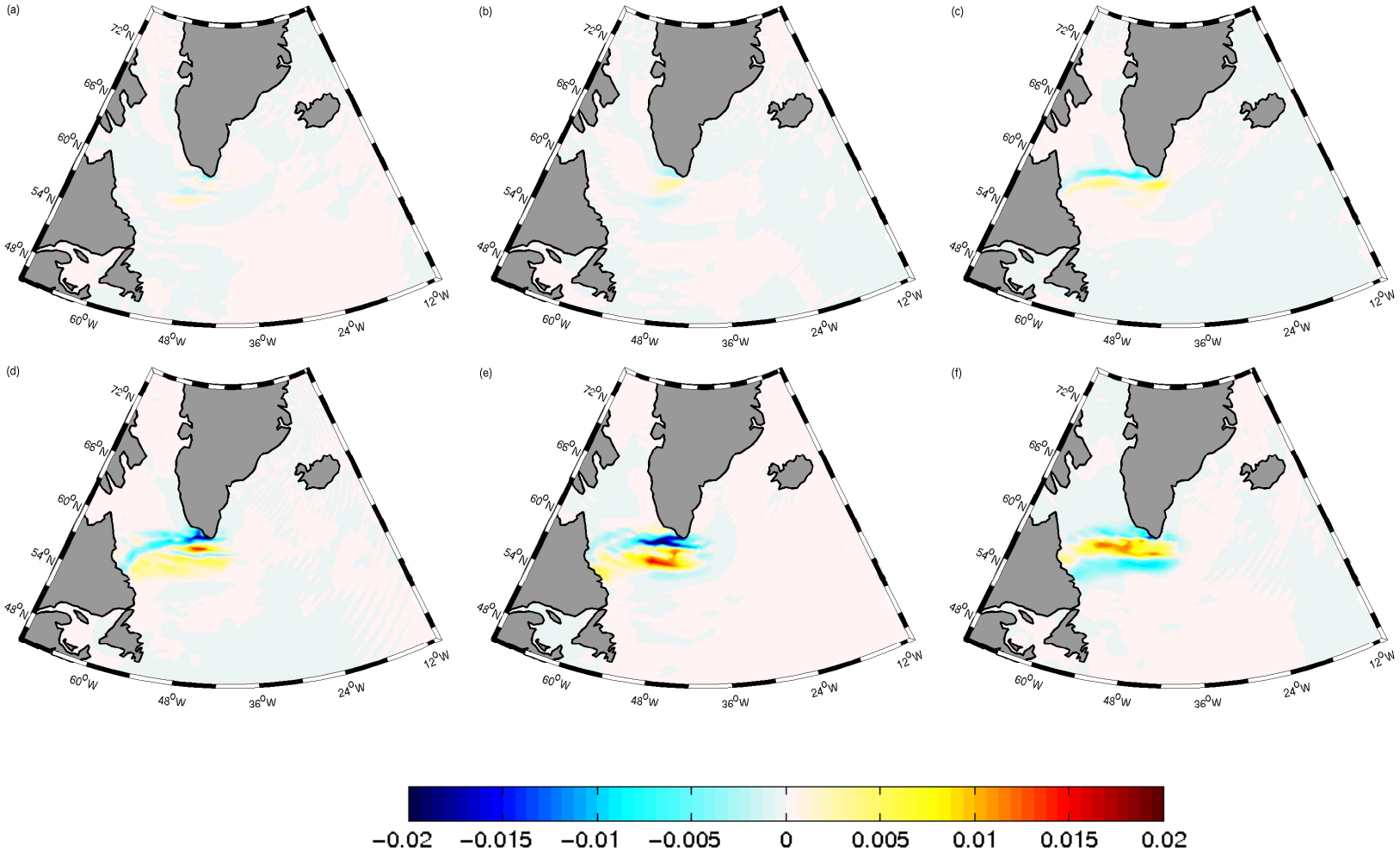

Figure 6.13: Surface vertical velocity anomaly at 6-hourly intervals (cm s^{-1}) during an easterly tip jet event. The start of the sequence, panel (a) corresponds to 0000Z, 24th January, 1980.

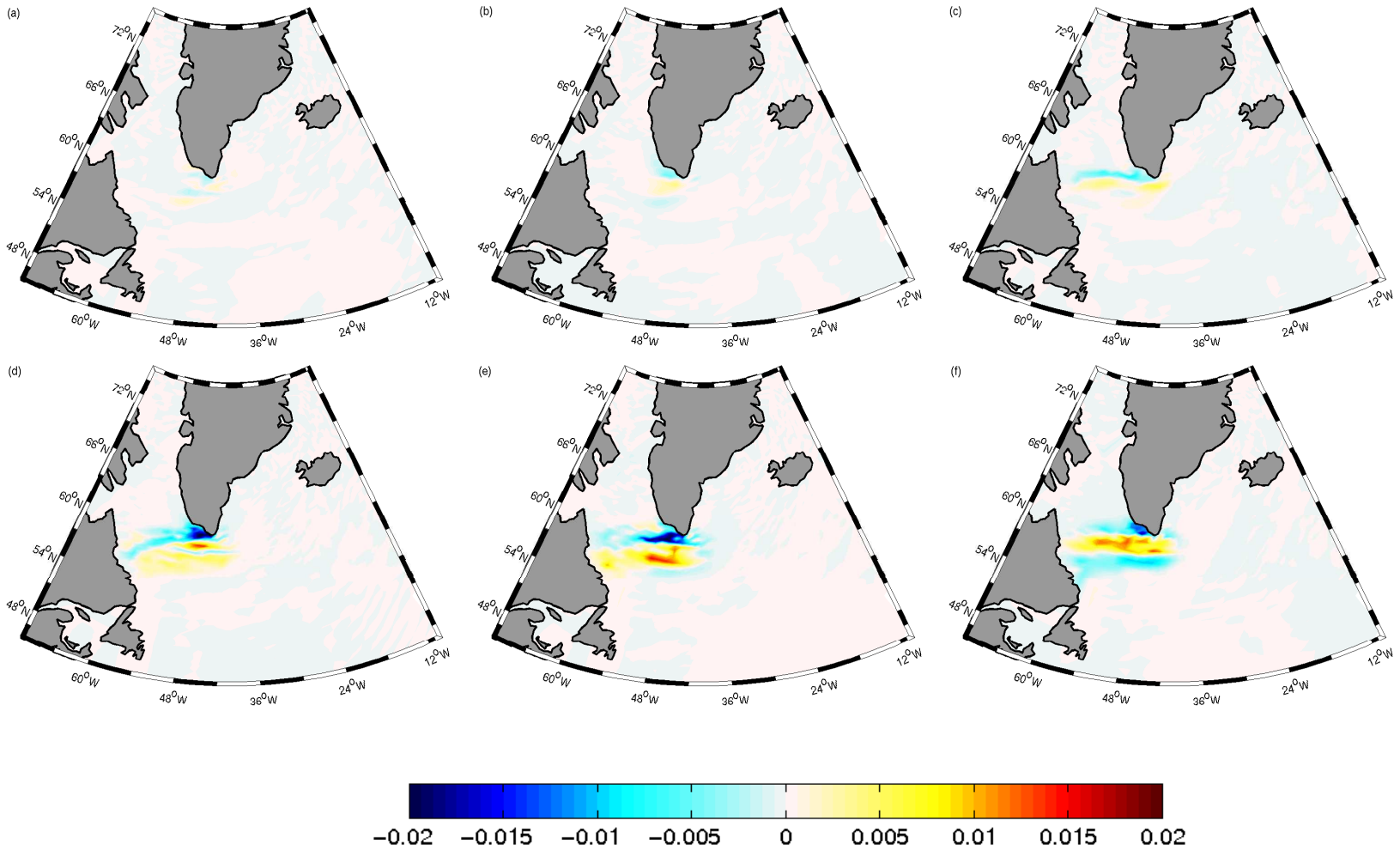

Figure 6.14: Vertical velocity anomaly at 6-hourly intervals (cm s^{-1}) during an easterly tip jet event on model level 6 (450 m). The start of the sequence, panel (a) corresponds to 0000Z, 24th January, 1980.

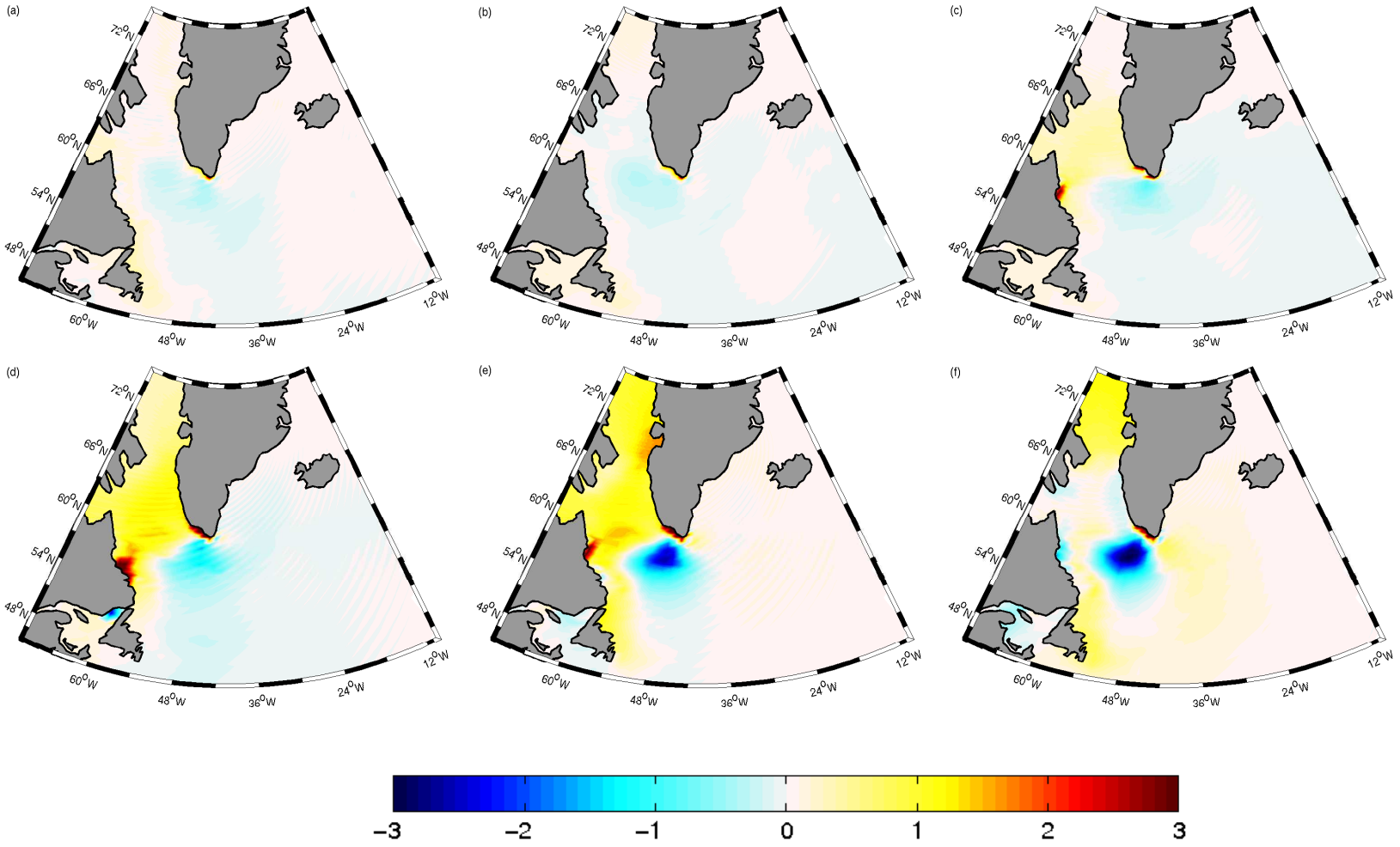

Figure 6.15: Free surface elevation anomaly at 6-hourly intervals (cm) during an easterly tip jet event. The start of the sequence, panel (a) corresponds to 0000Z, 24th January, 1980.

6.3 The Integrated Response to Tip Jets

6.3.1 Upper Ocean Temperatures

Although the ocean around Cape Farewell shows a fairly strong (albeit short-lived) dynamical response to a single tip jet, the short time period over which these occur results in a single tip jet event being unable to cause a significant change in the heat content of the ocean. However, given the high heat fluxes associated with these jets and the frequency with which they occur over a typical winter (Moore, 2003; Moore and Renfrew, 2005), their integrated effect may play a significant role in the modification of the heat content within the North Atlantic subpolar gyre. By altering the heat content of the upper ocean the tip jets may help precondition for, or trigger, open ocean convection and thus alter the production rates of LSW-like mode water in the Irminger and Labrador Seas (Pickart *et al.*, 2003a,b). Figure 6.16 shows the winter (JFM) temperature anomaly at 30 m for the winters of 1980, 1982, 1984, 1990, 1996 and 2000, caused by the westerly tip jet. In 1980 (Figure 6.16a), the anomaly is largely limited to the area directly underneath the climatological westerly jet and appear as a dipole, with a cold anomaly of around 0.1 °C to the north of and directly underneath the jet, and a small positive anomaly of up to 0.05 ° just to the south of this. As the integration proceeds, the negative anomaly of around 0.1 °C persists around Cape Farewell and the advection of this anomaly around the subpolar gyre results in a lesser cooling of 0.05 °C spreading throughout the the Labrador Sea and much of the Irminger Sea. By the end of 1984 (Figure 6.16c), this cooling has spread rather uniformly over much of the western subpolar gyre, however proceeding this the anomaly shows significant interannual variability. Note that from 1984 onwards there are some significant temperature anomalies which develop in the northern Labrador Sea, particularly apparent in the winter of 1996. These anomalies are not directly related to the inclusion of the westerly tip jet into the forcing fields, but rather to the sea-ice fields in the two runs, which tend to diverge at the ice edge. However, there is little evidence that these anomalies spread significantly into the interior of the ocean. Another interesting feature that is apparent in Figure 6.16 is the warming in the central and western subpolar gyre between 48 °N and 54 °N. This first becomes apparent as a very slight warming of 0.01 ° in the winter of 1984, and consistently increases in magnitude until the end of the integration in 2000, when it has strengthened to 0.05 °C. Again, this is not a direct response

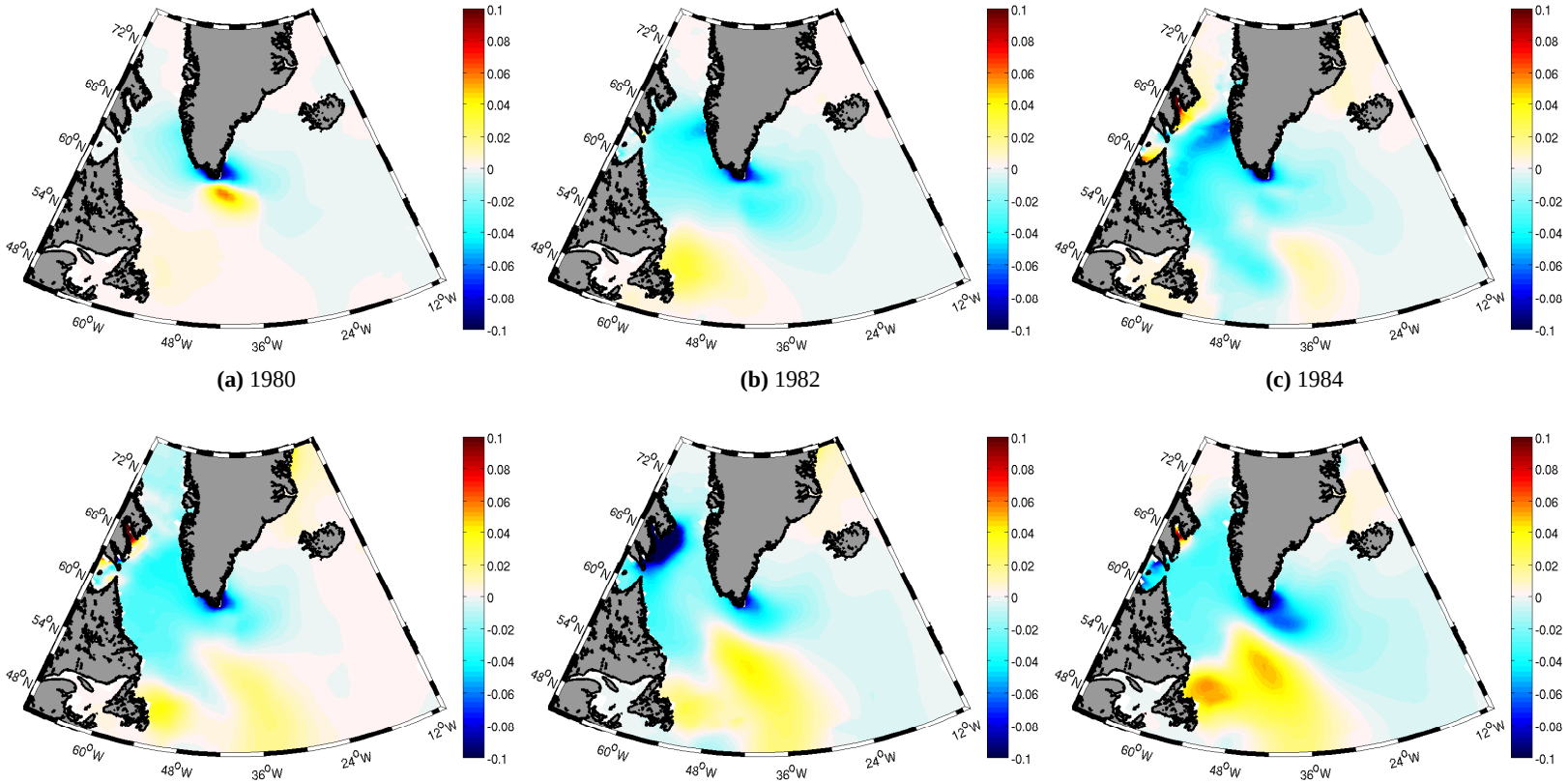

(a) 1980 **(b)** 1982 **(c)** 1984

(d) 1990 **(e)** 1996 **(f)** 2000

Figure 6.16: Annual average temperature anomalies at 30 m caused by the inclusion of the westerly tip jet into the atmospheric forcing fields.

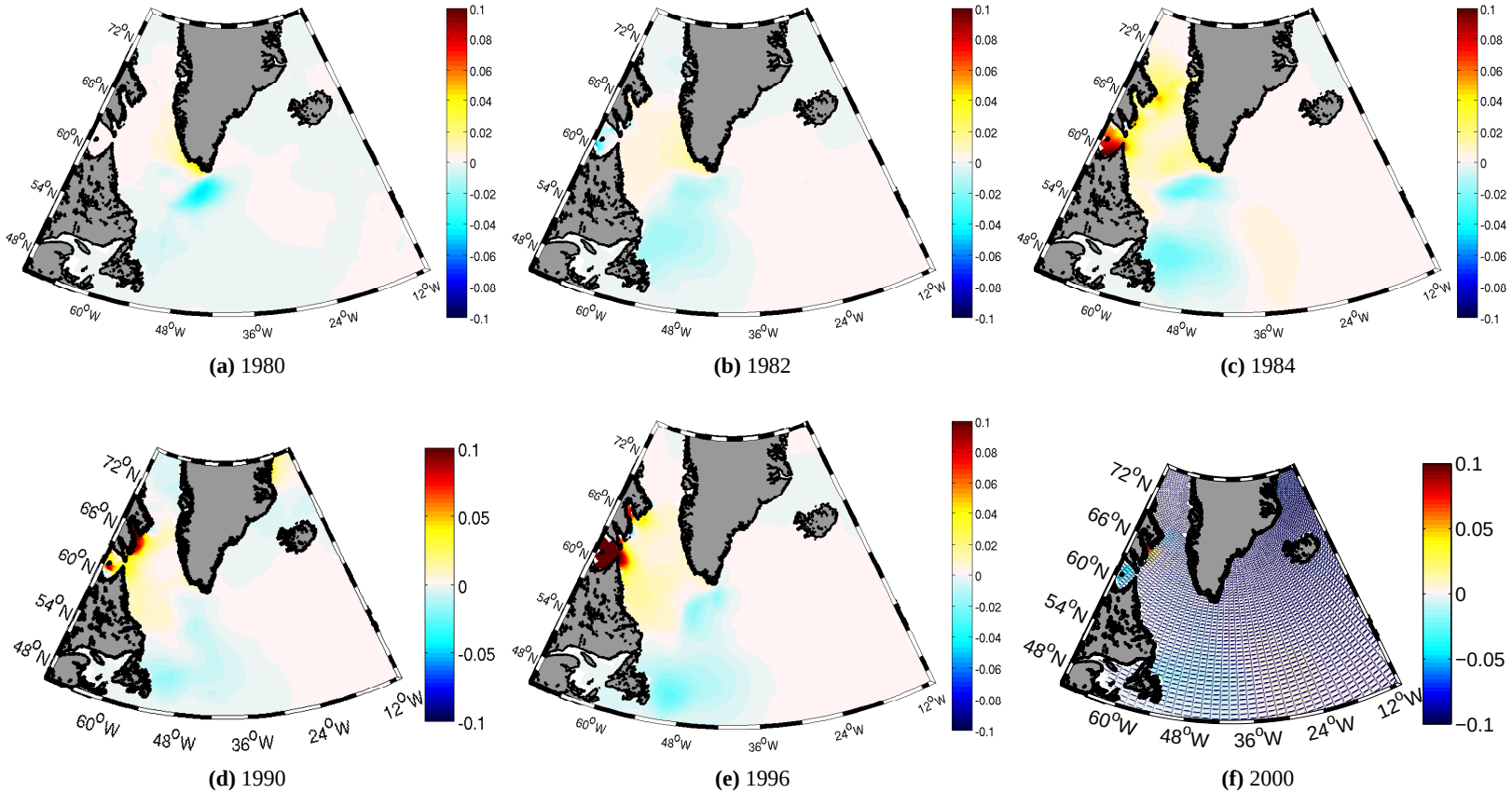

(a) 1980 **(b)** 1982 **(c)** 1984

(d) 1990 **(e)** 1996 **(f)** 2000

Figure 6.17: Annual average temperature anomalies at 30 m caused by the inclusion of the easterly tip jet into the atmospheric forcing fields.

to the heat flux changes imposed by the inclusion of the westerly jet, but is a result of the dynamical response of the ocean to the increased mechanical input and wind stress curl associated with the jet. This causes a redistribution of the advection of heat associated with the North Atlantic current. In particular, there is an increased flow of warm water into the Labrador Sea region. We will discuss this further shortly.

In Chapter 2 we argued, using a global reanalysis, that the atmospheric conditions that are dominant during easterly tip jets were such that these jets were unlikely to trigger open ocean convection in the secondary convection site in the south-east Labrador Sea. In Chapter 5 we saw that when parametrised, the easterly tip jet did not result in significantly altered air-sea heat fluxes. We would expect, therefore, that the inclusion of the easterly tip jet would result in only small changes in oceanic heat content. In Figure 6.17 we can see the changes in ocean temperature caused by the easterly tip jet for the same winters as in Figure 6.16. The easterly jet causes a very slight decrease in temperature of less that 0.02 °C in the vicinity of the easterly tip jet during the first winter of the integration (Figure 6.17a). However, in contrast to the westerly jet, this cooling anomaly does not strengthen and spread in the proceeding years; in fact the largest anomaly due to the inclusion of the easterly jet is seen in the first winter of the integration. By the winter of 2000 (Figure 6.17f) the temperature field is virtually indistinguishable from the control integration. Again, however, note that some relatively large temperature anomalies form of the fringes of the Labrador Sea as the sea-ice fields between the perturbation and control integrations begin to differ.

6.3.2 Mid-depth and Deep Ocean Temperatures

As the westerly tip jet removes a significant quantity of heat from the ocean, this results in an increase in convective activity as the surface waters become more dense. This increase in convection causes the surface temperature anomalies to penetrate deeper into the ocean interior. At 450 m (Figure 6.18) the temperature anomaly closely resembles that of the upper ocean. The cooling directly underneath the jet is slightly smaller at this depth, up to 0.08 °C, and the spatial pattern is somewhat smoother, but the signature of the jet is still clearly visible. The cold anomaly is also able to spread slightly further south at this depth as it is uninterrupted by the strong warming observed at the surface, although this

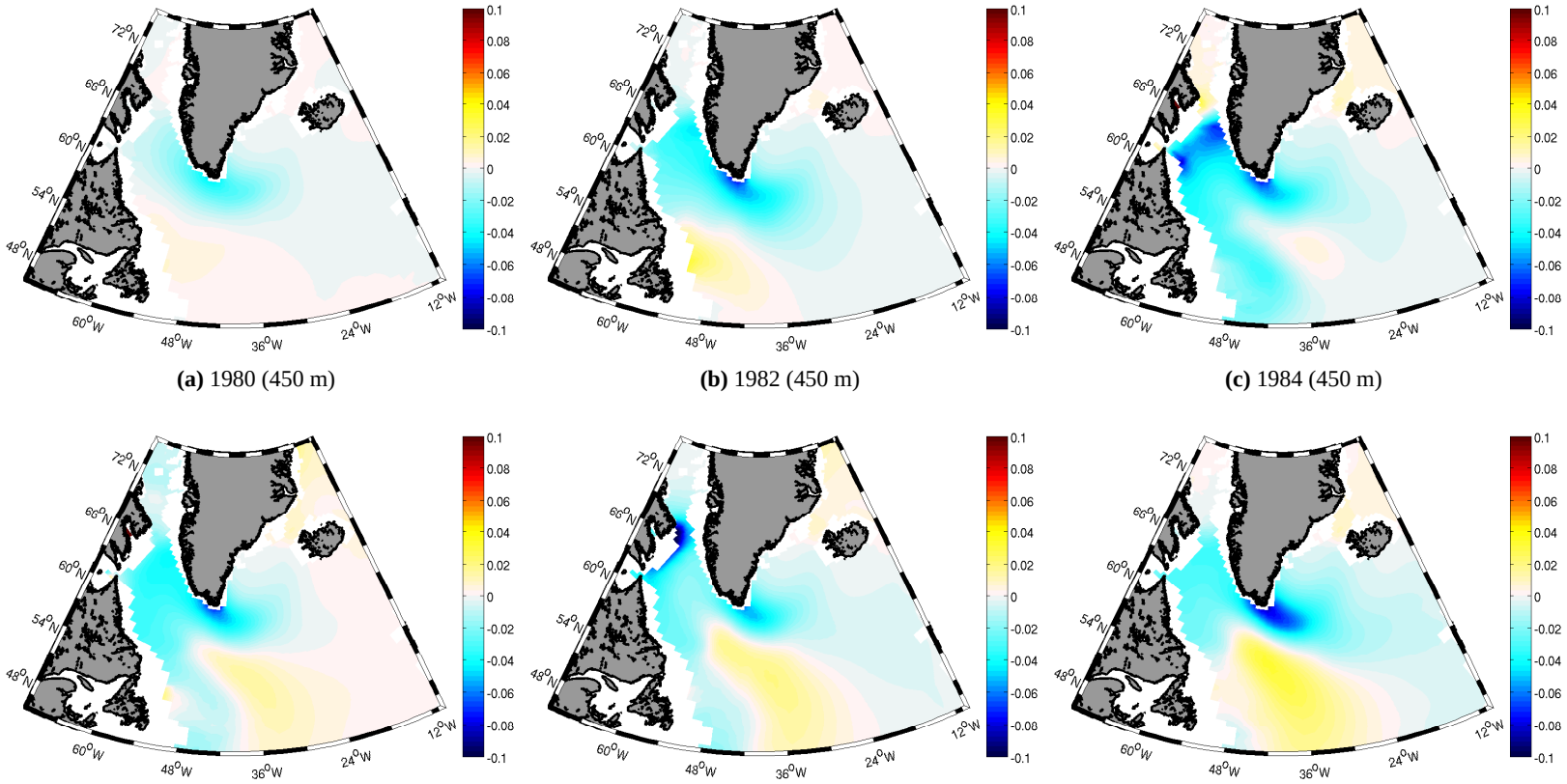

(a) 1980 (450 m) **(b)** 1982 (450 m) **(c)** 1984 (450 m)

(d) 1990 (450 m) **(e)** 1996 (450 m) **(f)** 2000 (450 m)

Figure 6.18: Annual average temperature anomalies at 450 m caused by the inclusion of the westerly tip jet into the atmospheric forcing fields.

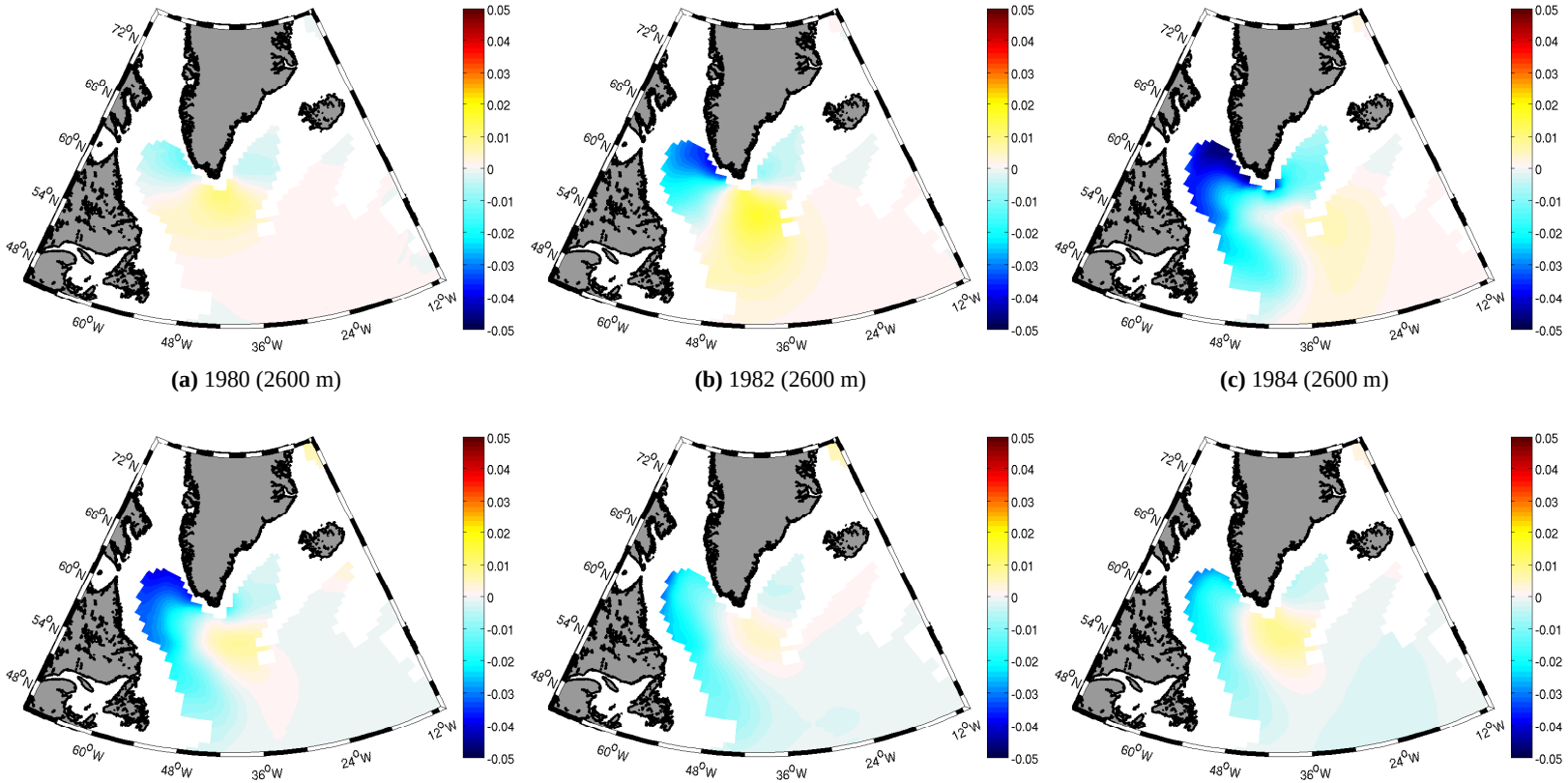

(a) 1980 (2600 m) **(b)** 1982 (2600 m) **(c)** 1984 (2600 m)

(d) 1990 (2600 m) **(e)** 1996 (2600 m) **(f)** 2000 (2600 m)

Figure 6.19: Annual average temperature anomalies at 2600 m caused by the inclusion of the westerly tip jet into the atmospheric forcing fields.

spreading of cool water is generally confined to the western boundary of the basin. The signature of the warm water from the North Atlantic current intruding into the Labrador basin is still apparent at 450 m, particularly from 1990 onwards, although the warming trend is not as strong as was observed in the surface waters, as the meridional temperature gradient decreases with depth.

In Figure 6.19 we can see the temperature anomaly in the deep ocean (2600 m, model level 12) due to the inclusion of the westerly tip jet in the atmospheric forcing fields. The trend directly underneath the tip jet, to the south and south-east of Cape Farewell is of the opposite sign to the temperature anomaly in the same location in the upper ocean, with a warming of up to 0.015 °C. This is because the dominant influence at this depth is not the surface cooling, transmitted to depth by static instability adjustment, but rather the vertical downwards mixing of heat caused by the strong input of mechanical energy at the surface. This results in an increase in the vertical shear in the flow and in turn to increased mechanical mixing. Note that the stratification at this depth is very low, thus any increase in the vertical shear of the flow will increase the vertical mixing as the Richardson number is increased.

On both flanks of this region of warming, in the Irminger and Labrador basins, are areas of cooling. In the Irminger Sea there is a cooling of up to 0.01 °C, which shows little in the way of interannual variability. The cooling is significantly stronger in the Labrador Sea, as the surface induced cold anomaly is advected around the subpolar gyre and into the deep western boundary current. The maximum cooling here is around 0.05 °C in the central Labrador Sea. Furthermore, the anomaly in the Labrador basin shows a distinct variability between winters. This is to be expected given the well documented interannual variability of the frequency of the westerly tip jet (Moore, 2003; Moore and Renfrew, 2005). As an example of this variability consider the winters of 1984 (Figure 6.19b), in which the maximum temperature anomaly at this depth is 0.05 °C, and 2000 (Figure 6.19f), where the anomaly peaks at around 0.015 °C. Thus, in our simulation, the inclusion of the westerly tip jet can account for over 0.03 °C of the interannual variability in temperature at depth within the Labrador basin. Schott *et al.* (2006) looked at the interannual variability in the deep western boundary current east of the Grand Banks, using a combination of moored current meters and shipboard CTD sections and ADCP data. They

included timeseries of temperature at 3000 m depth in the deep western boundary current, which showed only small variations in temperature at both interseasonal and interannual timescales. For example, the temperature at their K102 station (at 3000 m), recorded from mid-1999 to mid-2001 and again from mid-2003 to mid-2005 and showed temperatures generally ranging between 2.4 °C and 2.6 °C with extreme values no less than 2.3 °C and no more than 2.65 °C. The interannual variability at this location thus typically lies around 0.2–0.3 °C. Further studies of the variability of Labrador Sea water facilitated by Ocean Weather Ship Bravo (Lazier, 1980, 1988) suggest interannual variations in the deep water of the Labrador Sea of between approximately 0.15 °C and 0.35 °C, and the variation in the temperature of Labrador Sea Water in the Irminger Basin has been shown to again take similar values (Falina *et al.*, 2007). The variability in deep water temperature ($\sim$0.03 °C) in the Labrador Sea caused by the introduction of the tip jet could thus account for up to around 10% of the variability observed in the temperature of deep waters of the Labrador Sea and its exports further south in the deep western boundary current.

6.3.3 Mid-depth Ocean Velocities

In Figure 6.20 the JFM average mid-depth horizontal velocity anomalies caused by the inclusion of the westerly (a–c) and easterly (d–f) tip jets are shown. The most striking feature visible here is the cyclonic gyre which spins up in the southern Irminger Sea. This gyre is present from the first winter of the integration, and is always present in the velocity anomaly fields thereafter. In the first winter the feature is strongest directly underneath the tip jet, peaking at around 0.2 cm s^{-1}, however there is little signature further north. As the integration progresses this develops into a true gyre-like structure with anomalous velocities approaching 0.3 cm s^{-1} by the winter of 2000. We discussed in Chapters 1 and 2 that in order for open ocean convection to occur a number of prerequisites must be met. One of these is that a local recirculation must be present, which acts to trap water, allowing it to be repeatedly modified by strong atmospheric forcing, and also acts to dome isopycnals thus exposing more weakly stratified water to the atmosphere (Marshall and Schott, 1999). The gyre-like anomaly that we see spinning up in Figure 6.20(a–c) is ideally placed to precondition the area of the Irminger Sea from which the westerly tip jet can remove large quantities of heat (Doyle and Shapiro, 1999; Pickart *et al.*, 2003a; Moore

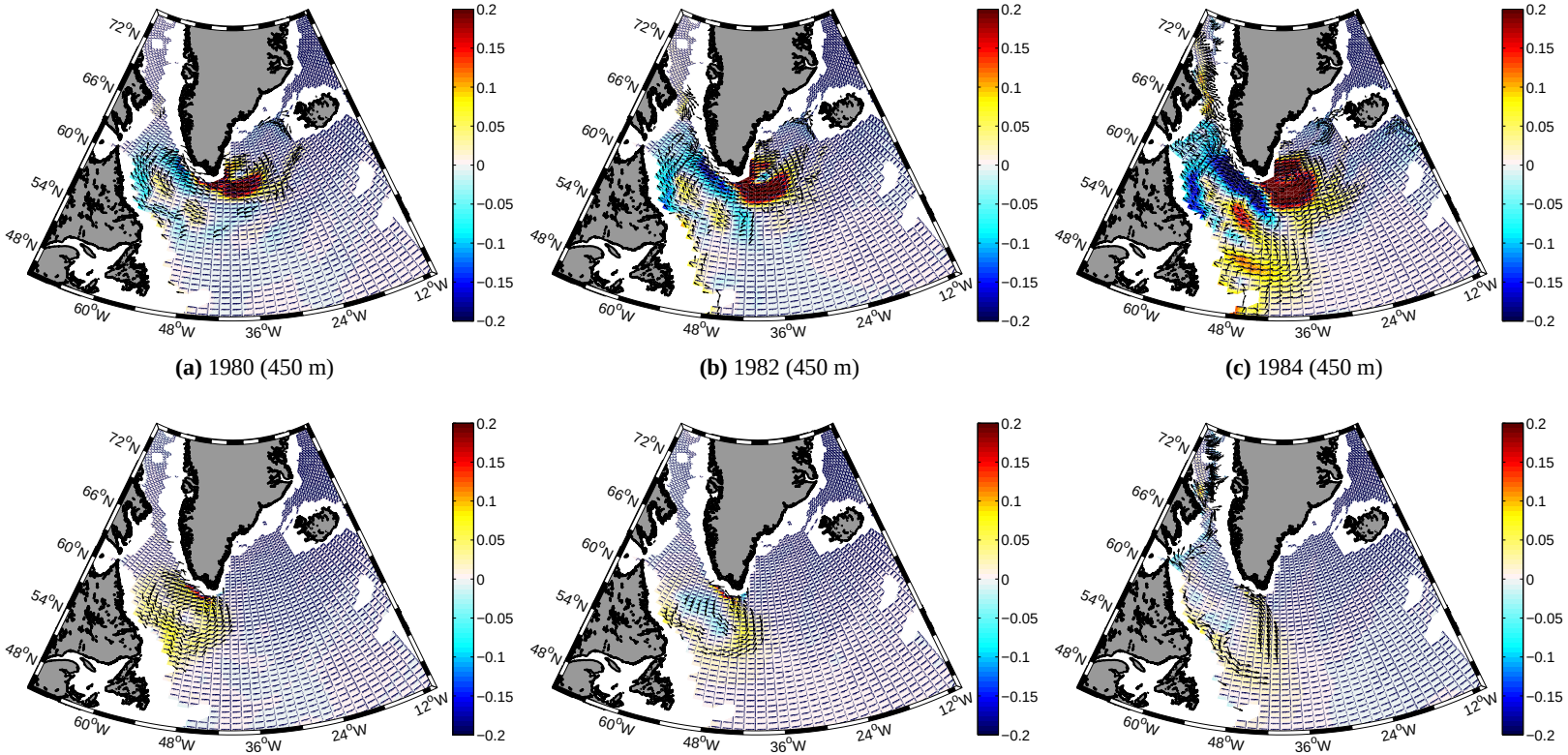

(a) 1980 (450 m) **(b)** 1982 (450 m) **(c)** 1984 (450 m)

(d) 1980 (450 m) **(e)** 1982 (450 m) **(f)** 1984 (450 m)

Figure 6.20: Annual average horizontal velocity anomalies (cm s^{-1}) at 450 m caused by the inclusion of the westerly (a–c) and easterly (d–f) tip jets into the atmospheric forcing fields. Vectors show the direction of the anomaly, plotted where the magnitude of the anomaly exceeds 10^{-2} cm s^{-1}.

and Renfrew, 2005). If deep convection does indeed occur in the Irminger Sea, therefore, the westerly tip jet may play an important role in preconditioning for and triggering convection in the Irminger Sea.

A second interesting feature apparent here is the weakening of the flow around the subpolar gyre in the Labrador Sea of up to 0.2 cm s^{-1}. This weakening is maintained throughout the integration, with winter mean anomalies generally lying between 0.1 and 0.2 cm s^{-1}. We discussed in the previous section the warming anomaly which occurred south of Cape Farewell and strengthened throughout the integration. We attributed this to an increased flow of relatively warm water from the Gulf Stream extension into the Labrador Sea and this is clear to see in Figure 6.20, with a peak anomaly of 0.1 cm s^{-1} in the southern Labrador Sea (e.g. in 1984). After this, the anomaly is present for the remainder of the integration, gradually growing to just in excess of 0.15 cm $s-1$ by the winter of 2000.

The response of the ocean at this depth to the easterly tip jet is weaker than to the westerly jet (Figure 6.20 d–f). There is a slight increase in the cyclonic flow around the Labrador Sea, particularly in the winter of 1980 when the velocity anomaly exceeds 0.05 cm s^{-1}, however this response weakens, and, for example in 1984 there is almost no deviation form the mean flow. The reasons for this weak response to the easterly tip jet are likely twofold. Firstly, as we have discussed, slightly fewer easterly than westerly tip jets are parametrised into the forcing fields. Secondly, as the easterly tip jet does not remove a significant amount of heat from the ocean surface, it does not increase convective activity and thus the increased momentum added at the surface is not effectively mixed downwards.

6.3.4 Deep Ocean Velocities

The velocity anomalies seen in the deep ocean (2600 m, Figure 6.21) are qualitatively similar to those seen at mid-depths. The westerly tip jet (Figure 6.21 a–c) results in a spin-up of the Irminger gyre in excess of 0.1 cm s^{-1}. This is of comparable magnitude to the anomaly seen much further up in the water column – i.e. the velocity response to the westerly jet in the Irminger basin is rather barotropic. Pickart *et al.* (2003a) noted that the Irminger gyre is extremely in barotropic nature, explaining why it is not readily

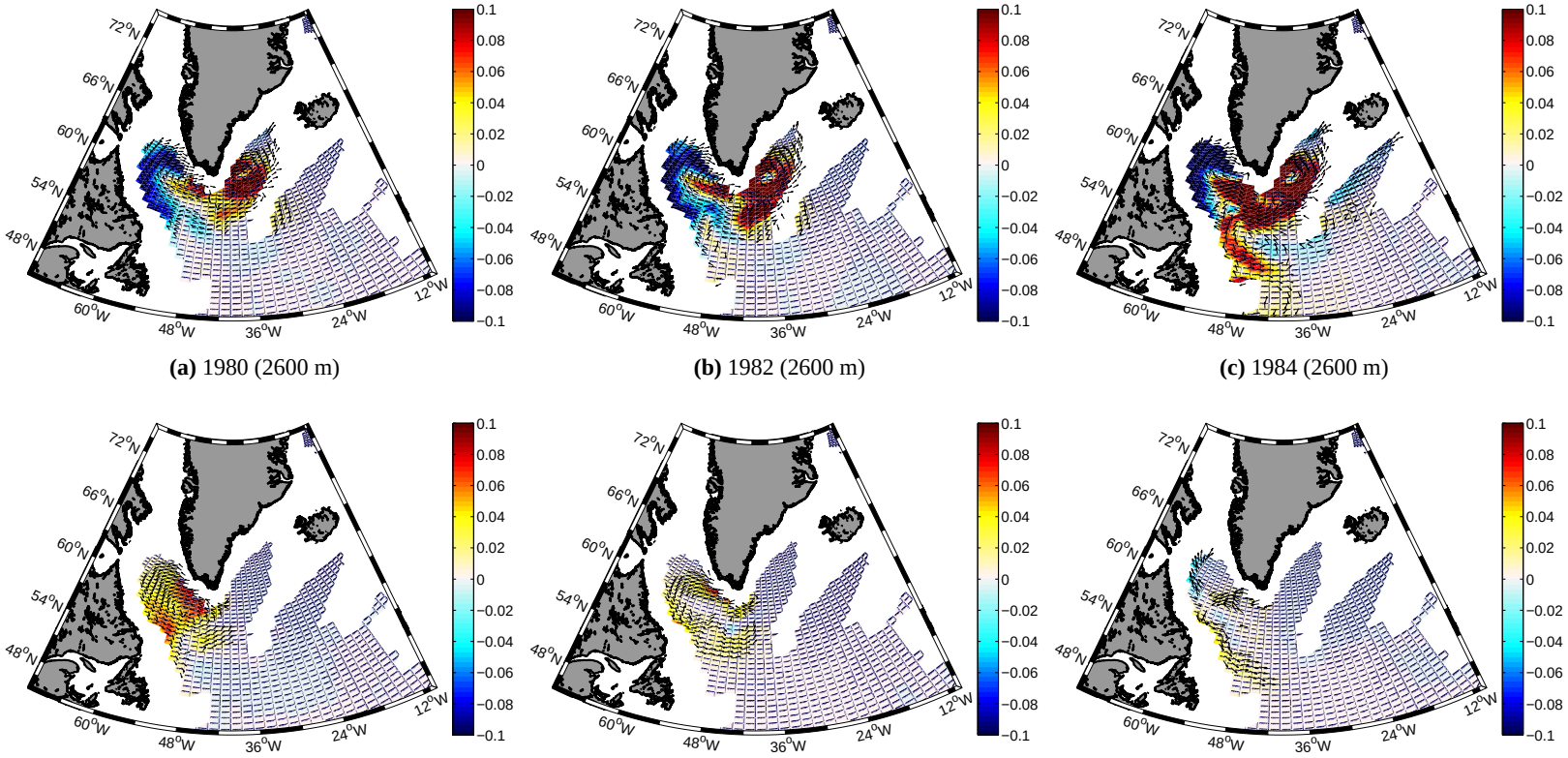

(a) 1980 (2600 m) **(b)** 1982 (2600 m) **(c)** 1984 (2600 m)

(d) 1980 (2600 m) **(e)** 1982 (2600 m) **(f)** 1984 (2600 m)

Figure 6.21: Annual average horizontal velocity anomalies (cm s^{-1}) at 2600 m caused by the inclusion of the westerly (a–c) and easterly (d–f) tip jets into the atmospheric forcing fields. Vectors show the direction of the anomaly, plotted where the magnitude of the anomaly exceeds 10^{-2} cm s^{-1}. Note the different colour scale to Fig. 6.20.

observed in the geostrophic velocities derived from T/S sections. It was thus not well observed until the mid-depth float displacement analysis of Lavender *et al.* (2000). The decrease in flow around the Labrador Sea is still apparent, particularly in the earlier years of the integration, when it is up to -0.1 cm s^{-1}. However there is a strengthening of the flow into the Labrador Sea (around 56 $^\circ$ N) which, as the integration progresses, leads to a slight acceleration of the deep western boundary current of up to 0.08 cm s^{-1}. However, this acceleration is only observed between the southern Labrador Sea and the Flemish Cap (Figure 6.21c).

The easterly tip jet again has very little impact on the model flow field, with only a very slight increase in the cyclonic flow around the Labrador Sea of up to 0.06 cm s^{-1}. It is worth noting that all of the mean velocity anomalies at depth are rather small. For example, at mid-depth, typical velocities in the subpolar gyre are around 5 cm s^{-1} (Lavender *et al.*, 2000). The westerly jet caused velocity anomalies typically of around 0.2 cm s^{-1}, or 5% of the mean flow, while the easterly jet made a much smaller difference. The deep western boundary current may be assumed to flow at around 10 cm s^{-1}—a conservative estimate, see for example Fischer and Schott (1997) and Rhein (1994)—and typical velocity anomalies at the depth of the deep western boundary current are 0.1 cm s^{-1}, or 1% of the mean flow.

6.3.5 Mixed-Layer Depth

One of the most important questions which must be addressed when considering the impact of Greenland's tip jets on the oceans is the ability of these jets to alter the production rates, and thus the volumes of, deep mode water in the northern subpolar gyre, be it canonical Labrador Sea Water or its slightly warmer, more saline Irminger Sea counterpart. We have addressed this question in a rather idealised 1-dimensional fashion for both the easterly and, briefly, westerly tip jets in Chapters 2 and 5, respectively. In this section and the next we consider changes in the mixed-layer depth and potential vorticity signals as indicators for changes in the production of mode water in the somewhat less idealised framework of the FRUGAL OGCM.

Figure 6.22 shows the anomalies in mixed-layer depth caused by the inclusion of the westerly and easterly tip jets averaged over the first and final winters of the integration,

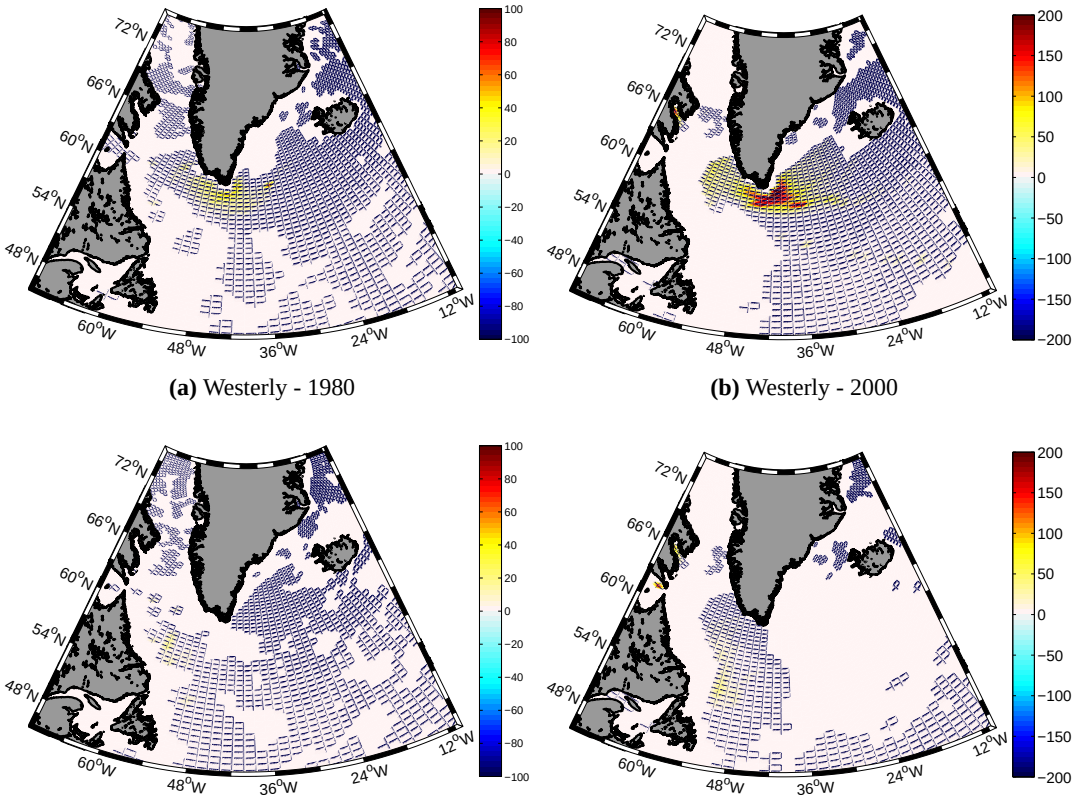

(a) Westerly - 1980 **(b)** Westerly - 2000

(c) Easterly - 1980 **(d)** Easterly - 2000

Figure 6.22: January-February-March average mixed-layer depth anomalies in the first and final years of the integration caused by inclusion of the westerly and easterly tip jets into the atmospheric forcing fields.

calculated as described in Section 6.1.3.1. The first point of note is that the easterly jet causes virtually no difference in the model mixed-layer depth. This is in good agreement with the work presented in Chapter 2, where we used a mixed-layer model and considerations of the synoptic-scale atmospheric state to argue that easterly tip jets were unable to force convection in the south-eastern Labrador Sea. This is because the ocean-atmosphere temperature and humidity gradients are simply not large enough to result in large heat fluxes. Recall from the bulk flux equations that without these air/sea temperature and humidity differences that the speed of the wind is largely immaterial in modifying the heat fluxes. One should also recall here, however, that although the relatively high resolution NARR fields suggest that there is no temperature or humidity gradient associated with the tip jets, it is possible that these are simply not represented in the reanalysis, but do exist. In this case we could be underestimating the true magnitude of both the easterly and westerly tip jet heat fluxes. It may seem surprising that the increased mechanical energy does not

lead to a deepening of the mixed-layer, however one must remember that the mixed-layer in the Labrador Sea is already extremely deep (particularly in the FRUGAL model, as will discussed shortly) and so this extra momentum which is added to the ocean surface by the parametrisation simply does not penetrate deep enough to cause a significant change in shear-driven mixing across the base of the mixed-layer.

In contrast, the westerly jet causes a significant and systematic increase in the depth of the mixed-layer around Cape Farewell and over much of the southern Irminger Sea. In Figure 6.22a we can see a relatively small and localised increase of up to 45 m in the mixed-layer depth. This anomaly grows each winter for the first few years of the integration, reaching a maximum of 150 m in JFM 1982 and 200 m in JFM 1984, which then remains the typical winter maximum anomaly for the rest of the integration. This deepening of the order of 200 m is fairly consistent with 1-dimensional studies of tip jet induced mixed-layer deepening. For example, Våge *et al.* (2009a) saw between 100 m and $\sim$400 m of mixed-layer deepening in response to the westerly tip jet, depending on the strength of the winter (related to the phase an magnitude of the NAO). Furthermore, in the previous chapter we used fluxes generated by the tip jet parametrisation to drive a 1-dimensional model, and observed a deepening of around 300 m. Despite this consistent response, this should only be considered indicative of the true response of the mixed-layer, as the stratification in the Labrador and Irminger Seas in the FRUGAL model is significantly weaker than in reality. This is due both to the coarse vertical resolution in FRUGAL and the importance of the mesoscale and sub-mesoscale in restratifying the ocean after the cessation of deep convection (Jones and Marshall, 1997). For example the presence of Irminger Rings (IRs; small, warm-cored eddies shed from Cape Desolation, north-west of Cape Farewell) are thought to play a significant role in restratifying the deep waters of the Labrador Sea after deep convection (Katsman *et al.*, 2004; Chanut *et al.*, 2008). These would be sub grid-scale and thus not represented in the FRUGAL model as IRs typically have a diameter of 15–30 km (Lilly *et al.*, 2003) and the resolution of the FRUGAL model in the Labrador Sea varies between 30 and 60 km.

Although the winter mixed-layer anomaly is relatively consistent between winters after 1984, it should be noted that this anomaly is not present all year round. In the boreal summer, heat fluxes generally act to warm the ocean and incoming solar radiation,

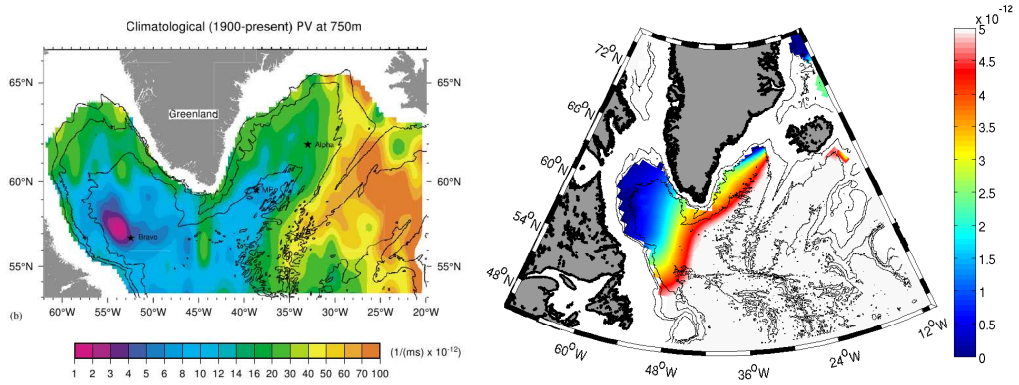

(a) **(b)**

Figure 6.23: (a) Climatological potential vorticity at 750 m in the North Atlantic from Pickart *et al.* (2003a); (b) Potential vorticity at 1000 m depth in the FRUGAL model at the start of the model integrations.

which can penetrate to depth, starts to provide a significant contribution to the surface heat budget. This leads to a well stratified 'buoyant cap' forming on the ocean which, as tip jets are rather rare in the summer, tends to remain largely unchanged between the control, westerly and easterly model runs. However, beneath this buoyant cap, the more weakly stratified water is still present in the westerly tip jet run, explaining why, once the parametrisation has caused a significant increase in the depth of the mixed-layer, it tends to re-emerge in proceeding winters (Deser *et al.*, 2003; Cassou *et al.*, 2007).

6.3.6 Potential Vorticity

As discussed earlier, potential vorticity is approximately conserved with the flow and is closely tied to the local stratification. It is thus used as a tracer for convectively-formed water masses such as Labrador Sea Water (Talley and McCartney, 1982). Figure 6.23(a) shows the climatological PV field at 750 m depth across the northern Atlantic, from Pickart *et al.* (2003a). Note that there is a very distinct minimum of less than 2×10^{-12} m^{-1} s^{-1} at the convective site in the central Labrador Sea, just to the north-west of Ocean Weather Ship Bravo, signifying a local minimum in the stratification. Extending south from Cape Farewell is a finger of water with increased potential vorticity of up to $\sim 20\times10^{-12}$ m^{-1} s^{-1} , and to the east of this in the Irminger Sea is another region of relatively low PV with a minimum of 10^{-11} m^{-1} s^{-1} , suggestive of the proposed secondary convective site in the Irminger Sea. Figure 6.23(b) shows the potential vorticity field at 1000 m in the FRUGAL model at the start of the integration. The values of potential

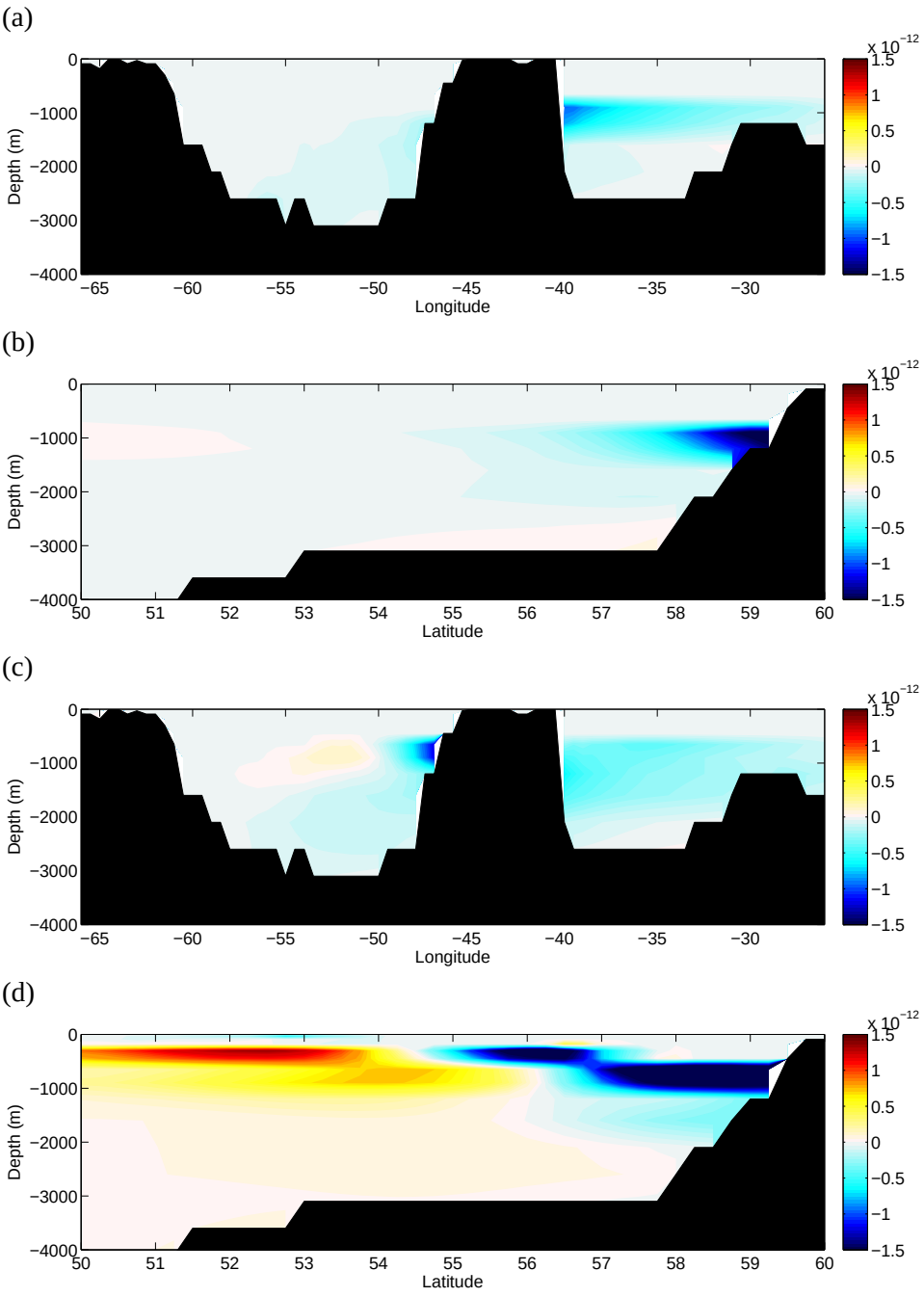

Figure 6.24: Annual average cross sections of potential vorticity anomaly (perturbation−control) in the first (1980, a & b) and final (2000, c & d) years of the model integrations. The zonal sections (a & c) are taken along 60 °N and the meridional sections (b & d) along 44 °W.

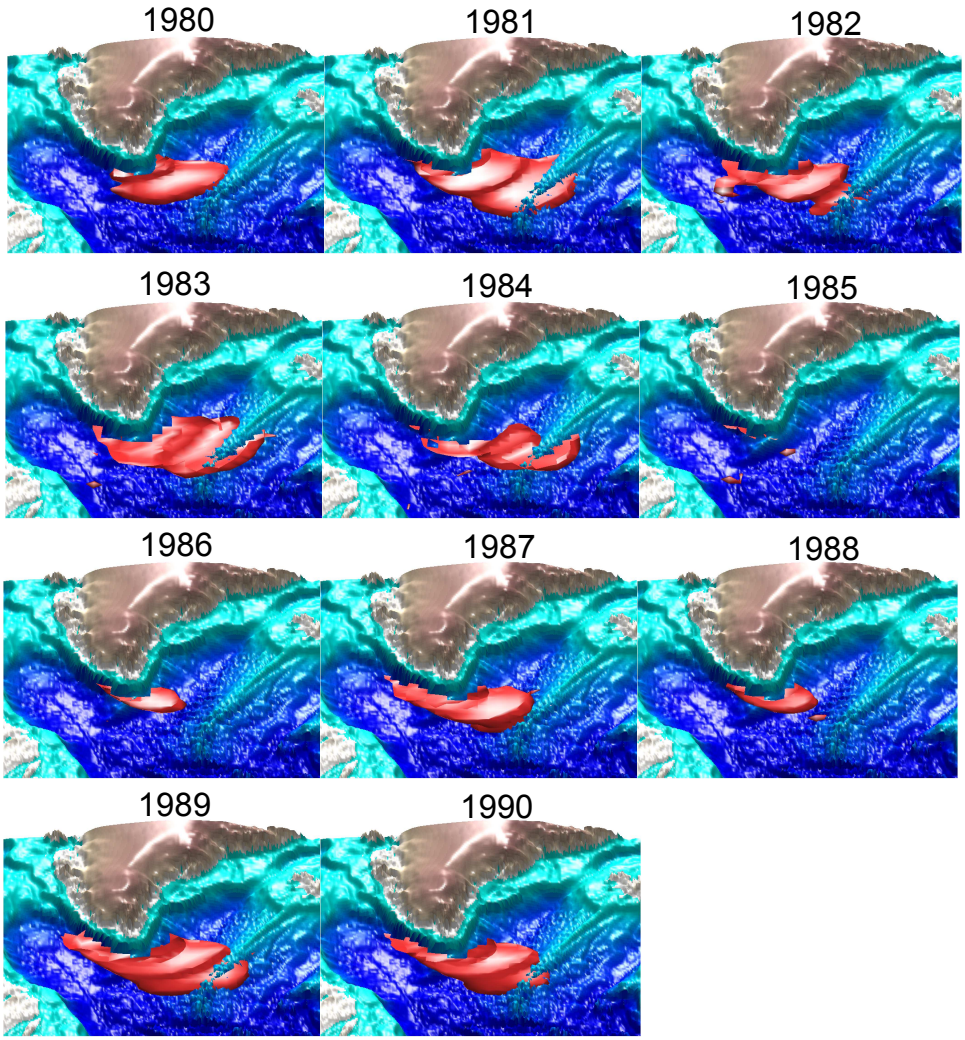

Figure 6.25: Isosurface plots of the North Atlantic region showing the volume of the potential vorticity anomaly fields bounded by the -0.2×10^{-12} m^{-1} s^{-1} isosurface. The plots are snapshots from the beginning of March in each year.

vorticity in the model are generally significantly lower than those observed, with values of less than 5×10^{-12} m^{-1} s^{-1} throughout the Labrador Sea. These low values do extend into the western Irminger Sea, however there is no distinct minimum in potential vorticity in the model's southern Irminger Sea. There is a minimum in evidence in the north of the basin, just to the south of the Denmark Strait, however this is most likely indicative of weakly stratified water overflowing the strait rather than in-situ deep convection.

In Figure 6.24 we can see annual average sections of potential vorticity anomaly (perturbation−control) caused by the westerly tip jet, taken east-west at 60 °N and north-south at 44°W for the first and final years of the integration. From the first year of the integration, a distinct negative PV anomaly appears to the east and south of Cape Farewell, between approximately 1000 m and 2000 m depth, with a decrease of $0.5 \times$

10^{-12} m^{-1} s^{-1} across much of the Irminger basin and up to 1.5×10^{-12} m^{-1} s^{-1} to the south of Cape Farewell. This corresponds to an increase in vertical mixing and thus to a decrease in static stability/stratification at these depths. Note that there is zero change in the potential vorticity fields above approximately 1000 m depth as the water column at these depths is essentially completely unstratified. The pattern of the PV anomaly in the final year of the integration shows a similar pattern to that in the first, however there are a few marked differences. The negative anomaly in the Irminger Sea extends deeper, to below 2000 m, however the maximum absolute anomaly in the Irminger Sea is smaller in 2000 than in 1980. There is, though, a relatively strong minimum in the Labrador Sea between approximately 900 m and 1100 m depth. The largest differences between the two years are seen in the section running south from Cape Farewell. The PV minimum extending south from Cape Farewell becomes significantly more extensive with a strong signal extending south of 55 °N. Also of note is that the PV signal north of 55 °N appears as two distinct minima at different levels. The southernmost of these, between 55 and 57 °N extending to only around 600 m in depth while the northernmost, between 57 and 60 °N extends to over 1000 m in depth. This is strongly suggestive of two separate periods of convective activity, with the resultant water masses spreading in the interim. Given the relatively large degree of spread, this most probably represents convective activity from two different winters.

The other obvious feature in Figure 6.24(b) is the relatively large intrusion of increased potential vorticity in the upper ocean, south of approximately 55 °N. We have discussed previously how the intermittent periods of strong wind stress curl in the Irminger Sea caused by the introduction of the westerly tip jet Pickart *et al.* (2003b) causes a slight change in the dynamics of the North Atlantic Current and subpolar gyre, resulting in an increase flow of relatively warm Gulf Stream water in towards the Labrador Sea. This explains what we see here: the increase of relatively warm surface water causes an increase in the local stratification and a corresponding increase in the potential vorticity field, with a maximum increase approaching 1.5×10^{-12} m^{-1} s^{-1} .

The extent and evolution of the core of the low PV anomaly caused by the introduction of the westerly tip jet can be seen in Figure 6.25, showning the volumes where the potential vorticity anomaly is less than -0.2×10^{-12} m^{-1} s^{-1} . In 1980, the shape and

extent of the anomaly closely resembles that of a typical westerly tip jet, and in following years this spreads primarily east over the Reykjanes Ridge, however it can also be seen to spread to the west, around the boundary of the Labrador Basin. Note that there is substantial year-to-year variability in the volume of water which is modified enough by the tip jet to result in a PV anomaly of less than -0.2×10^{-12} m^{-1} s^{-1} . In particular, in 1985, in which the winter value of the NAO was rather negative (a JFM idnex of -2.0[1]), there is almost no water bounded by this PV isosurface. This suggests that, at least in the FRUGAL model, the low PV signal caused by the tip jet is *not* well conserved and is mixed away rather rapidly. However, as we discussed previously, we have calculated PV through finite differencing potential density on a fairly coarse vertical resolution grid. It difficult to get an accurate estimate of the increased production of LSW using PV, due to the weak background stratification and coarde vertical resolution within the FRUGAL model. However, taking the LSW core to have a PV of less than 4×10^{-12} m^{-1} s^{-1} (a value which is confined to the convective site in the centre of the Labrador Sea in observations, Figure 6.23a, but is ubiquitous throughout the Labrador and much of the Irminger Seas in the model, Figure 6.23b) we see a maximum increase in LSW production over the first 10 years of the integration of 1.5%, with a mean increase of 0.3% and standard deviation of 0.4%. Thus the westerly jet does cause a measurable change in the production of LSW, as defined by its PV signature, in the FRUGAL model. We may speculate that in a higher resolution (particularly higher vertical resolution) model, the change in LSW production caused by the inclusion of the tip jet may be proportionally larger, however such an investigation is beyond the scope of this work.

6.4 Modified Transports

We have seen in the previous sections that Greenland's tip jets do have a measurable, if small, effect on the production of mode water in the North Atlantic subpolar gyre and causes a significant cooling in the deep ocean in the Labrador and Irminger Seas. It is well documented in the literature that the formation of deep water in the polar and subpolar North Atlantic is an important component of the global meridional overturning

[1] from `http://www.cgd.ucar.edu/cas/jhurrell/indices.data.html`, accessed 13/05/2010.

circulation (Talley and McCartney, 1982; Clarke and Gascard, 1983; Dickson and Brown, 1994; Dickson *et al.*, 1996). Variation in convective activity in the Greenland-Iceland-Norwegian, Irminger and Labrador Seas can thus influence the transport variability of the Atlantic subpolar gyre (Curry and McCartney, 2001; Bentsen *et al.*, 2004) and the meridional overturning circulation (Bentsen *et al.*, 2004; Cunningham *et al.*, 2007). In this section we give a brief discussion of the impacts of Greenland's tip jets on the large scale circulation of the North Atlantic and the meridional overturning circulation.

6.4.1 Atlantic Sub-polar gyre

The transport of mass around the Atlantic subpolar gyre is calculated within the model every 6 hours of the integration as the difference between the barotropic streamfunction at 40 °N and the maximum barotropic streamfunction between 50 and 80 °N in the Atlantic basin. The magnitude of the subpolar gyre transport can be seen in Figure 6.26(a). At the start of the integration the subpolar gyre (SPG) transport is around 15 Sv, and in the first five years this increases to around 27 Sv, although there is significant variability, with values as low as 10 Sv and as high as 50 Sv recorded. Following this peak transport at the end of 1985, there is a slight decrease in the strength of the gyre circulation for approximately two years, after which the circulation again tends to increase in strength. This trend continues until around 1994, when the circulation reaches a second maximum, and then declines for the remainder of the integration. Over the course of the integration, the mean value of the SPG transport is 21.2 Sv, with a standard deviation of 5.27 Sv. Observations of subpolar gyre transport at around 60 °N have been given as 13 Sv (Treguier *et al.*, 2005), 25 Sv Bacon (1997), 33.5 Sv Clarke (1984) to as high as 50 Sv (Reynauld *et al.*, 1995). Thus our SPG transport lies within the range observed, albeit at the lower end of these observations. It is interesting to note that the decline in the transport of the SPG after circa 1994 is also seen in observations. Häkkinen and Rhines (2004) used altimetry data, primarily from the TOPEX/Poseidon mission, to study the variability of the SPG and noticed a significant decline in the geostrophic transport from around 1994, and continuing until the end of the 1990s after which a distinct recovery was seen. They suggested that this decline was primarily due to the large 'swing' in the state of the NAO in the early-mid 1990s, when it changed from a generally positive to a generally negative state.

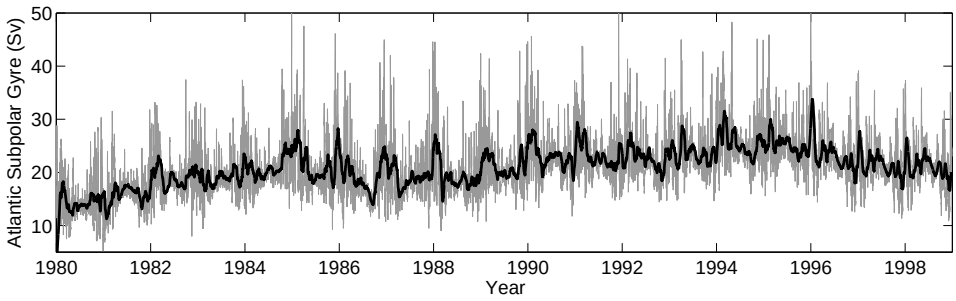

(a) Sub-polar gyre transport in the control integration

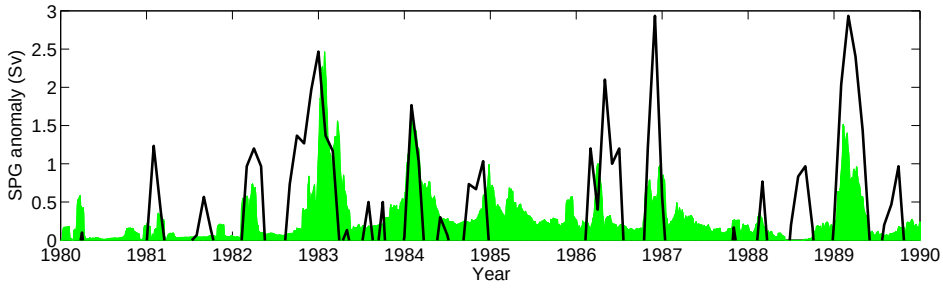

(b) SPG anomaly due to westerly jet, NAO overlaid

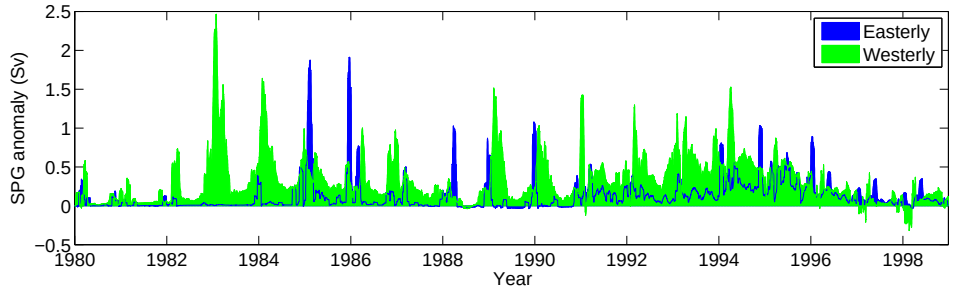

(c) SPG anomaly due to westerly and easterly jets

Figure 6.26: The evolution and tip jet induced anomaly of the transport of the Atlantic subpolar gyre. (a) The transport around the subpolar gyre in the control simulation, calculated as described in text. The grey line shows the transport at 6 hourly intervals and the thick black line a 30 day running mean; (b) 30 day running mean of the SPG anomaly caused by the westerly tip jet with positive phase of the 3 month running mean of monthly NAO indices overlaid; (c) 30 day running means of the anomaly to the subpolar gyre transport caused by the westerly and easterly tip jets.

This change in the NAO led to a decrease in the average cyclonic wind stress curl across the north Atlantic and a subsequent spin-down of the SPG, a relationship also noted by Curry and McCartney (2001). Using older, less accurate, altimetry Häkkinen and Rhines (2004) extended their analysis further back in time to suggest that the SPG circulation in the late 1990s was weaker than at any time in the previous two decades. This is not seen in our model integration, although this could easily be because the high temporal resolution forcing fields were still spinning the gyre up from the end of the relaxation spin-up.

The response of the subpolar gyre circulation to the introduction of the tip jets can

be seen in Figures 6.26 (b) and (c). In Figure 6.26(b) the 30 day running mean anomaly caused by only the westerly tip jet parametrisation is shown for the first 10 years of the integration. Overlaid on this is the positive phase of the three-monthly running mean of the monthly NAO index. There is a statistically significant (at the 95% level) relationship between the positive phase of the NAO and the and the magnitude of the subpolar gyre anomaly, with a correlation coefficient of 0.42 between 1980 and 1990. This is not a surprising result, although it is of note. We discussed in the previous paragraph that the SPG has been shown to correlate with the phase of the NAO over interannual time periods, due to the associated change in wind stress curl. We also know that the occurrence of the westerly tip jet (for example the 'tip jet index' discussed in the previous chapter) correlates extremely well with the NAO. Thus when the NAO is in a positive phase, and the tendency is for the subpolar gyre circulation to increase, the tip jet parametrisation is most active and is acting to increase this trend. In Figure 6.26(c) we can see the Atlantic subpolar gyre anomaly between 1980 and 1999 for both the westerly and easterly tip jets. The largest and most systematic difference is caused by the westerly tip jet with anomalies of up to 2.5 Sv, and numerous peaks above 1 Sv, although for limited periods the easterly jet can cause anomalies in excess of 1.5 Sv. Over the length of the integration, the westerly tip jet caused an average increase of 1.6% in the Atlantic SPG transport, although at certain times, for example the winters of 1983 and 1984 this could be as high as 5 or even 10%. The easterly jet caused an average increase in the SPG circulation of 0.67%, but again this exceed 5% for brief periods.

6.4.2 Meridional Overturning

The model meridional overturning transport, calculated as the maximum between 30 °N and 70°N of the depth integrated overturning streamfunction from the surface to the depth where the integral is maximised is shown in Figure 6.27(a). At the start of the integration, following the spin-up period, the model MOC is relatively weak, not exceeding 15 Sv in the 30 day running mean. However, the strength of the MOC gradually increases through the majority of the integration, reaching maximum values of around 26 Sv by 1996. After this, the MOC shows a slight weakening trend for the remainder of the integration. The average MOC over the entire integration is 18.47 $\pm$ 4.4 Sv, in very good agreement

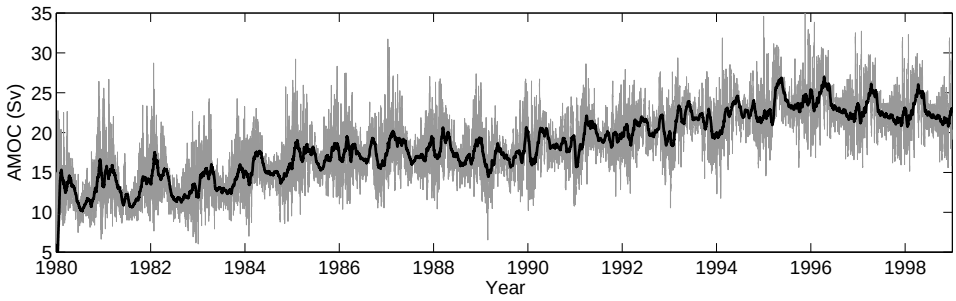

(a) Meridional overturning

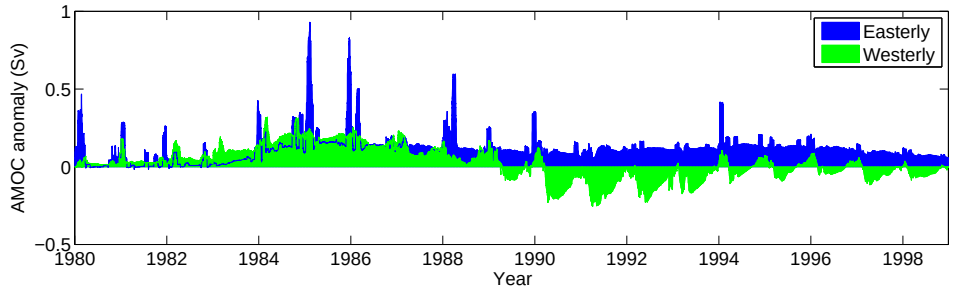

(b) MOC anomalies caused by westerly & easterly tip jets

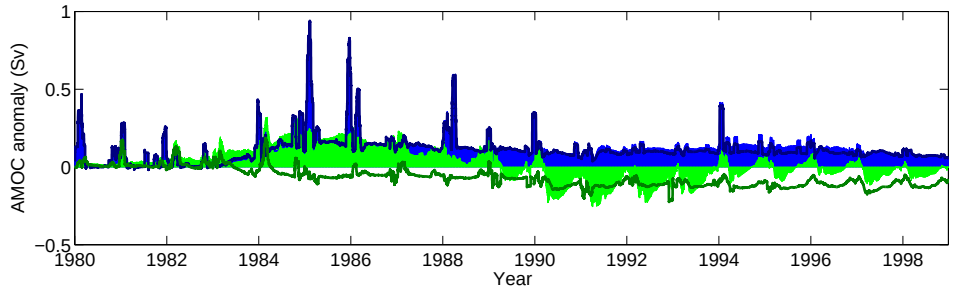

(c) As (b) but with mechanical-only tip jet forcing overlaid

Figure 6.27: The evolution and tip jet induced anomaly of the Atlantic meridional overturning circulation. (a) The meridional overturning circulation in the control simulation, calculated as described in text. The grey line shows the transport at 6 hourly intervals and the thick black line a 30 day running mean; (b) 30 day running mean of the MOC anomaly caused by the westerly and easterly tip jets; (c) As (b), with the MOC anomaly in the mechanical forcing only integrations overlaid (thick lines).

with the recent observations of Cunningham *et al.* (2007), who calculated an overturning transport of 18.7 $\pm$ 5.4 Sv. It is interesting to note that the onset of the decrease in the strength of the MOC occurs approximately 2 years after that of the SPG. This is in good agreement with previous modelling studies, for example that of Bentsen *et al.* (2004) who, in a study of ocean-only and coupled simulations, noted a strong, significant correlation at a lag of two years between mixing indices in the Labrador and Irminger Seas and PC1 of the Atlantic MOC.

Figure 6.27(b) shows the anomaly in the Atlantic MOC caused by inclusion of both

the westerly and easterly tip jets. During the first quarter of the integration, the westerly jet causes a gradual increase in the strength of the overturning, peaking at around 0.3 Sv in 1985. Following this, the response of the MOC gradually weakens until around 1990 at which point the tip jet is causing a similar-sized weakening of the MOC, although there is a more pronounced seasonal cycle present. After the start of 1994, the annually averaged MOC anomaly is essentially vanishingly small. It is not clear what is causing this change of behaviour after the first $\sim$10 years of the integration. It is possible that it is caused by the internal model variability becoming dominant as the control and perturbation model states drift apart (although similar behaviour has been seen in a number of test integrations), however it is interesting that this change in behaviour does approximately co-incide with appearance of the warm anomaly in the southern Labrador Sea discussed in Section 6.3.1. Over the complete integration, the westerly jet increases the MOC by only 0.1% (0.02 Sv), although the peak response of 0.37 Sv corresponds to around 2% of the mean transport. The response of the MOC to the inclusion of the easterly jet is both stronger and more systematic than that of the westerly jet. The peak response approaches 1 Sv and represents an increase of more than 5% over the control integration, however over the whole integration the easterly jet is responsible for only a 0.6% (0.11 Sv) increase in the Atlantic meridional overturning circulation.

6.4.3 Thermal versus Mechanical Forcing

We have discussed a number of times in this thesis that the easterly tip jet is associated with atmospheric conditions that prevent it from removing significant quantities of heat from the ocean. This raises the question of why the easterly jet is causing such a relatively large and systematic change to the MOC. To answer this we have modified the tip jet parametrisation to leave the heat flux fields unperturbed while still causing a perturbation to the wind stress fields. The results of these integrations are shown in Figure 6.27(c) as the thick lines overlying the shading. It is clear that when the heat flux fields are left unperturbed, the easterly jet causes an almost identical response as when the heat flux perturbations are included. This is not entirely surprising given that the heat fluxes associated with the easterly jet are generally small, however it does show that the mechanical input from mesoscale features such as tip jets can provide enough change to the

variability of the larger scale circulation to be worthy of consideration. More surprising is the response of the MOC to the mechanical forcing of the westerly jet. Almost from the start of the integration the mechanical input from the westerly jet acts to reduce the meridional overturning. By the end of the integration there is a seasonally varying 0.1–0.2 Sv ($\sim$0.8%) decrease in the overturning caused by mechanical input from the westerly tip jet. For much of the integration, therefore, the changes to the MOC caused by the perturbed heat flux and perturbed momentum flux fields are of opposite sign and act to cancel each other out, resulting in very small overall changes in the MOC. We do not have diagnostic output for the momentum only integrations, and thus a full investigation of the causes of this mechanically forced decrease in the MOC is beyond the scope of this work.

6.5 Summary

In this chapter we have used the parametrisation of Greenland's tip jets developed in Chapter 5 to perform a number of control/perturbation integrations in the FRUGAL ocean general circulation model. We also modified the parametrisation to only perturb the wind stress fields, leaving the heat flux fields unchanged.

Single tip jets were seen to have a strong impact on the velocity fields in the vicinity of Cape Farewell. In the upper ocean, horizontal velocity anomalies in excess of 70 cm s^{-1} were observed in response to both tip jets, dominating the average flow field for short periods of time. This strong response, however, was limited to the upper ocean and only a weak response, of around 2 cm s^{-1}, was observed at 500 m depth. The vertical velocity anomalies observed in response to both of the jets were both strong and relatively barotropic, extending well below the upper kilometre of the ocean. Distinct anomalies in the sea-surface height were also observed: the primary response to the westerly jet being an elongated area of elevated sea-surface height to the south of Cape Farewell, with the easterly jet resulting in an area of depressed sea-surface height to the south-west of Cape Farewell.

The average response of the ocean to many winters of forcing by the westerly jet included a relatively strong, barotropic spin-up of the cyclonic gyre in the Irminger basin and a cooling at all depths in the Labrador basin. In the deep ocean, this cooling was confined to the western boundary of the basin, where a cooling of up to 0.05 °C could account

for a significant amount of the interannual variability in the deep ocean temperatures. In the upper ocean, a warming trend was observed in the southern Labrador Sea, caused by an increased flow of warm water from the north Atlantic current in to the western subpolar gyre. The integrated response to the easterly tip jet is significantly weaker, with negligible temperature anomalies in the deep ocean and only weak average velocity anomalies.

One of the questions we have addressed in this chapter is the impact of the tip jet on production of Labrador Sea Water. While it is difficult to derive an accurate estimation of the change in LSW production, due in no small part to the inherently weak stratification in the FRUGAL model, there are strong indications that the westerly tip jet significantly alters the production of mode water. Winter mixed-layers around Cape Farewell and in the southern Irminger Sea were seen to increase by over 200 m, comparable to the deepening seen in response to tip jets in more idealised studies. In addition, the potential vorticity field, an oft-used tracer for convectively-formed water masses, is significantly altered around Cape Farewell and in the Irminger Basin. Using a PV threshold of 4×10^{-12} m^{-1} s^{-1}, indicative of deep convection in observations, but present throughout the Labrador and Irminger Seas in the model, the volume of LSW is seen to increase by over 1.6%.

The westerly tip jet is seen to have a significant impact on the transport of the Atlantic subpolar gyre, with transient increases of up to 10%. The response to the easterly tip jet is weaker, however it still peaks at around 5% of the mean flow. The easterly jet has the stronger impact on the meridional overturning circulation, almost entirely through the input of mechanical energy. The increased heat fluxes introduced by the westerly jet do, in general, act to increase the strength of the MOC, however this is tempered by tendency of the mechanical input introduced by the westerly tip jet to decrease the strength of the overturning.

Chapter 7

Summary & Conclusions

In this thesis we have investigated various aspects of Greenland's tip jets with a view to improving our understanding of their impact on the oceans. In Chapter 2 we investigated speculation that air-sea energy exchange forced by the easterly tip jet may be an important process driving mixed-layer deepening in the south-east Labrador Sea. It was found, however, that this hypothesis was incorrect: the synoptic-scale situation required for the formation for easterly tip jets results relatively in warm, moist atmospheric conditions over the Labrador Sea, and correspondingly low air-sea heat fluxes. We went on, in Chapter 3, to evaluate the performance of ECMWF and NCEP/NCAR (re)analyses in simulating mesoscale atmospheric features around Greenland, by comparing these models to observations from low-level flights during the Greenland Flow Distortion Experiment (GFDex). The performance of Remote Sensing Systems (RSS) QuikSCAT retrievals of the high wind speeds around Greenland were also evaluated. It was found that, in general, the high wind speeds in the mesoscale systems around Greenland were underestimated in the analyses and this led us, in Chapter 5, to develop a parametrisation of Greenland's tip jets which allows these features to be more accurately represented in atmospheric wind fields. When this is combined with in-situ bulk heat flux estimates, it allows the full impact of Greenland's tip jets to be seen in ocean general circulation models. We adapted the FRUGAL OGCM to incorporate this parametrisation and, in Chapter 6, performed 20 year integrations of the model, forced by 6-hourly ECMWF ERA-40 data with and without the tip jet parametrisation included. This allowed an investigation into the importance of tip jet representation in a global ocean model.

7.1 Oceanic convection forced by the easterly tip jet?

The mid-depth circulation map of the North Atlantic published by Lavender *et al.* (2000) showed that both the Irminger Sea and the south-east Labrador Sea had approximately the same preconditioning state that was known to exist in the central Labrador Sea, where the deepest mixed-layers in the subpolar gyre are formed. Doyle and Shapiro (1999) suggested that the westerly tip jet was associated with sufficiently strong atmosphere-ocean heat exchange to force oceanic convection in the Irminger Sea. In the following years, a number of both observational and modelling studies investigated this idea. Bacon et al. (2003) noted a mixed layer of around 1000 m depth in the southern Irminger Sea, and it was shown that this was most likely formed in-situ, rather than being advected from the Labrador Sea where open-ocean deep convection is known to occur. Pickart et al. (2003a) noted, furthermore, that the mid-depth potential vorticity field in the Labrador and Irminger Seas were inconsistent with a Labrador-Sea-only source of Labrador Sea water. Pickart et al. (2003b) used an idealised OGCM with a simple representation of the tip jet, showing that such a representation could force convection to depths in excess of 2000 m. Vage et al. (2008) described observations of mixed-layer depth from moorings placed in the southern Irminger Sea in the winters of 2002/03 and 2003/04 . These winters were relatively mild, and deep mixed-layers were not observed, however there was evidence of mixed-layer deepening in response to the Greenland westerly tip jet. A one dimensional mixed-layer model suggested that in a stronger (more NAO+) winter, that the tip jet could cause significant mixed-layer deepening, and mixed-layer depths in excess of 1000 m may be formed. While these studies prove neither that deep convection occurs in the Irminger Sea or that it is forced by the Greenland tip jet, they are highly suggestive of both. This led others (Moore, 2003; Moore and Renfrew, 2005; Martin and Moore, 2007) to speculate that the easterly tip jet may well play a similar role in deepening the mixed-layer in the preconditioned area in the south-east Labrador Sea. To investigate this hypothesis, we first gathered temperature and salinity data from profiling floats in the area of the south-east Labrador Sea recirculation, which were released in the winter of 1996/1997 during the Labrador Sea Deep Convection Experiment. These were used to calculate the evolution of the mixed-layer over this winter in this relatively small geographical area, with the results corroborating those of Lavender *et al.* (2002). Timeseries of heat, moisture and

momentum flux over the south-east Labrador Sea were extracted for this winter from the ECMWF ERA-40 reanalysis and used to force an implementation of a 1-dimensional mixed-layer model as described by Price *et al.* (1989). It was found that when this model was initialised with temperature and salinity profiles obtained from the floats during the early winter, that the onset and extent of mixed-layer deepening was well reproduced by the model, at least until the onset of restratification in spring. The contribution of the easterly tip jet to this mixed-layer deepening was investigated by removing any data points from the forcing timeseries where easterly jets were deemed to be present and replacing these with average winter values – effectively 'interpolating over' the easterly tip jets. This had very little effect on the development of the mixed-layer, implying that the easterly tip jet is not an important mechanism in winter-time mixed-layer deepening in the south-east Labrador Sea.

To investigate why easterly tip jets are not associated with mixed-layer deepening, a composite analysis of high heat flux events over the south-east Labrador Sea was carried out. This revealed that high heat fluxes in this region are associated with cold-air outbreaks from the North American continent and synoptic conditions that are conducive to the formation of westerly tip jets, i.e. a low-pressure system located between Greenland and Iceland. This places the south-east Labrador Sea in the same convective regime as the Irminger Sea, and to some extent the Labrador Sea (cold-air outbreaks which force convection in the central Labrador Sea can also be related to a low pressure system in the northern Labrador Sea). This analysis was repeated for two further winters with strongly negative (-2.32) and positive ($+2.44$) NAO indices, with the same result: high heat fluxes in the south-east Labrador Sea are associated with a low pressure system between Greenland and Iceland. A back trajectory model was also employed to investigate the history of air parcels comprising both high heat flux events and easterly tip jet events. As expected from the composite analysis, air parcels which were found over the south-east Labrador Sea during high heat flux events generally originated to the west and north-west as cold, dry air advected off North America. Air parcels found in easterly tip jets, conversely, generally originated to the north-east or south-east of Cape Farewell, and were strongly modified by the ocean as they moved across it, becoming too warm and moist to result in strongly elevated heat fluxes by the time that they reached the south-east Labrador Sea.

While we believe that these results are robust, it should be noted that they are based on only three winters of the ECMWF ERA-40 reanalysis, a relatively coarse global reanalysis product which can be deficient in its representation of high wind speeds and strong heat fluxes around Greenland. There is thus scope to make these results more robust, and thus strengthen these conclusions. In particular, in recent months and years, higher resolution global reanalyses, such as the ECMWF-Interim analysis, ir regional reanalyses such as the NCEP NARR data-set (which perform well around Greenland, see Renfrew et al., 2009) have become available. A longer climatology of high heat flux events in the south-east Labrador Sea using one of these higher resolution analyses should allow a more definite conclusion on the role of easterly tip jets in forcing mixed-layer deepening in the south-east Labrador Sea.

7.2 Representation of Greenland's mesoscale systems in the analyses

The Greenland Flow Distortion Experiment (GFDex) focused on an aircraft-based observational campaign, run out of Keflavìk, Iceland in the late winter of 2007/2008. The campaign aimed to investigate the dynamics of mesoscale weather systems around Greenland, the air-sea interactions associated with these systems and the influence of increased observations on the predictability of weather systems downstream, over western and northern Europe, through the use of targeted observations. The campaign involved a number of flights with low-level ($\sim$30 m) legs, which allowed the accurate measurement of surface-level atmospheric variables, such as temperature, humidity and wind speed and direction, as well as sea-surface temperature. This unique data-set allowed the validation of atmospheric analysis and reanalysis products in high wind speed conditions, over the subpolar seas where they have been seen to perform poorly in the past (e.g. Renfrew et al., 2002).

The analysis was performed for ECMWF operational analysis at T511 truncation (approximately 40 km, the highest resolution we had access to) and at T159 truncation (the resolution of the ERA-40 reanalysis, which does not cover the GFDex period), the NCEP/NCAR reanalysis, which is run at T62 truncation and available on a 2.5° grid. QuikSCAT winds retrieved using the RSS algorithm at 0.25° were also compared to aircraft-recorded winds. To perform the comparison, aircraft data, which were average

values over a 2 minute ($\sim$12 km) run, were mapped on to standard levels (10 m for winds, 2 m for temperature and humidity) using stability dependent adjustment (see Renfrew et al., 2002; Fairall et al., 2003) and analysis data/QuikSCAT winds were linearly interpolated to the position of the aircraft.

Both ECMWF products were seen to perform reasonably well in wind speed, direction, temperature and humidity although these fields were too spatially smooth, even at spatial scales which the T511 product should have been capable of adequately resolving. This is in agreement with work presented by Chelton et al. (2006) which showed that reanalysis surface wind fields tend to lack power at all scales less than around 1000 km. One of the major failings of the ECMWF analyses was their inability to simulate the strongest wind speeds (regression slopes of between 0.7 and 0.8 mean that at wind speeds approaching 30 m s^{-1} these analyses will underestimate the true wind speed by more than 5 m s^{-1}. This leads to an average bias of -0.18 N m^{-2} and -0.16 N m^{-2} in estimating the air-sea momentum transfer for the low and high resolution ECMWF products, respectively. Despite the low wind speed bias, ECMWF heat fluxes were well represented and generally within observational error bounds. The lower resolution ECMWF product out performed the higher resolution product in simulating surface turbulent heat fluxes, but this was due to compensating effects of slightly underestimating both the 2 m temperature and the 10 m wind field.

In general, the NCEP reanalysis did not compare so favourably to the observations; with a resolution of 2.5°, it is simply too coarse to correctly simulate the mesoscale features associated with flow distortion around Greenland. In particular, the model showed almost no skill in reproducing the observed 2 m relative humidity field. As has been seen in previous studies, we see that the NCEP reanalysis tends to significantly over estimate surface turbulent heat fluxes in the subpolar seas, as the boundary-layer scheme is inappropriate for areas of high winds speeds and large air/sea temperature gradients. We thus conclude that the NCEP reanalysis should not be used to force ocean models especially where air/sea interaction in the subpolar seas are being considered, without a flux correction.

The RSS QuikSCAT winds performed well in general, and reproduced the spatial

gradients in wind speed observed by the aircraft well, which is unsurprising given the relatively high resolution of the data-set, and the independence of neighbouring grid points. However, at high wind speeds, QuikSCAT tended to overestimate the strength of the wind. It is worth noting that other QuikSCAT retrieval algorithms—notably the NASA-DIRTH algorithm which was evaluated in a paper of which this study was a part—performs somewhat better in high wind speed conditions than the RSS retrieval algorithm, although still with some overestimation (Renfrew *et al.*, 2009; Moore *et al.*, 2008).

Given the relatively favourable performance of the ECMWF analyses around Greenland in comparison to the NCEP reanalysis, we chose to use the ECMWF operational and ERA-40 (re)analyses for the modelling part of this study. However, given the under-representation of small scale phenomena with high wind speeds still present in the ECMWF analyses, it is necessary to improve the representation of tip jets in these analyses before they are used to study the impacts of tip jets on a model ocean.

In this Chapter we described various biases in ECMWF and NCEP (re)analyses and QuikSCAT winds. However, one should bear in mind here that although the aircraft-based GFDex measurements are of a very high quality, that the data-set is only small, and that there may be somewhat of an under-sampling problem, due mainly to the upto-an-order-of-magnitude difference in the spatial scale between the GFDex measurements (12 km) and the (re)analysis fields (varying from 40 km to ¿ 200 km). Thus any biases or errors presented here should be thought of as indicative, but not conclusive.

7.3 Incorporating tip jets into atmospheric forcing fields

Having seen that mesoscale weather systems around Greenland, such as tip jets, are generally too smoothly and weakly represented in the ECMWF (re)analyses, it became apparent that in order to study the impact of tip jets in a general ocean circulation model, it was necessary to find a method of improving the representation of tip jets in the analysis. The approach we took is a ‘bogussing’ technique, similar to that of Condron *et al.* (2008), who inserted polar mesocyclones into the surface wind field using an idealised vortex structure, and Hu and Meehl (2009), who inserted idealised hurricane tracks into a coupled atmosphere-ocean general circulation model. We based our parameterization on a database of QuikSCAT winds of both easterly and westerly tip jets observed between

mid-1999 and 2007. It was noted that the jets could be described simply by a linear relationship between the maximum wind speed in the analysis over the Irminger Sea and that observed by QuikSCAT, and a linear decrease in wind speed along the centre of, and across, the jet. The exact path taken by tip jets varies from jet to jet, however it was found that the path of the jets could be well approximated by the geostrophic wind in the case of the westerly tip jet or the 10 m wind in the case of the easterly tip jet. Thus our tip jet parameterization only requires near-surface winds and mean sea-level pressure fields. No external information is required. This 'self-contained' nature of the parameterization means that it may be incorporated into coupled atmosphere-ocean general circulation models at the coupling stage, meaning the impact of these mesoscale jets on the coupled climate system can potentially be evaluated.

We looked at the impact of the parameterization on the variability of the wind speeds field around Greenland from a variety of perspectives. Firstly, though the construction of composite wind speed fields over the data set of tip jets we showed that, on average, the parameterization reproduces the strength, location and extent of the tip jet very accurately, especially in the case of the westerly tip jet. Secondly, Weibull distributions and power spectra were also constructed from the 10 m ECMWF wind fields with and without the parameterization, and QuikSCAT winds over the Irminger Sea. The parameterization was not able to to remove all of the low wind speed bias in the ECMWF wind field, as this tends to occur even away from the core of the jet where the parameterization leaves the wind field unchanged, however the Weibull curve of the modified wind field showed a significant increase in the probability of observing a wind speed greater than 17 m s^{-1}. The Weibull curve of the modified wind speed field also more closely resembled the shape of that of the QuikSCAT curve. Chelton *et al.* (2006) showed that reanalyses wind fields tend to lack power at scales of less than around 1000 km. Calculation of the power spectral density of the wind fields around Greenland also showed this behaviour, and the inclusion of the parameterized tip jets was seen to improve this under-representation of small scale wind speed variability. However, as there are numerous other sources of mesoscale wind speed variability around Greenland, again the parameterization could did not account for all of the missing power at these spatial scales.

To provide an example of the impact that the enhanced tip jet forcing may have on

mixed-layer development though a typical winter (in this case 1980), we returned to the 1-D mixed-layer model initially used in Chapter 2. Timeseries of total heat and momentum fluxes were extracted from a single grid point in the Irminger Sea both with and without the parameterization and applied to the mixed-layer model (which was initialised with temperature and salinity profiles recorded in the Irminger Sea in the late autumn). When forced by the unperturbed timeseries, the mixed-layer depth at the end of the integration was around 1000 m versus around 1175 m when forced by the perturbed timeseries. During the middle of the simulation, the mixed-layer forced by the perturbed timeseries reached a maximum of around 250 m deeper than that in the unperturbed run.

Although the parameterization provides a relatively good representation of the structure and speed of tip jets—and through in-situ turbulent heat flux calculations the associated air/sea energy exchange—there are almost certainly improvements that could be made. When developing the parameterization, we considered the surface wind field, as well as surface humidity and temperature fields, all of which are important in setting the strength of air/sea fluxes, however we did not consider whether there are any predictable mesoscale features in the precipitation fields in high resolution analyses which are not seen in lower resolution analyses, and could thus be somehow incorporated into the parameterization. It may also be possible to improve the method by which the tip jet parameterization is called. At the moment this relies on simple speed and direction criteria in the wind field around Cape Farewell. While this approach is fairly successful—approximately the correct number of tip jets are inserted into the wind field and these correlate well with the state of the NAO—it does not give any consideration to the synoptic conditions associated with tip jets and is thus disregarding potentially useful information. Finding a method of using synoptic-scale information in the parameterization as well as the simple wind speed/direction criteria currently used could help to minimise any false positives or false negatives when modifying the wind field. Finally, we should note that phenomena similar to Greenland's tip jets are thought to occur in other oceanographically important areas of the world, notably the Antarctic Peninsula, for example Parish (1983). It would be interesting to see if the parameterization developed here could also be used in these locations.

As we have noted previously, the tip jet parameterisation does not perturb either the

surface temperature or humidity fields, and thus sensible and latent heat fluxes are only modified by changing the 10 m wind speed. We justified this by the absence of any temperature or humidity signature in the North American Regional Reanalysis (NARR), which seems to be of a high enough resolution to give a relatively realistic representation of mesoscale features around Greenland (Renfrew et al., 2009). It is possible, however, that these features do exist in reality, but are simply not reproduced in the NARR. We may thus speculate how heat fluxes may be modified if there are indeed mesoscale temperature and humidity features associated with Greenland's tip jets. It seems to the author that there is no reason to expect a significant change in either temperature or humidity simply through the acceleration of air as a tip jet is formed. If there is such a signal, therefore, this will most likely arise from an increased advection of air off the Greenland landmass. Such air will almost certainly be colder and drier than the air masses forming the tip jets, which will be either of maritime origin, or at least modified continental air. It is thus likely that any temperature or humidity signals associated with tip jets will act to increase the sensible and latent heat fluxes, respectively. Note that the presence or otherwise of these possible temperature and humidity gradients will be difficult to prove conclusively, probably requiring measurements from an aircraft, which is capable of recording low-level temperatures across a tip jet during its lifetime.

While we have done everything we can to reduce a possible strong wind bias in the parameterisation, due to basing it on QuikSCAT which may be biased high at strong wind speeds, one should bear in mind that the parameterisation probably represents an upper limit to the impact of tip jets on the ocean (notwithstanding possible temperature and humidity effects, which are discussed below).

7.4 Modelling the oceanic impacts of tip jets

In Chapter 6, we modified the FRUGAL ocean general circulation model to use the tip jet parameterization developed in the previous chapter, and ran 20 year simulations: (i) without the tip jets (a control run); (ii) with only the westerly tip jet ; (iii) only the easterly tip jet; (iv) with both tip jets included. These control/perturbation experiments allowed us to gain an understanding of the impact of the tip jets on the model ocean. Note that when both jets were included (case iv), the results were largely just an additive combination of

the westerly and easterly tip jet cases, and thus did not warrant a separate discussion.

The easterly jet was seen to have very little effect on the temperature of the subpolar Atlantic, consistent with the findings in Chapter 2 that the synoptic conditions associated with the easterly tip jet are not favourable for strong atmosphere-ocean heat exchange. In contrast, the westerly tip jet caused a surface cold anomaly of up to 0.2 °C to spread around much of the Labrador Sea and parts of the Irminger Sea. In the deep ocean, the westerly tip jet caused a cold anomaly of up to 0.05 °C to move around the deep western boundary current. This cold anomaly showed significant interannual variability, and could account for approximately 10% of the observed interannual temperature variability. The westerly tip jet was also seen to be responsible for a strengthening of the cyclonic gyre in the Irminger Sea, suggesting that the jet may not only be responsible for triggering convection in the Irminger Sea (due to the very strong heat fluxes associated with it) but it may also play an important role in preconditioning the ocean east of Cape Farewell for convection. The impact of the jets on convection was evaluated by considering changes to the depth of the mixed-layer and the production of anomalously low areas of potential vorticity. As expected, the easterly tip jet did not significantly perturb either of these properties, however the westerly jet resulted in a deepening of the mixed-layer in excess of 200 m around Cape Farewell and a distinct negative anomaly of potential vorticity in the Irminger and Labrador Seas, suggestive of a weaker local stratification.

The westerly tip jet was seen to cause significant increases to the Atlantic subpolar gyre transport, in excess of 2.5 Sv when the NAO was in a strong positive phase, while the easterly jet caused a more modest, but still significant, increase of up to 1.5 Sv. Unexpectedly, the easterly jet caused the larger increase in the meridional overturning circulation, although this increase was still relatively modest, reaching a maximum of around 0.9 Sv for short periods, with an average increase in overturning over the length of the simulation of only 0.1 Sv. A modification of the tip jet parameterization which allowed the mechanical forcing associated with the tip jet to be represented without changing the heat flux fields showed that this increase was almost entirely due to mechanical input. Heat fluxes associated with the westerly tip jet tended to increase the meridional overturning circulation, however the mechanical input had the opposite effect, and by the end of the integration, these competing influences meant that there was little-to-no net change in the

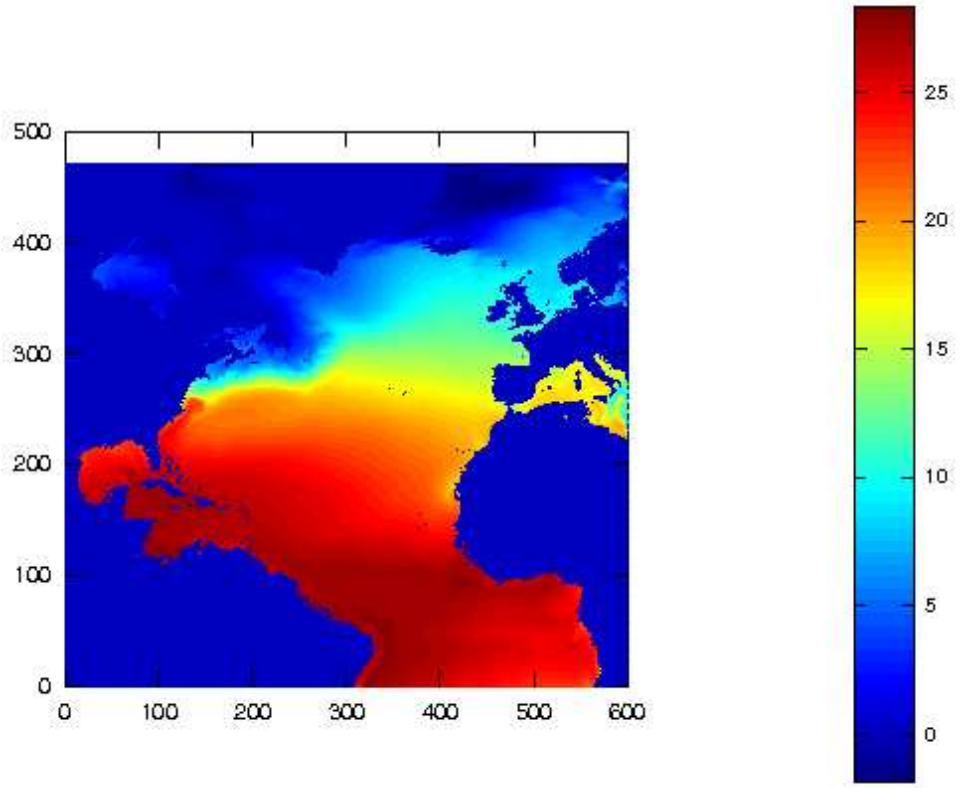

Figure 7.1: Sea-surface temperature (°C) in a 1/5° North Atlantic configuration of the MIT-gcm. Such high resolution regional models may be useful for process studies of the impact of tip jets on the ocean.

overturning.

Both the fast response of the ocean to single tip jets, and the longer time-scale, climatically important changes to the ocean caused by many winters of tip jets have been examined. The FRUGAL model, with its relatively high resolution around Greenland, allowing physical processes to be well represented, and lower resolution in the Southern Ocean allowing long integrations to be undertaken relatively efficiently. The FRUGAL model, however, does have its drawbacks. Particularly the model is not under active development, and many of the parameterizations in the model are becoming rather dated. The model is also not designed to be run across multiple processors, meaning that longer or higher resolution integrations than we have undertaken here are probably not feasible.

There are thus a number of different possible avenues of exploration with regards to modelling the impact of Greenland's tip jets on the ocean. The fast, local response of the ocean could be better studied in a higher-resolution ocean model with improved vertical

mixing parameterizations. For example, Figure 7.1 shows SST after a two-week integration in a 1/5° regional model of the North Atlantic, which we forced with seasonal ECMWF fluxes, setup in the framework of the MIT-gcm (Marshall et al., 1997). Such a resolution would allow a better representation of air-sea interaction associated with the tip jet. Haine *et al.* (2009) used a high resolution setup of MIT-gcm covering the Denmark Strait region to assess the impact of high-resolution high-frequency meteorological forcing on the circulation around Greenland. MIT-gcm can also be configured in a non-hydrostatic mode, which could allow a detailed study of oceanic convection associated with tip jets in suitably small, high resolution domains around Cape Farewell.

At the other end of the spectrum are climate-scale integrations, either long ocean-only integrations, or coupled atmosphere-ocean simulations. The former will, for the foreseeable future, rely on relatively low resolution integrations, usually with low frequency (i.e. monthly) atmospheric forcing fields. Clearly the tip jet parameterization could not be applied directly to such an integration, however the parameterization could be run 'off-line' to generate control and tip jet monthly average heat and momentum flux fields, and these could then be used to force a low resolution ocean model for long (100 year+) integrations.

When discussing the tip jet parameterization, we noted that it was suitable for incorporating into a coupled climate model at the coupling stage, and current/next generation models are in the range where resolution is high enough for the tip jet parameterization to work correctly and low enough for the parameterization to be required. Given the inevitable trade-offs that occur between model complexity, resolution and integration length, this is likely to remain the case for some time to come. Although the parameterization could only be applied to the air-sea flux fields, and not as a true source of momentum in the atmosphere, this would still be a very useful method of evaluating potential feedbacks between the atmosphere and ocean forced by the tip jet, such as the mechanism proposed by Bakalian *et al.* (2007) whereby the latitude of the Icelandic low affects the frequency of wintertime westerly tip jets at a lag of 2 years, introduced by a slow signal propagation around the North Atlantic basin. There is currently much interest in the possible predictability of the climate system on decadal timescales, particularly in the North Atlantic region (Sutton and Allen, 1997). The interaction of processes in the mixed-layer

processes and non-local processes (e.g. Rossby wave propagation) are thought to be important in this potential predictability (Le Provost and Flemming, 1998). It thus may be important to improve the representation of mesoscale atmospheric features, like tip jets, through parameterizations such as those presented in Chapter 5 in climate models aiming to predict climate on decadal timescales, for example those used in the Intergovernmental Panel on Climate Change (IPCC) simulations.

The results presented in this chapter should be thought of only as indicative, and as guidance of where to focus future research in this field. This is not due to problems with the experiment design, or indeed the tip jet parameterisation, but rather reflects some potentially serious shortcomings of the FRUGAL model. Chief among these is the resolution of the model, which reaches a maximum of around 0.3 degrees in the GIN Seas. While such a resolution gives a reasonable representation of the larger scale dynamics, it is still far too coarse to resolve the dynamic scales involved in open ocean convection and deep water formation, which has been a focus of this study. As we will discuss shortly, however, the parameterisation can easily be adapted to be used in newer, higher resolution models, and possibly at some point in a non-hydrostatic model, allowing convective processes to be explicitly resolved, rather than relying on the bulk static adjustment model employed in FRUGAL.

7.5 Final thoughts

In this thesis I have investigated, and made progress on understanding, the impacts of Greenland's tip jets on convection and circulation in the subpolar Atlantic, primarily through using a combination of simple and more complicated numerical models. Some avenues for further research in this vein have been outlined throughout these conclusions. Numerical models are undoubtedly extremely useful tools in understanding atmospheric and oceanic circulation, however they are only able to provide hypotheses, and we must remember that these can only be confirmed or denied through observations. There is now much circumstantial evidence that the westerly tip jet does force deep convection in the Irminger Sea, and that the easterly jet does not do so in the Labrador Sea. In order to confirm this, however, further observations are required, and despite the difficulty in obtaining such wintertime observations in the subpolar seas, the author believes this is a

worthwhile endeavour.

References

Aagaard, K. (1970), Wind Driven transports in the Greenland and Norwegian Sea, *Atmos. Ocean*, *17*, 319–337.

Astraldi, M., and G. P. Gasparini (1992), The Seasonal Characteristics of the Circulation in the North Mediterranean Basin and Their Relationship With the Atmospheric-Climatic Conditions, *J. Geophys. Res.*, *97*(C6), 9531–9540.

Bacon, S. (1997), Circulation and Fluxes in the North Atlantic between Greenland and Ireland, *J. Phys. Oceanogr.*, *27*, 1420–1435.

Bacon, S., W. J. Gould, and Y. Jia (2003), Open-ocean convection in the Irminger Sea, *Geophysical Research Letters*, *30*, 1246.

Bakalian, F., S. Hameed, and R. Pickart (2007), Influence of the Icelandic Low latitude on the frequency of Greenland tip jet events: Implications for Irminger Sea Convection, *J. Geophys. Res.*, *112*, C04,020.

Beare, M. I. (1998), The Southampton-East Anglia (SEA) Model: a General Purpose Parallel Ocean Model, *Phys. Chem. Earth*, *23*, 505–509.

Bentsen, M., H. Drange, T. Furevik, and T. Zhou (2004), Simulated variability of the Atlantic meridional overturning circulation, *Climate Dynamics*, *22*(6), 701–720.

Bigg, G. R., S. R. Dye, and M. R. Wadley (2005), Interannual variability in the 1990s in the northern Atlantic and Nordic Seas, *J. Atmos. and Ocean Sci.*, *10*, 123–143.

Bourassa, M. A., D. M. Legler, J. J. O'Brien, and S. R. Smith (2003), SeaWinds validation with research vessels, *J. Geophys. Res.*, *108*, 3019.

Broecker, W. S. (1987), The Biggest Chill, *Natural History*, *96*, 74–82.

Broecker, W. S. (1991), The Great Ocean Conveyor, *Oceanography*, *4*, 79–89.

Broecker, W. S. (1997), Thermohaline Circulation, the Achilles Heel of Our Climate System: Will Man-Made CO2 Upset the Current Balance?, *Science*, *278*(5343), 1582–1588.

Bryan, K. (1969), A numerical method for the study of the circulation of the world ocean, *Journal of Computational Physics*, *4*(3), 347 – 376.

Bryan, K., and M. D. Cox (1972), The circulation of the world ocean: A numerical study. Part I, A Homogeneous Model, *J. Phys. Oceanogr.*, *2*, 319–335.

Bryden, H. L., and S. Imawaki (2001), *Ocean Circulation and Climate*, Academic Press.

Bryden, H. L., H. R. Longworth, and S. A. Cunningham (2005), Slowing of the Atlantic meridional overturning circulation at 25° N, *Nature*, *438*(7068), 655–657.

Businger, S. (1985), The synoptic climatology of polar low outbreaks, *Tellus A*, *37A*(5), 419–432.

Caccia, J. L., G. B., B. Bénech, B. Campistron, and P. Drobinski (2004), Vertical velocity and turbulence aspects during Mistral events as obseved by UHF wind profilers, *Ann. Geophys.*, *22*, 3927–2936.

Cammas, J.-P. e. a. (1999), FASTEX IOP17 cyclone: Introductory synoptic study with field data., *Q. J. Royal. Met. Soc.*, *125*, 3393–3414.

Cassou, C., C. Deser, and M. A. Alexander (2007), Investigating the Impact of Reemerging Sea Surface Temperature Anomalies on the Winter Atmospheric Circulation over the North Atlantic, *Journal of Climate*, *20*(14), 3510–3526.

Centurioni, L., and W. Gould (2004), Winter Conditions in the Irminger Sea Observed with Profiling Floats, *Journal of Marine Science*, *62*, 313–336.

Chanut, J., B. Barnier, W. Large, L. Debreu, T. Penduff, J. M. Molines, and P. Mathiot (2008), Mesoscale Eddies in the Labrador Sea and Their Contribution to Convection and Restratification, *J. Phys. Oceanogr.*, *38*, 1617–1643.

Charney, J. G., R. Fjörtoft, and J. Von Neumann (1950), Numerical Integration of the Barotropic Vorticity Equation, *Tellus*, *2*, 237–254.

Chelton, D. B., and M. H. Freilich (2005), Scatterometer-Based Assessment of 10-m Wind Analyses from the Operational ECMWF and NCEP Numerical Weather Prediction Models, *Monthly Weather Review*, *133*(2), 409–429.

Chelton, D. B., M. H. Freilich, J. M. Sienkiewicz, and J. M. Von Ahn (2006), On the use of QuikSCAT scatterometer measurements of surface winds for marine weather prediction, *Monthly Weather Review*, *134*(8), 2055–2071.

Clarke, R. A. (1984), Transport through the Cape Farewell–Flemish Cap section, *Rapp. P.-V. Reun. Cons. Int. Explor. Mer*, *185*, 120–130.

Clarke, R. A., and J.-C. Gascard (1983), The Formation of Labrador Sea Water. Part I: Large-Scale Processes, *Journal of Physical Oceanography*, *13*(10), 1764–1778.

Condron, A., G. R. Bigg, and I. A. Renfrew (2006), Polar Mesoscale Cyclones in the Northeast Atlantic: Comparing Climatologies from ERA-40 and Satellite Imagery, *Monthly Weather Review*, *134*, 1518–1533.

Condron, A., G. R. Bigg, and I. A. Renfrew (2008), Modelling the impact of polar meoscale cyclones on ocean circulation, *J. Geophys. Res.*, *113*, C10,005.

Cox, M. D. (1984), *A primitive equation, three-dimensional model of the ocean*, Tech. rep., GFDL Ocean Group.

Cunningham, S. A., and T. W. N. Haine (1995), Labrador Sea Water in the Eastern North Atlantic. Part I: A Synoptic Circulation Inferred from a Minimum in Potential Vorticity, *Journal of Physical Oceanography*, *25*(4), 649–665.

Cunningham, S. A., T. Kanzow, D. Rayner, M. O. Baringer, W. E. Johns, J. Marotzke, H. R. Longworth, E. M. Grant, J. J.-M. Hirschi, L. M. Beal, C. S. Meinen, and H. L. Bryden (2007), Temporal Variability of the Atlantic Meridional Overturning Circulation at 26.5°N, *Science*, *317*(5840), 935–938.

Curry, R. G., and M. S. McCartney (2001), Ocean Gyre Circulation Changes Associated with the North Atlantic Oscillation*, *Journal of Physical Oceanography*, *31*(12), 3374–3400.

Danabasoglu, G., and J. C. Mc Williams (1995), Sensitivity of the Global Ocean Circulation to Parameterizations of Mesoscale Tracer Transports, *Journal of Climate*, *8*(12), 2967–2987.

Davis, R. E. (1998), Autonomous floats in WOCE., *Int. WOCE Newsletter*, *30*, 48pp.

de Boyer Montégut, C., G. Madec, A. S. Fischer, A. Lazar, and D. Iudicone (2004), Mixed layer depth over the global ocean: An examination of profile data and a profile-based climatology, *J. Geophys. Res.*, *109*(C12), C12,003.

Deser, C., M. A. Alexander, and M. S. Timlin (2003), Understanding the Persistence of Sea Surface Temperature Anomalies in Midlatitudes, *Journal of Climate*, *16*(1), 57–72.

Dickson, R., J. Lazier, J. Meincke, P. Rhines, and J. Swift (1996), Long-term coordinated changes in the convective activity of the North Atlantic, *Progress In Oceanography*, *38*(3), 241–295.

Dickson, R. R., and J. Brown (1994), The production of North Atlantic Deep Water: Sources, rates, and pathways, *J. Geophys. Res.*, *99*(C6), 12,319–12,341.

Dörnbrack, A., M. Weissmann, S. Rahm, R. Simmet, O. Reitebuch, R. Busen, L. R. Oberpfaffenhofen, and H. Ólafsson (2004), Wind Lidar Observations in the Lee of Greenland, in: *Extended abstracts, 11th Conference on Mountain Meteorology and the Annual Mesoscale Alpine Progremme*.

Doyle, J. D., and M. A. Shapiro (1999), Flow Response to Large-Scale Topography: The Greenland Tip Jet, *Tellus*, *51*, 728–748.

Dritschel, D. G., and M. H. P. Ambaum (1997), A contour-advective semi-Lagrangian algorithm for the simulation of fine-scale conservative fields, *Q. J. Royal. Met. Soc.*, *328*, 129–160.

Eady, E. T. (1949), Long Waves and Cyclone Waves, *Tellus*, *1*, 33–52.

Ebuchi, N., H. C. Graber, and M. J. Caruso (2002), Evaluation of Wind Vectors Observed by QuikSCAT/SeaWinds Using Ocean Buoy Data, *Journal of Atmospheric and Oceanic Technology*, *19*(12), 2049–2062.

Ellett, D. J. (1993), The north-east Atlantic: A fan-assisted storage heater?, *Weather*, *48*, 118–126.

England, M. H. (1993), Representing the global-scale water masses in ocean GCMs, *J. Phys. Oceanogr.*, *23*, 1523–1552.

Fairall, C. W., E. F. Bradley, J. E. Hare, A. A. Grachev, and J. B. Edson (2003), Bulk Parameterization of Air-Sea Fluxes: Updates and Verification for the COARE Algorithm, *Journal of Climate*, *16*(4), 571–591.

Falina, A., A. Sarafanov, and A. Sokov (2007), Variability and renewal of Labrador Sea Water in the Irminger Basin in 1991–2004, *J. Geophys. Res.*, *112*, C01,006.

Fischer, J., and F. A. Schott (1997), Seasonal transport variability of the Deep Western Boundary Current in the equatorial Atlantic, *J. Geophys. Res.*, *102*(C13), 27,751–27,769.

Font, J., P. Puig, J. Salat, A. Palanques, and M. Emelianov (2007), Sequence of hydrographic changes in NW Mediterranean deep water due to the exceptional winter of 2005, *Sci. Mar.*, *71*, 339–346.

Gaillard, F., Y. Desaubies, U. Send, and F. Schott (1997), A four-dimensional analysis of the thermal structure in the Gulf of Lion, *J. Geophys. Res.*, *102*, 12,515–12,537.

Ganachaud, A., and C. Wunsch (2000), Improved estimates of global ocean circulation, heat transport and mixing from hydrographic data, *Nature*, *408*(6811), 453–457.

Garrett, C., and W. Munk (1979), Internal Waves in the Ocean, *Annual Review of Fluid Mechanics*, *11*(1), 339–369.

Gascard, J.-C. (1973), Vertical motions in a region of deep water formation, *Deep Sea Research and Oceanographic Abstracts*, *20*(11), 1011 – 1027.

Gascard, J.-C., A. J. Watson, M.-J. Messias, K. A. Olsson, T. Johannessen, and K. Simonsen (2002), Long-lived vortices as a mode of deep ventilation in the Greenland Sea, *Nature*, *416*, 525–527.

Gill, A. (1982), *Atmosphere-Ocean Dynamics*, Academic Press.

Griffies, S. M., A. Gnanadesikan, R. C. Pacanowski, V. D. Larichev, J. K. Dukowicz, and R. D. Smith (1998), Isoneutral Diffusion in a z-Coordinate Ocean Model, *Journal of Physical Oceanography*, *28*(5), 805–830.

Grossman, R. L., and A. K. Betts (1990), Air-Sea Interaction during an Extreme Cold Air Outbreak from the Eastern Coast of the United States, *Monthly Weather Review*, *118*(2), 324–342.

Haidvogel, D. B., and A. Beckmann (1999), *Numerical Ocean Circulation Modeling*, Imperial College Press.

Haine, T. W. N., S. Zhang, G. W. K. Moore, and I. A. Renfrew (2009), On the impact of high-resolution, high frequency meteorological forcing on Denmark-Strait ocean circulation, *Q. J. Royal. Met. Soc.*, *135*, 2067–2085.

Häkkinen, S. (2001), Variability in sea surface height: A qualitative measure for the meridional overturning in the North Atlantic, *J. Geophys. Res.*, *106*(C7), 13,837–13,848.

Häkkinen, S., and P. B. Rhines (2004), Decline of Subpolar North Atlantic Circulation During the 1990s, *Science*, *304*(5670), 555–559.

Harold, J. M., G. R. Bigg, and J. Turner (1999), Mesocyclone activity over the North-East Atlantic. Part 1: vortex distribution and variability, *International Journal of Climatology*, *19*(11), 1187–1204.

Hay, C., G. W. K. Moore, and R. S. Pickart (2009), A case study of a Greenland lee cyclogenesis event and the subsequent spawning of a tip jet, *Tellus*, p. Submitted.

Hellerman, S., and M. Rosenstein (1983), Normal Monthly Wind Stress Over the World Ocean with Error Estimates, *Journal of Physical Oceanography*, *13*(7), 1093–1104.

Hong, X., R. M. Hodur, and P. J. Martin (2007), Numerical Simulation of Deep-Water Convection in the Gulf of Lion, *Pure and Applied Geophysics*, *164*(10), 2101–2116.

Hoskins, B. J., and P. J. Valdes (1990), On the Existence of Storm-Tracks, *Journal of the Atmospheric Sciences*, *47*(15), 1854–1864.

Hu, A., and G. A. Meehl (2009), Effect of the Atlantic hurricanes on the oceanic meridional overturning circulation and heat transport, *Geophys. Res. Lett.*, *36*, L03,702.

Huang, R. X., and S. Russell (1994), Ventilation of the Subtropical North Pacific, *Journal of Physical Oceanography*, *24*(12), 2589–2605.

Hurrell, J. W. (1995), Decadal Trends in the North Atlantic Oscillation: Regional Temperatures and Precipitation, *Science*, *269*, 676–679.

Hurrell, J. W., and C. Deser (2009), North Atlantic climate variability: The role of the North Atlantic Oscillation, *J. Mar. Syst.*, *78*, 28–41.

Johnson, G. C., M. J. McPhaden, and E. Firing (2001), Equatorial Pacific Ocean Horizontal Velocity, Divergence, and Upwelling*, *Journal of Physical Oceanography*, *31*(3), 839–849.

Jones, H., and J. Marshall (1997), Restratification after Deep Convection, *Journal of Physical Oceanography*, *27*(10), 2276–2287.

Josey, S. A. (2001), A Comparison of ECMWF, NCEP-NCAR, and SOC Surface Heat Fluxes with Moored Buoy Measurements in the Subduction Region of the Northeast Atlantic, *Journal of Climate*, *14*(8), 1780–1789.

Josey, S. A. (2003), Changes in the heat and freshwater forcing of the eastern Mediterranean and their influence on deep water formation, *J. Geophys. Res.*, *108*, 3237.

Josey, S. A., E. C. Kent, and P. K. Taylor (2002), Wind stress forcing of the ocean in the SOC climatology: Comparisons with the NCEP-NCAR, ECMWF, UWM/COADS, and Hellerman and Rosenstein Datasets, *Journal Of Physical Oceanography*, *32*(7), 1993–2019.

Kallberg, P., and P. Berrisford (2005), *ERA-40 Atlas*, Tech. rep., ECMWF.

Kara, A. B., P. A. Rochford, and H. E. Hurlburt (2000), An optimal definition for ocean mixed layer depth, *J. Geophys. Res.*, *105*, 16,803–16,821.

Katsman, C. A., M. A. Spall, and R. S. Pickart (2004), Boundary Current Eddies and Their Role in the Restratification of the Labrador Sea*, *Journal of Physical Oceanography*, *34*(9), 1967–1983.

Killworth, P. D., D. J. Webb, D. Stainforth, and S. M. Paterson (1991), The Development of a Free-Surface Bryan-Cox-Semtner Ocean Model, *Journal of Physical Oceanography*, *21*(9), 1333–1348.

King, J. C., and J. Turner (1997), *Antarctic Meteorology and Climatology*, Cambridge University Press.

Klein, T., and G. Heinemann (2002), Interaction of katabatic winds and mesocyclones near the eastern coast of Greenland, *Meteorological Applications*, *9*(04), 407–422.

Kristjánsson, J. E., and H. McInnes (1999), The impact of Greenland on cyclone evolution in the North Atlantic, *Q. J. Royal. Met. Soc., 125*, 2819–2834.

LabSeaGroup (1998), The Labrador Sea Deep Convection Experiment, *Bulletin of the American Meteorological Society, 79*(10), 2033–2058.

Lamb, P. J. (1984), On the mixed-layer climatology of the north and tropical Atlantic, *Tellus, 36A*, 292–305.

Large, W., and S. Yeager (NCAR), *Diurnal to decadal global forcing for ocean and seaice models: the data sets and climatologies*, Tech. rep., 2004.

Lascaratos, A., W. Roether, K. Nittis, and B. Klein (1999), Recent changes in deep water formation and spreading in the eastern Mediterranean Sea: a review, *Prog. Oceanogr., 44*, 5–36.

Lavender, K. L., R. E. Davis, and W. B. Owens (2000), Mid-depth recirculation observed in the interior Labrador and Irminger seas by direct velocity measurements, *Nature, 407*, 66–69.

Lavender, K. L., R. E. Davis, and W. B. Owens (2002), Observations of Open-Ocean Deep Convection in the Labrador Sea from Subsurface Floats, *Journal of Physical Oceanography, 32*(2), 511–526.

Lazier (1995), *The Salinity Decrease in the Labrador Sea over the Past Thirty Years. In Natural Climate Variability on Decade-to-Century Time Scales,*, National Academy Press.

Lazier, J. (1973), The renewal of Labrador sea water, *Deep Sea Research and Oceanographic Abstracts, 20*(4), 341 – 353.

Lazier, J., R. Hendry, A. Clarke, I. Yashayaev, and P. Rhines (2002), Convection and restratification in the Labrador Sea, 1990-2000, *Deep Sea Research Part I: Oceanographic Research Papers, 49*(10), 1819 – 1835.

Lazier, J. R. (1988), Temperature and salinity changes in the deep Labrador Sea, 1962-1986, *Deep Sea Research Part A. Oceanographic Research Papers, 35*(8), 1247 – 1253.

Lazier, J. R. N. (1980), Oceanographic Conditions at Ocean Weather Ship Bravo, 1964–1974, *Atmosphere-Ocean, 18*, 227–238.

Le Provost, C., and N. C. Flemming (Eds.) (1998), *"The EuroGOOS Atlantic Workshop Report", EuroGOOS Publication No. 9*, Southampton Oceanography Centre.

Leaman, K. D., and F. A. Schott (1991), Hydrographic Structure of the Convection Regime in the Gulf of Lions: Winter 1987, *Journal of Physical Oceanography, 21*(4), 575–598.

Levitus, S., and T. P. Boyer (1994), *World Ocean Atlas 1994.*, NODC.

Lilly, J. M., and P. Rhines (2002), Coherent Eddies in the Labrador Sea Observed from a Mooring, *J. Phys. Oceanogr., 32*, 585–598.

Lilly, J. M., P. B. Rhines, F. Schott, K. Lavender, J. Lazier, U. Send, and E. D'Asaro (2003), Observations of the Labrador Sea eddy field, *Progress In Oceanography, 59*(1), 75 – 176.

Manca, B. B., V. Kovacevic, M. Gacic, and D. Viezzoli (2002), Dense water formation in the outhern Adriatic Sea and spreading into the Ionian Sea in the period 1997–1999, *Journal of Marine Systems*, *33*, 133–154.

Marotzke, J., and J. Willebrand (1991), Multiple Equilibria of the Global Thermohaline Circulation, *Journal of Physical Oceanography*, *21*(9), 1372–1385.

Marshall, J., and F. Schott (1999), Open ocean deep convection: Observations, models and theory, *Review of Geophysics*, *37*(1), 1–64.

Martin, P. J. (1985), Simulation of the Mixed Layer at OWS November and Papa With Several Models, *J. Geophys. Res.*, *90*(C1), 903–916.

Martin, R., and G. W. K. Moore (2007), Air-sea interaction associated with a Greenland reverse tip jet, *Geophysical Research Letters*, *34*(24), L24,802.

McCartney, and Talley (1984), Warm-to-cold water conversion in the northern North Atlantic Ocean, *J. Phys. Oceanogr.*, *14*, 922–935.

MEDOC-Group (1970), Observation of formation of deep water in the Mediterranean Sea, *Nature*, *227*, 1037–1040.

Mesinger, F., and A. Arakawa (1976), *Numrical methods used in atmospheric models*, Tech. rep., GARP Publication series No. 14.

Mesinger, F., G. DiMego, E. Kalnay, K. Mitchell, P. C. Shafran, W. Ebisuzaki, D. Jovi?, J. Woollen, E. Rogers, E. H. Berbery, M. B. Ek, Y. Fan, R. Grumbine, W. Higgins, H. Li, Y. Lin, G. Manikin, D. Parrish, and W. Shi (2006), North American Regional Reanalysis, *Bulletin of the American Meteorological Society*, *87*(3), 343–360.

Miller, J. R. (1976), The Salinity Effect in a Mixed Layer Ocean Model, *Journal of Physical Oceanography*, *6*(1), 29–35.

Millot, C. (1987), The Circulation of the Levantine Intermediate Water in the Algerian Basin, *J. Geophys. Res.*, *92*, 8265–8276.

Mills, B. J., and M. R. Anderson (2003), Monitoring a Piteraq strom system using DMSP imagery and QuikSCAT wind data., in: *12th Conf. on Satellite Meteorology and Oceanography.*

Montgomery, M. T., and B. F. Farrell (1992), Polar Low Dynamics, *J. Atmos. Sci.*, *49*, 2484–2505.

Moore, G. (2003), Gale Force Winds Over the Irmnger Sea to the East of Cape Farewell, Greenland, *Geophysical Research Letters*, *30*, 1894.

Moore, G. W. K., R. S. Pickart, and I. A. Renfrew (2008), Buoy observations from the windiest location in the world ocean, Cape Farewell, Greenland, *Geophys. Res. Lett.*, *35*, L18,802.

Moore, G. W. K., and I. A. Renfrew (2005), Tip jets and barrier winds: A QuikSCAT climatology of high wind speed events around Greenland, *Journal of Climate*, *18*, 3713–3725.

Moore, G. W. K., and P. W. Vachon (2002), A polar low over The Labrador Sea: Interactions with topography and an upper-level potential vorticity anomaly, and an observation by RADARSAT-1 SAR, *Geophys. Res. Lett.*, *29*(16), 1773–.

Obchinnikov, I. M., V. I. Zats, V. G. Krvosheya, and A. I. Udodov (1985), Formation of Deep Eastern Mediterranean waters in the Adriatic Sea, *Oceanology, 25*, 704–707.

Ólafsson, H., and P. Bougeault (1996), Nonlinear flow pas an elliptic mountain ridge, *J. Atmos. Sci., 53*, 2465–2489.

Outten, S. D., I. A. Renfrew, and G. N. Petersen (2009), An easterly tip jet off Cape Farewell, Greenland. Part II: Simulations and dynamics, *Q. J. Royal. Met. Soc., 135*, 1934–1949.

Pacanowski, R., and S. G. H. Philander (1981), Parameterization of vertical mixing in numerical models of tropical oceans, *J. Phys. Oceanogr., 11*, 1443–1451.

Pagowski, M., and G. W. K. Moore (2001), A Numerical Study of an Extreme Cold-Air Outbreak over the Labrador Sea: Sea Ice, Air-Sea Interaction, and Development of Polar Lows, *Monthly Weather Review*, *129*(1), 47–72.

Parkinson, C., and W. Washington (1979), A Large-Scale Numerical Model of Sea Ice, *J. Geophys. Res., 84*, 311–337.

Parkinson, C. L., J. C. Comiso, H. J. Zwally, D. J. Cavalieri, P. Gloersen, and W. J. Campbell (1987), *Arctic sea ice, 1973–1976: Satellite passive-microwave observations*, Tech. rep., NASA.

Pavia, E. G., and J. J. O'Brien (1986), Weibull Statistics of Wind Speed over the Ocean, *Journal of Climate and Applied Meteorology*, *25*(10), 1324–1332.

Pedlosky, J. (1987), *Geophysical Fluid Dynamics*, Springer.

Petersen, G. N., H. Ólafsson, and J. E. Kristjánsson (2003), Flow in the Lee of Idealized Mountains and Greenland, *Journal of the Atmospheric Sciences*, *60*(17), 2183–2195.

Petersen, G. N., and I. A. Renfrew (2009), Aircraft-based observations of air-sea fluxes over Denmark Strait and the Irminger Sea during high wind speed conditions, *Quarterly J. Royal Meteorol. Soc., 135*, 2030–2045.

Pickart, R. S., N. G. Hogg, and W. M. Smethie (1989), Determining the Strength of the Deep Western Boundary Current Using the Chlorofluoromethane Ratio, *Journal of Physical Oceanography*, *19*(7), 940–951.

Pickart, R. S., M. A. Spall, M. H. Ribergaard, G. W. K. Moore, and R. F. Milliff (2003a), Deep convection in the Irminger Sea forced by the Greenland tip jet, *Nature*, *424*, 152–156.

Pickart, R. S., F. Straneoa, and G. W. K. Moore (2003b), Is Labrador Sea Water formed in the Irminger basin?, *Deep Sea Research, 50A*, 23–52.

Pickart, R. S., D. J. Torres, and R. A. Clarke (2002), Hydrography of the Labrador Sea During Active Convection, *J. Phys. Oceanogr., 32*, 428–457.

Price, J. F., R. A. Weller, and R. Pinkel (1989), Diurnal cycling: Observations and models of the upper ocean response to diurnal heating, cooling, and wind mixing, *J. Geophys. Res., 91*, 8411–8427.

Quilfen, Y., C. Prigent, B. Chapron, A. A. Mouche, and N. Houti (2007), The potential of QuikSCAT and WindSat observations for the estimation of sea surface wind vector under severe weather conditions, *J. Geophys. Res., 112*, C09,023.

Rahmstorf, S. (1993), A fast and complete convection scheme for ocean models, *Ocean Modelling*, *101*, 9–11.

Rahmstorf, S. (1995), Bifurcations of the Atlantic thermohaline circulation in response to changes in the hydrological cycle, *Nature*, *378*, 145–149.

Rahmstorf, S., M. Crucifix, A. Ganopolski, H. Goosse, I. Kamenkovich, R. Knutti, G. Lohmann, R. Marsh, L. A. Mysak, Z. Wang, and A. J. Weaver (2005), Thermohaline circulation hysteresis: A model intercomparison, *Geophys. Res. Lett.*, *32*, L23,605.

Rasmussen, E. A., and J. Turner (2003), *Polar Lows. Mesoscale Weather Systems in the Polar Regions*, Cambridge University Press.

Read, J. F., and W. J. Gould (1992), Cooling and freshening of the subpolar North Atlantic Ocean since the 1960s, *Nature*, *360*(6399), 55–57.

Ren, X., W. Perrie, Z. Long, and J. Gyakum (2004), Atmosphere-Ocean Coupled Dynamics of Cyclones in the Midlatitudes, *Monthly Weather Review*, *132*(10), 2432–2451.

Renfrew, I. A., and G. W. K. Moore (1999), An Extreme Cold-Air Outbreak over the Labrador Sea: Roll Vortices and Air-Sea Interaction, *Monthly Weather Review*, *127*(10), 2379–2394.

Renfrew, I. A., G. W. K. Moore, P. S. Guest, and K. Bumke (2002), A Comparison of Surface Layer and Surface Turbulent Flux Observations over the Labrador Sea with ECMWF Analyses and NCEP Reanalyses, *Journal of Physical Oceanography*, *32*, 383–400.

Renfrew, I. A., G. W. K. Moore, *et al.* (2008), The Greenland Flow Distortion Experiment, *Bulletin of the American Meteorological Society*, *Sep*, 1307–1324.

Renfrew, I. A., S. D. Outten, and G. W. K. Moore (2009), An easterly tip jet off Cape Farewell, Greenland. Part I: Aircraft observations, *Q. J. Royal. Met. Soc.*, *135*, 1919–1933.

Reynauld, T., A. Weaver, and R. Greatbatch (1995), Summer mean circulation of the northwestern North Atlantic, *J. Geophys. Res.*, *100*, 779–816.

Reynolds, R. W., and T. M. Smith (1994), Improved Global Sea Surface Temperature Analyses Using Optimum Interpolation, *Journal of Climate*, *7*(6), 929–948.

Rhein, M. (1994), The Deep Western Boundary Current: tracers and velocities, *Deep Sea Research Part I: Oceanographic Research Papers*, *41*(2), 263 – 281.

Rind, D., P. deMenocal, G. Russell, S. Sheth, D. Collins, G. Schmidt, and J. Teller (2001), Effects of glacial meltwater in the GISS coupled atmosphere ocean model - 1. North Atlantic Deep Water response, *Journal of Geophysical Research-atmospheres*, *106*(D21), 27,335–27,353.

Rixen, M. e. a. (2005), The Western Mediterranean Deep Water: A proxy for climate change, *Geophys. Res. Lett.*, *32*, L12,608.

Roach, A. T., K. Asgaard, and F. Carsey (1993), Coupled Ice-Ocean Variability in the Greenland Sea, *Atmosphere-Ocean*, *31*, 319–337.

Roether, W., B. B. Manca, B. Klein, D. Bregant, D. Georgopoulos, V. Bietzel, V. Kovacevic, and A. Luchetta (1996), Recent changes in Eastern Mediterranean Deep Waters, *Science*, *271*, 333–335.

Rogers, J. C., and M.-P. Hung (2008), The Odden ice feature of the Greenland Sea and its association with atmospheric pressure, wind, and surface flux variability from reanalyses, *Geophys. Res. Lett.*, *35*, L08,504.

Rudels, B., D. Quadfasel, H. Friedrich, and M.-N. Houssais (1989), Greenland Sea Convection in the Winter of 1987-1988, *J. Geophys. Res.*, *94*(C3), 3223–3227.

Sampe, T., and S.-P. Xie (2007), Mapping High Sea Winds from Space: A Global Climatology, *Bulletin of the American Meteorological Society*, *88*(12), 1965–1978.

Schott, F., and K. D. Leaman (1991), Observations with Moored Acoustic Doppler Current Profilers in the Convection Regime in the Golfe du Lion, *Journal of Physical Oceanography*, *21*(4), 558–574.

Schott, F., M. Visbeck, and J. Fischer (1993), Observations of Vertical Currents and Convection in the Central Greenland Sea During the Winter of 1988–1989, *J. Geophys. Res.*, *98*(C8), 14,401–14,421.

Schott, F., M. Visbeck, U. Send, J. F. nad L. Stramma, and Y. Desaubies (1996), Observations of Deep Convection in the Gulf of Lions, Northern Mediterranean, during the Winter of 1991/92, *J. Phys. Oceanogr.*, *26*, 505–524.

Schott, F. A., J. Fischer, M. Dengler, and R. Zantopp (2006), Variability of the Deep Western Boundary Current east of the Grand Banks, *Geophys. Res. Lett.*, *22*, L21S07.

Schröder, K., G. P. Gasparini, M. Tangherlini, and M. Astraldi (2006), Deep and intermediate water in the western Mediterranean under the influence of the Eastern Mediterranean Transient, *Geophys. Res. Lett.*, *33*, L21,607.

Schroeder, K., A. Ribotti, M. Borghini, R. Gorgente, A. Perilli, and G. P. Gasparini (2008), An extensive western Mediterranean deep water renewal between 2004 and 2006, *Geophys. Res. Lett.*, *35*, L18,605.

Scorer, R. S. (1988), Sunny Greenland, *Quart. J. Roy. Meteor. Soc.*, *114*, 3–29.

Semtner, A. J. (1974), *A general circulation model for the World Ocean.*, Tech. rep., University of California, Los Angeles, Dept. Meteor. Tech.

Smith, S. D. (1988), Coefficients for sea surface wind stress, heat flux, and wind profiles as a function of wind speed and temperature, *J. Geophys. Res.*, *93(C12)*, 15,467–15,472.

Smith, S. R., D. M. Legler, and K. V. Verzone (2001), Quantifying Uncertainties in NCEP Reanalyses Using High-Quality Research Vessel Observations, *Journal of Climate*, *14*(20), 4062–4072.

Spall, M. A. (1991), A Diagnostic Study of the Wind- and Buoyancy-Driven North Atlantic Circulation, *J. Geophys. Res.*, *96*(C10), 18,509–18,518.

Spall, M. A., and R. S. Pickart (2003), Wind-Driven Recirculations and Exchange in the Labrador and Irminger Seas*, *Journal of Physical Oceanography*, *33*(8), 1829–1845.

Spencer, M. W., C. Wu, and D. G. Long (1997), Tradeoffs in the design of a spaceborne scanning pencil-beam scatterometer, *IEEE Trans. Geosci. Remote Sens.*, *35*, 115–126.

Stömmel, H. (1961), Thermohaline Convection with Two Stable Regimes of Flow, *Tellus*, *13*(2), 224–230.

Sun, B., L. Yu, and R. A. Weller (2003), Comparisons of Surface Meteorology and Turbulent Heat Fluxes over the Atlantic: NWP Model Analyses versus Moored Buoy Observations*, *Journal of Climate*, *16*(4), 679–695.

Sutton, R. T., and M. R. Allen (1997), Decadal predictability of the north Atlantic sea surface temperature and climate, *Nature*, *388*, 563–567.

Sy, A., M. Rhein, L. J. R. N., K. P. Koltermann, J. Meincke, A. Putzka, and M. Bersch (1997), Surprisingly rapid spreading of newly formed intermediate waters across the North Atlantic Ocean, *Nature*, *386*, 675–679.

Talley, L. D., and M. S. McCartney (1982), Distribution and Circulation of Labrador Sea Water, *J. Phys. Oceanogr.*, *12*, 1189–1205.

Thompson, R. O. R. Y. (1976), Climatological models of the surface mixed layer of the ocean, *J. Phys. Oceanogr.*, *6*, 496–503.

Thompson, S. R. (1995), Sills of the Global Ocean: A compilation, *Ocean model*, *109*, 7–9.

Treguier, A. M., S. Theetten, E. P. Chassignet, T. Penduff, R. Smith, L. Talley, J. O. Beismann, and C. Bning (2005), The North Atlantic Subpolar Gyre in Four High-Resolution Models, *Journal of Physical Oceanography*, *35*(5), 757–774.

Trenberth, K. E., and J. M. Caron (2001), Estimates of Meridional Atmosphere and Ocean Heat Transports, *Journal of Climate*, *14*(16), 3433–3443.

Uppala, S. M., P. W. Kllberg, A. J. Simmons, U. Andrae, V. D. C. Bechtold, M. Fiorino, J. K. Gibson, J. Haseler, A. Hernandez, G. A. Kelly, X. Li, K. Onogi, S. Saarinen, N. Sokka, R. P. Allan, E. Andersson, K. Arpe, M. A. Balmaseda, A. C. M. Beljaars, L. V. D. Berg, J. Bidlot, N. Bormann, S. Caires, F. Chevallier, A. Dethof, M. Dragosavac, M. Fisher, M. Fuentes, S. Hagemann, E. Hlm, B. J. Hoskins, L. Isaksen, P. A. E. M. Janssen, R. Jenne, A. P. Mcnally, J.-F. Mahfouf, J.-J. Morcrette, N. A. Rayner, R. W. Saunders, P. Simon, A. Sterl, K. E. Trenberth, A. Untch, D. Vasiljevic, P. Viterbo, and J. Woollen (2005), The ERA-40 re-analysis, *Q. J. Royal. Met. Soc.*, *131*, 2961–3012.

Våge, K., R. S. Pickart, G. W. K. Moore, and M. H. Ribergaard (2008), Winter mixed-layer development in the central Irminger Sea: The effect of strong, intermittent wind events, *Journal of Physical Oceanography*, *38*, 541–565.

Våge, K., R. S. Pickart, V. Thierry, G. Reverdin, C. M. Lee, B. Petrie, T. A. Agnew, A. Wong, and M. H. Ribergaard (2009a), Surprising return of deep convection to the subpolar North Atlantic Ocean in winter 2007-2008, *Nature Geosci*, *2*(1), 67–72.

Våge, K., T. Spengler, H. C. Davies, and R. S. Pickart (2009b), Multi-event analysis of the westerly Greenland tip jet based upon 45 winters in ERA-40, *Q. J. Royal. Met. Soc.*, *35*, 1999–2011.

Visbeck, M., J. Fischer, and F. Schott (1995), Preconditioning the Greenland Sea for deep convection: Ice formation and ice drift, *J. Geophys. Res.*, *100*(C9), 18,489–18,502.

Wadhams, P., J. C. Comiso, E. Prussen, S. Wells, M. Brandon, E. Aldworth, T. Viehoff, R. Allegrino, and D. R. Crane (1996), The development of the Odden ice tongue in the Greenland Sea during winter 1993 from remote sensing and field observations, *J. Geophys. Res.*, *101*(C8), 18,213–18,235.

Wadhams, P., J. Holfort, E. Hansen, and J. P. Wilkinson (2002), A deep convective chimney in the winter greenland sea, *Geophys. Res. Lett.*, *29*(10), 1434.

Wadley, M. R., and G. R. Bigg (2002), Impact of flow through the Canadian Archipelago and Bering Strait on the North Atlantic and Arctic circulation: An ocean modelling study, *Quarterly Journal of the Royal Meteorological Society*, *128*(585), 2187–2203.

Wallace, D. W. R., and J. R. N. Lazier (1988), Anthropogenic chlorofluoromethanes in newly formed Labrador Sea Water, *Nature*, *332*(6159), 61–63.

Wentz, F., D. K. Smith, C. A. Mears, and C. L. Gentemann (2001), Advanced algorithms for QuikScat and SeaWinds/AMSR, *Geoscience and Remote Sensing Symposium*, *3*, 1079–1081.

Willis, J. K. (2010), Can in situ floats and satellite altimeters detect long-term changes in Atlantic Ocean overturning?, *Geophys. Res. Lett.*, *37*(6), L06,602.

Worthington, L. (1970), The Norwegian Sea as a mediterranean basin, *Deep Sea Research and Oceanographic Abstracts*, *17*(1), 77 – 84.

Wunsch, C., and R. Ferrari (2004), Vertical Mixing, Energy, and the General Circulation of the Oceans, *Annu. Rev. Fluid Mech.*, *36*, 281–341.

Wüst, G. (1935), Die Stratosphäre, *Wissenschaftliche Ergebnisse der Deutschen Atlantischen Expedition auf dem Vermessungs- und Forschungsschiff „Meteor" 1925–1927*, *6*, 109–288.

Yashayaev, I. (2007), Hydrographic changes in the Labrador Sea, 1960-2005, *Progress In Oceanography*, *73*(3-4), 242–276, observing and Modelling Ocean Heat and Freshwater Budgets and Transports.

Zeng, X., M. Zhao, and R. E. Dickinson (1998), Intercomparison of Bulk Aerodynamic Algorithms for the Computation of Sea Surface Fluxes Using TOGA COARE and TAO Data, *Journal of Climate*, *11*(10), 2628–2644.